

A polystyrene modified sponges for effective oil/water separation

Balaji T. Khogare^{1,2}, S. R. Kulal², K. K. Rangar², G. D. Salunkhe², P. G. Pawar³,
M.H. Karenavar⁴, P. M. Kadam⁵ and Sanjay S. Latthe^{1*}

¹ Self-cleaning Research Laboratory, Department of Physics, Raje Ramrao College,
Jath 416 404, Maharashtra, India.

² Department of Chemistry, Raje Ramrao College, Jath 416 404, Maharashtra, India

³ Shivaji Polytechnic College, Sangola 413307, Maharashtra, India.

⁴ Department of Zoology, Raje Ramrao College, Jath 416 404, Maharashtra, India

⁵ K.W.C. College, Sangli, Maharashtra, India, Corresponding author*: latthes@gmail.com

Abstract

We present a polystyrene modified sponge for the selective absorption of oil from water effectively. The process of modifying sponge does not require any elaborate synthesis processes or equipment and it is not environmentally hazardous, thus promoting potential in environmental applications. The proposed polystyrene modified sponge can be elastically deformed into any size and shape, and it can be compressed repeatedly in air or liquids without collapsing. Therefore, absorbed oils and organic solvents can be readily removed and reused by simply squeezing the polystyrene coated sponge, enabling excellent recyclability. Oil-water separation using unmodified/pristine and polystyrene modified sponge was studied. Oil mixed in water was effectively separated using polystyrene modified sponge whereas water trace was observed in separated oil during oil-water separation experiments using pristine sponge.

Keywords: Polystyrene, Sponge, Oil spill cleanup, Water remediation, Superhydrophobic.

1. Introduction

With the increasing awareness of environmental protection and need for water recycling, there is a growing demand for technologies that can efficiently absorb, remove, and transfer oil spills or organic contaminants from water. For example, accidents of ships in the sea can often result in release of spill oil in seawater and rivers can also be contaminated by wastewater from industry. To mitigate this problem, numerous of oil sorbent materials such as nanocomposites [1-3], foams [4-8], and carbon nanotube materials [9, 10] have been developed. However, these materials are usually requiring cost consuming and complicated processes to fabricate, while others show poor efficiency in oil removal, exhibiting low sorption capacity and poor selectivity for the uptake of spilled oils. Therefore, demand for finding novel materials with high absorption capacity, high selectivity, easy fabrication, and low cost is highly imperative.

Solution immersion is a simple but versatile platform that can enable easy adjustment of the surface structure and composition required for special wetting behaviors; and it also allows for the large-scale producing of functional coatings on almost any substrate, which makes it scalable and versatile for oil-water separation applications. Thus, solution immersion holds a great potential for

functionalizing base materials toward solving the aforementioned problems that occur with the previous oil-water separation materials.

Herein, superhydrophobic and oleophilic sponges are fabricated by polystyrene through a solution immersion process. It is found that water droplets can roll off these material surfaces easily, while organic liquids such as hexane can wet them completely. Exploiting these materials superhydrophobicity and superoleophilicity, the obtained materials were applied to separate oil from water efficiently. This study contributes the development of advanced oil-water separation materials for practical applications.

2. Experimental

2.1 Materials

Polystyrene (average Mw ~ 192,000) was purchased from SIGMA-ALDRICH, Co., USA. Toluene (99.5%) was purchased from Loba Chemie Pvt. Ltd., Mumbai, India. Hexane was purchased from Spectrochem Pvt. Ltd., Mumbai, India and sponge were purchased from a local store and cleaned with acetone and deionized water sequentially in an ultrasonic cleaner before use.

2.2 Preparation of polystyrene (PS) solution

A 5, 10, 20, and 30 mg/ml polystyrene was weighed in four 50 ml size glass beaker and dissolved in toluene using an ultrasonic cleaner.

2.3 Preparation of the polystyrene (PS) coated sponge

A 2.5 X 2.5 cm piece of sponge was first cleaned with distilled water and dried at room temp. The as dried sponge was then dipped into a polystyrene solution for 10 min. Then, the polystyrene modified sponge was removed from beaker and placed to dry in oven at 100 °C for 1 h to obtain superhydrophobic sponge.

Result and Discussion

2.4 Measurement of contact angle (CA)

Importantly, the proposed polystyrene sponge has both properties of hydrophobicity and oleophilicity. To demonstrate these properties, we first measured the water contact angle to investigate the surface wettability of the PS modified polystyrene sponge. When a water droplet is allowed to sit on the surface of the PS modified polystyrene sponges, the contact angle indicates high hydrophobicity (>120-130°) (Fig. 1).

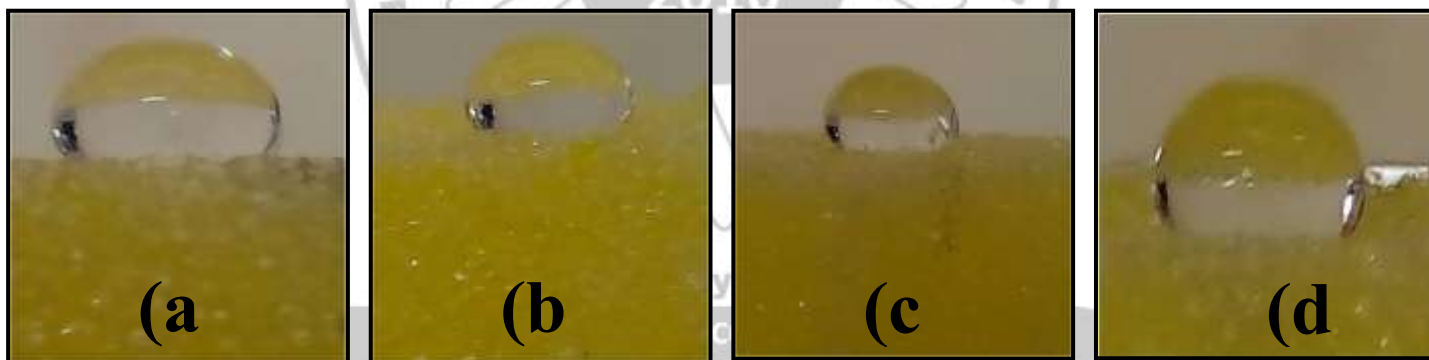
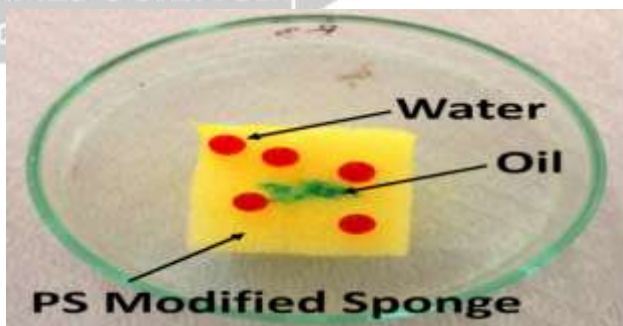


Fig. 1: (a) PS (5 mg/ml) modified sponge having $\theta = 122^\circ$. (b) PS (10mg/ml) modified sponge having $\theta = 125^\circ$. (c) PS (20mg/ml) modified sponge having $\theta = 120^\circ$. (d) PS (30mg/ml) modified sponge having $\theta = 122^\circ$.

Fig. 2: PS (30 mg/ml) modified sponge showing high hydrophobicity (water droplet colored with methyl red indicator) and strong superoleophilicity (chloroform colored with green color).



PS Solution (Concentration)	5 mg/ml	10 mg/ml	20 mg/ml	30 mg/ml
Contact angle (θ)	122°	125°	120°	122°

2.5 Removal oil from water using PS modified sponge and unmodified sponge

The oil absorption process is illustrated in Fig. 3. Fig. 3 show the process of chloroform (dyed with green color) being absorbed by the PS (30mg/ml) modified sponge from an oil-water mixture in a static system. When the PS modified sponge is placed in the mixture, it selectively absorbs chloroform from the mixture. An only concern is that the PS can be dissolved by the chloroform from PS modified sponge and so the PS modified sponge cannot be reused after 3-4 cycles of oil-water separation. However, other oils which are no miscible with PS can be used for oil-water separation purpose using this PS modified sponge.

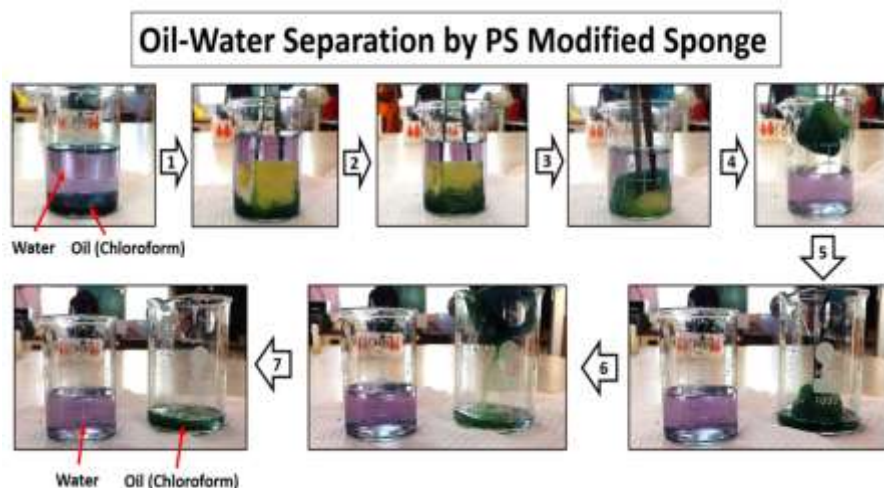


Fig. 3: By utilizing the PS (30 mg/ml) modified sponges with hydrophobic and oleophilic properties, a layer of oil (chloroform dyed with green color) was removed by adding PS modified sponges to the oil.



Fig. 4: Unmodified/pristine sponge used for chloroform/water mixture separation.

3. Conclusion

We have developed an inexpensive method for converting normal sponge into the superhydrophobic sponge by using polystyrene. This polystyrene modified sponge has advantages of large availability, low-cost, and mechanical flexibility. Meanwhile, the polystyrene coated sponge exhibit high oil/water selectivity in the cleanup of oil from water. Therefore, this kind of polystyrene coated sponge might be a promising substitute for the conventional absorbent materials used in the large-scale removal of oil spills from water surfaces.

Acknowledgement

This work is financially supported by DST-INSPIRE Faculty Scheme, Department of Science and Technology (DST), Government of India. [DST/INSPIRE/04/2015/000281].

References

1. Y. Chu, Q. M. Pan. Three-dimensionally macroporous Fe/C nanocomposites as highly selective oil-absorption materials. *ACS Appl Mater Interfaces* 2012;4:2420–5.
2. S. Y. Tao, Y. C. Wang, Y. L. An. Superwetting monolithic SiO₂ with hierarchical structure for oil removal. *J Mater Chem* 2011;21:11901–7.
3. D. D. Nguyen, N. H. Tai, S. B. Lee, W. S. Kuo. Superhydrophobic and Superoleophilic properties of graphene-based sponges fabricated using a facile dip coating method. *Energy Environ Sci* 2012;5:7908–12.
4. X. C. Gui, J. Q. Wei, K. L. Wang, A. Y. Cao, H. W. Zhu, Y. Jia. Carbon nanotube sponges. *Adv Mater* 2010;22:617–21.
5. D. P. Hashim, N. T. Narayanan, J. M. Romo-Herrera, D. A. Cullen, M. G. Hahm, P. Lezzi. Covalently bonded three-dimensional carbon nanotube solids via boron induced nanojunctions. *Sci Rep* 2012;2:363–70.
6. P. Calcagnile, D. Fragouli, I. S. Bayer, G. C. Anyfantis, L. Martiradonna, P. D. Cozzoli. Magnetically driven floating foams for the removal of oil contaminants from water. *ACS Nano* 2012;6:5413–9.
7. Q. Zhu, Q. M. Pan, F. T. Liu. Facile removal and collection of oils from water surfaces through superhydrophobic and superoleophilic sponges. *J Phys Chem C* 2011;115:17464–70.
8. Q. Zhu, Y. Chu, Z. K. Wang, N. Chen, L. Lin, F. T. Liu. Robust superhydrophobic polyurethane sponge as a high reusable oil-absorption material. *J Mater Chem A* 2013;1:5386–93.
9. C. Lee, S. Baik. Vertically-aligned carbon nano-tube membrane filters with superhydrophobicity and superoleophilicity. *Carbon* 2010;48:2192–7.
10. X. C. Gui, H. B. Li, K. L. Wang, J. Q. Wei, Y. Jia, Z. Li. Recyclable carbon nanotube sponges for oil absorption. *Acta Mater* 2011;59:4798–804.

When a water droplet (colored with methyl red indicator) is allowed to sit on the surface of the PS (30mg/ml) modified sponge and shows high hydrophobicity. In contrast to its high hydrophobicity, the PS (30mg/ml) modified sponge shows strong superoleophilic properties. For instance, when a transformer oil (chloroform) dyed with green colour was placed on the surface of the PS (30mg/ml) modified sponge, it was quickly absorbed into the sponge (Fig. 2).

An unmodified/pristine sponge was also studied for comparison (Fig. 4). Unmodified sponge was dipped in the mixture of chloroform (dyed with pink color)/water. The sponge can absorb chloroform as well as water and the sponge can be squeezed in another cleaned beaker, but there is no separation of chloroform from water.

Cobalt rich Ferrite for Magnetostrictive Sensor

S. G. Kakade^{1,2#}, R.C. Kambale¹ and Y. D. Kolekar^{1#}

¹Department of Physics, Savitribai Phule Pune University, Pune - 411 007

²Department of Physics, Sir Parashurambhau College, Pune - 411 030

Corresponding Author: sundipkakade@gmail.com; ydk@physics.unipune.ac.in

Abstract

Erbium (Er) substituted cobalt rich magnetostrictive nanocrystalline cobalt ferrites have been synthesized by sol gel auto combustion method. X- ray diffraction study confirms the spinel crystal structure and the purity of samples. The effect of Er concentration on the structural, magnetic and magnetostrictive properties of cobalt rich cobalt ferrite has been studied. The pure phase formation of spinel cubic lattice for erbium (Er) substitution was observed till the solubility limit ($x \leq 0.10$) and the secondary orthoferrite phase of ErFeO_3 begins to form for higher concentration of Erbium. All the samples show the typical hysteresis behavior with decrease in magnetization due to weak superexchange interaction. The Er substituted cobalt rich cobalt ferrites shows higher value of magnetostrictive coefficient; $\lambda_{\text{max}} = 210$ ppm at lower applied field with the maximum value of magnetomechanical coupling coefficient ($d\lambda/dH = 327 \times 10^3$ ppm/Oe). The obtained results are significant for magnetostrictive sensing application.

Introduction

It is well known and accepted that among the spinel ferrite family, the cobalt based ferrite are most versatile and hard ferrimagnetic material. Cobalt ferrite shows the unique properties like high coercivity (5400 Oe), high magneto-crystalline anisotropy, moderate saturation magnetization (80 emu/g) at 300 K and Faraday rotation.¹⁻² A large fraction of empty interstitial sites makes the spinel structure a very open and favorable to cation migration.¹⁻² The Co^{2+} ions in CFO exhibit a strong spin-orbit (L-S) coupling and induces the large magnetocrystalline anisotropy. Moreover, the magnetic behavior of the materials will vary with Co^{2+} site occupation.² The most remarkable size dependent property of the magnetic particles is an increase in the coercivity compared to that of bulk material with the decrease in the particle size. In order to enhance the magnetocrystalline anisotropy and magnetostrictive properties, the partial substitution of Fe by Co and Er in CFO matrix has been proposed.

Experimental details

Synthesis:

Er ion substituted cobalt rich cobalt ferrite compounds, with x ranging from 0.00 to 0.20, were prepared by sol gel auto combustion route. The analytical reagent (AR) grade nitrates such as $\text{Co}(\text{NO}_3)_2 \cdot 6\text{H}_2\text{O}$, $\text{Fe}(\text{NO}_3)_3 \cdot 9\text{H}_2\text{O}$, $\text{Er}(\text{NO}_3)_3 \cdot 5\text{H}_2\text{O}$ and citric acid ($\text{C}_6\text{H}_8\text{O}_7 \cdot \text{H}_2\text{O}$) were used as raw precursors. An appropriate amounts of metal nitrates and citric acid with (1:1) were dissolved in

deionized water to form a mixed solution; Ammonia (in liquid form: NH_4OH) was added, drop by drop, into the solution and pH (≈ 7) was maintained, helpful to stabilize nitrate-citrate solution under the heating at 60 °C with continuous stirring to homogenize the solution and to form the redox mixture of citric acid and metal nitrates for combustion reaction. The sol was changed into a gel at 80 °C and then in xerogel. Continuous heating to the xerogel was maintained until a self-propagating combustion process occurred and the black powder was obtained. The calcination and sintering temperatures was determined from the thermo gravimetry-differential thermal analysis (TG-DTA). To overcome drying stresses, increasing the contribution to the legends and also to strengthen the sol gel network, liquid ammonia was used as a drying control chemical additives.¹ It also plays the role of chelating agents to trap the metal cations to form their network in the reaction.

Result and Discussion

Magnetic and Magnetostrictive Properties

The magnetic hysteresis loops obtained for $\text{Co}_{1.1}\text{Fe}_{1.9-x}\text{Er}_x\text{O}_4$ ($x = 0.0-0.2$) at 300 K are shown in Fig. 1. All the compositions exhibit typical ferrimagnetic hysteresis loop. In the present study, the decrease of magnetization with Er^{3+} content may be explained by a combination of more lattice defects and weaker magnetic superexchange interactions between A and B sites in the ferrites.^{1,3} As, Er^{3+} ions have larger ionic radii than Fe^{3+} , the Er^{3+} substitution may distorts the lattice and

eliminates the homogeneous composition, so causes the deterioration in μ_B . Furthermore, because of their large ionic radii, Er^{3+} ions may replace Fe^{3+} on *B* sites thus reducing the magnetic moment as well as decreasing the strong Fe^{3+} - Fe^{3+} negative interaction resulting from Er^{3+} incorporation due to antiferromagnetic coupling.^{1,3}

The magnetostrictive properties depend upon the processing parameters such as synthesis

method, pressure applied while making pellets, sintering atmosphere, temperature and sintering time.³⁻⁴ Recently, Bulai et al. shows the maximum magnetostrictive coefficient $\lambda_{\text{max}}=160$ ppm at an applied field of 7kOe for $\text{Er} = 0.03$ in bulk CFO. However, the λ_{max} obtained at lower field is 25 ppm for the applied fields of 2.2kOe.

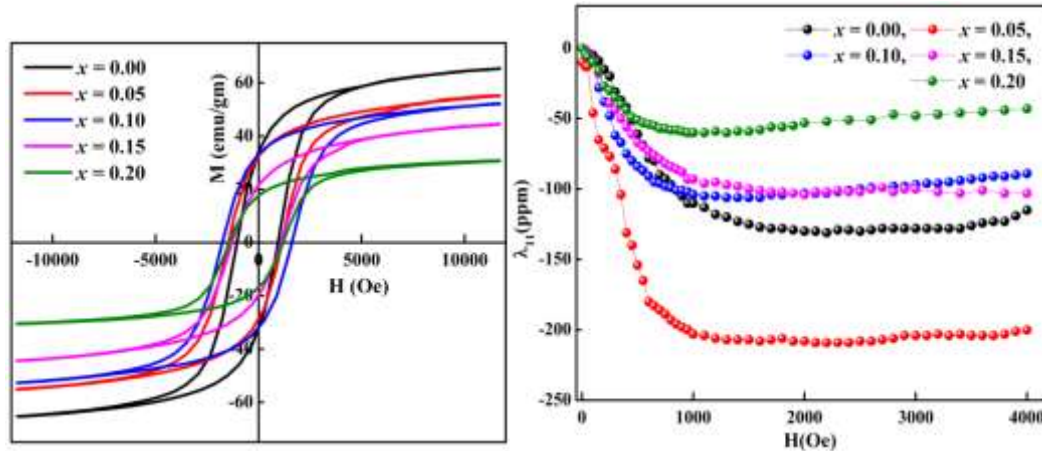


Fig.1. (a) Magnetic hysteresis loops and (b) Magnetostrictive coefficient (λ_{11}) for $\text{Co}_{1.1}\text{Fe}_{1.9-x}\text{Er}_x\text{O}_4$

For $\text{Er} = 0.05$ in Co rich CFEO, the observed magnetostrictive coefficient values i.e. $\lambda_{\text{max}}=210$ ppm for the same fields are much higher than the reported values.⁵ It has been observed that the magnetostrictive coefficient and strain derivative is maximum for $x = 0.05$. The strain derivative i.e. $(d\lambda/dH)_H$, for $\text{Er} = 0.05$ in cobalt rich cobalt ferrite observed to be three times more than cobalt rich cobalt ferrite and then decreases. This may be accountable due to the important

contribution of easy axis (100) at lower fields. The slope $(d\lambda/dH)$ i.e. magnetomechanical coupling factor is mostly related to the stress sensitivity of the magnetization, and it is an indication of the potential performance of a magnetomechanical sensor.³⁻⁴ It is proposed that erbium ions tend to replace iron ions at octahedral site and there may be the migration of Co^{2+} ions from octahedral site to tetrahedral site due to which there is a decrease in magnetostriction for $x \geq 0.15$.

Conclusions

The structural, magnetic and magnetostrictive properties of cobalt rich magnetostrictive ferrites were evaluated. X-ray diffraction studies confirm the purity of the samples. Magnetic properties are observed to be strongly dependent on Er ion substitution. For $\text{Er} = 0.05$ in cobalt rich cobalt ferrite shows the maximum value of magnetostriction coefficient and strain derivative at lower applied field. Magnetic and magnetostrictive properties authenticate the significance of prepared samples for memory storage and stress sensing applications.

Reference:

1. C. V. Ramana, Y. D. Kolekar, K. Kamala Bharathi, B. Sinha and K. Ghosh, *J. Appl. Phys.* **114**, (2013) 183907.
2. S. G. Kakade, Y. Ma, R. S. Devan, Y. D. Kolekar and C.V. Ramana, *J. Phys Chem. C*, 2016, **120** (2016) 5682.
3. S. J. Lee, C. C. H. Lo, P. N. Matlage, S. H. Song, Y. Melikhov, J. E. Snyder, D. C. Jiles, *J. Appl. Phys.*, 2007, **102**, 073910.
4. G. S. N. Rao, O.F. Caltun, K. H. Rao, P. S. V. SubbaRao, B. P. Rao, *J. Magn.Magn. Mater.*, 2013, **341**, 60.
5. S. G. Kakade, R. C. Kambale, C. V. Ramanna and Y. D. Kolekar, *RSC Adv.*, 2016, **6**, 33308.

Changes the Nano Particle (Zinc) During Leaf Senescence in Sericultural Crop *MORUS ALBA LINN*

S. K. Khade

Department of Botany, Smt. Meenalben Mehta College, Panchagani

(Arts, Commerce & Science) . Tal: Mahabaleshwar

Dist: Satara. (Maharashtra) – 412805.

Email – skkhade2006@yahoo.com

ABSTRACT

An attempt has been made to study changes in the nano particle (zinc) during leaf senescence in mulberry (*Morus alba* Linn.). The leaf senescence was accompanied with the changes in the activity of nano particle (zinc) during leaf senescence in the three mulberry cultivars namely M5 (K2), V1 and S36 . The changes in zinc content during leaf senescence in mulberry cultivars viz. M5 (K2), V1 and S36 are represented in figure, it is clear that, the zinc content in the senescent leaves is lower than the mature and young leaves in three cultivars of mulberry viz. M5 (K2), V1 and S36.

Keywords – Nano particle Zinc, *Morus alba* Linn.

Introduction

The important agro industry sericulture involves rearing of silkworms for the commercial production of the silk. Mulberry (*Morus alba* Linn.) leaves are used as food while rearing monophagous silkworm, *Bombyx mori* Linn. (Ullal and Narasimhanna, 1981). Cocoon production depends mainly on nutrient composition of mulberry leaves. (Krishnaswami *et al.*, 1971; Bhuyian, 1981). Many aspects like health and growth of the larvae, cocoon quality and raw silk quality are also influenced by quality of leaf. In addition to involving verities, different practices have been worked out to raise leaf production including irrigation, pruning and training types, application of fertilizers, etc. (Koul and Bhagat, 1991; Singh and Koul, 1997; Pandit *et al.*, 1999). Ganga (2003) suggested that, over mature and yellow leaves with low protein content should be discarded to other nutritious feed to the worms. Mulberry leaves are extensively utilized as silkworm feed, these appears an excellent forage for feeding and supplementing ruminants, in fact, there are several places where mulberry leaves are used traditionally as feed in mixed forage diets for ruminants and there have also been several studies on

a. Preparation of acid digest

Acid digestion method of Toth *et al.*, (1948) has been followed for the analysis of inorganic constituents. Leaves of different categories (young, mature and senescent) of the three mulberry cultivars (M5 (k2), V1 and S 36) were collected from the field grown plants of similar age under

the use of mulberry for cows and other domestic animals (Sanchez, 2000). A team of nutritional scientists in India has even suggested that the powdered leaves of white mulberry (*Morus alba* L.) might make good, nutritious, non toxic and low cost food ingredients for *Paratha*, the traditional food item of breakfast and dinner of the Indian diet (Srivastava *et al.*, 2003). The leaves also are reported to have some medicinal value and mulberry leaf tea is taken in some parts of India (Zepada, 1997 and Bellini *et al.*, 2000). Due to all the above reasons, understanding the study of senescence process of this economically important leaf material was thought worthwhile. For this purpose three promising cultivars of mulberry (M5 (K2), V1 and S36) have been selected. During present study nutritional constituents of young, mature and senescent leaves from three cultivars of mulberry (viz- M5, V1 and S36) studied has been compared. Hence, in order to have further insight in to the above problem, a fate of activity of zinc content during leaf senescence in the three cultivars of mulberry (viz.M5 (K2), V1and S36) has been studied in the present investigation.

Material and Method

identical growing conditions. These were washed with water blotted to dry and then kept in oven at 60⁰C till a constant weight was obtained. The oven dried plant material was randomly mixed and powdered. Five hundred milligrams of oven dried powder of leaves was transferred to 150 ml capacity beaker to which 20 ml concentrated HNO₃ were

added. The beaker was covered with watch glass and kept till the primary reactions subside. Then these beakers were heated slowly to dissolve solid particles. After cooling to room temperature, 10ml of perchloric acid (60%) were added to it and mixed thoroughly. Then the beaker was heated strongly until a clear and colorless solution (about 2-3 ml) was obtained. It was then cooled and transferred quantitatively to 100 ml capacity volumetric flask, diluted to 100 ml with distilled water and kept

Result and Discussion

The changes in zinc content during leaf senescence in mulberry cultivars viz. M5 (K2), V1 and S36 are represented in figure. It is clear that, the zinc content in the senescent leaves is lower than the mature and young leaves in three cultivars of mulberry namely M5 (K2), V1 and S36. Among various trace elements, the zinc nutrition of plants has attracted a considerable attention of plant physiologists in recent years. This element acts for different enzymes like dehydrogenase, peptidases, carbonic anhydrase, etc. It is also essential for activity of enzymes aldolase, isomerase, transphosphorylases and DNA polymerase (Marschner, 1986). Since, Zn (II) does not undergo reduction under any conditions compatible with life, its role as metalloenzyme is inherently different from that of other metals like Cu and Fe, which are capable of redox reactions (Tziveleka, *et al.*, 1999). It is necessary for maintaining auxin in an active state and also for biosynthesis of tryptophan, a precursor of Auxin – IAA. Zn plays a role in membrane stability by regulating the level of oxidizing O₂ species (Pinton *et al.*, 1994). Zinc is also essential constituent of superoxide dismutase. Recent studies have indicated close involvement of zinc in RNA transcription machinery. Aftab Hussain *et al.*, (1993) indicated that increase in ribonuclease activity may be used to identify Zn deficiency in French bean leaves. Zn deficiency in wheat plant decreases NR activity and NO₃ content (Harper and Paulsen, 1969). Ghildiyal *et al.*, (1986) have observed a decrease in protein, nitrogen content and increase in free amino acid content of linseed varieties under Zn deficiency which indicates that Zn is playing a prominent role in nitrogen

overnight. Next day the extract was filtered through Whatman No.44 (ashless) filter paper. Filtrate so obtained was used for estimation of different inorganic constituents.

b. Estimation of - Zinc.

Zinc was estimated using Atomic Absorption Spectrophotometer (Perkin Elmer 3030). In case needed, appropriate dilution of plant acid digest was made with distilled water.

metabolism. In Zn deficient roots, uptake of nutrients is altered (Cakmak and Marschner, 1990). The concentration of sulphhydryl groups at the surface of plasma membrane is lowered (Welch and Norvell, 1993) and proton pumping activity in isolated plasma membrane vesicle is depressed (Pinton *et al.*, 1993). The most characteristic visible symptoms of zinc deficiency in dicotyledons are stunted growth due to shortening of internodes (“rosetting”) and a drastic decrease in leaf size (little leaf). Deficiency in zinc is reported to cause chlorotic conditions of the mulberry leaves (Rangaswami *et al.*, 1978). The critical deficiency levels of Zn are below 15–20 mg kg⁻¹ dry weight of leaves and critical toxicity levels of zinc in leaves of crop plants are more than 400–500 mg kg⁻¹ dry weight basis (Marschner, 1986). Due to similarities with ion radius of bivalent cations, excess Zn can shift certain physiological equilibria by local competition at various sites (Hihara and Sonoike, 2001). Hence, at high concentration, Zn can become toxic and can impair plant growth and metabolism. But some zinc hyperaccumulator species such as *Thalpi caerulescens* also exist which accumulate as much as 40,000 µg Zn without any adverse effect on their metabolism (Kochian, 2000). In the mulberry leaves, zinc is present in trace amount (McDowell, 1997). Hill *et al.*, (1979) noticed marked decline in Zn element during senescence of wheat leaves. Himelblau and Amasino (2001) observed that during leaf senescence nutrients are mobilized to seeds, storage organs or new vegetative growth. Plants are reported to contain multiplicity of zinc transporters (Kochian, 2000). They reported that during leaf senescence in *Arabidopsis thaliana* L.

level of Zn dropped significantly indicating that this

is nutrient is mobilized from senescing leaves.

The values presented in the part- 'Results and Discussion' represent average of three independent determinations.

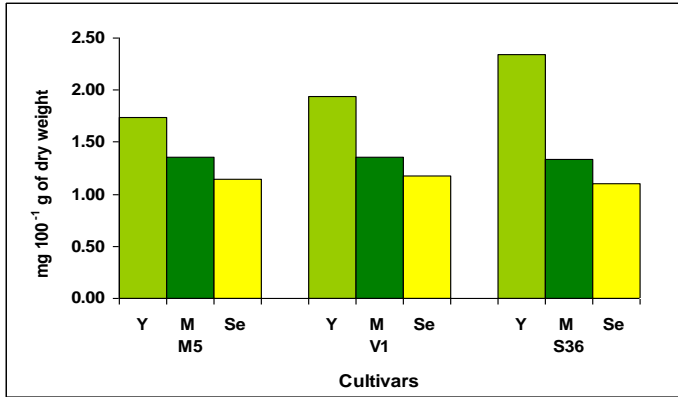


Fig. changes the nano particle (zinc) during leaf senescence in sericultural crop *morus alba* linn (Y = Young, M = Mature and Se = Senescent)

Conclusion

The present study with three mulberry cultivars also indicated slight retranslocation of Zn form senescent leaves to other plant parts. Since the level of zinc is lowered in the senescent leaves.

Acknowledgement

Author is thankful to Principal Dr. A.R.Gade Smt. Meenalben Mehta College (Arts, Commerce & Science) Panchagani. for his continuous encouragement and availability of laboratory aids during research work.

References

- Aftab-Hussain, I. S.; Rama Rao, S. and Prasad, T. G. (1993). Influence of zinc on the ribonuclease activity in french beans (*Phaseolus vulgaris*). *Indian J. Plant Physiol.*, 36: 71-72.
- Bellini, E.; Giordani, E. and Roger, J.P. (2002). Il gelso da frutto L' Informatore Agrario, 7: 89-93.
- Bhuyian, N. I. (1981). "Manual of Bangladesh Silk Production" Bangladesh Agricultural University, pp. 60.
- Cakmak, I. and Marschner, H. (1990). Decrease in nitrate uptake and increase of proton release in zinc deficient cotton, sunflower and buckwheat plants. *Plant and Soil*, 129: 261-268
- Ganga, G. (2003). Comprehensive Sericulture. Vol. I. (Publ.) Moriculture Oxford & IBH Publishing House Co. Pvt. Ltd. New Delhi, pp. 168 – 183.
- Ghildiyal, M. C.; Pandey, M. and Sirohi, G. S. (1986). Proline content in linseed varieties as influenced by zinc nutrition. *Indian J. Plant Physiol.*, 24: 368-374
- Koul, A. and Bhagat, R. L. (1991) : Effect of winter pruning on the spring leaf yield in mulberry. *Ind. J. Seric.* 30 : 131 – 134.
- Krishanaswami, S., Kumararaj, S., Vijayraghavan, K. and Kasiviswanathan, K. (1971). *Ind. J. Seric.*, 9 (1): 79.
- Marschner, H. (1986). Mineral nutrition of higher plants. Pub. Academic Press, New York.
- McDowell, L. R. (1997). Minerals for grazing ruminants in Tropical region. (Publ.) University of Florida, Institute for food and Agriculture Science USA
- Pandit, R., Singh, D., Ram, K., and Koul, A. (1999) : Effect of stump height on leaf yield in extensive plantation of mulberry. *Life Sci. Reporter* 1 : 15 – 17.
- Pinton, R.; Cakmak, I. and Marschner, H. (1994). Zinc deficiency enhanced NAD (P) dependent superoxide radical production in plasma membrane vesicles isolated from roots of bean plants. *J. Exp. Bot.*, 45: 45-50
- Rangaswami, G.; Narasimhanna, M. N.; Kasiviswanathan, K. and Jolly, M. S. (1978). Manual on sericulture, Volume 1, Mulberry cultivation. Food and Agriculture Organization of the United Nations, Rome, pp. 150
- Sanchez, M. D. (2000). Mulberry: an exceptional forage available almost worldwide! FAO Electronic conference on mulberry for animal production.
- Harper, J. E. and Paulsen, G. M. (1969). Nitrogen assimilation and protein synthesis in wheat seedlings as affected by mineral nutrition. II Micronutrient. *Plant Physiol.*, 44: 636-640.
- Hihara, Y. and Sonoike, K. (2001). Regulation, inhibition and protection of photosystem I. In: Regulation of Photosynthesis. (Eds) Aro, E. M. and Andersson, B. (Pub.) Dordrecht: Kluwer, Acad. pp. 507-531
- Hill, J.; Robson, A. D. and Loneragan, J. F. (1979). The effect of copper supply on the senescence and there translocation of nutrients of the oldest leaf of wheat *Triticum aestivum* cultivar gamenya. *Ann. of Botany*, 44(3): 279-288
- Himelblau, E. and Amasino, R. M. (2001). Nutrient mobilized from leaves of *Arabidopsis thaliana* during leaf senescence. *Journal of plant Physiology*, 158(10): 1317-1323.
- Kochian, L. V. (2000). Biochemistry and Molecular Biology of plants. (Eds.) Buchnan B.; Gruissam, W. and Jones, R. *American Society of Plant Physiologists*, pp 1204-1249. <http://www.fao.org/livestock/fgr/mulberry/papers/html/mulbvar2.htm>
- Singh, D. and Koul, A. (1997) : Effect of spacing on leaf yield in mulberry. *J. Seric.*, 5: 17 – 19.
- Srivastava, S.; Kapoor, R.; Thathola, A. and Srivastava, R. P. (2003). Mulberry (*Morus alba*) leaves as human food: a new dimension of sericulture. *Int. J. Food Sci. Nutr.*, 54(6): 411-416.
- Toth, S. J.; Prince, A. L.; Wallace, A. and Mikkelsen, D. S. (1948). Rapid quantitative determination of eight mineral elements in plant tissue vy systematic procedure involving use of a flame photometer. *Soil Sci.*, 66: 459-466.
- Tziveleka, L.; Kalidas, A.; Hegedus, A.; Kissimon, J.; Promobona, A.; Horvath, G and Argyroudi-Akoyunoglou, J. (1999). The effect of cadmium on chlorophyll and light harvesting complex biosynthesis in greening plants. *Z. Natureforsch.*, 54c:740-745.
- Ullal, S. R. and Narasimhanna, M. N. (1981). "Handbook of practical sericulture", CSB, Bangalore.
- Welch, R. M. and Norwell, W. A. (1993). Growth and nutrient uptake by barley (*Hordeum vulgare* L. cv. Nerla) studies using an N (2-hydroxyethyl) ethylene dinitrilotriacetic acid–buffered nutrient solution technique II. Role of zinc in the uptake and root leakage of mineral nutrients. *Plant Physiol.*, 101: 627-631
- Zepeda, J. (1997). El arbol de oro. *Los. Medio Ambiente*, 47:28-29

Nitrogen dioxide sensing properties of nanostructured zinc oxide thin film grown by Sol-gel method

A. R. Nimbalkar^a, N. B. Patil^a, M. G. Patil^{b*}

^a Research Scholar, JJT University, Jhunjhunu, Rajasthan, 333001.

^b Department of Physics, Dattajirao Kadam Arts, Science and Commerce College, Ichalkaranji

*Corresponding Author: marutipatil1956@gmail.com

Abstract

Nitrogen dioxide (NO₂) sensing properties of ZnO thin film synthesized by simple Sol-gel spin coating method are studied. The structural, optical and gas sensing properties of the thin film is studied by using X-ray diffraction (XRD), field emission scanning electron microscopy (FESEM), UV-Visible spectroscopy (UV-VIS). X-ray diffraction and scanning electron microscopy showed that the ZnO thin films have hexagonal wurtzite crystal structure. The optical band gap of deposited film is found to be 3.15 eV. The ZnO thin film shows the highest gas response to NO₂ at 200 °C operating temperature. Maximum response up to 2.30 is achieved towards 10 ppm NO₂ at 200 °C operating temperature. ZnO films are highly selective towards NO₂ in comparison with other gases like H₂S, Cl₂ and LPG.

Keywords: ZnO thin film, NO₂ gas, XRD, Gas sensor.

1. Introduction

Zinc oxide is a multifunctional material in II-VI semiconductor group and having a broad energy band gap (3.37 eV), large exciton binding energy of 60 meV at room temperature and high thermal, mechanical stability at room temperature make it attractive for potential use in different fields like sensors, electrical, piezoelectric devices etc.[1-3].

Gas sensors have been used for the detection of toxic environmental pollutant gasses such as NO, NO₂, and CO, etc. and for the prevention of hazardous gas leaks, which comes from the many industrial processes. There are numbers of types of gas sensors that have been used to detect various toxic gasses: catalytic gas sensors, infrared gas sensors, semiconductor gas sensors, etc. However, gas sensors based on metal-oxides that are playing a vital role in the detection of toxic pollutants. The two types of metal oxide material gas sensors that have been used are p-type such as nickel oxide and cobalt oxide or n-type such as tin dioxide, titanium oxide, iron oxide and zinc oxide. ZnO was leading material in gas sensing because a large variety of nanostructures in form of nanoparticles, nanowires, nanobelts, nanorods or nanotetrapods have been synthesized i.e., with morphologies ideal for gas sensing [4-7].

In this study, ZnO thin film was synthesized by the sol-gel spin coating technique to obtain homogeneous films.

2. Experimental details

ZnO thin films were synthesized by the sol-gel method, zinc acetate ((CH₃.COO)₂ Zn.2H₂O) with 99.5% purity (Thomas Baker) as a source of zinc oxide and RG grade ethanol was used. Zinc acetate (0.2 M) was added to 40 ml of ethanol and stirred at 60°C for 60 min., leading to the formation of a clear and homogeneous solution. The solution was deposited on to a glass substrate by a single wafer spin processor (APEX Instruments, Model spin NXG-P1). After setting the substrate on the substrate holder of the spin coater, the prepared solution (~0.2 ml) was dropped and spin-coated at 2000 rpm for 30 seconds in an air and dried on a hot plate at 100 °C for 5 min, the above procedure repeated 5 times. The as-prepared film was annealed at 400 °C for 60 min in an ambient air to obtain nanocrystalline ZnO film.

The structural properties of the films were investigated by X-ray diffraction (XRD) (Bruker D2 phaser) using filtered Cu K α radiation (1.54056Å). Morphological study of the films was carried out using field emission scanning electron microscopy (FESEM, JEOL 2300, Japan). The optical absorption spectra of ZnO thin films were obtained using UV-Vis Spectrophotometer-1800 (Shimadzu) in the 300–800 nm-wavelength range. NO₂ sensing measurements were measured at 200 °C, the change in resistance was monitored continuously and recorded using Keithley (6514)

electrometer incorporated into a PC during the measurements.

3. Results and discussion

3.1. Structural studies

Fig.1 shows the X-ray diffraction spectra and FESEM image of ZnO thin film annealed at temperature 400 °C for 60 min and the result shows that the ZnO material grows hexagonal wurtzite crystal structure. The X-ray pattern of the film matches with the JCPDS card no. 79-0205 and it shows main significant peaks viz. (1 0 0), (0 0 2), (1 0 1), (1 0 2), (1 1 0), (1 0 3) and (1 1 2). The average value of grain size of ZnO was determined using Scherrer formula and the average grain size was found to be 70 nm [6]. The lattice constants calculated from the present data are $a = 3.2316 \text{ \AA}$ and $c = 5.1839 \text{ \AA}$. The FESEM image show randomly distributed nanoparticles with average grain size of 70 nm and a porous structure consisting of grains with different sizes separated by voids [3].

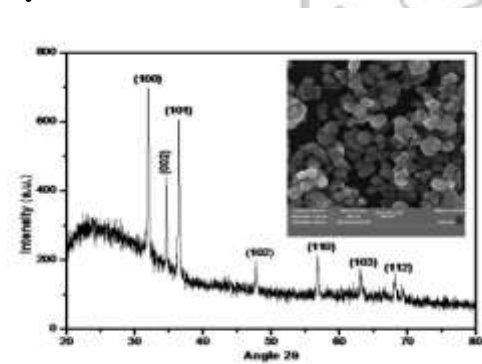


Fig.1. XRD pattern and FESEM image of a ZnO thin film annealed at 400°C for 60 min. repeating the spin-coating cycle 5 times.

3.2. Optical study

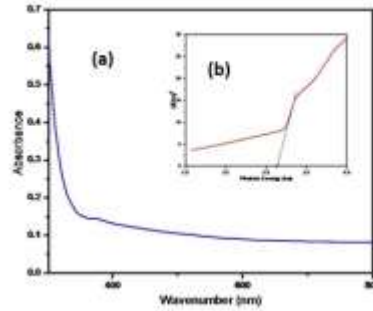


Fig.2. (a) The absorbance spectra of ZnO thin film at room temperature (b) The graph of $(Ah\nu)^2$ versus $h\nu$ plots.

Fig. 2 (a) shows the absorbance with the wavelength region of 300–800 of nanocrystalline ZnO thin film. The optical band gap of the sample calculated from the intercept on the energy axis of $(Ah\nu)^2$ against $h\nu$ graph (Fig. 2. (b)), which was found to be 3.15 eV [8].

3.3. Gas sensing performance

The as-prepared ZnO thin film was tested to different gasses such as LPG, H_2S , Cl_2 and NO_2 at 200°C for 10 ppm gas concentrations. Fig.3. shows the sensor response = $\Delta R/R_0$ versus time, (where ΔR is the change in resistance and R_0 is the value of baseline) for ZnO thin film at 200°C. It shows maximum response up to 2.30 is achieved towards

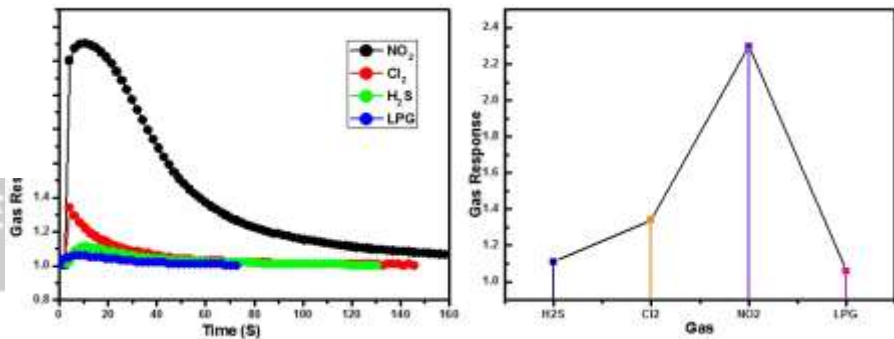


Fig.3. Gas response versus time graphs for ZnO thin film 10 ppm NO_2 in presence of other gasses [9-10].

4. Conclusions

ZnO thin film has been successfully synthesized by sol-gel spin coating method technique. ZnO material grows hexagonal wurtzite crystal structure with different grains sizes. The optical band gap of the film is 3.15 eV. The ZnO thin film is sensitive as well as fast in responding to NO_2 gas against the other interfering gasses for 10 ppm gas concentrations. The different grains sizes improved the sensing performance to NO_2 gas at 200 °C.

References

1. V. B. Patil et.al. J Mater Sci: Mater Electron (2009).
2. A. Muthuvinayagam et al Ar. of Applied Science Research, (2011)
3. C.S. Prajapati, P.P. Sahay, Applied Surface Science 258 (2012) 2823
4. K. Arshak, I. Gaidan, Materials Science and Engineering B 118 (2005)
5. M.C. Carotta et al Sensors and Actuators B 137 (2009) (164–169).
6. S. L. Patil et J Mater Sci: Mater Electron (2010) 21:1332–1336.
7. Sergiu T. Shishiyanu, et al Sensors and Actuators B 107 (2005)
8. Said Benramache, Achour Rahal, Boubaker Benhaoua, Optik 125 (2014)
9. S. Öztürk, N. Kılınc et al Thin Solid Films 520 (2011) 932–938.
10. S.D. Shinde et al Journal of Alloys and Compounds 528 (2012) 109

Synthesis and characterization of Dy Doped Co-Zn ferrite by sol-gel auto combustion method

Shivaji R. Kulal^{*1}, Krishna K. Ranagar¹, Dadasaheb V. Rupnawar², Vashistha M. Gurame³, Dipak S. Rajmane⁴, Ramchandra B. Patil⁵, Vijay S. Jadhav⁵

¹Department of Chemistry, Raje Ramrao Mahavidyalaya Jath, Sangli, Maharashtra

²Department of Chemistry, Lal Bhadur Shastri College Satara, Maharashtra

³Department of Chemistry, Shivaji Mahavidyalaya Barshi, Solapur, Maharashtra

⁴Department of chemistry, Shrimant Babasaheb Deshmukh College, Sangli, Maharashtra

⁵Raje Ramrao Mahavidyalaya Jath, Sangli, Maharashtra. * Corresponding address: Tel: +91 9405578543
E-mail address: srkulal@gmail.com

Abstract

Dysprosium doped Co-Zn ferrites were synthesized by sol-gel auto combustion method. These synthesized compounds were characterized by using XRD, SEM, FTIR, EDS and TEM. The XRD study of Dy doped Co-Zn ferrite shows in Cubic spinel phase. Particle size obtained from TEM analysis was found to be 44 nm.

Keywords: Nanocrystalline, sol-gel, FTIR, SEM.

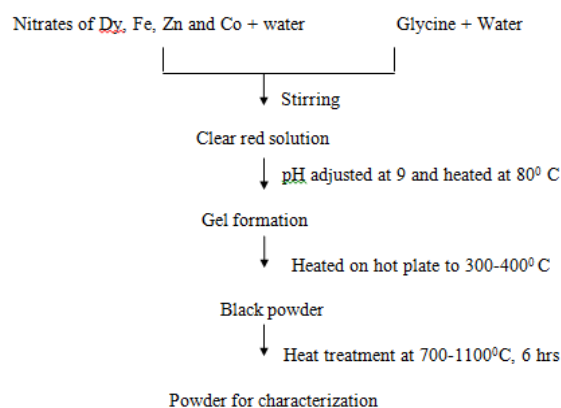
1. Introduction

Rare earth substituted different ferrites are becoming promising materials for various applications. Addition of small amount of rare earth ions to ferrite sample alters their electrical, magnetic and structural properties depending upon the type and amount of rare earth element used. Rare earth ions can be divided into two categories, one with the radius close to Fe ions and other with the radius greater than Fe ions [1]. This difference in the ionic radii will lead to micro strain which may results in the deformation of spinel structure [2]. The substitution of rare earth ions into the ferrite led to replacement of Fe³⁺ by rare earth ions and limited solubility in the spinel lattice due to their large ionic radii [3]. The rare earth ions are found to be promising additives to improve the magnetic properties of ferrites [4-7]. Among the rare earth doped ferrites, the Sm doped Cu-Zn ferrite [8] and La doped Ni-Cu-Zn ferrite [9] exhibit promising results from technological point of view. The spinel ferrites are effective catalysts for the number of industrial processes such as catalytic alkylation [9], combustion of methane [10] decomposition of alcohols and hydrogen peroxide [11] and oxidative dehydrogenation of hydrocarbons [12]. These applications mainly depend upon microstructure and surface properties of the fine powders which depend upon the method of preparation [13]. Sol-gel auto combustion method [14] was proved to be simple and economic way to prepare nano scale ferrite powder. Generally

in this method metal nitrate salts are used as reactants and glycine [15], urea [16] and citric acid [17] used as fuel. Sol-gel auto combustion method has the advantages of using inexpensive precursors, low external energy consumption and resulting nano sized, homogenous highly reactive powder.

In the present investigation sol-gel auto combustion method [17] has been used for the synthesis of Dysprosium doped Co-Zn ferrite. These ferrite materials were characterized by using XRD, FTIR, SEM, EDS, TEM, electrical resistivity, magnetic hysteresis and TGA-DTA. Catalytic activity of this Dysprosium doped Co-Zn ferrite material was studied for the decomposition of hydrogen peroxide.

Scheme 1. Flowchart of sol-gel auto combustion synthesis of Dy-Co-Zn ferrite



2. Experimental

Reagent grade purity chemicals were used. Zinc nitrate, cobalt nitrate, iron nitrate, dysprosium nitrate and glycine solutions were prepared in

deionized water. In a beaker 0.25 M zinc nitrate solution was taken, dropwise 0.25 M cobalt nitrate solution was added to it followed by addition of 0.25 M iron nitrate solution and dysprosium nitrate solution. Glycine solution was added to this mixture and P^H was adjusted to 9 by adding

3. Results and Discussion

3.1. XRD Analysis

Figure 1 shows the XRD pattern of calcined sample at 950⁰C for 6 hours. This pattern corresponds to peaks of (100), (220), (311), (222), (400), (422), (511), (440). These polycrystalline nanoparticles exhibit cubic spinel structure ZnFe₂O₄ (JCPDS 89-1012), CoFe₂O₄ (JCPDS.22-1080) and Dy doped ferrite [13]. Lattice parameters of Co_{0.50}Zn_{0.50}Fe_{2-x}Dy_xO₄ with [x= 0.0, 0.025, 0.050, 0.075] were observed in the range 8.44 to 8.34 Å. The average grain size of this system is calculated by Debye-Scherrer equation to the half intensity width of (311) peak.

$$d = 0.9 \lambda / \beta \cos \theta$$

Where λ is the wave length of CuKα = 1.54 Å, β is the calibrated half intensity width of the selected diffraction peak (degrees) and θ is the Bragg's angle (half of the peak position angle). From this equation the average size of Co_{0.50}Zn_{0.50}Fe_{2-x}Dy_xO₄ with [x= 0.0, 0.025, 0.050, 0.075] nanoparticles was estimated to be 30 to 40 nm. Slight decrease in the X-ray density (d_x) and physical density from x= 0.0 to x = 0.075 was observed. The porosity increases with increase in x from 0.0 to 0.075. The

Table-1 Lattice constants, crystallite size, X-ray density, physical density and porosity for Co_{0.5}Zn_{0.5}Fe_{2-x}Dy_xO₄ System

Sr. No.	Co _{0.50} Zn _{0.50} Fe _{2-x} Dy _x O ₄	Lattice Constants (Å)	Crystal lite Size (nm)	X – ray density (d _x)	Physi cal Densi ty (d _B)	Porosit y (P)(%)
1	x = 0.0	8.44	30.18	5.271	4.793	9.06
2	x = 0.025	8.37	35.24	5.225	4.765	9.63
3	x = 0.050	8.36	39.10	5.171	4.693	9.66
4	x = 0.075	8.34	40.42	5.142	4.562	11.26

The elemental analysis of the sample was carried out by using energy dispersive X-ray spectrometer (EDS) and is shown in figure 3. The EDS result clearly shows that Co_{0.50}Zn_{0.50}Fe_{2-x}Dy_xO₄ contains Dy, Co, Zn, Fe and O without any impurity.

ammonia solution with contineous stirring. This content was stirred and heated at 80⁰ C for 3 hours to obtain gel. This gel was heated on hot plate at 300-400⁰ C to obtain the Dy-Co-Zn ferrite powder. This powder was calcinated at 700-1100⁰C for 6 hrs and used for characterization (Scheme 1).

X-ray densities (d_B) are higher than physical densities (d_x). It is noticed that the lattice constant decreases with increasing the Dy concentration in the lattice. Lattice parameters, crystallite size, physical density, X-ray density and porosity of these nanoparticles are summarized in table 1.

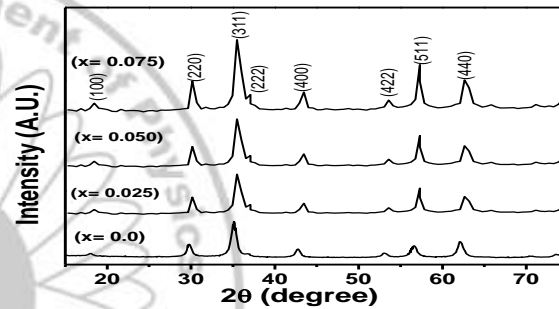


Fig.1 XRD pattern of Co_{0.50}Zn_{0.50}Fe_{2-x}Dy_xO₄ System

3.2. SEM and EDS Analysis

The SEM micrographs of Co_{0.50}Zn_{0.50}Fe_{2-x}Dy_xO₄ synthesized by sol- gel auto combustion method are given in figure 2. The composition Co_{0.5}Zn_{0.5}Fe_{2-x}Dy_xO₄ (x=0.075) shows fibrous reticulated mesh like morphology (fig.3) The average grain size increases with increasing the Dy content in the Co-Zn ferrite.

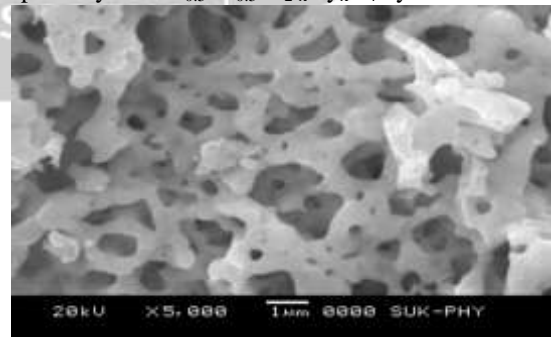
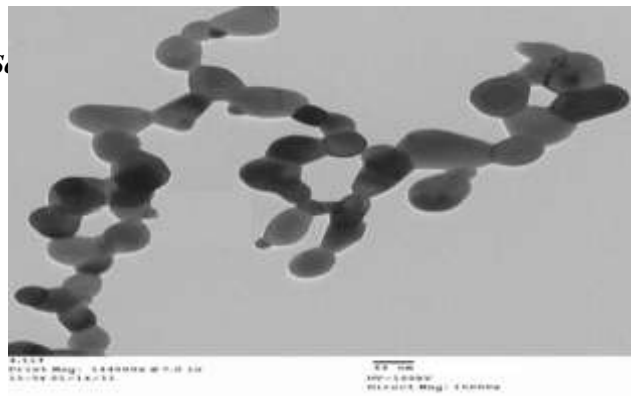
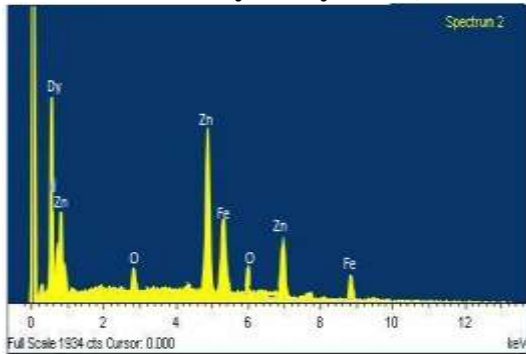


Fig.2 SEM micrograph for Co_{0.50}Zn_{0.50}Fe_{2-x}Dy_xO₄ System (x=0.075)

Fig.3 Energy Dispersive Spectrum of $\text{Co}_{0.50}\text{Zn}_{0.50}\text{Fe}_{2-x}\text{Dy}_x\text{O}_4$ System ($x=0.025$)



TEM images of the nanoparticles of $\text{Co}_{0.50}\text{Zn}_{0.50}\text{Fe}_{2-x}\text{Dy}_x\text{O}_4$ system with ($x=0.050$) are given in fig.5.

3.3. Infrared Study

FTIR spectra of $\text{Co}_{0.50}\text{Zn}_{0.50}\text{Fe}_{2-x}\text{Dy}_x\text{O}_4$ system are given in figure 4. The spectra show characteristic two strong absorption bands in the range of 600 to 450 cm^{-1} . The highest one is at 560 cm^{-1} corresponds to intrinsic stretching vibrations of the metal at the tetrahedral site and lowest band is observed at 455 cm^{-1} corresponds to octahedral site [13-14]. When Dy concentration in the system was increased, the highest band is shifted towards high frequency side and lowest band remains unaltered. Due to the larger ionic size of Dy ion than metal ions at octahedral site, the Dy ion does not occupy the octahedral site and it remains at the interstitial sites, this leads to increase in highest band towards high frequency side.

3.4. Transmission Electron Microscopy Study

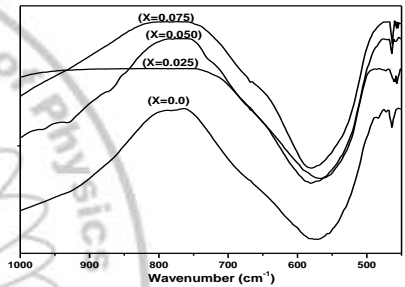


Fig.4 Infrared spectra of $\text{Co}_{0.50}\text{Zn}_{0.50}\text{Fe}_{2-x}\text{Dy}_x\text{O}_4$ System ($0 \leq x \leq 0.075$)

TEM image has no agglomeration and has bead like appearance. Particle size obtained from TEM (Fig. 5) it was found to be 44 nm which is in proximity with the value obtained from XRD pattern.

Fig.5 Transmission electron spectrum of $\text{Co}_{0.50}\text{Zn}_{0.50}\text{Fe}_{2-x}\text{Dy}_x\text{O}_4$ System ($x=0.050$)

4. Conclusions

A simple sol-gel auto combustion process using glycine was employed to synthesize Dy doped Co-Zn ferrite nanoparticles. Size of nanoparticles was found to be 44 nm and was obtained by calcination at 950°C for 6 hours. EDS analysis of the nanomaterials confirm that the material is composed of Co, Zn, O, Dy and Fe without any impurity. Particle size obtained from TEM analysis was found to be in good agreement with the value obtained from XRD pattern. The unit cell parameter 'a' increases linearly with the decrease in Dy concentration.

Acknowledgement

One of the authors (SRK) is thankful to Dr. S. Y. Hongekar, Principal, Rajee Ramrao Mahavidyalaya Jath, Dist- Sangli for constant encouragement during the research work.

References:

- Costa A. C. F. M. et al., 2003, J. Magn. Magn. Mater., 256 174.
- Das B. K., 1981, Preparation and Characterization of Mater. (Ed) J. M Honing, and C. N. R. Rao, New York, Academic Press .
- Gibson M. A. and Hightower J. W., 1976, J. Catal., 41, 420.
- Hwang C. C., Tsai J. S. and Huang T. H., 2005, Mat. Chem. Phys., 93, 330.
- Jacobo S. E. et al, 2004, J. Magn. Magn. Mater., 272-276, 2253.
- Kazi H. M. and Mansour S. F., 2006, J. Phys. Chem. Solids, 67, 1643.
- Moniva E., et al 2004, App. Catal. A:Gen., 277, 119.
- Ravindranathan P. and Patil K. C., 1987, Ceram. Bull., 66, 688.
- Rezlescu N., Rezlescu E., Pasicu C. and Craus M. L. 1994 J. Phys.:Condens. Matter, 6, 5707.
- Rezlescu N., Rezlescu E., Mangeron P. D., Rezlescu L. and Pasicu C. 1997, J. Phys. Stat. Sol., 162, 673.
- Roy P. K., Nayak B. B. and Bera J., 2008, J. Magn. Magn. Mater., 320, 1128. Sattar A. A. and El-Shokrofy K.M., J. Phys., 4 1997 245.
- Sattar A. A., Wafik A. H., El-Shokrofy K. M. and El-Tabby M. M., 1999, Status Solidi A, 171 563.
- Shaikh A. M., Jadhav S. A. and Watawe S. C., 2000, Mater. Lett., 44 192. Solyman S., 2006, Cera. Inter., 32, 755.
- Spretz R. et al , 2000, J.Catal., 194, 167.
- K. Sreekumar and S. Sugunan, J. Mol. Catal. A: Chem., 185 2002 259.
- Z. Yue, Li L et al 1999, Mat. Sci. Engg. B., 64, 68.
- Zhao L., Yang H., Yu L., Cui Y., Zhao X. and Feng S., 2006, J. Magn. Magn. Mater., 3

Low Temperature Synthesis of CoFe_2O_4 Particles by Acrylic Acid – Glycine Assisted Sol-Gel Autocombustion: Structural and Magnetic Properties

Tulshidas C. Darvade, P.S. Kadhane, B.G. Baraskar, Y.D.Kolekar and R.C. Kambale
Department of Physics, Savitribai Phule Pune University, Pune - 411007, Maharashtra, India.

Email: rckambale@gmail.com

Abstract:

Low temperature synthesis (~ 600 °C) of CoFe_2O_4 particles was done by acrylic acid -glycine assisted modified sol gel autocombustion route. The Phase purity and crystal lattice symmetry were identified from the x-ray diffraction studies at room temperature. The FTIR spectra also showed the two characteristics absorption bands clearly evidences the formation of spinel lattice symmetry with tetrahedral and octahedral sites. The microstructural analysis confirms the agglomeration and spherical like fine particle which is characteristic feature of combustion technique. The ferrimagnetic nature of synthesized CoFe_2O_4 particles was confirmed by measuring magnetic hysteresis loop at room temperature. Thus, the present low temperature combustion technique may be useful to develop the mass production of ferrites for electrical and magnetic applications.

1. Introduction

Cobalt ferrite, CoFe_2O_4 belongs to spinel lattice family having the general chemical formula AB_2O_4 , and it can be derived from the magnetite $\text{Fe}^{2+}\cdot\text{Fe}_2^{3+}\text{O}_3$ by replacement of the Fe^{2+} ion by other divalent metal ions like Ni, Mg, Fe, etc. It is also possible to replace Fe^{3+} by trivalent metals ions like Al^{3+} , Ga^{3+} etc. The CoFe_2O_4 has inverse spinel structure in which Co^{2+} ions occupies the octahedral B site and Fe^{3+} ions can occupies the both tetrahedral A site and octahedral B site. The spinel ferrimagnetic oxides are the useful candidates for designing the transformer cores as well as magnetic recording media due to their moderate structural, electrical and magnetic properties which are sensitive to the method of preparation. The ferrites have the wide range of applications, but mainly suffered from their high quality scale production at low temperature [2]. Cobalt ferrite, CoFe_2O_4 is one of the technologically important ferrites with high coercivity, moderate magnetization and very high magneto crystalline anisotropy [3]. Therefore, in present work we have developed the low temperature (~ 600 °C) synthesis technique i.e. acrylic acid-glycine assisted (two fuel assisted) sol-gel autocombustion route useful for many industries to develop the mass production of ferrites for electrical and magnetic applications. Since, the sol-gel autocombustion method is one of the suitable method to obtain the desired composition controlled as well as high yield products with greater homogeneity and fine particle size at very low

processing temperature. In the present work an attempt is made to synthesize the traditional cobalt ferrite by acrylic acid-glycine assisted sol gel combustion; investigated the structural, microstructural and magnetic properties.

2. Experimental details

The CoFe_2O_4 was synthesized by acrylic acid-glycine assisted modified sol gel combustion route. The stoichiometric amounts of $\text{Co}(\text{NO}_3)_2\cdot 6\text{H}_2\text{O}$, and $\text{Fe}(\text{NO}_3)_3\cdot 9\text{H}_2\text{O}$ metals nitrates acts as oxidizing agents and the fuel i.e glycine and acrylic acid acts as a reducing agent was used for the combustion reaction [1]. The oxidizer to fuel i.e. (O/F) ratio of the redox mixture for combustion calculated by using total oxidizing and total reducing valencies of the oxidizer (O) and fuel (F), which serve as numerical coefficients so that (O/F) ratio becomes unity in order to release maximum energy during combustion reaction. According to principles used in propellants chemistry, the oxidizing and reducing valencies of various elements are considered as follows :C=4, H=1, O=-2, N=0, Co=+2, Fe=+3 etc. Here nitrogen valence to be considered zero, because during redox reaction it transforms into molecular form. Thus, the oxidizing valence of divalent metal nitrate $\text{Co}(\text{NO}_3)_2$ becomes -10; for trivalent $\text{Fe}(\text{NO}_3)_3$, it is -15, which should be balanced by the total reducing valencies in the fuel; acrylic acid ($\text{C}_3\text{H}_4\text{O}_2 = +12$)-glycine ($\text{C}_2\text{H}_5\text{NO}_2 = +9$), which add up to +21. Hence, for stoichiometric composition of the redox mixture, in order to release the maximum energy for the reaction, require that $-40+21n=0$ or $n=1.90$ mol

of fuels out of these, 1.08 mol of acrylic acid and 0.80 mol of glycine. Therefore, the molar proportion of oxidizing metal nitrates and reducing fuels (acrylic acid-glycine) is $\text{Co}^{2+}:\text{Fe}^{3+}:\text{acrylic acid}:\text{glycine} = 1:2:1.08:0.80$. 0.1 M solution of oxidizer as well as reducing agents were prepared separately in deionized and stirred for 1h for homogeneity on magnetic stirrer. The oxidizer solution looks to be light yellowish in which the stoichiometric acrylic-glycine solution added to form the redox mixture for the combustion reaction. Then the resultant solution was dehydrated slowly on a hot plate with continuous stirring until the viscous gel formed. On further heating, the temperature of the gel increased and at a certain temperature i.e at decomposition temperature fuels the auto-ignition of the gel took place with evolution of gases. During ignition the flames and smoke are produced, and the products left behind are voluminous and fluffy loose powder that responded to a magnet. The obtained synthesized cobalt ferrite powder was ground well in agate mortar then it is sintered at 600°C for 12 hours.

3. Results and discussion

3.1. Phase Analysis

The cobalt ferrite samples was characterized by an X-ray powder diffractometer (XRD, Bruker AXS D8 Advace) using Cu-K α radiation ($\lambda=1.540\text{\AA}$) at 40kV and 35mA. The Reitvield fitted XRD pattern of CoFe_2O_4 nanoparticles sintered at 600°C is shown in Fig.1. The obtained XRD pattern compared with the standard data (JCPDS PDF # 22-1086), and hence confirms the formation of cobalt ferrite nanoparticles without any secondary phase formation. The crystalline size 'D' of the sintered cobalt ferrite has estimated form the high intense peak (311) using Scherer equation.

$$D = \lambda k / \beta \sin\theta \quad (1)$$

The lattice parameter is calculated for high intense peak (311) using Bragg's equation. $a = d_{hkl}(h^2 + k^2 + l^2)^{1/2} \quad (2)$

The theoretical density, ρ_x is calculated using the relation

$$\rho_x = \frac{8M}{Na^3} \quad (3)$$

Where, M molecular weight of CoFe_2O_4 , N is Avogadro's number and a^3 is the volume of the

cubic unit cell. The calculated structural properties such as lattice constant, crystallite size and X-ray density are shown in Table1.

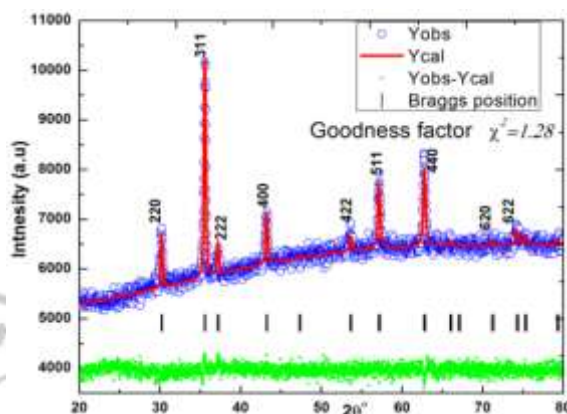


Fig.1.Rietveld refined x-ray diffraction pattern of CoFe_2O_4 sintered at 600°C for 12hours. Figure shows observed intensity (Yobs), calculated intensity (Ycalc) and difference in observed and calculated intensities (Yobs- Ycalc). Braggs positions of different peaks are at the baseline as small markers (|) and goodness of fit (χ^2) is 1.28.

Table 1 Structural properties of CoFe_2O_4 sintered at 600°C for 12hours.

Composi tion at (600°C)	Lattice Parame ter a (nm)	Crysta llite size D (nm)	X-ray densit (g/cc)
CoFe_2O_4	0.85 2	34.33	5.038

3.2. SEM Analysis

SEM micrograph of cobalt ferrite sintered at 650°C was obtained by using Analytical Scanning Electron Microscope (Model JEOL, 6360). The micrographs of samples are taken with at different magnification are shown below Fig.2. shows SEM micrographs of CoFe_2O_4 sample sintered at 600°C which clearly reveals the formation of clusters of fine particles clinging together or spherical like.



Fig.2. SEM Micrographs spectra of CoFe₂O₄ sintered at 600°C for 12 hours.

3.3. Magnetic properties

The magnetic properties are studied by vibrating sample magnetometer (Lake shore 7303). The room temperature ferrimagnetic nature of CoFe₂O₄ was confirmed by magnetic hysteresis loop as shown in fig.3. The observed magnetic parameters such as saturation magnetization M_s , remanent magnetization M_r and coercivity H_c for CoFe₂O₄ are shown in the table 2. The magnetic moment per formula unit in Bohr magneton (η_B) was calculated by using the following relation is $2.05\mu_B$.

$$\eta_B = \frac{M \times M_s}{5585} \quad (4)$$

where M is the molecular weight of CoFe₂O₄ and M_s is saturation magnetization (emu/gm).

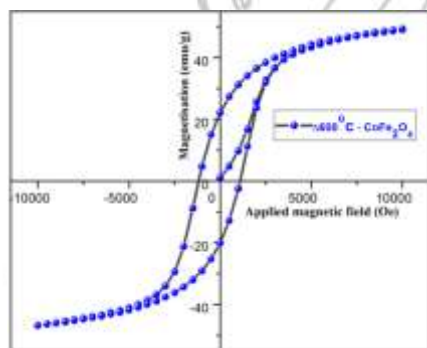


Fig.3. Magnetic (M-H) hysteresis loop of CoFe₂O₄ sintered at 600°C for 12 hours.

3.4. FTIR Analysis

The formation of spinel lattice symmetry with tetrahedral and octahedral site for CoFe₂O₄ was evidenced from the existence of two absorption bands in FTIR spectra shown in fig.4. accordingly Waldron [4]. Two significant absorption bands (ν_1) and (ν_2) are observed at 586 and 444 cm⁻¹ corresponds to the tetrahedral and octahedral sites of spinel lattice respectively.

Acknowledgments

RCK thankfully acknowledges the BCUD Savitribai Phule Pune University for financial support through research grant (RG-31).

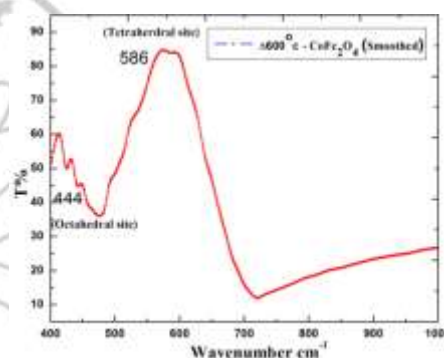


Fig.4. FTIR spectra of CoFe₂O₄ sintered at 600°C for 12 hours.

Table 2 Magnetic properties for CoFe₂O₄ sintered at 600°C for 12 hours.

Composition at 600°C	Saturation magnetization M_s (emu/g)	Coercivity H_c (Oe)	Remanence M_r (emu/g)	η_B (μ_B)
CoFe ₂ O ₄	49.28	1179	22.16	2.05

4. Conclusion

We have successfully developed the low temperature synthesis method i.e. acrylic acid-glycine assisted modified sol gel combustion for high yield production of CoFe₂O₄ at low processing temperature i.e. 600°C. XRD study confirms the cubic spinel structure formation without any impurity. The micrographs show the agglomerated grainy microstructure. FTIR spectra show the existence of two prominent absorption bands corresponding to tetrahedral and octahedral site of the spinel lattice. The room temperature magnetic hysteresis loop confirms the ferromagnetic nature of CoFe₂O₄.

References

1. R. C. Kambale K. M. Song, and N. Hur low temperature synthesis of nanocrystalline Dy³⁺ doped cobalt ferrite: structural and magnetic properties JAP 110,053910(2011).

2. T. Yu, Z. X. Shen, Y. Shi, and J. Ding, J. Phys. Condens. Matter 14(37), L613–L618 (2002).
3. Microstructural and antibacterial properties of zinc-substituted cobalt ferrite nanopowders synthesized by sol-gel... Article in Journal of Applied Physics · October 2012 DOI: 10.1063/1.4761987
4. R.D. Waldron, Physics Rev 99, 1727 (1955)

Ternary (Mn:Co:Ru) Oxides Thin films for supercapaitors

¹Dattatray Sutrave, ²Bhanudas Karche, ¹Sangam Gaikwad, ¹Shahaji Madale, ¹Sangeeta Jogade,
¹Electronics Department, D.B.F Dayanand College of Arts and Science, Solapur, Maharashtra 413003
² Physics Department SM. Mahavidyalay Akluj, Maharashtra 413101.
Corresponding Author: mshahaji@gmail.com

Abstract

In the present work. $\text{MnO}_2:\text{Co}_3\text{O}_4:\text{RuO}_2$ composite thin films were prepared by Sol-gel spin coat method with Manganese acetate, Cobalt acetate and Ruthenium trichloride as precursors. The XRD patterns showed crystalline behaviour with orthorhombic, cubic and tetragonal phase for MnO_2 , Co_3O_4 and RuO_2 respectively. The SEM images revealed the formation of well adherent and porous structure of grains. Films also shows the Tetragonal shapes of grain with spongy surface From electrochemical analysis it is found that, $\text{MnO}_2:\text{Co}_3\text{O}_4:\text{RuO}_2$ composite films showed maximum specific capacitance of 440 F/g at 10mV/s scan rate, specific energy 158.76 Wh/kg, and specific power 83.04 KW/kg. Furthermore 75% stability is retained after 1000 cycles exhibiting good cyclic stability and long cycle life. These results suggest that, $\text{MnO}_2:\text{Co}_3\text{O}_4:\text{RuO}_2$ composite thin film can be a good electrode material for supercapacitor.

Key words: Sol-gel, MnO_2 , Co_3O_4 , RuO_2 Composite oxide, Specific capacitance

1. Introduction

The properties of nanocomposite films depend not only upon the individual components used but also on the morphology and the interfacial characteristics. Recently, various nanocomposite films consisting of either metal-metal oxide, mixed metal oxides, polymers mixed with metals or metal oxides, or carbon nanotubes mixed with polymers, metals or metal oxides have been synthesized and investigated for their application as active materials for supercapacitors. Design of the nanocomposite films for such applications needs the considerations of many factors, for example, the surface area, interfacial characteristics, electrical conductivity, nanocrystallite size, surface and interfacial energy, etc., all of which depend significantly on the material selection, deposition methods and deposition process parameters. Materials can be deposited in the form of thin film on a substrate by a variety of methods such as physical vapour deposition, chemical vapour deposition, wet-chemical processes such as sol-gel and electrochemical deposition and spray pyrolysis etc. [1].

It is believed that transition metal oxides are good candidates as electrode materials, because they have variation in oxide states which is suitable for effective redox charge transfer [2,3]. Non-noble oxides such as NiO, Co_3O_4 , RuO_2 , MnO_2 are very promising candidates for electrode materials in supercapacitors [4-5]. However, the relatively low specific capacitance needs to be improved for

supercapacitor application. Recent research is focused on increasing the specific capacitance of the oxides by introducing other oxides technology [6-7]. In this study, $\text{MnO}_2:\text{Co}_3\text{O}_4:\text{RuO}_2$ composite oxides as electrode materials were prepared by Sol-gel spin coat method.

2. Experimental

Sol-gel Preparation and deposition

At first 0.02M solution of cobalt acetate $[(\text{CH}_3\text{COO})_2\text{Co}.4\text{H}_2\text{O}]$ and manganese acetate $[\text{C}_4\text{H}_6\text{MnO}_4.4\text{H}_2\text{O}]$ Ruthenium Trichloride $[\text{RuCl}_3.n\text{H}_2\text{O}]$ were prepared in a double distilled water and isopropyl alcohol. The prepared solution was stirred for 4 hours and then aged for 48 hours to get viscous solution. Then resultant sol-gel is spin coated on steel substrate to obtain thin film electrodes. Before deposition substrates were scrubbed with zero grade polish paper and cleaned in ultrasonic bath for 15 minutes.

3. Result And Discussion

a. Structural analysis by XRD

Structural analysis was carried out by D2 PHASER diffractometer with steps one degree per minute using source $\text{CuK}\alpha 1$ with $\lambda = 1.54184 \text{ \AA}$. The 2θ angle is varied from 10° to 90° . The fig.1 shows the XRD pattern for $\text{MnO}_2:\text{Co}_3\text{O}_4:\text{RuO}_2$ composite oxide thin films. XRD pattern exhibited crystalline nature with orthorhombic [8] and cubic phase [9] for MnO_2 , Co_3O_4 films respectively and tetragonal for RuO_2 The XRD pattern of $\text{MnO}_2:\text{Co}_3\text{O}_4:\text{RuO}_2$ composite films shows dominating peaks of Three oxides and two new peaks

of MnO_2 . The details of lattice constants are given in table.1. The lattice constant are matching with the standard values indicating the presence of all three oxides.

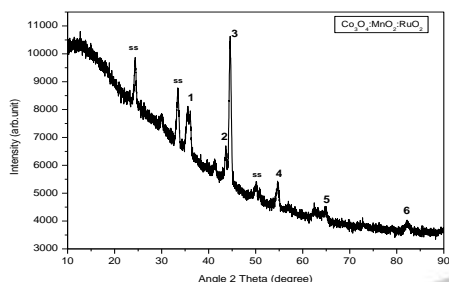


Fig. 1 XRD patterns of MnO_2 , Co_3O_4 and $\text{MnO}_2:\text{Co}_3\text{O}_4$ composite oxide thin films

2.2 Surface Morphology

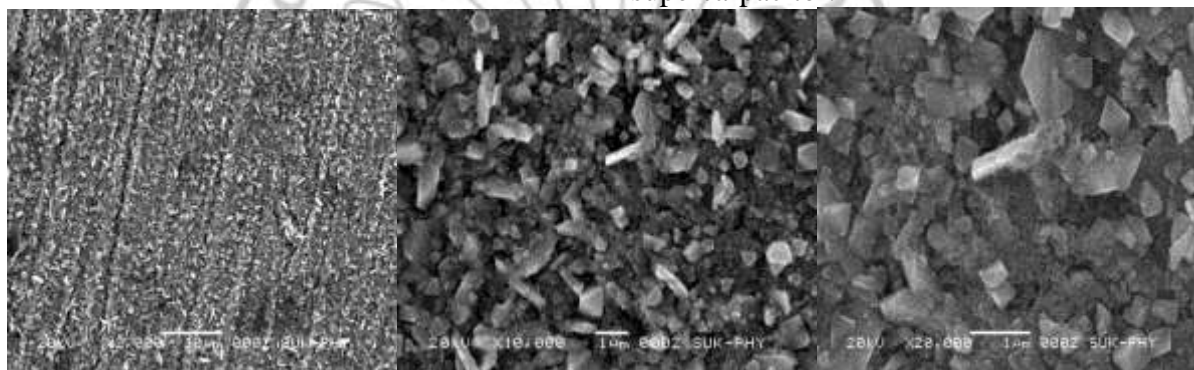


Figure. 2 SEM micrographs of $\text{MnO}_2:\text{Co}_3\text{O}_4:\text{RuO}_2$ composite thin films.

2.3 Electrochemical Analysis

2.3.1 Cyclic Voltammetry

The CV measurements were performed with $\text{MnO}_2:\text{Co}_3\text{O}_4:\text{RuO}_2$ composite thin films as working electrodes and platinum wire as counter electrode and SCE as a reference electrode in 0.1 M KOH electrolyte. Fig. 3 shows the cyclic voltammograms, with varying potential windows such as 0.65V to -1.3V at various scan rates 10, 20, 40, 60, 80 and 100mV/sec. From CV analysis, $\text{MnO}_2:\text{Co}_3\text{O}_4:\text{RuO}_2$ composite films showed maximum specific capacitance of 440 F/g, at 10mV/s scan rate. [10]

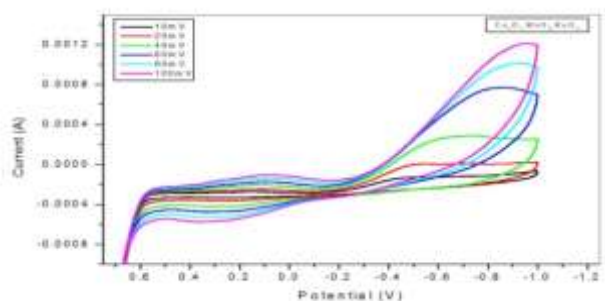


Figure.3 Cyclic Voltammograms of ternary (Co:Mn:Ru) oxide electrode

2.3.2 Cyclic Stability

Since the $\text{MnO}_2:\text{Co}_3\text{O}_4:\text{RuO}_2$ composite film gave the highest capacitance, we investigated the stability of the film for longer votammograms upto 1000 cycles at the scan rate of 500mVs^{-1} in 0.1M KOH electrolyte lasting about 3hour, is shown in fig. 4. The 75% stability is retained after 1000th cycle,

the value of specific capacitance is decreased by a comparably small amount which may be due to

detachment during early cycles in the electrolyte. [11]

charging/discharging

Manganese Oxide			Calculated			Standard			
Peak no.	Plane	d	a	b	c	a	b	c	JCPDS
2	120	2.18	9.892	3.913	2.837				
4	411	1.67				9.322	4.4533	2.8482	82-2169
5	520	1.43							
6	412	1.17							
Cobalt oxide			Calculated			Standard			
3	400	2.07	8.124						
4	422	1.67	8.218			8.085	8.085	8.085	82-2169
Ruthenium Oxide			Calculated			Standard			
1	101	2.50	4.50	4.50	3.15	4.52	4.52	3.12	
3	210	2.02							88-0322
5	310	1.42							

V at a current density of 1mA cm^2 in 0.1 M KOH electrolyte as shown in fig. 5. It is observed that charging-discharging time are almost same. From CP, the supercapacitive parameters such as specific energy, specific power and

coulombic efficiency were calculated. $\text{MnO}_2:\text{Co}_3\text{O}_4:\text{RuO}_2$ composite films exhibited specific energy 158.76 Wh/kg , and specific power 83.04 KW/kg . The coulombic efficiency of the electrodes was found to be 100%.

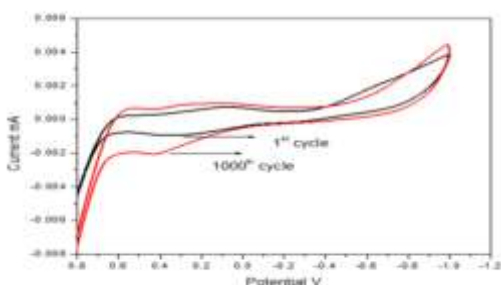


Fig.4.

2.3.3 Chronopotentiometry

Typical charging and discharging curves for $\text{MnO}_2:\text{Co}_3\text{O}_4:\text{RuO}_2$ composite electrodes were measured between the voltage range of -0.6 to $+0.6$

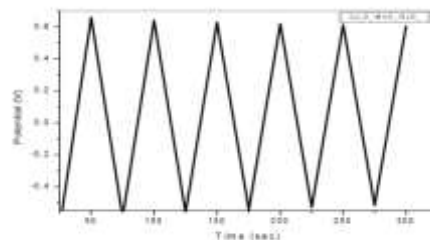


Fig. 5 Charge-discharge curves of oxide electrodes

Conclusion

This study shows successful synthesis of $\text{MnO}_2:\text{Co}_3\text{O}_4:\text{RuO}_2$ composite oxide thin films as confirmed by the different characterizations such as XRD, SEM, CV, Stability and Chronopotentiometry. XRD revealed the formation of metal oxides which are crystalline in nature, the XRD pattern of composite film include dominating peaks of both metal oxides. The lattice mismatch between pure and composite films indicate significant variations occurred on the structures and properties of composite thin film to some extent. The SEM images clearly indicated the enhanced porous nature of $\text{MnO}_2:\text{Co}_3\text{O}_4:\text{RuO}_2$ composite oxide as compared to pure thin films. Cyclic Voltammety, and Charge-discharge techniques revealed that $\text{MnO}_2:\text{Co}_3\text{O}_4:\text{RuO}_2$ composite oxide electrode exhibited good electrochemical behaviour. It has been also observed that value of specific capacitance is more for composite electrode as compared to pure electrodes.

Acknowledgement

Authors wish to acknowledge the U.G.C, New Delhi for financial support through the Major Research Project F No. 42-123/2013(SR).

References

- Dongfang Yang, Industrial Materials Institute, National Research Council Canada, www. intechopen.com
- A. K. Shukla, S. Sampath, K. Vijayamohanan, Current Science. 2000, 79, 1656.
- P. J. Hall, M. Mirzaeian, S. I. Fletcher, F. B. Sillars, A. J. R. Rennie, G. O. Shitta-Bey, G. Energy & Environmental Science. 2010, 3, 1238.
- V. Srinivasan, J.W. Weidner. J Electrochem Soc, 2000, 147, 880.
- W.U Meng-qiang, Jia-hui, Shu-ren, et al. J Power Sources, 2006, 159:365.
- W. Yong, Z. Xiao, J. Electrochimica Acta, 2004, 49: 1957-1962.
- S. L. Kuo, J. F. Lee, N. L. Wu, J Electrochem Soc, 2007, 154: A34-A38.
- JCPDS card No. 82-2169
- JCPDS card No. 78-1969
- W.C. Chen, T.C. Wen and H. Teng, Electrochim. Acta, 48 (2003) 641.
- F. Rafik, H. Guolous, R. Gallay, A. Crausaz and A. Berthon, J. Power Source, 165, (2007) 928.

Suzuki-Miyaura coupling catalyzed by Palladium nanoparticles generated from Multi functionalized ionic liquid

D. S. Gaikwad^{a*}, K. A. Undale^a, D. M. Pore^b, S. N. Korade^b, S. A. Sonavane^b

^aDepartment of Chemistry, Vivekanand College, Kolhapur, Maharashtra 416003, India

^bDepartment of Chemistry, Shivaji University, Kolhapur, Maharashtra 416 004, India

*E-mail: dgchemistry@gmail.com; Tel.: +91 231 2658612; fax: +91 231 2658840

Abstract

Here in we report, a novel, multi functionalized task specific ionic liquid which induces reaction in water and acts as a reducing as well as stabilizing agent for in situ formation of palladium nanoparticles (Pd-Nps). The generated palladium nanoparticles were characterized by UV-visible spectroscopy, transmission electron microscopy (TEM) analysis. These in situ synthesized palladium nanoparticles with particle size below 10 nm exhibited a high catalytic activity in the Suzuki cross-coupling of aryl halide with aryl boronic acid without using external phosphine ligand. The aqueous system containing ionic liquid along with Pd-NPs was recycled for eight times, without significant loss of catalytic activity.

Key words

Ionic liquid, Suzuki-Miyaura coupling reaction, Palladium Nanoparticles, Transmission Electron Microscopy

1. Introduction

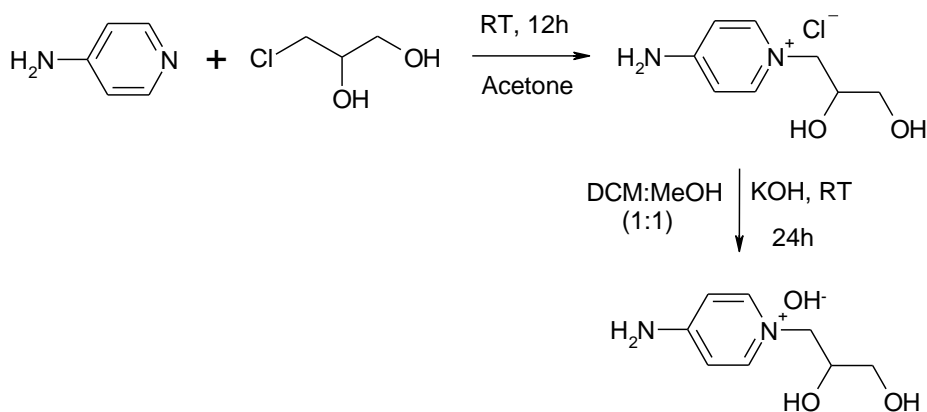
The catalytic activity of metal nanoparticles (NPs) symbolizes a prosperous resource for chemical processes, engaged both in industry and in academics.^{1,2} The synthesis of NPs is of great current interest and it has a potential future. They have applications in diverse fields, including energy conversion and storage, chemical manufacturing, biological applications, and environmental technology.^{3,4} The use of NPs as efficient catalysts in organic reactions has attracted considerable interest in recent times in the context of green chemistry because of their benign character and ease of preparation.⁵ Numerous catalytic systems based on metal nanoparticles immobilized in ionic liquids (ILs) have been developed for hydrogenation, oxidation, alkylation, and C-C coupling reactions under both single-phase and multiphase conditions. In fact, there are some quite outstanding reviews on the preparation, characterization, and use (including in catalysis) of soluble metal nanoparticles in ILs.⁶ This is because ILs poses several unique properties, such as negligible vapor pressure, no miscibility with non-polar solvents, and reasonable thermal and chemical stability with excellent electrical conductivity.⁷ Owing to these unique properties, more attention has been focused on the synthesis of new ionic liquids with functional groups, so-called "task-specific" ionic liquids

(TSILs) which will act as reducing as well as stabilizing agent for NPs.

Palladium-catalyzed C-C couplings reactions such as Suzuki, Heck, Sonogashira, Stille and Negishi reactions as the most common couplings which have developed into an important tool in organic synthesis, predominantly for pharmaceutical and agrochemical purposes.⁸ Among them Suzuki coupling⁹ have specially attracted the attention of many researchers, in essence due to the small loading of metal required to afford high turnover frequencies,¹⁰ so that the term "homeopathic palladium" is currently employed. The reaction, however, suffers from a number of drawbacks such as catalyst loss into the product formation, catalyst decomposition and poor reagent solubilities. We take for granted that, these problems might be resolved by the use of newly synthesized ionic liquid. As part of a continuing effort in our laboratory towards the development of new methods in green process,¹¹ we herein disclose a novel protocol for the Suzuki coupling reaction using in situ generated Pd NPs by the use of TSIL as a reducing as well as stabilizing agent. The desired carbon-carbon bond formation proceeded under mild conditions with high efficiency and good functional group tolerance.

Results and discussion

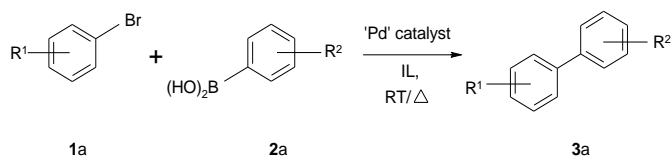
Initially we have synthesized a novel multi functionalized ionic liquid.



Scheme 1: Synthesis of Novel Multi functionalized ionic liquid

Keeping the basic things in mind which are required for synthesis of NPs and further completion of coupling reaction, we focused to synthesis such IL which will fulfill these all requirements (**Scheme 1**). We carried out first quaternisation of 4-amino pyridine and 3-chloro-1,2-diol in acetone at room temperature and increased the basicity of the ionic liquid by incorporating OH⁻ on reaction with potassium hydroxide. The cation of IL contains amino functional group which increases basicity (4-amino pyridine has Pka 9.17) of the ionic liquid and the diol functionality acts as a reducing as well as stabilizing agent for Pd NPs. The formation of IL was confirmed by characterizing its ¹H and ¹³C NMR, and we delighted that spectra confirmed the formation of desired multifunctional IL.

After synthesizing IL, we investigated its use in Suzuki coupling reaction and carried out a model reaction with 4-Iodoanisole **1**, phenylboronic acid **2**, Pd(OAc)₂ as a catalyst and synthesized IL i.e. [ADPPY][OH] (20 mol%) in water. When reaction was carried out at room temperature after prolonged reaction time we observed very negligible product, but when the same was carried out at 80°C reaction completed 100%. Results of this preliminary survey are shown in Table 1.



Scheme 2: A Typical Suzuki-Miyaura Coupling reaction

Table 1. Optimization of the reaction conditions

Entry	Catalyst	Base (mol%)	Temp. (°C)	Yield (%) ^b
1	Pd(PPh ₃) ₄	[ADPPY][OH] (20)	RT	20
2	Pd(PPh ₃) ₄	[ADPPY][OH] (20)	80	60
3	Pd ₂ (dba) ₃	[ADPPY][OH] (20)	80	40
4	Pd/C	[ADPPY][OH] (20)	80	10
5	Pd(OAc) ₂	[ADPPY][OH] (20)	RT	45
6	Pd(OAc)₂	[ADPPY][OH] (20)	80	99
7	Pd(OAc) ₂	[ADPPY][OH] (30)	80	99
8	PdCl ₂	[ADPPY][OH] (30)	80	90

^a Reaction conditions: 4-Iodoanisole (1 mmol), phenylboronic acid (1.1 mmol), Pd(OAc)₂ (2 mol%), water (5 mL), ^b Isolated yields.

We also explored the effect of the amount of [ADPPY][OH] and the ratios of substrates on the model reaction. The results are listed in Table 2. We found that 20 mol% of [ADPPY][OH] (entries 2, 4 and 5) is sufficient to promote the coupling reaction. A ratio of 4-Iodoanisole to phenyl boronic acid of 1: 1.1 is sufficient to the almost conversion (entry 4).

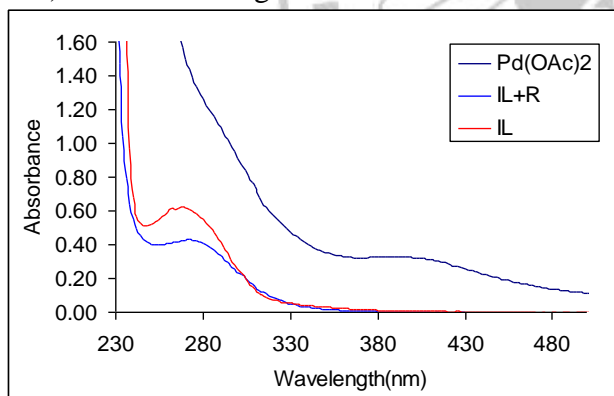
Table 2 The effect of the amount of [ADPPY][OH] and the ratio of substrates on the reaction^a

Entry	Ratio	[ADPPY][OH]	Yield
1	1:1	20 mol%	~0%
2	1:1.1	20 mol%	60%
3	1:1.1	30 mol%	99%
4	1:1.1	20 mol%	10%
5	1:1.1	20 mol%	45%
6	1:1.1	20 mol%	99%
7	1:1.1	30 mol%	99%
8	1:1.1	30 mol%	90%

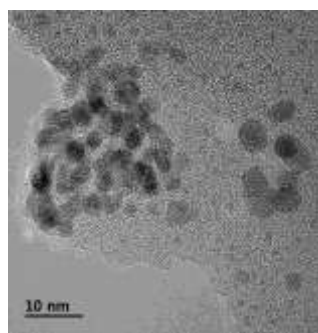
	substrate : boronic acid	(mol%)	(%) ^b
1	1 : 1.0	5	58
2	1 : 1.0	10	71
3	1 : 1.1	5	79
4	1 : 1.1	20	91
5	1 : 1.5	20	86

Reaction conditions: 4-Iodoanisole, phenylboronic acid, Pd(OAc)₂ (2 mol%), [ADPPY][OH], DMF (1.0 mL), 80 °C; ^b Isolated yields.

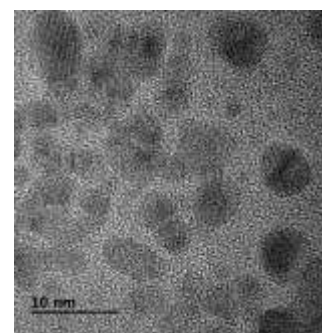
After the completion of reaction, we have extracted the reaction mixture by diethyl ether to separate the synthesized biaryls. Then the aqueous phase have been analysed by recording UV-Vis spectrum in acetone medium and compared the same with that of Pd(OAc)₂ (Fig. 4). The absorption at 405 nm due to Pd(OAc)₂ disappeared from the reaction mixture due to the formation of palladium nanoparticles. These obtained Pd-Nps is characterized by transmission electron microscopy (TEM) as shown in Fig 5.



(a)



(b)

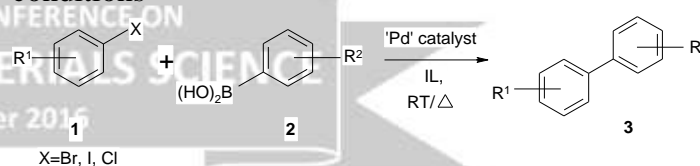


(c)

Fig. 1: (a) UV-Vis Spectra of reaction mixture after completion of reaction (b) & (c) TEM analysis of separated Pd NPs

We chose the optimized reaction conditions as; 1 mmol aryl halides, 1.1 mmol phenylboronic acids, 20 mol% of [ADPPY][OH], 2 mol% Pd(OAc)₂ and 5 mL water at 80 °C. A variety of electron donating and electron withdrawing aryl halides and various substituted phenylboronic acids were then explored as substrates, and the results are listed in Table 3. We found that aryl bromides and iodides reacted with phenylboronic acid efficiently, giving the good to excellent yields. It was observed that, aryl iodides gave higher yields than the corresponding bromides (Table 3, entries 1–7 vs. 8, 9). It was also scrutinized that, aryl halides bearing an electron-withdrawing group (Table 3, entry 11, 12) gave lower yields.

Table 3. The reactions of aryl halides and phenylboronic acids under the optimized reaction conditions^a



Entry	Aryl Halide	Boronic Acid	Time in min	Yield (%) ^b
a	R ¹ =H, X=I	R ² =H	30	91
b	R ¹ =H, X=Cl	R ² =4-OMe	30	88
c	R ¹ =H, X=Br	R ² =2-Me	30	79
d	R ¹ =4-Me, X=Br	R ² =H	30	89
e	R ¹ =4-Me, X=I	R ² =4-OMe	35	83
f	R ¹ =4-OMe, X=I	R ² =H	35	88
g	R ¹ =4-OMe, X=I	R ² =4-OMe	35	71
h	R ¹ =4-CN, X=Br	R ² =H	45	77
i	R ¹ =4-CN, X=Br	R ² =4-OMe	45	75
j	R ¹ =4-NO ₂ , X=I	R ² =H	50	54

k	R ¹ =4-NO ₂ , X=I	R ² =4-OMe	50	47
l	R ¹ =4-COMe, X=Br	R ² =H	40	76
m	R ¹ =4-OMe, X=Br	R ² =4-OMe	40	69
n	R ¹ =4-OMe, X=Br	R ² =2-Me	45	87
o	1-Naphthyl Iodie	R ² =H	40	55

^a Reaction conditions: aryl halide (1 mmol), boronic acid (1.1 mmol), Pd(OAc)₂ (5 mol%), [ADPPY][OH] (10 mol%), DMF (1.0 mL) at 65 °C. ^b Isolated yield based on the aryl halides.

Green chemistry legislations direct us to minimize the waste and conservation energy. In this standpoint, recycling of catalyst is highly warranted. Hence, we carried out the recyclability study of ionic liquid-PdNPs catalytic system for the model reaction. Gratifyingly, it was observed that the catalytic system can be reused effectively for 8 times without significant loss of activity providing excellent yields of products (**Fig. 2**).

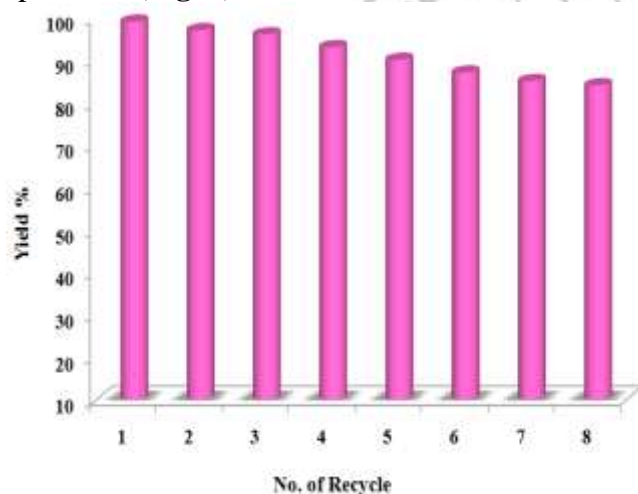


Fig. 2 Reusability of catalytic system (Ionic liquid & Pd NPs)

Experimental Section

Chemicals (Spectrochem, Mumbai) and palladium sources (Spectrochem, Mumbai) were used as received. All reactions were carried out aerobic condition in predried glassware. Infrared spectra were recorded on a Perkin-Elmer FT-IR-783 spectrophotometer. ¹H NMR and ¹³C NMR spectra were recorded on a Bruker AC spectrometer (300 MHz for ¹H NMR and 75 MHz for ¹³C NMR), using CDCl₃ as solvent and tetramethylsilane (TMS) as an internal standard. Chemical shifts (δ) are expressed in parts per million (ppm) and coupling constants are expressed in hertz (Hz).

Synthesis of Ionic Liquid:

To a vigorously stirred solution of 4-amino pyridine (10 mmol) in acetone (25 mL), 3-chloro-1,3-propane diol (11 mmol) was slowly added at room temperature and stirred reaction mixture for 12 h.. After completion of reaction acetone was decanted and the remaining viscous oil was repeatedly washed with diethyl ether to yield transparent viscous ionic liquid, which was dried in vacuum.

The IL obtained from first step 4-amino-1-(2,3-dihydroxy-propyl)-pyridinium chloride [ADPPy][Cl] (10 mmol) was then dissolved in dichloromethane:methanol (1:1) and cooled at 0°C followed by addition of potassium hydroxide (11 mmol) and stirred it for 24 h at room temperature. The suspension was filtered to remove the precipitated potassium chloride salt and the solvent was evaporated under reduced pressure furnished 4-amino-1-(2,3-dihydroxy-propyl)-pyridinium hydroxide [ADPPy][OH].

Typical Procedure for Suzuki-Miyaura Coupling reaction:

In the optimized procedure, [ADPPy][OH] (20 mol%) was added to a mixture of the aryl halide (1 mmol), phenylboronic acid (1.1 mmol), Pd(OAc)₂ (2 mol%) and water (5 mL) in a 25 mL round-bottomed flask. The reaction mixture was stirred at 80 °C until complete conversion of aryl halide had taken place (monitored by TLC). After completion, the reaction mixture was extracted with diethyl ether (5 X 3 mL) and the combined organic extracts were dried over anhydrous sodium sulfate and evaporated under vacuum, leaving the crude product, which was purified by column chromatography. All products have been reported previously, and their identities were confirmed by ¹H NMR and ¹³C NMR spectroscopy.

Conclusions

In conclusion, we have developed an eco-benign method for Suzuki-Miyaura coupling by employing a novel IL-PdNPs catalytic system. In-situ generation of PdNPs is assisted by novel multi functionalized ionic liquid which also reduces and stabilizes them. The catalytic system can be reused at least for 8 times without any significant loss in catalytic activity which is one of the green aspects of method. Novelty of the protocol is exploration of novel efficient catalytic system for Suzuki coupling along with additional features viz. operational simplicity, reusability of the catalytic system, shorter reaction time, avoidance of conventional volatile organic solvents, no waste formation, 100 % atom economy, easy work up procedure, etc. Thus we believe that our findings portend significant gains toward achieving ideal transformations.

Spectral Data: Spectra Data of Ionic Liquid: 4-amino-1-(2,3-dihydroxy-propyl)-pyridinium hydroxide [ADPPy][OH].

Viscous yellow liquid, ¹H NMR (DMSO-d⁶, 300 MHz, TMS): 3.20 (1H, m), 3.25 (1H, m), 3.72 (1H, s), 3.97 (1H, m), 4.27 (1H, m), 4.81 (1H, s), 5.06 (1H, m), 5.43 (1H, d), 6.85 (2H, d, J=6Hz), 8.09 (2H, d, J=9Hz), 8.31 (2H, s), ¹³C NMR (CDCl₃, 75 MHz, TMS): 60.07, 63.14, 70.86, 109.49, 143.56, 159.54.

Spectral Data of selected compounds:

Entry a, Table 3: White solid, mp 70–72°C; IR (KBr): 3034, 1569, 1481, 1428, 728, 696 cm⁻¹; ¹H NMR (CDCl₃, 300 MHz, TMS): d 7.39–7.44 (2H, m, ArH), 7.49–7.54 (4H, m, ArH), 7.66–7.69 (4H, m, ArH). ¹³C NMR (CDCl₃, 75 MHz, TMS): 127.22, 127.30, 128.80, 141.32

Entry I, Table 3: White solid, mp 120–121°C; IR (KBr): 3073, 2998, 1678, 1602, 1403, 1359, 1283, 1263, 961, 842, 765, 721, 691 cm⁻¹; ¹H NMR (CDCl₃, 300 MHz, TMS): 2.65 (3H, s, CH₃), 7.42–7.48 (3H, m, ArH), 7.62–7.69 (4H, m, ArH), 8.04 (2H, d, J=7.2 Hz, ArH). ¹³C NMR (CDCl₃, 300 MHz, TMS): 26.61, 127.21, 127.26, 128.21, 128.89, 128.93, 135.89, 139.89, 145.78.

References:

- 1 Senanayake, S. D.; Stacchiola, D.; Rodriguez, J. A. *Acc. Chem. Res.* 2013, 46, 1702–1711.
- 2 Bordiga, S.; Groppo, E.; Agostini, G.; van Bokhoven, J. A.; Lamberti, C. *Chem. Rev.* 2013, 113, 1736–1850.
- 3 Laurent, S.; Forge, D.; Port, M.; Roch, A.; Robic, C.; Vander Elst, L.; Muller, R. N. *Chem. Rev.* 2008, 108, 2064–2110.
- 4 Gawande, M. B.; Branco, P. S.; Parghi, K.; Shrikhande, J. J.; Pandey, R. K.; Ghumman, C. A. A.; Bundaleski, N.; Teodoro, O.; Jayaram, R. V. *Catal. Sci. Technol.* 2011, 1, 1653–1664.
- 5 (a) Astruc, D. *Inorg. Chem.* 2007, 46, 1884–1894; (b) Astruc, D.; Lu, F.; Aranzaes, J. R. *Angew. Chem., Int. Ed.* 2005, 44, 7852–7872; (c) Polshettiwar, V.; Baruwati, B.; Varma, R. S. *Green Chem.* 2009, 11, 127–131; (d) Reetz, M. T.; Westermann, E. *Angew. Chem., Int. Ed.* 2000, 39, 165–168; (e) Durand, J.; Teuma, E.; Gomez, M. *Eur. J. Inorg. Chem.* 2008, 3577–3586.
- 6 (a) Dupont, J.; Scholten, J. D. *Chem. Soc. Rev.* 2010, 39, 1780–1804; (b) Prechtel, M. H. G.; Scholten, J. D.; Dupont, J. *Molecules* 2010, 15, 3441–3461; (c) Migowski, P.; Dupont, J. *Chem. Eur. J.* 2007, 13
- 7 (a) Jairton Dupont, Roberto F. deSouza, and Paulo A. Z. Suarez, *Chem. Rev.* 2002, 102, 3667–3692. (b) Thomas Welton, *Chem. Rev.* 1999, 99, 2071–2083.
- 8 Fernando Fernandez, Beatriz Cordero, Jerome Durand, Guillermo Muller, Francois Malbosc, Yolande Kihn, Emmanuelle Teumaa, Montserrat Gomez, Dalton *Trans.*, 2007, 5572–5581.
- 9 (a) Christopher J. Mathews, Paul J. Smith, Tom Welton, *Journal of Molecular Catalysis A: Chemical* 214 (2004) 27–32. (b) Hengquan Yang, Xiaojing Han, Guang Li, Yunwei Wang, *Green Chem.*, 2009, 11, 1184–1193. (c) Christopher J. Mathews, Paul J. Smith, Thomas Welton, *Chem. Commun.*, 2000, 1249–1250. (d) Yi-Yuan Peng, Jinbiao Liu, Xiaoli Lei, Zenlan Yin, *Green Chem.*, 2010, 12, 1072–1075. (e) Xue Yang, Zhaofu Fei, Tilmann J. Geldbach, Andrew D. Phillips, Christian G. Hartinger, Yongdan Li, Paul J. Dyson, *Organometallics* 2008, 27, 3971–3977. (f) James McNulty, Alfredo Capretta, Jeff Wilson, Jeff Dyck, George Adjabenga, Al Robertson, *Chem. Commun.*, 2002, 1986–1987. (g) Marco Lombardo, Michel Chiarucci, Claudio Trombini, *Green Chem.*, 2009, 11, 574–579. (h) R. Rajagopal, Dilip V. Jarikote, K. V. Srinivasan, *Chem. Commun.*, 2002, 616–617.
- 10 (a) J.G. de Vries, *Can. J. Chem.*, 2001, 79, 1086–1092. (b) D. H. B. Ripin, D. E. Bourassa, T. Brandt, M. J. Castaldi, H. N. Frost, J. Hawkins, P. J. Johnson, S. S. Massett, K. Neumann, J. Phillips, J. W. Raggon, P. R. Rose, J. L. Rutherford, B. Sitter, A. M. Stewart, M. G. Vetelino, L. L. Wei, *Org. Process Res. Dev.*, 2005, 9, 440–450. (c) S. Kotha, K. Lahiri and D. Kashinath, *Tetrahedron*, 2002, 58, 9633–9695.
- 11 (a) Gaikwad, D. S.; Park, Y. K.; Pore, D. M. *Tetrahedron Lett.* 2012, 53, 3077–3081; (b) Patil, J. D.; Korade, S. N.; Patil, S. A.; Gaikwad, D. S.; Pore, D. M. *RSC Adv.* 2015, 5, 79061–79069.

A Comparative Study of Structural and Morphological Properties of Pristine and Mn Doped Ruthenium Oxide Thin Films

P.S Joshi^{1*}, S.M. Jogade², S.D. Gothe³ and D.S Sutrave²

^{1*}Walchand Institute of Technology, Solapur-413006, Maharashtra, India.

²D.B.F Dayanand College of Arts and Science, Solapur, 413002, Maharashtra, India.

³Sangameshwar College Solapur, 413003, Maharashtra, India

Abstract:

Mn-doped and pristine Ruthenium Oxide composite nanostructures in thin film form were prepared on stainless steel substrates by sol-gel spin coating method. The wt % of Mn was increased as 0.1, 0.2, 0.5, 1 and 2 %. The X-ray diffraction study showed crystalline behaviour for both pristine and doped films with porous morphology. The variation in lattice constants for both RuO₂ and MnO₂ was observed with increase in doping percentage. EDAX spectrum showed the successful doping of Mn in RuO₂. The infrared spectrum of as deposited pristine RuO₂ thin film depicted strong absorption bands at 880.41 cm⁻¹ and 749.52 cm⁻¹ indicating the stretching mode of Ru=O and O-Ru-O respectively. The absorption peaks attributed to the -OH bending vibrations along with Mn atoms were also seen.

Keywords: Pristine RuO₂, Mn doped RuO₂, XRD, SEM, FTIR, EDAX.

1. Introduction

Low resistivity, good thermal stability, high resistance to chemical corrosion, these desirable characteristics have attracted Ruthenium Oxide for its diverse applications in various fields [1-6]. It is well known that the capacitance of RuO₂ electrode results from redox pseudocapacitance. However, the current response resembles an ideal capacitor, which is a “rectangular” shape under cyclic voltammetry. It has been widely used in supercapacitor because of its good catalytic properties [7]. Even though RuO₂ has a great advantage in terms of a wide potential range of highly reversible redox reactions with high specific capacitance, it is expensive. Therefore, it is desirable to develop a process for the preparation of thin film RuO₂ electrodes to reduce their cost as capacitor electrodes [8]. Another metal oxide Manganese oxide is of considerable importance in technological applications due to its natural abundance coupled with environmental compatibility and also intensively investigated as promising electrode material in electrochemical capacitors [9-11]. In the current work, thin films of pristine Ruthenium oxide and Mn doped Ruthenium oxide were preferred as the form of the samples to be synthesized because the controlled synthesis of materials as thin films is an elementary step in many applications.

2. EXPERIMENTAL

Here attempts are made for the synthesis of pristine RuO₂ Mn doped RuO₂ thin films so as to

minimize the quantity of Ruthenium material and to achieve the required results. For this, sol-gel spin coating deposition technique was used which allows the uniform deposition of the gel on the substrate. Also the structural, morphological and electrochemical properties in terms of XRD, SEM, EDAX, FTIR were studied with increasing doping percentage of Mn in RuO₂. For doped samples, Ruthenium trichloride and manganese trichloride solution of molarity 0.01 M each were prepared. Then weight percentage of Mn was increased as 0.1 %, 0.2%, 0.5%, 1% and 2%. To these five different solutions, isopropyl alcohol was added. After stirring and setting for 24 hours gel was formed. Then the gel was deposited on properly cleaned SS substrates in spin coater unit. After annealing, uniform and thin films were obtained. Figure 1. shows the flow chart of doped thin film preparation.

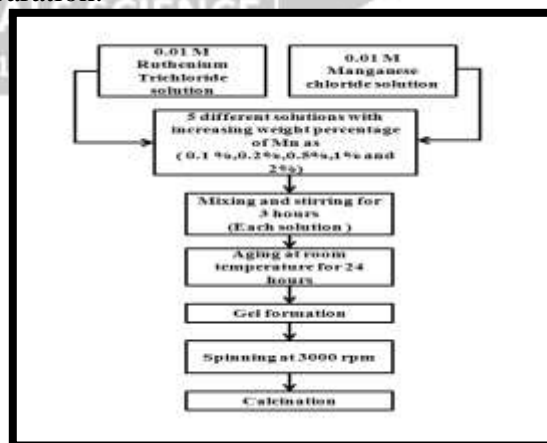


Figure1. Flow chart of thin film preparation by the sol-gel spin coat route.

3. Results and Discussions:

3.1 Structural Properties

The X-ray diffraction pattern of as deposited pristine RuO₂ and Mn doped RuO₂ thin films thin films is shown in Fig.2.

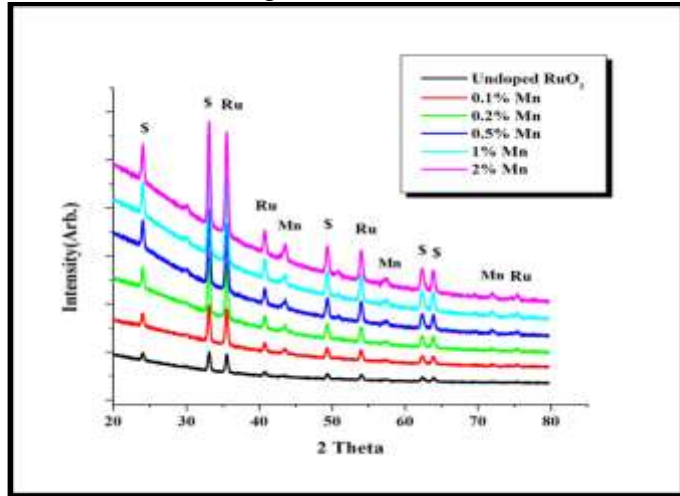


Figure 2. XRD of Undoped and Mn doped RuO₂ thin films.

The experimental data showed the crystalline nature of RuO₂ with tetragonal structure (JCPDS Card No.-88-0322) having lattice constants of $a = b = 4.4933 \text{ \AA}$, $c = 3.1061 \text{ \AA}$ with $d = 2.55, 2.22, 1.68$ and 1.28 corresponding to Miller Indices [011], [111], [211] and [202] respectively which are in good agreement with JCPDS card. Similarly tetragonal structure of MnO₂ film (JCPDS Card No.-82-2261) with lattice constants $a = b = 4.4192 \text{ \AA}$, and $c = 2.8566 \text{ \AA}$ with $d = 2.06, 1.62, 1.31 \text{ \AA}$ corresponding to Miller indices [410], [210] and [112] respectively which are also in good agreement with JCPDS card. The peaks which are labelled as “\$” correspond to stainless steel. It was observed from XRD that there is a shift in 2 theta to higher values for every observed dominant peak of RuO₂ and the intensity of corresponding peaks has also been decreased with increasing doping concentration of Mn. The change in intensity in RuO₂ as well as MnO₂ peaks with increase in doping concentration of Mn for respective 2 theta values is shown in Figure 3 .

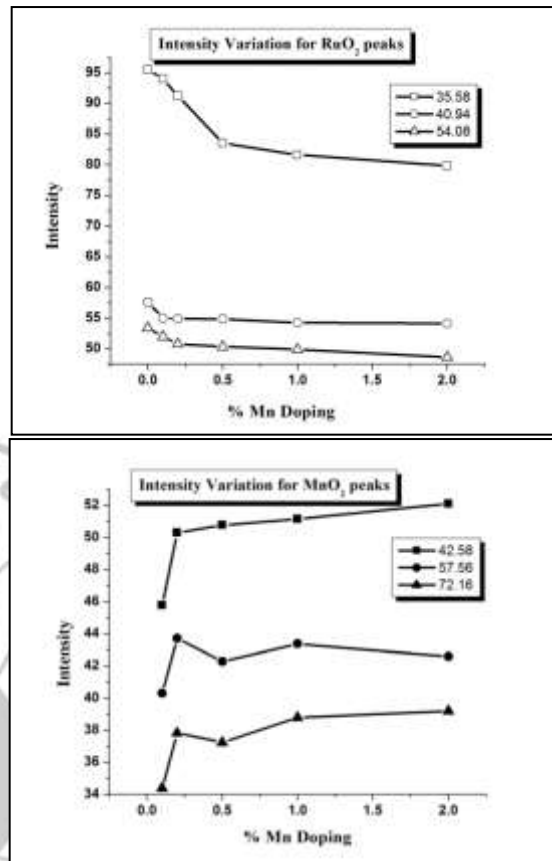


Fig 3. Intensity variation for RuO₂ and MnO₂ peaks at different 2 theta with increasing % doping of Mn.

Usually on doping, the peak intensity decreases which might be due the change in electron density or might be due to point defects. Intensity change is related to adsorption on surface while change in theta indicates inter-layer change. Shift of Bragg peaks to lower values of the diffraction angle, increases lattice parameter. The variations in lattice constants are given in table 1.

	RuO ₂		MnO ₂	
	a = b	c	a = b	C
Pure thin films	4.52 A°	3.12 A°		
Mn doped RuO ₂ thin films	4.49 A°	3.10 A°	4.42 A° 4.40 A° (std)	2.86 A° 2.87 A° (std)

Table 1. Increase in lattice parameters in RuO₂ and MnO₂ due to increase in doping percentage of Mn

3.2 Morphological Properties

The two-dimensional surface morphological study of thin films has been carried out from SEM image for 0.12 mg/cm² film thickness. Figure 4. shows the SEM image pristine RuO₂ thin film. The SEM image showed non-uniformly distributed aggregates giving rise to a high surface roughness. Such porous and “mud-cracked” morphology is favourable for penetration of electrolyte.

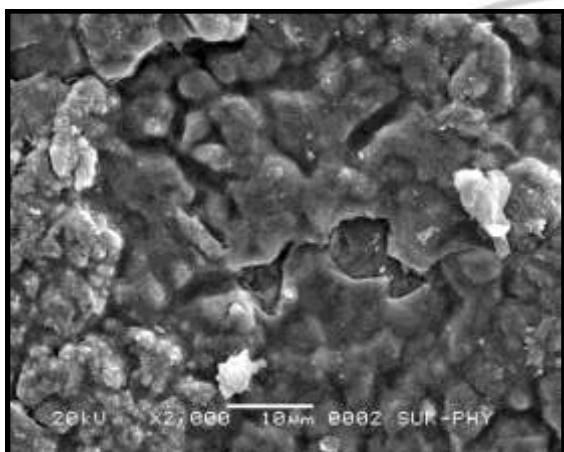


Figure 4. Surface Morphology of pristine RuO₂ thin film.

The surface morphological images of Mn doped RuO₂ thin films with increasing doping concentration of Mn for higher magnification are depicted in figure 5.

The morphology showed that the substrate is well covered with RuO₂ material. The porous structure created due to the interconnected structure can also

be clearly seen. It is evident from SEM images that the various randomly distributed interconnected macropores are present over the substrate. It is clearly seen that the number of pores and their size was increased with doping concentration from 0.1 to 1 at % Mn doping. But for 2 at % of Mn doping the number of pores and their size was changed considerably.

Sufficient void spaces in and between the pores, pore size distribution and such porous structure greatly assist the ion diffusion from the electrolyte into the electrode, which raise the specific capacitance. Admirable electrochemical performance as an electrode for a supercapacitor could be demonstrated due to the interconnected structure [12].

EDX is a characterisation technique that provides elemental composition of various constituent elements in a material. The abscissa of the EDX spectrum indicates the ionization energy and ordinate indicates the counts.

Higher the counts of a particular element, higher will be its presence at that point or area of interest. The elements of deposits on the top of SS, pristine RuO₂ and Mn doped RuO₂ were studied using EDX spectrums. The presence of Ni, Fe, Cr belongs to SS (fig.6. a) and the presence of elements such as Ru and O is assigned to the formation of RuO₂ (fig.6 b). Mn incorporated in (fig. 4. c) RuO₂ shows successful doping. There was increment in the weight percentage of Mn with increase in doping percentage.

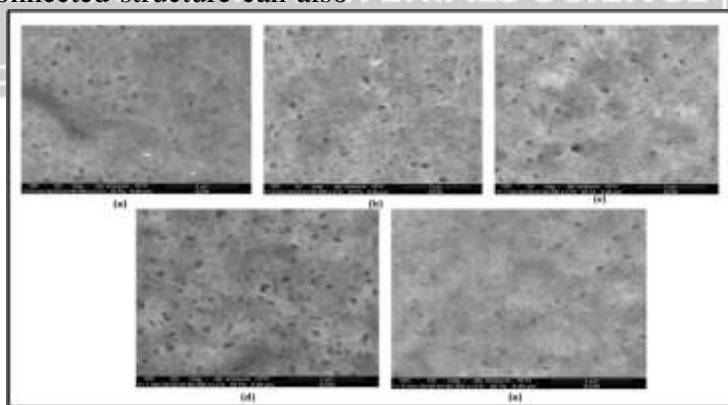


Fig. 5. SEM images for Mn doped RuO₂ samples (a) 0.1 at % (b) 0.2 at% (c) 0.5 at% (d) 1 at% (e) 2 at%.

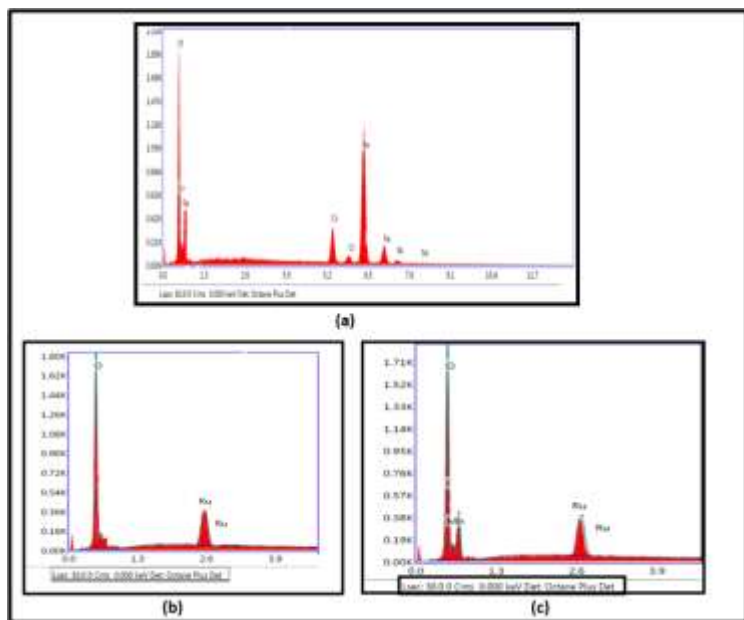


Figure 6. EDX Spectrum : a) Empty SS b) pristine RuO₂ c) Mn doped RuO₂ deposited pristine RuO₂ thin film depicts strong absorption bands at 880.41(II) cm⁻¹ and 749.52 (I) cm⁻¹ indicating the stretching mode of Ru = O and O – Ru - O [13]. The absorption band at 3410 cm⁻¹ (III) is attributed to the stretching vibration stretching vibrations of OH⁻. This result indicated that, as deposited film contained hydroxide and other bonds, which indicates that formation of hydrous ruthenium oxide that may play important role in capacitive behavior [14]. The absorption peaks around 1650 cm⁻¹ may be attributed to the –OH bending vibrations along with Mn atoms [15].

3.3 FTIR Spectroscopy

For study of surface features of materials and for the examination of absorbed molecules on a solid surface, Fourier Transform infrared spectroscopy is a well known technique. IR spectroscopy was used to obtain additional information on the phases as well as structure transformations of RuO₂ and MnO₂ phases.

Figure 7. describes the dependence of optical spectra in the range 500 cm⁻¹ to 4000 cm⁻¹ for Ruthenium Oxide thin films. The infrared spectrum of as

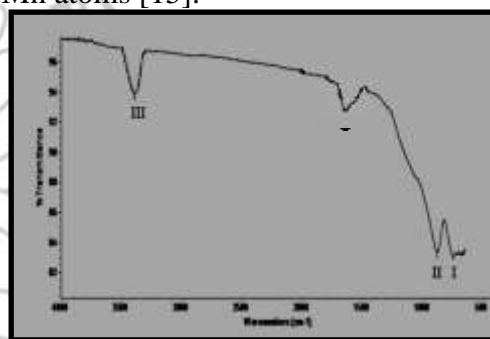


Figure 7. FTIR Spectrum of Mn doped RuO₂ Thin Film.

4. Conclusion

From the above results it can be concluded that Sol-gel spin coating technique can be used as an efficient and cheap method for the synthesis of pristine and Mn doped ruthenium oxide thin films. It showed the admirable variations in structural and morphological properties with increase in Mn wt % doping. There as an increase in lattice constants with doping. EDAX spectrum showed the successful doping of Mn in RuO₂. The infrared spectrum of as deposited pristine RuO₂ thin film depicted strong absorption bands at 880.41 cm⁻¹ and 749.52 cm⁻¹ indicating the stretching mode of Ru=O and O-Ru-O respectively. The absorption peaks attributed to the –OH bending vibrations along with Mn atoms were also seen.

Acknowledgments:

The authors wish to acknowledge the U.G.C , New Delhi for financial support through the major research project F.No-42-123/2013(SR).

References:

1. L.KrusinElbaum, M.Wittmer, D.S.Yee, *Appl.Phys.Lett*, 50(1987), 1879
2. A.Belkind, Z.Orban, J.L.Vossen, J.A.Wollam, *Thin Solid Films*, 50,(1992), 242
3. E. Kolawa, et al , *Appl.Phys.Lett*, 50(1987), 854
4. M. Deepa, A.K. Srivastava, K.N. Sood, S.A. Agnihotry, *Nanotechnology*, 17 (2006) 2625
5. V.R. Shinde, T.P. Gujar, C.D. Lokhande, *Sens. Actuators B* 120 (2007)
6. S. Karuppuchamy, K. Nonomura, T. Yoshida, T. Sugiura, H. Minoura, *Solid State Ionics* , 151 (2002) 19
7. D.S Sutrave, P.S Joshi, S.D Gothe, S.M Jogade, *International Journal of Chemtech Research*, 6- 3,(2014), 1991.
8. B.O Park , C.D Lokhande , H.S Park , K..D Jung, O.S Joo , *J Power Sources*, 134, (2004), 148
9. S. C. Pang and M. A. Anderson, *Journal of Materials Research*, 15-10,(2000), 2096.
10. S. F. Chin, S. C. Pang, and M. A. Anderson, *Journal of the Electrochemical Society*, 149-4 (2002), A379
11. S. F. Chin and S. C. Pang, *Materials Chemistry and Physics*, vol. 124-1(2010), 29.
12. Liu, Y. et al Manganese Dioxide nanosheet arrays grown on graphene oxide as an advanced electrode material for supercapacitors. *Electrochim. Acta* 111, 707-712(2013).
13. P.S Joshi, D.S Sutrave, *International Journal for Research in Applied Science and Engineering Technology*, Ruthenium Oxide: Thin film and Electrochemical Properties , 4-V-III, (2016), 765-772
14. W. Sugimoto et al *J. Electrochem. Soc.*, 151 (2004) A1181
15. M. Ocana, *Colloid Polym.Sci*, 278(2000)443

Mn Doped Co_3O_4 Thin Film Electrodes: CV Analysis for Supercapacitor Application

*Sangeeta Jogade. **Preeti Joshi, *Sagar Gaikwad, *Sutrave. D. S

*Department of Electronics, D. B. F. Dayanand College of Arts and Science, Solapur, MS. India

**Walchand Institute of Technology, Solapur, MS. India

Corresponding Author : sutravedattatray@gmail.com

Abstract

A series of manganese (Mn)-doped Cobalt oxide (Co_3O_4) thin films were deposited on steel substrate by sol-gel spin coat method and investigated the impact of doping concentrations of Mn in Cobalt ranging from 0.001% to 1%. Cyclic Voltammetry technique was used for the electrochemical characterizations of supercapacitor cells fabricated using the Mn doped Co_3O_4 thin films as their electrodes. The characterization of the doped electrodes showed a notable effect of the Mn concentration on electrochemical properties and consistently found that with increase in Mn concentration performance of supercapacitor goes on improved, accordingly 1%Mn doped electrode exhibited higher specific capacitance and good cyclic stability compared to other electrodes with different doping concentrations.

1. Introduction

Electrochemical supercapacitors (ESs) are considered important energy efficiency devices for rapid energy storage and delivery. Among the advantages of ESs are high power density, environmentally friendly, long cycle life, high efficiency, wide range of operating temperatures, environmental friendliness and safety. ESs also serve as a bridging function for the power/energy gap of traditional dielectric capacitors. These characteristics have made ESs very competitive for applications in electric hybrid vehicles, digital communication devices such as mobile phones, digital cameras, electrical tools, pulse laser technique, uninterruptible power supplies, and storage of the energy generated by solar cells [1-3].

Co_3O_4 thin film and series of Mn incorporated Co_3O_4 thin films deposited by sol-gel spin coat method and investigated the influence of doping concentrations of Mn in Cobalt such as 0.001% to 1% on electrochemical properties. The deposited samples were denoted by different codes such as, S1, S2, S3, S4, S5, S6, S7 and S8 throughout the paper. Where S1=0%Mn, S2=0.001%Mn, S3=0.005%Mn, S4=0.01%Mn, S5=0.05%Mn, S6=0.1%Mn, S7=0.5%Mn and S8=1%Mn doping in cobalt. There are many electrochemical techniques for the characterization of supercapacitor exist, in the present work, cyclic voltammetry (CV) is used for the characterization of thin film electrodes. The capacitive behaviour of Co_3O_4 and Mn doped Co_3O_4 electrodes have been studied.

2. Cyclic Voltammetry Analysis

Voltammetry is basically referred to as a technique with the common characteristics that the potential of the working electrode is controlled and the resulting current flow is measured. The cyclic voltammogram gives us information on the possible redox reactions of the system, including the Faradaic insertion and extraction reaction, electrode processes, the determination of thermodynamics and kinetics of electron transfer at the electrode/electrolyte interface. It is often employed as a first method to characterize the system. The technique involves sweeping the electrode potential between two predetermined values at a known sweep rate [4]. In the present study, several sweep rates in the range from 10 to 100 mV/s were used to study scan rate effect on performance of electrodes and scan rate of 500mV/s was used to test the stability of electrodes.

2.1 Effect of Scan Rate

The cyclic voltammetry study is carried out with Co_3O_4 thin film electrode and Mn doped Co_3O_4 thin film electrode as working electrodes and platinum wire as counter electrode and SCE as a reference electrode in 0.1M KOH electrolyte. Figure. 1 shows the CV curves of Co_3O_4 (S1) electrode and Mn doped Co_3O_4 (S2 to S8) electrodes. Scan rate is varied from 10 to 100mV/s such as 10mV/s, 20mV/s, 40mV/s, 60mV/s, 80mV/s and 100mV/s in the potential window ranging from -1.3V to 0.65V. From the figures, it is proven that potential window as well as current associated with the CV curve increases with increase in scan rate. Which indicates

that voltammetric current is directly proportional to the scan rates of CV and this is an good indication of

supercapacitive behaviour [5-7]

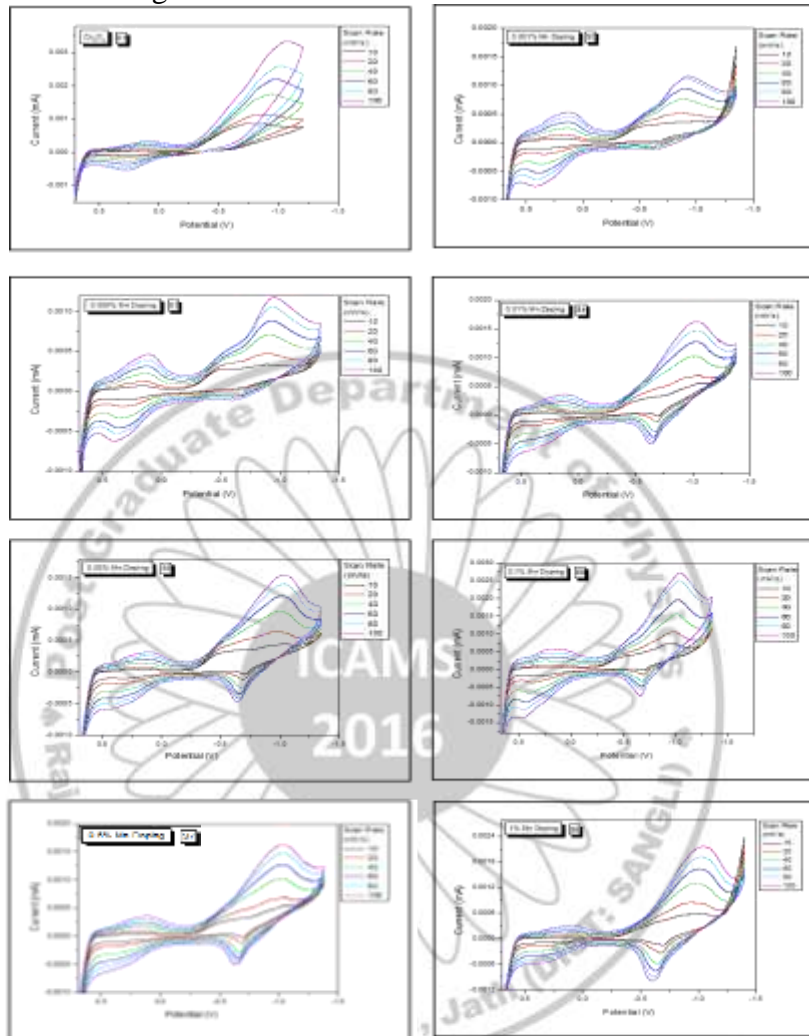


Fig. 1 Cyclic voltammograms of thin film electrodes from S1 to S8

From the CV curves, it is observed that the reduction and oxidation peaks are visible. This indicates that the electrochemical capacitance of the electrodes mainly results from pseudocapacitance. It is also observed that in comparison with doped films, Co_3O_4 film showed small current and small potential window. In contrast, doped films have high potential window, large current and good reversible redox activity. The calculated values of specific capacitance (SC) with respect to Mn doping concentrations for different scan rates 10mV to 100 mV/s are plotted in the figure 2. All the electrodes exhibited a common trend of decreasing specific capacitance values against an increasing scan rate. It

is well known that for very low scan rates, the specific capacitance values are higher because the ions have a much longer time to penetrate and reside in the electrode pores and form electric double layers, which are needed to generate higher capacitance.

As evidenced from figure 2, for lower Mn concentrations (electrodes S2 to S6) there is no much change in the values of SC with variable scan rates. It may be due to the fact that at lower content of Mn incorporation, Co species sustain the redox transition. The charge and mass transfer resistance do not decrease (IR drop) suddenly. At higher content of Mn incorporation (electrodes S7 and S8), SC value decreases rapidly. Because at higher %Mn

incorporation the charge and mass transfer resistance of Mn/Co species decrease.

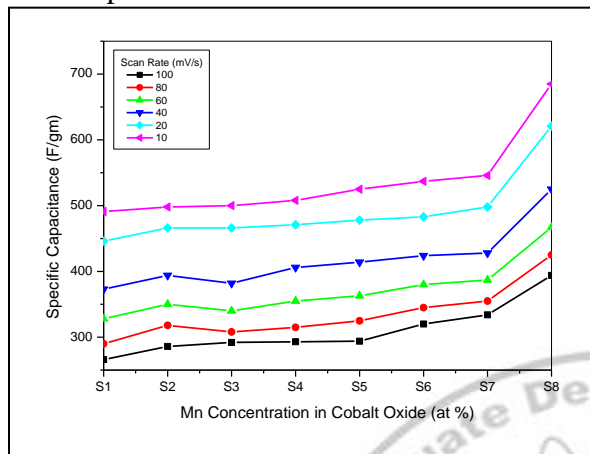


Fig. 2 Graph of Specific capacitance with Mn concentration at different scan rates

We can also observe as the Mn doping concentration increases specific capacitance increases from 492 to 675F/g at 10mV/s scan rate, 451 to 620F/g at 20mV/s, 371 to 524F/g at 40mV/s, 327 to 465F/g at 60mV/s, 287 to 424F/g at 80mV/s, and 265 to 383F/g at 100mV/s. This is due to increase in Mn ion concentration which increases the electrical conductivity of the films. Here electrode S8 (1%Mn) showed better SC for all scan rates as compared to others.

Electrode S8 showed large area under curve and high value of current as evidenced from CV leading to maximum value of SC, it may be due to capacitive favorable phase of Mn: Co_3O_4 formed at that incorporation leading to optimal Mn incorporation and formation of good porous nature of the sample as evidenced from SEM [8]. The interconnected crystallites of both Co_3O_4 and MnO_2 may create many micro pores, which help in electrolyte transport and provide large surface area for charge transport reaction for easy ionic intercalation between species leading to the increase in SC value of S8.

2.2 Stability Study

Retaining of specific capacitance for long cycles at higher scan rate operation condition is essential for practical applicability of a supercapacitor. Figure 3 shows CV plots of S1(0%Mn), S3(0.005%Mn), S6(0.1%Mn) and

S8(1%Mn) electrodes in 0.1 M KOH at higher scan rate 500mV/sec for 1st and 1000th cycles.

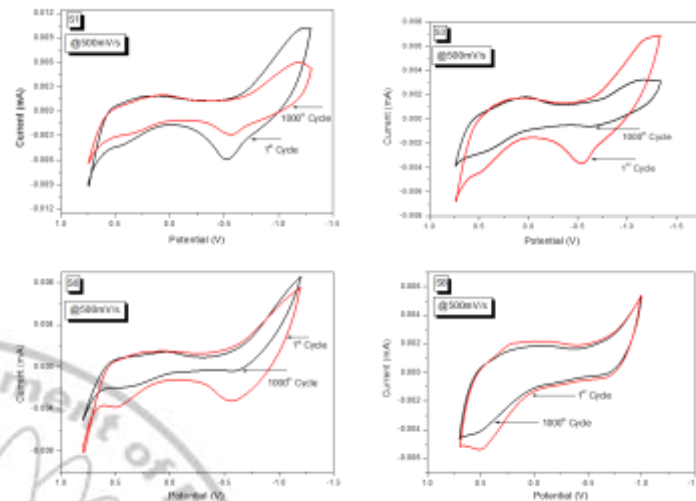


Fig. 3 CV curves of S1, S3, S6 and S8 electrodes for 1st and 1000th cycle at 500mV/s scan rate

Figure 4 shows the overall stability result, which indicates that S8 electrode behaves reversibly as an excellent supercapacitor material for a large number of potential cycles. The Co_3O_4 revealed the cyclic stability up to 66% over 1000 cycles. It indicates that the material behaves reversibly as a good capacitor material for a large number of potential cycles. Wang et al have reported the value of cyclic stability for Co_3O_4 nanowires up to 90% over 500 potential cycles [9].

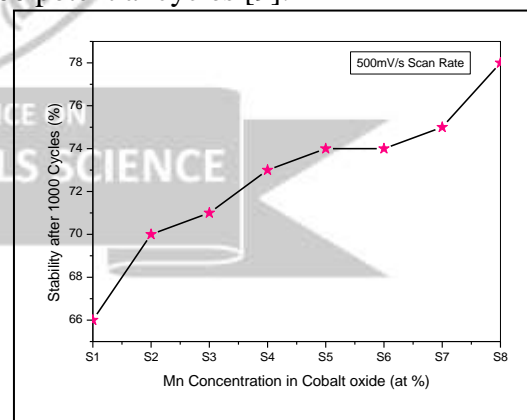


Fig. 4 Cyclic stability of all electrodes for 1000 cycles at 500mV/s scan rate

After Mn incorporation stability of the electrodes were improved. Compared to other electrodes, electrode S8 (1% Mn) exhibited good stability of nearly 80% as evidenced in the figure. 3 (d). Clearly there are no major changes between

CV's and the total area/charges enclosed by both curves are probably similar to each other, illustrating the stable nature of electrode in the energy storage application. The specific capacitance values are decreased by a comparably small amount with

number of cycles may be due to the loss of active material caused by the dissolution or detachment, during the early charging and discharging cycles in the electrolyte

3. Conclusion

Characterization by CV methods consistently found that increase in Mn concentration improved the electrochemical properties of the electrodes. The electrode with 1% Mn exhibited better specific capacitance and cyclic stability compared to other doped electrodes. The specific current of the cyclic voltammograms varies linearly with scan rates in the range of 10mV/s to 100mV/s, demonstrating a high power characteristic for all the electrodes. The specific capacitance obtained for 1% Mn electrode 675 F/g at 10 mV/s scan rate still retaining a considerable specific capacitance of 383F/g at a high scan rate of 100mV/s. It showed a high cyclic stability of about 90% over 1000 cycles. In comparison with pure Co₃O₄ electrode, manganese doped oxide material showed better supercapacitive performance, among which electrode 1% Mn can be considered as a promising candidate for supercapacitor materials.

References

1. B. E Conway, Plenum Publishers, New York, 1, (1999)
2. L. T. Lam, Louey, J. Power Sources, 158, 1140, (2006)
3. T. A. Miller, Electrochim Acta, 52, 1703, (2006)
4. W.C. Chen, T.C. Wen and H. Teng, Electrochim. Acta, 48 (2003) 641
5. F. Rafik, H. Guolous, R. Gallay, and A. Berthon, J. Power Source, 165, 928.
6. D. S. Sutrave, S. M. Jogade, S. D. Gothe, International Journal for Research in Applied Science & Engineering Technology, Volume 4, Issue IV, (2016)
7. A. D. Jagdale, V. S. Kumbhar, C. D. Lokhande, J. Colloid and Interference Science, 406, 225, (2013)
8. S. M. Jogade, D. S. Sutrave, V.B. Patil, Int. Journal of Engineering Research and Application, 41-46, (2016)
9. X.Wang, X. Liu, J. Wang, J. Mater. Sci. Mater. Electron. 601, 22, (2011)



Investigations on Ca and Zr Modified BaTiO₃ Ferroelectric Lead Free Ceramics

S. D. Chavan^a, R. M. Kharade^b, A. N. Tarale^b, S. G. Chavan^b, D. J. Salunkhe^{b*}

^aDepartment of Physics, D.B.F. Dayanand college of Arts and Science Solapur, 413002, India.

^bNano-composite laboratory, K.B.P. Mahavidyalaya, Pandharpur, Solapur, 413304, India.

Email – salunkhedj@rediffmail.com

Abstract –

The paper reports synthesis, crystal structure, dielectric properties and P-E hysteresis loop of (Ba_(1-x)Ca_(x))(Zr_(y)Ti_(1-y))O₃ (BCZT) compositions with x = 0.05, 0.075 and y = 0.075, 0.10. The BCZT compositions are synthesized via ceramic route of synthesis. The studies on crystal structure show tetragonal crystal structure. The investigations on dielectric properties show diffuse phase transition. All BCZT compositions exhibit satisfactory dielectric constant and low tanδ. The value of the relaxation parameter γ ranges between 1 and 2 shows relaxor nature. The investigations on the P-E hysteresis loop reveal that all BCZT compositions possess useful values of maximum polarization (P_{max}) and remnant polarization. The present observations suggest that all BCZT compositions could be useful lead free ferroelectric compositions.

Key words: Solid State Reaction, Dielectric properties, Relaxor nature.

1. Introduction

Ferroelectric materials with perovskite structures are useful for microelectronic devices. The most widely used ferroelectric material is BaTiO₃(BT). The structure of unit cell is temperature dependent. There are three phase transitions in order of decreasing temperature (120°C, 5°C, -90°C) [1]. The substitution of Sr, Pb, Ca and Zr into BT shows interesting ferroelectric properties. Zhuang et al. reported that addition of even a small quantity of Ca ions at Ti-sites leads to a diffused phase transition curve and lowers the phase transition temperatures [2]. Tiwari et al. reported that calcium doping increases the phase transition temperatures of BCT ceramics and Ba²⁺ substitution by Ca²⁺ leads to diffused transition curve. Earlier it was believed that Ca substitution decreases the Curie temperature [3]. Recently, it has been reported that Ca doping can also increase the Curie temperature depending on the powder preparation method & the site occupancy of calcium [4]. The paper report crystal structure, dielectric constant as a function of temperature and frequency, ferroelectric hysteresis loop of a compositions having a general formula [Ba_(1-x)Ca_(x)](Zr_(y)Ti_(1-y))O₃ (BCZT) for x= 0.05, 0.075 & y = 0.075, 0.1.

2. Experimental

The BCZT solid solutions have been synthesized via ceramic route of synthesis using the precursors BaCO₃, SrCO₃, ZrO₂ and TiO₂ of AR grade. The stoichiometric amounts of the precursors were well

mixed together and ground for 2 hours in an agate mortar with pestle. The calcination was carried out at 1150°C. The calcined powder was mixed with a polyvinyl acetate (PVA) binder solution and compacted into disk shaped samples. The final sintering process was carried out at 1200°C for 24 h. The Bruker D8 advance X-ray diffractometer was used for the determination of X-ray diffractograms. The HP4284A LCR-Q meter was used for the measurements of dielectric constant(ε), loss tangent tanδ. P-E hysteresis loops were determined using P-E loop tracer, Marine India Pvt. Limited.

3. Result and Discussion

3.1 Structural Analysis

Fig.1 show X-ray diffractograms of (Ba_{0.95}Ca_{0.05})(Ti_{0.90}Zr_{0.10})O₃(BCZT1), (Ba_{0.95}Ca_{0.05})(Ti_{0.925}Zr_{0.075})O₃(BCZT2) and (Ba_{0.925}Ca_{0.075})(Ti_{0.925}Zr_{0.075})O₃(BCZT3) respectively. The presence of sharp and well defined diffraction peaks indicate that this composition has a degree of crystallinity at a long range. The result suggest that Ca²⁺ and Zr⁴⁺ have been successfully incorporated into BaTiO₃ lattice to form inhomogeneous solid solution, It is seen that the composition under investigations are polycrystalline in nature and all the peaks in the spectra could be accurately indexed using standard JCPDS data. Further, no peak corresponding to any impurity phase is observed in the X ray diffractograms.

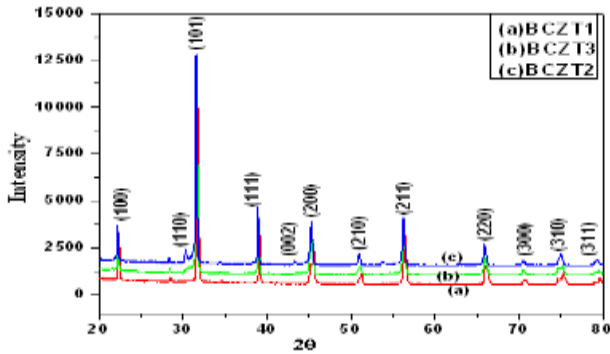


Fig.1: XRDs of BCZT Compositions.

3.2 Dielectric Properties

Fig. 2 shows variation of dielectric constant (ϵ) as a function of temperature (T) at different frequencies for BCZT1 composition. It is seen that the value of ϵ increases gradually to a maximum value ϵ_{max} with increases in temperature up to the transition temperature T_c and then decreases smoothly, where T_c shifts to higher temperature with the increases of frequency. This is a typical behavior of a relaxor ferroelectric. Table 1 shows the maximum value of ϵ (ϵ_{max}), loss tangent $Tan\delta$ at T_c ($Tan\delta_{Tc}$) and T_c for various frequencies for the BCZT1 composition. To parameterize this observe variation of ϵ versus T behavior, the ϵ in the paraelectric region is fitted to an equation [5, 6]

$$\frac{1}{\epsilon} = \frac{1}{\epsilon_{max}} + \frac{(T-T_c)^\gamma}{2 \epsilon_{max} \delta^2} \quad 1 \leq \gamma \leq 2$$

(1)

Table 1— T_c , ϵ_{max} , $Tan\delta_{Tc}$, γ and δ for BCZT1 composition.

Frequency Hz	T_c	ϵ_{max}	$Tan\delta_{Tc}$	γ	$\delta \cdot 10^{-4}$
100	101.38	767.75	0.0414	2.098	0.0802
1K	105.18	728.32	0.0232	1.923	1.844
10K	110.96	706.32	0.0231	1.844	0.272
100K	114.26	688.06	0.0312	1.791	2.166
1M	116.50	453.33	0.205	1.663	0.529

3.3. Ferroelectric Properties

Fig.3 shows P–E hysteresis loop for BCZT1, BCZT2 and BCZT3 compositions. It is observe that the P–E hysteresis loops are slim, which are characteristic of relaxor ferroelectric. The area within loop is proportional to the loss tangent.

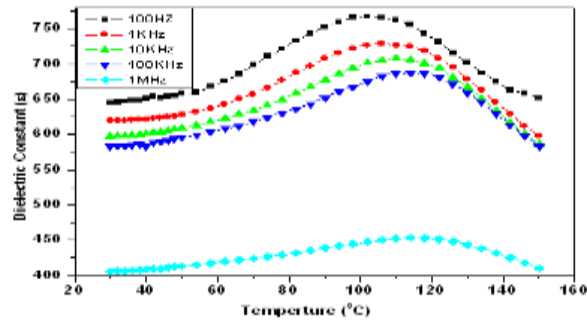


Fig.2: Variation of ϵ Vs. T for BCZT1 composition.

The diffusivity γ gives information on the character of the phase transition; for $\gamma=1$, a normal Curie Weiss law is obtained, for $\gamma=2$, it describes a complete diffuse phase transition. The plot of $\log(1/\epsilon - 1/\epsilon_{max})$ versus $\log(T - T_c)$ shows linear relationship for BCZT1 composition. By fitting Eqⁿ.1 to the data, the values of γ and δ are determined and are also shown in Table 1. It is seen that $1 \leq \gamma \leq 2$. This observation suggests that BCZT1 composition possess a diffuse phase transition characteristics [7]. BCZT2 and BCZT3 also show similar behavior like BCZT1. The nonlinear behavior for BCZT1, BCZT2 and BCZT3 confirms the existence of diffuse phase transition characteristics.

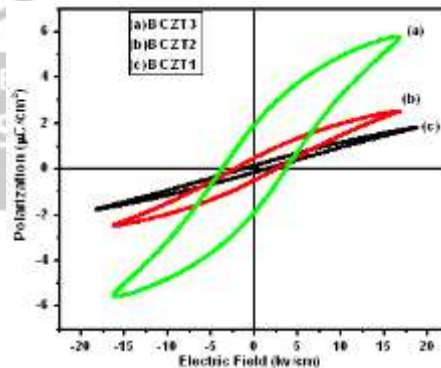


Fig.3: P–E Hysteresis loops of BCZT Compositions.

Due to slim P–E hysteresis loops all compositions possesses low loss tangent. Also all BCZT compositions possesses a relaxor contribution, may be partial in case of BCZT2 and BCZT3 also possesses low loss tangent. It is already reported that substitution of Zr leads to the reduction of

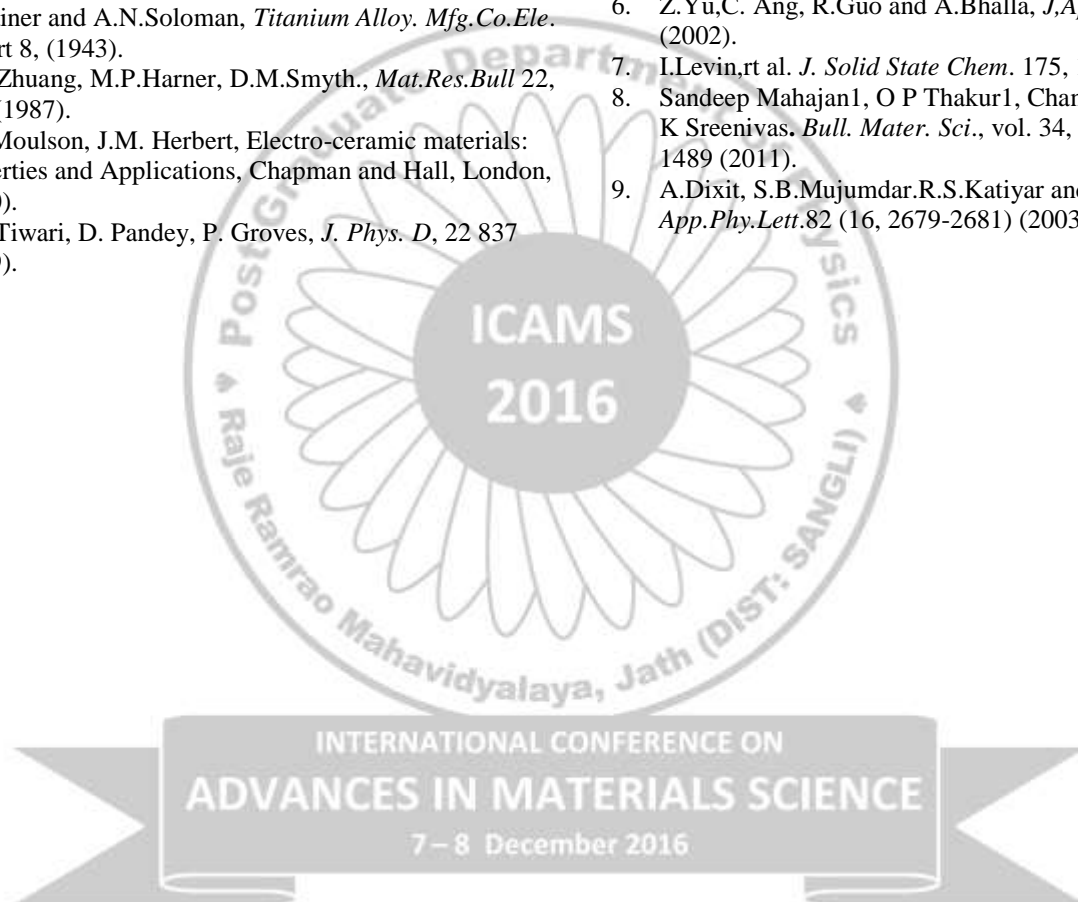
hysteresis loss and lead to slim hysteresis loop [8,9].

4. Conclusion

The ferroelectric compositions BCZT are synthesized using ceramic route of synthesis. The room temperature XRD study suggests that all compositions are polycrystalline in nature. The dielectric properties show a diffuse phase transition. All compositions exhibited a satisfactory dielectric constant and low dielectric loss $\tan \delta$. The value of the relaxation parameter γ ranges between 1 and 2 indicate the relaxor nature. The compositions possess useful values of maximum polarization (P_{max}) and remnant polarization (P_r). Thus BCTZ compositions could be useful lead free ferroelectric compositions.

References:

1. E.Wainer and A.N.Soloman, *Titanium Alloy. Mfg.Co.Ele.* Report 8, (1943).
2. Z.Q.Zhuang, M.P.Harner, D.M.Smyth., *Mat.Res.Bull* 22, 1329(1987).
3. A.J. Moulson, J.M. Herbert, *Electro-ceramic materials: Properties and Applications*, Chapman and Hall, London, (1990).
4. V.S. Tiwari, D. Pandey, P. Groves, *J. Phys. D*, 22 837 (1989).
5. G.A.Smolenskii and A.I Agranovskya, *Sov.Phys.Tech.Phys.*3,1380 (1958).
6. Z.Yu,C. Ang, R.Guo and A.Bhalla, *J,Appl.Phys.*92, 2655 (2002).
7. I.Levin,rt al. *J. Solid State Chem.* 175, 170-181(2003).
8. Sandeep Mahajan1, O P Thakur1, Chandra Prakash, and K Sreenivas. *Bull. Mater. Sci.*, vol. 34, No. 7, pp. 1483–1489 (2011).
9. A.Dixit, S.B.Mujumdar.R.S.Katiyar and A.S. Bhall, *App.Phy.Lett.*82 (16, 2679-2681) (2003).



Effect of molarity of cationic source on cyclic Voltammetry of Fe₃O₄ electrodes

A. V. Thakur, S. B. Ubale, B. J. Lokhande*

email: bjlokhande@yahoo.com*

*School of Physical Sciences, Solapur University, Solapur 413 255, M.S., India.

Abstract

Present study emphasizes the effect of molar concentration on the cyclic voltammetric performance of the Fe₃O₄ flexible electrodes (FE)s synthesized using successive ionic layer adsorption and reaction (SILAR) technique. For aqueous route synthesis, FeCl₃ and NaOH solutions were used as cationic and anionic sources respectively. Molar concentration of FeCl₃ was varied from 0.2 M to 0.8 M with step increments of 0.2 M. X-ray diffraction (XRD) patterns of the FEs show peaks at $2\theta = 43.46^\circ$ and 44.54° indicating the formation of orthorhombic Fe₃O₄ crystals. The scanning electron microscopic (SEM) image of FE prepared with 0.2 M FeCl₃ shows nano-clusters with interconnected nanograins of approximate size 10 nm. Cyclic voltammetric analyses indicate the decrease in specific capacitance with the increase in molar concentration of cationic precursor. For the electrode prepared with 0.2 M FeCl₃ as precursor, the maximum specific capacitance (SC) observed at 100 mVs⁻¹ in 1 M NaOH was 444.44 Fg⁻¹.

Keywords: Thin films, electron microscopy, cyclic voltammetry, Fe₃O₄.

1. Introduction

Various transition-metal oxides, such as RuO₂, Co₃O₄, NiO, Fe₂O₃, IrO₂, SnO₂, MnO₂, etc., are being studied for the supercapacitor applications. RuO₂ is the most preferable material for supercapacitors because of its high specific capacitance, excellent reversibility, and long cycle life. High cost, less abundance and toxic nature have limited the commercial use of RuO₂. Accordingly, there is a strong incentive to find alternative electrode materials, which are inexpensive and exhibit pseudocapacitance similar to that of hydrous amorphous RuO₂. The researchers have been trying to use oxides of manganese [2], nickel [3], cobalt [4], vanadium [5] and copper [6] as electrode materials. Iron oxide, can be the good choice as an electrode material for supercapacitors. Iron oxide thin films have been prepared by various methods, such as the sol-gel [7], chemical vapour deposition [8] and electrodeposition [9], spray pyrolysis [10]. Among these chemical methods, successive ionic layer adsorption and reaction (SILAR) is low cost and low temperature soft chemical solution method. The SILAR method is relatively a new and less investigated method, which is based on sequential reaction on the substrate surface. Rinsing follows each reaction, which enables heterogeneous reaction between the solid phase and the solvated ions in the solution. SILAR method has its own advantages such as layer-by-layer growing mode, excellent material utilization efficiency, and good control over the deposition process along with the film thickness and

large-scale deposition capability on any type of substrate [11,12]. The molarity of precursors is one of the major factors that affects the morphology and the electrochemical behaviour of the electrodes. Thus it will be interesting to study the effect of molar concentrations of precursor FeCl₃ on the electrochemical behaviour of Fe₃O₄ flexible electrodes in the light of cyclic voltammetry. Hence in the present work, it was decided to study the effect of molarity of the precursor FeCl₃ on the cyclic voltammetric performance of Fe₃O₄ flexible electrodes.

2. Experimental

2.1 Materials

In the synthesis work, FeCl₃ and NaOH purchased from SD fine chemicals were used as source materials without any further purification. Double distilled water was used solvent for all the experiments.

2.2 Electrode preparation

Stainless steel (SS) strips of 304 grade (size = 1cm X 5cm) were used as a conducting substrate material. SS Strips were mirror polished using polish paper (grade 600) to get the rough finish. To allow the proper deposition of the electrode material by adsorption, the strips were ultrasonicated for 20 minutes to make them free from the dirt, oil, stains etc. FeCl₃ was used as cationic precursor and NaOH was used as anionic precursor. The molar concentration of anionic precursor was kept constant as 0.1 M while the molar concentration of cationic precursor was varied from 0.2 M to 1M to study its effect on cyclic voltammetric behavior of

the prepared FEs. SS strips were immersed in cationic precursor for 10 s and anionic precursors for 10 s. These strips were pressure cleaned by the jets of double distilled water after each immersion. This is done to remove loosely bound, un-oxidized, partially oxidized radical. This completes one SILAR deposition cycle. For every molar variation of cationic source, 120 such SILAR cycles were carried out. The FEs prepared with 0.2M, 0.4 M, 0.6 M and 0.8 M concentrations of FeCl₃ were named as M₂, M₄, M₆ and M₈, respectively.

Table 1. Sample codes and preparative parameters of FEs

Sample codes	FeCl ₃ molarity (M)	NaOH molarity (M)	Dipping time (s)	Number of SILAR cycles	Annealing temperature (K)
M ₂	0.2 M	0.1M	10 S	120	673.15
M ₄	0.4 M	0.1M	10 S	120	673.15
M ₆	0.6 M	0.1M	10 S	120	673.15
M ₈	0.8 M	0.1M	10 S	120	673.15

2.3 Characterization

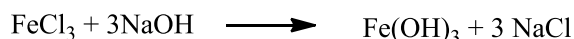
The structural characterizations of all uniformly deposited FEs were taken by using X ray diffraction (XRD) patterns given by X-ray diffractometer (Ultima IV Rigaku D/max2550Vb +18 kw with CuKα, λ = 1.54056 Å, Japan) in the range of diffraction angle (2θ) between 10°– 90° to study the nature of formed material, scanning electron microscopic (SEM) analyses were carried out by using scanning electron microscope (SEM S4300 HITACHI, Japan) to check the surface morphology of FE. Weight of the deposited material was measured by weight difference method using high accuracy analytical microbalance (Tapson-100TS, USA) with least count 10⁻⁵ g. Electrochemical characterization of the deposited FEs were carried out using Electrochemical analyzer (CHI 408C, USA) with standard three electrodes cell in which along with working electrode, platinum wire as a counter electrode and saturated Ag/AgCl as a reference electrode were used.

3. Results and discussion

3.1 Film formation mechanism

In the cationic bath the compound FeCl₃ splits up into Fe³⁺ cations and Cl⁻ anions. In anionic bath, the NaOH splits up to give Na⁺ and OH⁻ ions respectively. The double displacement reaction

occurs to give Ferric hydroxide films Fe(OH)₃. Which on annealing at 673.15 K gives stable magnetite phase (Fe₃O₄). Reaction mechanism is given below.



3.2 Structural elucidation

The XRD analysis of FEs M₂, M₄, M₆ and M₈ was carried to check the effect of molar concentration of the precursors on the crystallinity and lattice plane arrangement during the nucleation and growth of the material (Figure 1). The XRD pattern of the optimized sample show crystalline nature with the peaks corresponding to the formation of Fe₃O₄. The details of diffraction angle (2θ), plane orientation (miller indices), and interplanar spacing (d) as per the 760956 are given in the table 2.

Table 2. Different parameters from XRD patterns for FEs M₂, M₄, M₆ and M₈

JCPDS card no	Standard 2θ	Observed 2θ	Standard 'd'	Observed 'd'	h	k	l
760956	43.467	43.640	2.0802	2.0724	2	2	7
	44.500	44.547	2.0343	2.3600	1	2	7

Scanning electron microscopy (SEM) was carried out to check the surface morphology of the optimized samples M₂ and M₈. The SEM images clearly indicate that the surface morphology of FEs changes with molar concentration of the cationic source FE M₂ shows nano-clusters with interconnected nanograins of approximate size 10 nm. The morphology vary as the molar concentration of precursor is increased to 0.8M for which the nanograins are not interconnected and the size of nanograins is increased as seen for M₈.

3.3 Cyclic voltammetric study

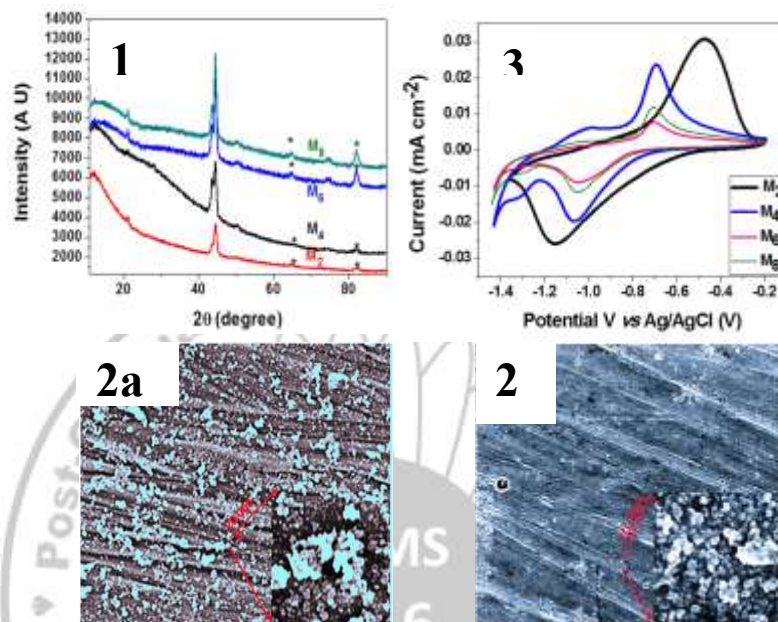
FEs M₂ M₄ M₆ and M₈ were subjected to the cyclic voltammetric (CV) analysis at 100 mV s⁻¹ in 1M NaOH. Figure 3 shows the CV curves for different samples. Following formula was used to calculate the specific capacitance (SC) of the prepared FEs from the CV curves.

$$SC = \frac{c}{W} = \frac{\int_{V_1}^{V_2} I dv}{W(V) \frac{dV}{dt}} \quad 1$$

It was observed that, area under curve hence the current integral is largest for M₂ among all FEs. The

variations in the values of SC with the molar variations of the cationic source are mentioned in the table 3. This might be due to the fact that, with increase in the molar concentration of the cationic precursor, the crystallite size increases and the

interconnections between them decrease hence the current integral goes on decreasing and hence the specific capacitance. The specific capacitance was found minimum for the sample M₈.



Figures 1. XRD patterns of FEs M₂, M₄, M₆ and M₈ prepared with different molar concentrations of FeCl₃
 2a. SEM of M₂ prepared with 0.2M FeCl₃, 2b. SEM of M₈ prepared with 0.8M FeCl₃
 3. Cyclic Voltammograms of samples with different molarities at 100mV/S

Table 3. Variation of specific capacitance with variations in molar conc. of cationic source

Sample Code	Molar Conc. Of Cationic source	Specific capacitance (SC)
M ₂	0.2M	444.444
M ₄	0.4M	241.739
M ₆	0.6M	208.09
M ₈	0.8M	113.4

4. Conclusion

SILAR synthesis of Fe₃O₄ flexible electrodes is possible using SILAR method. The FE M₂ prepared with 0.2 M Fe₃O₄, demonstrate nano-clustered morphology having interconnected nanograins shows high specific capacitance. The cyclic voltammetry reveals the pseudocapacitive nature. Decrease in specific capacitance with increase in molar concentration of cationic source has been observed.

References

- [1] B.E. Conway, Electrochemical Supercapacitors, Scientific Fundamentals and Technological Applications, Kluwer Academic/Plenum Press, New York, 1999.
- [2] D.P. Dubal, D.S. Dhawale, R.R. Salunkhe, V.J. Fulari, C.D. Lokhande, J. Alloys Compd. 497 (2010) 166.
- [3] K.W. Nam, K.B. Kim, J. Electrochem. Soc. 149 (2002) 346.
- [4] C. Lin, J.A. Ritter, B.N. Popov, J. Electrochem. Soc. 145 (1998) 4097.
- [5] H.Y. Lee, J.B. Goodenough, J. Solid State Chem. 148 (1999) 81.
- [6] D.P. Dubal, D.S. Dhawale, R.R. Salunkhe, V.S. Jamdade, C.D. Lokhande, J. Alloys Compd. 492 (2010) 26.
- [7] S. Duhan, S. Devi, Int. J. Electron. Eng. 2 (2010) 89.
- [8] T. Maruyama, Y. Shinyashiki, Thin Solid Films 333 (1998) 203.
- [9] N. Nagarajan, I. Zhitomirsky, J. Appl. Electrochem. 36 (2006) 1399.
- [10] J.D. Desai, H.M. Pathan, S.K. Min, K.D. Jung, O.S. Joo, Appl. Surf. Sci. 252 (2005) 1870.
- [11] H.M. Pathan, C.D. Lokhande, Bull. Mater. Sci. 27 (2004) 85.
- [12] A. V. Thakur, B. J. Lokhande, e-polymers aop, DOI 1515/2016-0160

Enhanced NO₂ Sensing Properties of WO₃ Thin Film on Alumina Substrate

V. V. Ganbavle

Dattajirao Kadam Arts Science and Commerce College Ichalkaranji-416115, INDIA

E-mail: vinayakganbavale@gmail.com Phone: +91-9960073358

Abstract

The present study explores enhancement in (nitrogen dioxide) NO₂ sensing properties of sprayed (tungsten oxide) WO₃ thin film by using alumina substrate. The film consisting of spherical grains possesses monoclinic crystal structure. WO₃ thin film sensor exhibited 162% response in 9 s towards 100 ppm NO₂ at optimized operating temperature of 200 °C. The lower detection limit achieved was 10 ppm with 40% response at 200 °C. Sensitivity of the sensor when operated at optimized temperature was 1.36%/ppm over the range of 20-100 ppm NO₂. The sensor was identified to be highly selective towards NO₂ in presence of various gases H₂S, NH₃, LPG, SO₂ and CO.

Keywords: Thin films; Sensors; Selectivity; Sensitivity

1 Introduction

With the advancement in industrialization and domestic activities, various gases are liberated at the workplaces and residences [1]. As the detection of various harmful and polluting gases is an issue of great concern, there is increasing demand for development of reliable, efficient yet economical gas sensors. NO₂ is one of the major air pollutants which can cause acid rains, photochemical smog, a range of harmful effects on lungs and respiratory system. NO₂ in air is detectable by its odour when its concentration is high enough but it also anesthetize the nose; thus when it is leaked, an external sensing agency is necessary for detection of NO₂. Metal oxide semiconductor (MOS) based gas sensors have been proved efficient for detecting the polluting gases [2]. WO₃ is one of the potential MOS which shows highest response and selectivity towards NO₂ [3]. One-dimensional single-crystalline γ -WO₃ nanorods were synthesized via hydrothermal method and the sensor was operated at 250 °C towards 20-600 ppm NO₂ [4]. Graphene-WO₃ nanocomposite thin-layer sensors were synthesized by drop coating method and NO₂ sensing properties were studied by varying graphene:WO₃ ratio [5]. There is considerable effect of substrates used for thin film deposition on the gas sensing properties [9,10]. Reports are available discussing the enhancement in response of WO₃ thin film sensors deposited on alumina substrates [6-8]. The present paper briefs an attempt to enhance the NO₂ sensing of WO₃ thin film sprayed on alumina substrate.

2 Experimental

Alumina substrates of 2 cm² area (Ants lab, Mumbai) were used for deposition of WO₃ thin films. Peroxotungstic acid having 0.15 mM concentration and 100 ml volume was sprayed at the rate of 5 ml/min onto the preheated alumina substrates at 425 °C substrate temperature [11]. Gas sensing measurements were carried out using locally fabricated gas sensing unit equipped with Keithley electrometer (6514) with sensor of size 1 cm × 1 cm. Various canisters of 2000 ppm gas concentration (Shreya Enterprises, Mumbai, India) were used as source of analyte gases.

3 Results and discussion

3.1 Structural and morphological study

Figure 1(a) shows X-ray diffraction (XRD) pattern of WO₃ thin film deposited on alumina substrate. The observed peak positions match well with the JCPDS card no. 43-1035. Triplet of peaks at 23.28°, 23.79°, 24.36° is assigned to (002), (020), (200) planes which corresponds to monoclinic crystal structure. Preferential growth direction of the film is along (200) plane; crystallite size calculated using Scherrer formula for the same plane was 86 nm. Figure 1(b) shows scanning electron microscopy (SEM) image of WO₃ thin film deposited on alumina substrate. Spherical grains of size 1-3 μ m are observed in comparison with the wire like morphology of sprayed WO₃ films when deposited on glass substrates at the same deposition parameters [11,12]. The voids between the grains increase the effective surface area of the film which renders more gas diffusion thus, enhances the response. Interconnected grains with large necks facilitate the conduction of electrons by formation of the

conduction channels. This increases the number of electrons available for charge transfer with the gas molecules and thereby response of the film.

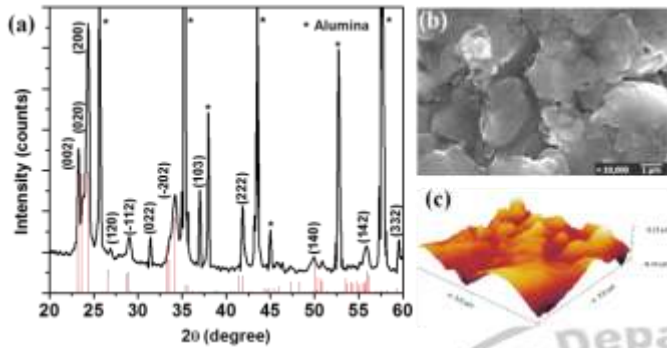


Figure 1: (a) XRD pattern, (b) SEM and (c) AFM image of WO₃ thin film.

Figure 1 (c) shows atomic force microscopy (AFM) image scanned over 3 μm² area. In accordance with the XRD and SEM discussions, film deposited on alumina substrate has larger crystallite and grain sizes which are apparent in AFM image. High surface roughness (170 nm) of the film is an effect of the high surface roughness of alumina substrate. This indicates that use of alumina substrate is a means to alter the surface microstructure of film and hence the response.

3.2 Gas sensing studies

3.2.1 Optimization of operating temperature of sensor

Operating temperature of the sensor was optimized by operating it over 50-250 °C and the corresponding response towards 100 ppm NO₂ was measured (Figure 2). The film could not show response at 50 °C, as the adsorption and charge transfer reactions hardly take place at such a low temperature.

However, at 100 °C and onwards, film responds and significant response was observed with further increase in temperature. An irreversible response was observed at 100 °C where the sensor resistance could not regain its initial value even after 50 min. Maximum response of 162% was observed at 200 °C and for still higher temperature (250 °C) it dropped down due to the higher rate of desorption than that of adsorption. Response and recovery times are influenced by the variations in operating temperature due to change in rate of reactions [13].

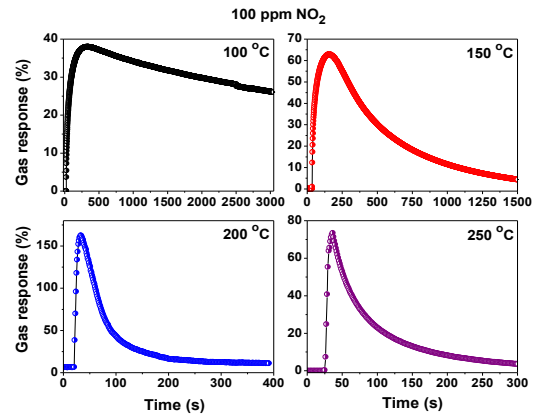


Figure 2 Transient response of WO₃ thin film at different operating temperatures.

The monomolecular adsorption is favored at fully oxidized surface and the adsorption by dissociation prominently takes place at oxygen deficient centers [14,15]. Due to the enhanced transducer function, more gas molecules are adsorbed at the boundaries and in the surface. This increases the width of the double Schottky barrier and hence the resistance of film after adsorption of NO₂. Detailed NO₂ sensing mechanism by WO₃ thin film is explained elsewhere [14].

3.2.2 Effect of NO₂ concentration on response and selectivity

It is explicable that the response of the sensor increases with increase in NO₂ concentration (Figure 3). The response saturates at higher concentrations because, even though the gas concentration increases, the number of sites available in the film for adsorption and charge transfer remains the same. Also, due to large number of gas molecules available for adsorption, response and recovery times of the sensor increase with increase in gas concentration. When molecules are present in large number it takes longer time to complete the adsorption and desorption and/or dissociation reaction which enhances the kinetics and response of sensor. Sensitivity of the film is 1.36 %/ppm over 20-100 ppm NO₂, which is higher than that observed for WO₃ film deposited on glass substrate [13]. This can be attributed to high surface roughness of the WO₃ film on alumina substrate.

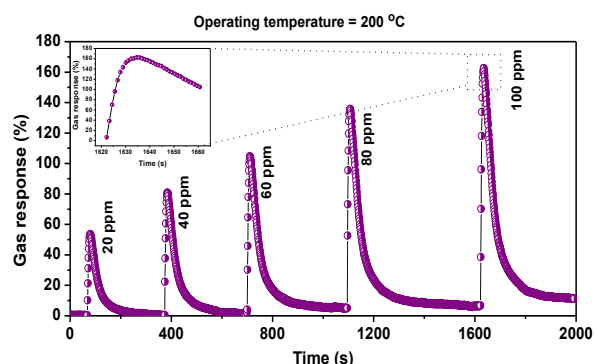


Figure 3 Transient response of WO_3 thin film towards various NO_2 concentrations.

Selectivity of the sensor was studied by exposing it to various gases. A bar graph of response towards various gases of 100 ppm concentration is shown in Figure 4. It is clearly seen in the figure that the sensor is highly selective towards NO_2 in the mist of various gases due to the higher electron affinity of NO_2 than the other test gases [16]. Higher selectivity distinctly observed towards NO_2 in the presence of SO_2 is remarkable since SO_2 is another major co-existing air pollutant.

Reproducibility of the sensor was tested for 10 ppm NO_2 for five consecutive measurements (inset of Figure 4). The sensor showed promising reproducible response with negligible variation over

five consecutive measurements. The response was constant for all the measurements except the small shift in baseline of the response curve. This shift is due to the incomplete removal of NO_2 molecules from the sensor surface within the stipulated time. Lower detection limit of 10 ppm achieved for the sensor is half of the Immediately Dangerous to Life or Health (IDLH) concentration of NO_2 .

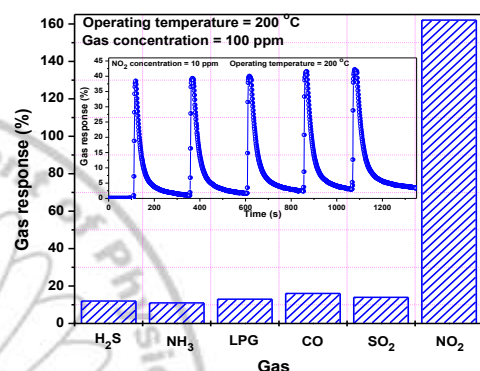


Figure 4 Selectivity of WO_3 thin film towards various gases. Inset: Reproducible response towards 10 ppm NO_2 .

4 Conclusions

Response of WO_3 thin film deposited on alumina substrate towards a range of NO_2 concentrations for different operating temperatures was measured. Spherical grains were observed having larger grain and crystallite size and high surface roughness as compared with the WO_3 films deposited on glass substrates. Fast, reproducible and selective response was observed towards NO_2 at 200 °C operating temperature. Lower detection limit achieved was 10 ppm showing 40% response. The response and recovery times were 163 and 9 s, respectively towards 100 ppm NO_2 . The sensor exhibited 1.36 %/ppm sensitivity over 20-100 ppm NO_2 . The WO_3 thin film deposited on alumina substrate exhibited higher response, better selectivity and lower response time. The use of alumina substrate considerably enhances the response of WO_3 films towards NO_2 .

References

1. Yaqoob U, Phan DT, Uddin-Iftokhar AS, Chung GS (2015). <http://doi.org/10.1016/j.snbs.2015.06.137>
2. Korotcenkov G., Mater Sci Eng B Solid-State Mater Adv Technol 2007; 139:1-23.
3. Fine GF, Cavanagh LM, Afonja A, Binions R., Sensors 2010;10:5469-502.
4. Patil VB, Adhyapak PV, Patil PS, Suryavanshi SS, Mulla IS, Ceram Int 2015; 41:3845-52.
5. Srivastava S, Jain K, Singh VN, Singh S, Vijayan N, Dilawar N, Gupta G. Senguttuvan TD, Nanotechnology 2012;23:205501.
6. Yan W, Hu M, Zeng P, Ma S, Li M, Appl Surf Sci 2014;292:551-5.
7. Lee DS, Nam KH, Lee DD, Thin Solid Films 2000; 375:142-6.
8. Song S-W, Kang I-S, Sensors Actuators B Chem 2008;1 29:971-6.
9. Chung W-Y, Sakai G, Shimanoe K, Miura N, Lee D-D, Yamazoe N, Sensors Actuators B Chem 2000;65:312-5.
10. Battiston GA., Gerbasi R, Porchia M, Marigo A, Thin Solid Films 1994;239:186-91.
11. Ganbavle VV, Kim JH, Rajpure KY, J Electron Mater 2015;44:874-85.
12. Bathe SR, Patil PS, Sol Energy Mater Sol Cells 2007; 91:1097-101.
13. Ganbavle VV, Mohite SV, Agawane GL, Rajpure KY, J Colloid Interface Sci 2015;451:245-54.
14. Wetchakun K, Samerjai T, Tamaekong N, Liewhiran C, Siriwong C, Kruefu V, Sensors Actuators, B Chem 2011;160:580-91.
15. Ganbavle VV, Mohite SV, Kim JH, Rajpure KY, Curr Appl Phys 2015;15:84-93.
16. Stănoiu A, Simion CE, Somăcescu S, Sensors Actuators, B Chem 2013;186:687-94.

Chemical Bath Deposition of CuS/CdS Heterojunction for Photoelectrochemical Application

A.S. Jadhav, S.S. Karande, V. M. Bhuse*

Thin Film Research Laboratory, Department of Chemistry, Government Rajaram College, Kolhapur, 416004, India. *Corresponding author: E-mail: vijaykbhuse13@gmail.com, Fax: 0231-2531989. Ph: 0231-2691100

Abstract

Nano-structured CdS-CuS heterojunction films have been grown successfully on conducting substrates by using Chemical Deposition Method. The films are characterised using X-Ray Diffraction (XRD), Scanning Electron Microscopy (SEM), Optical Absorption and tested for Photo-electrochemical Applications. XRD pattern of CuS-CdS show peaks corresponding to CuS (hexagonal) and CdS (cubic) phases. Optical absorption studies revealed presence of absorption edge corresponding to CuS as well as CdS. Photo-electrochemical properties using a conventional two electrode system with ferro-ferricyanide electrolyte showed a higher conversion efficiency of 1.8% as compared to individual CuS and CdS photoelectrodes.

1. Introduction

The issue of energy has become the most imperative topic of the twenty first century. An excessive dependence on the combustion of non-renewable fossil fuels carries not only ecological problems but also harsh ongoing impacts on the global economy and society [1]. There is need for cost-effective, efficient, and environmentally benign energy conversion devices that can power energy demanding areas [2]. Among these, solar to electrical energy conversion system has always been a fascinating thought-provoking and challenging frontier for the Science and Technological applications [3].

Inorganic semiconductor are considered as the key material for converting sunlight into electricity. The basic underling this conversion involves the following sequence of the process; absorption of photon of light, breaking of bonds to generate electron-hole pairs (excitations), separation of pairs at depletion layer and collection across the load [3]. In solar cell application, an important challenge is to select the semiconductor material with suitable band gap and high absorption coefficient. A heterojunction of CdS-CuS is gaining much importance in harnessing solar energy since both of them are having high absorbance coefficient ($\alpha > 10^4 \text{cm}^{-1}$), CdS, a transparent material (n-type, band gap 2.42eV) forms a junction with CuS (p-type, with bulk band gap 1.21 eV) both of them can be used as absorber material [4].

Fabrication of CdS-CuS heterojunction is possible by various methods such as vacuum evaporation, sputtering, chemical vapour

deposition, electrochemical deposition, dip growth, successive ion adsorption and reaction etc [5-8]. Chemical bath deposition and ion exchange method, among all, have attracted considerable interests because of their lower expenses, simplicity and large area deposition of chalcogenide material [9]. To construct the heterojunction, the chemical deposition method is promising method since it is able to overcome a mismatch between the length scales required for light absorption and diffusion of minority carriers within the conductor. The fabrications of heterojunctions can be performed through solution phase and ion exchange methods, the later involves the diffusion and exchange of cations in an initial crystal by new cations from solution [10].

In the present investigation, we report the chemical deposition of Cu/CuS/CdS heterojunction and studies on the morphological, optical, electrical and photochemical properties.

2. Experimental Procedure

2.1 Preparation of CuS Thin Film: All chemicals were A.R grade and used without further purification. A n type CuS film was deposited on conducting copper sheet (0.3 mm) via dip method. To get deposit of CuS, the substrates were dipped in 0.1M Polysulphide solution for five minutes. The obtained black layer of CuS thin film was washed with deionised water, dried naturally and stored in a desiccators. CuS film was annealed at 373 K for 5 hr and used for depositing CdS layer on it.

2.2 Fabrication of CuS/CdS Heterojunction: An another transparent window CdS semiconductor layer was deposited onto Cu/ CuS film by using

chemical bath deposition (CBD) technique. A bath solution contained cadmium sulfate (5 ml, 0.1 M), thiourea (5ml, 0.1M), ammonia (40 ml, 28%), The TEA (5 ml) and 50 ml deionised water. The pH of the bath solution is adjusted to 12 by addition sufficient quantity of ammonia. The Cu/CuS substrates were mounted on a special substrate holder and rotated in the bath with the help of stepper motor with a speed of ~40 rpm. The deposition temperature was maintained at 323K. The reaction continued for 1 h to obtain yellowish-orange coloured CdS thin film. The obtained heterojunction film is washed with deionised water several times, dried naturally and kept in desiccator and used for further investigation.

The obtained films have been characterised using X-ray Diffraction, Scanning Electron Microscopy and Absorption Spectroscopy. Photo electrochemical measurement of Cu/CuS/CdS was carried out using two electrode system using graphite rod as counter electrode and potassium ferro-ferricyanide as an electrolyte under 10 mW/cm² illumination.

3. Results and discussion

XRD pattern provide information about phase of material and grain size of and the used along with element conformation. Figure 1 shows the XRD pattern of the annealed CuS-CdS heterojunction thin film taken on copper substrate. The pattern shows number of peaks corresponding to metallic copper, CuS (Hexagonal, JCPDS Card No 75-2233) and CdS (Cubic, JCPDS Card No 10-0454), accordingly peaks are marked in Fig. 1. The peaks due to metallic copper (substrate) are intense and identified as the reflections at 43.3, 50.5, 74.1 and 89.9 due to (111), (200), (220) and (311) planes respectively (JCPDS No.01-085-1326). The peaks at 2θ angle of diffraction 29.5, 32.1, 33.1, 48.3, 53.1 have been identified as reflection originating from (102), (103), (006), (110), (108) planes of hexagonal CuS respectively (JCPDS Card No 75-2233), while the peaks at 2θ angle of diffraction 26.6, 30.0, 43.9, 52.2 are reflections due to (111), (200), (220) and (311) planes of cubic CdS respectively (JCPDS Card No 10-0454). The

crystallite size calculated using Scherer equation was 150 Å

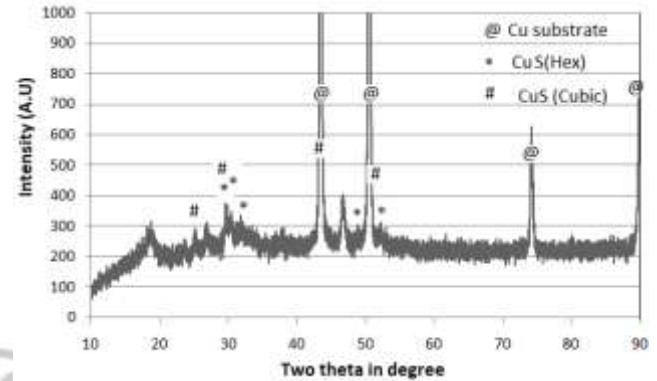


Fig.1: XRD of CuS/CdS

A surface morphology is considered as an important parameter in solar energy conversion since the grain type, size and grain boundaries largely decides the electronic transport phenomenon. Figure 2 shows SEM of CuS/CdS film. The morphology show adherent stacked nano-sheet like structures with some over growth.

An efficient solar absorber should have band gap energy corresponding to the maximum of solar spectrum (in visible region). Figure 3 shows the absorption spectra of CuS-CdS. The band gap energy (E_g) can be calculated by extrapolating the straight light portion to wavelength axis.

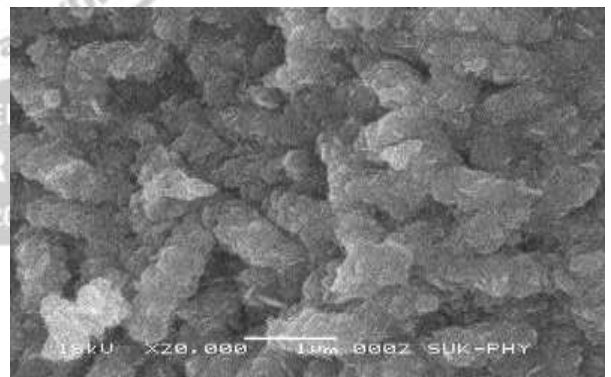
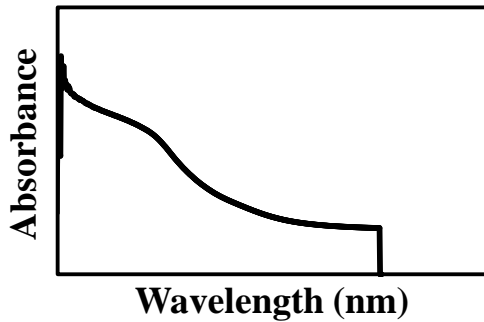


Fig.2: SEM image of CuS/CdS

The band gap can be calculated from relation; E_g (in eV) = 1242/λ(in nm). The absorption spectrum shows two absorption edge corresponding to two band gaps at 1.45 and 2.48, which roughly matches

with the bulk bandgap of CuS and CdS respectively.



Fig, 3

The conversion efficiency of PEC Cell of the following configuration Cu/CuS/CdS heterojunction/ 0.1 M Potassium ferro-ferricyanide electrolyte/ was calculated to be 1.8%, with $V_{max} = 0.516$, $J_{max} = 0.349$ mA, $J_{sc} = 0.646$ mA and $V_{oc} = 0.780$ V. The efficiency for above cell configuration was found to be higher than individual cell efficiencies (for CuS- 0.8 % and for CdS 0.6%).

Conclusions:

Nano-structured CdS-CuS heterojunction film has been grown on conducting substrates by CBD method. Film showed double optical band gap corresponding to bulk CuS and CdS. PEC device constructed using conventional two electrode system with ferro-ferricyanide electrolyte showed a 1.8% conversion efficiency, higher than the individual CuS and CdS semiconductor electrodes.

References:

- 1] Y. Abdu, A.O Musa, Bayero, Journal of Pure and Applied Sciences, 2(2) (2009) 8-12.
- 2] Y. J. Wang, D. P. Wilkinson and J. J. Zhang, Chem. Rev. 111 (2011) 7625–7651.
- 3] S. K. Deb, Sol. Energy Mater. Sol. Cells 88 (2005) 1-10
- 4] V. S. Taur, R. A. Joshi, A. V. Ghule, R. Sharma RenewableEnergy,38(2012)21.
- 5] D.R Acosta, C.R Magana, A.I Martinez, A Maldonado, Sol Ene Mater Sol Cell 82 (2004) 11.
- 6] N. Romeo, Bosio A, Romeo A. Sol Energ Mater Sol Cell 94(2010) 2-7.
- 7] J. R Mann, N Vora, I.L Repins. Sol Energy Mater Sol Cell 94 (2010)333-377.
- 8] ASAC Diniz. Renew Energy 36 (2011) 1153-65.
- 9] M. Sam, M.R. Bayati, M. Mojtahedi, K. Janghorban, ApplSurf.Sci.257(2010)1449-1453
- 10] A. W Eggleston, M. J. Moses, Sol. Cells 14 (1985) 1 –11.

Luminescence Properties of CaS:Ce Nanophosphors Embedded in PDMS Polymer Matrix

Madhushree G Bute^{1*}, Geeta Sharma², Suresh W. Gosavi^{2*}

¹Department of Technology, Savitribai Phule Pune University, Ganeshkhind Pune-411 007, India.

² Centre for Advanced Studies in Material Science and Solid State Physics, Department of Physics, Savitribai Phule Pune University, Ganeshkhind, Pune - 411007, INDIA,

Email: swg@physics.unipune.ac.in and madhushree.physics@gmail.com

Abstract:

Luminescent CaS:Ce nanophosphor was synthesized via solid state diffusion method, and embedded in PDMS (Polydimethylsiloxane) polymer matrix, for increasing its chemical stability. The XRD pattern and PL spectra suggests that CaS:Ce maintain its identity in PDMS polymer matrix. Surface morphology of as prepared samples, analysed using SEM reveals nanobelts like structure. The fluorescence microscopy of luminescent-PDMS shows uniform distribution of CaS:Ce particles in PDMS. Further studies on luminescent-PDMS composite in saturated relative humidity at room temperature for different time intervals shows that CaS:Ce particles in PDMS remains chemically stable.

Introduction :

Alkaline earth sulphides phosphors are fluorescent over large number of excitation wavelengths and exhibits high quantum yield. Out of these, Calcium sulphide doped with cerium has been used for variety of applications and also studied for dosimetry applications because of deep traps in it [1]. However its tendency to react with carbon dioxide (CO₂), water (H₂O) and O₂, present in the environment restrict its usage in various applications [2]. Recently few attempts have been made to improve the stability of alkaline earth sulfides by sulfuration fluxing agents and oxide coating agents. Number of encapsulation techniques has been also utilized to improve the stability of sulfide phosphors [3]. Some groups have also made attempts to use polymers such as poly(lauryl methacrylate) (PLMA), poly(methyl methacrylate) for polymer-quantum dots composites [4]. Hongoo song et.al reported PMMA-(CdSe)ZnS composite [5] for green or red LED applications, Jin Wook Lee et.al reported semiconductor QDs and polymer composites [6]. To the best of author's knowledge PDMS-CaS:Ce polymer composite is not yet reported.

Polydimethylsiloxane (PDMS) can be a good matrix for holding a luminescent material owing to its properties such as water resistant, transparent in visible range, chemical stability up to 200 °C and flexible. The aim of the present study is to incorporate the CaS:Ce in the PDMS successfully and to understand whether polymer matrix influences the luminescence of CaS:Ce and further

to studied the chemical stability of this polymer composite against humidity exposure.

Experimental:

CaS:Ce nano particles were synthesized via solid state diffusion method [7]. Polydimethylsiloxane (PDMS) (Sylgard 184 Silicone Elastomer, Dow Corning Corporation) pre-polymer was mixed with crosslinker and CaS:Ce for 15 min followed by degassing for 30 min. Luminescent Polymer films were produced by spin-coating above mixture on a glass slide. The polymerization of the film was achieved by placing the samples in a hot air oven at 40 °C for 8 hrs. The film thickness was 400 µm. These films can be removed from glass giving free standing luminescent polymer films.

X-Ray diffraction analysis of CaS:Ce and luminescent-PDMS was performed using a Bruker D8 Advance x-ray diffractometer with Cu K α . UV-Visible spectra of the PDMS was recorded using HP8452A UV-visible spectrometer. Fluorescence images were captured using Zeiss Epi-fluorescence Microscope, (Axiop 40) with a photographic attachment. Photoluminescence measurements were carried out on an ACTON spectrometer (SpectraPro-300i) connected to a photomultiplier tube (Acton Research, PD-438) as a detector with a xenon lamp as an excitation source attached to another monochromator (SpectraPro-150i).

The CaS:Ce powder and luminescent-PDMS films were kept in glass desiccators and subjected to controlled humidity for 6 -48 hrs, with the interval of 6 hr.

Result and Discussion:

XRD pattern of as synthesized and composite sample, shown in Fig.1(a) indicated single phase cubic structure (JCPDS-ICDD database 77-2011). The average crystallite size of as-prepared CaS:Ce particles was found to be $\sim 50 \pm 0.5$ nm.

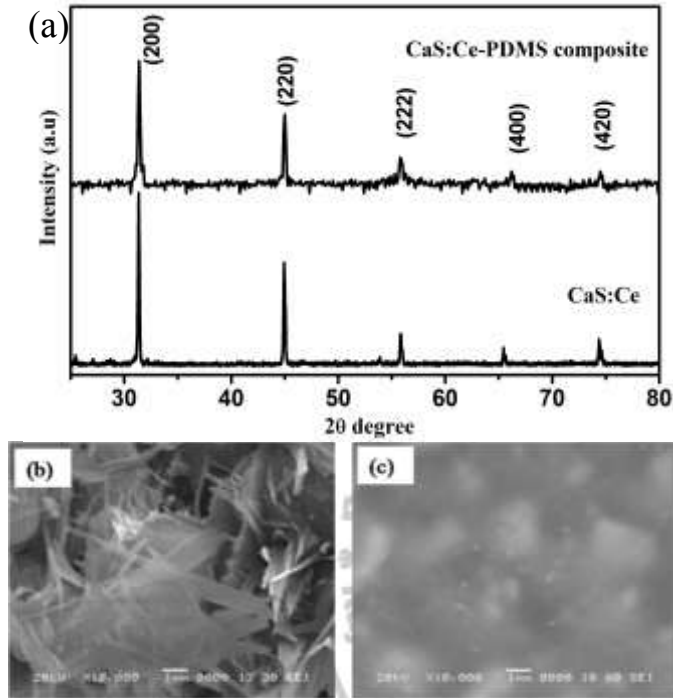


Fig.1. (a) XRD of CaS:Ce nanophosphor and CaS:Ce-PDMS composite. SEM of (b) CaS:Ce nanophosphor (c) CaS:Ce-PDMS composite.

For powder CaS:Ce lattice parameter was found to be 5.686 \AA and for luminescent-PDMS it was 5.694 \AA which suggest that CaS:Ce kept its

identity in PDMS polymer matrix. Fig.1(b,c). shows the SEM images of CaS:Ce and CaS:Ce-PDMS composites. Nano belt like structure of CaS:Ce was observed, however the SEM images of CaS:Ce-PDMS composites indicates the homogeneous coating of PDMS on CaS:Ce particle surfaces.

For confirming the compatibility of PDMS with CaS:Ce, a UV-Visible absorption spectrum of PDMS was recorded. As shown in Fig.2(a) PDMS is transparent in the emission (500nm-700nm) and excitation range (400nm-500nm) of CaS:Ce. The blue light from excitation source and green emission from CaS:Ce will not be absorbed in PDMS, confirming it as a good holding matrix for CaS:Ce. The Fluorescence microscopic images of luminescent-PDMS films (Fig 2(b)) shows uniform distribution of CaS:Ce nanophosphor in PDMS. Fig.2(c) shows free standing CaS:Ce-PDMS composite film in normal and Fig.2(d)UV light.

The emission spectrum of CaS:Ce (Fig 3 (b)) at an excitation wavelength of 450 nm (Fig 3 (a)) shows the characteristic emission of Ce^{3+} , i.e. a peak at 505 nm (Fig 3 (b)) with a shoulder at 565 nm [8]. Similar PL characteristics (excitation and emission) of luminescent PDMS as that of CaS:Ce indicates that PDMS does not interact with CaS:Ce (Fig.3.(a,b)).

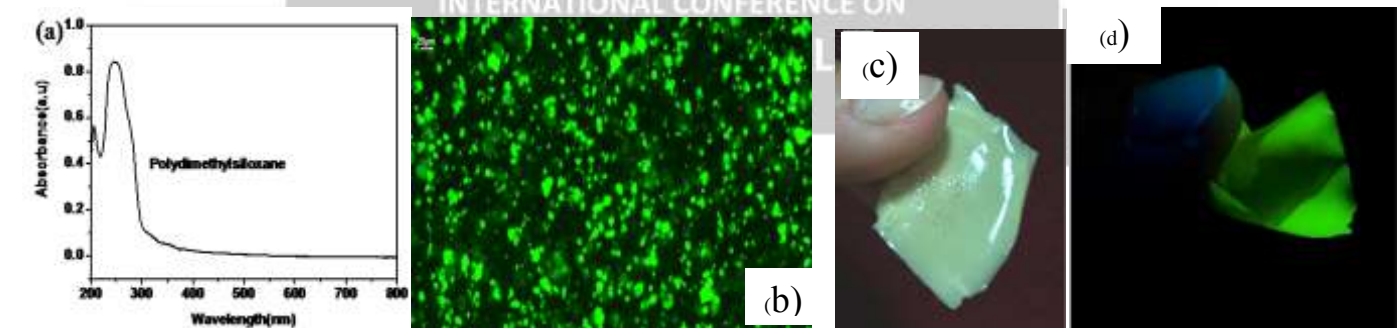


Fig.2. (a) UV Absorption Spectrum of PDMS transparent in visible region. (b) Fluorescence microscopic images of luminescent-PDMS and free standing CaS:Ce-PDMS composite in (c) normal light (d) UV light.

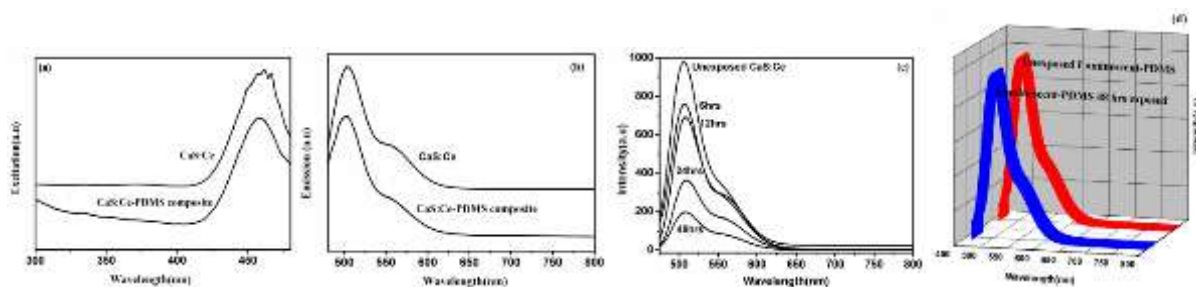


Fig.3. (a) Excitation Spectrum (b) Emission Spectrum of CaS:Ce and CaS:Ce-PDMS composite. (c) . Emission spectra of Humidity exposed CaS:Ce nanophosphor. (d) Humidity effect on CaS:Ce-PDMS composite.

When CaS:Ce was exposed to saturated relative humidity at room temperature for 6 hrs, 12 hrs , 24 hrs and 48 hrs, luminescence intensity observed to decrease continuously with increasing exposure time (Fig. 3(c)), it may be due to reaction of moisture with nanophosphor particles [4].

However no decay in the emission intensity after humidity exposure was observed in case of luminescent-PDMS films even after 48hrs of exposure (Fig. 3(d)). Thus the coating of PDMS around CaS:Ce has surely prevented it from reacting with moisture and further degradation.

Conclusion

We have successfully synthesized CaS:Ce luminescent nanobelts, which are embedded in PDMS polymer matrix. XRD and PL studies confirmed, PDMS as a chemically inert holding matrix for CaS:Ce. The uniform distribution of CaS:Ce nanophosphors in PDMS was evident by fluorescent microscopic images and SEM. The effect of saturated relative humidity exposure on luminescent-PDMS films was not observed. Thus PDMS provides shielding to CaS:Ce against humidity exposure. We obtained flexible fluorescent composites, which may be used in new types of electronic or optical devices and applications.

Acknowledgment

One of the authors MGB would like to thank the University Grants Commission- Dr. D S Kothari Postdoctoral Fellowship Scheme (DSKPDF) India, for the financial support.

References

1. A. N. Georgobiani, A. N. Gruzintsev, T. V. Nikiforova, X. Xurong and Y. Wang, Inorganic Materials, 36 (2000) 1083-1087.
2. Karl A. Gschneidner, LeRoy Eyring Handbook on physics and chemistry of rare earths, vol-28 pg 269.
3. N. Avci, J. Musschoot, P.F. Smet, K. Korthout, A. Avci, C. Detavernier and D. Poelman. J. Electrochem. Soc., 156 (2009), pp. J333–J337.
4. Lee J, Sundar V S, Heine J R, Bawendi M G and Jensen K F 2000 Adv. Mater. 12 1102
5. Hongjoo Song, Seonghoon Lee, Nanotechnology 18 (2007) 055402 (6pp).
6. Jinwook Lee, Vikram C. Sundar, Jason R. Heine, Mouni G. Bawendi, and Klavs F. Jensen Adv. Mater. 2000, 12, No. 15, August 2.
7. Geeta Sharma, S.W. Gosavi, S P Lochab Nafa Singh. Optics: Phenomena, Materials, Devices, and Characterization
8. D. Jia, R.S. Meltzer and W.M. Yen. J. Lumin., 99 (2002), p. 1.

Synthesis of NiCo₂O₄ nanowalls for preparation of high performance supercapacitor electrodes

R. B. Waghmode, A. P. Torane

Solid State Physics Laboratory, Department of Physics, Yashwantrao Chavan Institute of Science, Satara, MS, India

Email: appasahebtorane@yahoo.in, ratnamalawaghmode@gmail.com

Abstract:

In present article, NiCo₂O₄ nanowalls have been directly grown on a stainless steel substrate surface, using a facile chemical bath deposition (CBD) method and utilized for energy storage application. The prepared thin films are characterized for their structural, morphological and wettability studies, respectively. The NiCo₂O₄ nanowalls exhibit maximum specific capacitance of 634 F/g at scan rate of 5mV/s. The specific capacitive retention 92.5 % is obtained after 1000 cycles. From this study it can be concluded that the low cost and environmental friendly CBD method could be used to deposit efficient NiCo₂O₄ nanowalls for supercapacitor application.

Keywords: Spinel nickel cobalt oxide; thin film; NiCo₂O₄ nanowalls; chemical bath deposition; supercapacitor

1. Introduction:

Nowadays, in order to solve global energy demand and problem of environmental pollution; researchers developed cost-effective, eco-friendly fresh and reproducible energy devices. Among these devices supercapacitors have attracted considerable research interest due to their high energy and power density, long cycle life, fast charging and discharging [1, 2]. Based on the electrode materials and energy storage mechanism, supercapacitors can be divided into two categories: electrochemical double layer capacitors (EDLCs) that are based on charge separation at the electrode/electrolyte interface and another pseudocapacitors, where the charge is stored using the redox based faradic reactions [3–6]. Unfortunately, performance of EDLC cannot meet ever-growing need of the high energy density and power density because of their low specific capacitance [7]. As a potential alternative to these materials, various pseudocapacitive materials such as transition metal oxides have been used as electrode materials and which can deliver higher capacitance compared with the EDLCs [8, 9].

Among the various pseudocapacitive electrode materials RuO₂ shows high specific capacitance; however, its high cost limit practical application of RuO₂ [10]. Most of these materials usually suffer from low capacitance, low cycling stability and low conductivity [11]. Recently ternary nickel cobalt oxide (NiCo₂O₄) has caught much research attention because it offers many

advantages such as comparative capacitance, low cost and environmental friendliness. Previous reports show that NiCo₂O₄ possesses a much better electronic conductivity and electrochemical activity than single nickel oxide or cobalt oxide. It is therefore expected to get better redox reactions than the two corresponding single component oxides [12, 13]. Up to now different nanostructures of NiCo₂O₄ have been synthesized with different morphologies like; nanoparticles[16], nanowires[14], nanotubes[15], nanosheets[16] and microspheres[17].

Herein, NiCo₂O₄ nanowalls thin films were successfully synthesized by using a CBD method. The structural, morphological and electrical properties of NiCo₂O₄ nanowalls thin film have been investigated. To the best of author's knowledge there is no any single report on the deposition of NiCo₂O₄ nanowalls thin films by using CBD method with higher capacitance.

2. Experimental details:

The deposition of NiCo₂O₄ thin films was carried out by following same process with some modifications, as we previously reported [18]. NiCo₂O₄ thin films were synthesized by a simple, cost effective, chemical bath deposition (CBD) method. Analytical grade nickel chloride (NiCl₂·6H₂O), cobalt chloride (CoCl₂·6H₂O), urea (CH₄N₂O) and cetyltrimethylammonium bromide (CTAB, C₁₉H₄₂BrN) were purchased from Loba chemicals ltd and used without further purification. The deposition of NiCo₂O₄ thin films, the reaction

bath was prepared in 50 ml beaker, to which 0.2 M $\text{NiCl}_2 \cdot 6\text{H}_2\text{O}$ and 0.4 M $\text{CoCl}_2 \cdot 6\text{H}_2\text{O}$ were taken. Further, 0.2 M $\text{CH}_4\text{N}_2\text{O}$ and 0.5g CTAB was added and stirred for 15 min to obtain a clear pink solution. The mirror polished steel substrates (polished with zero grade polish paper and ultrasonically cleaned with double distilled water) were mounted vertically in reaction bath. Then, the temperature of reaction bath was maintained at 80°C for 5 h. After deposition, the thin films were rinsed 2 to 3 times in double distilled water. Finally, as deposited thin films were annealed to 400°C in air for 3 h to convert hydroxide form in to pure oxide form. The deposited thin films were uniform, well adherent, black coloured and reproducible.

2.3 Characterizations

The crystal structure of the deposited thin film was studied by X-ray diffraction (XRD) technique (Bruker D-8 diffractometer) using $\text{Cu K}\alpha$ ($\lambda = 1.5418 \text{ \AA}$) radiation in 20° to 80° 2θ range. The surface morphology and chemical composition of thin film were studied by using scanning electron microscope (SEM) of model (JEOL model 6360). The Raman spectra were examined by using micro-Raman Renishaw spectrometer of wavelength 532 nm. The electrochemical measurements were carried out on Autolab PGSTAT101 electrochemical work station using three electrode cell configurations. For measurement platinum was used as a counter electrode, Ag/AgCl as a reference electrode and NiCo_2O_4 thin film as a working electrode. The mass of the active materials was calculated from the weight difference of the stainless steel substrate before and after deposition of NiCo_2O_4 thin films. Electrochemical impedance spectroscopy (EIS) measurements were carried out in a frequency range from 0.1 Hz to 100 kHz with an amplitude 5 mV at open circuit potential.

3. Results and discussion

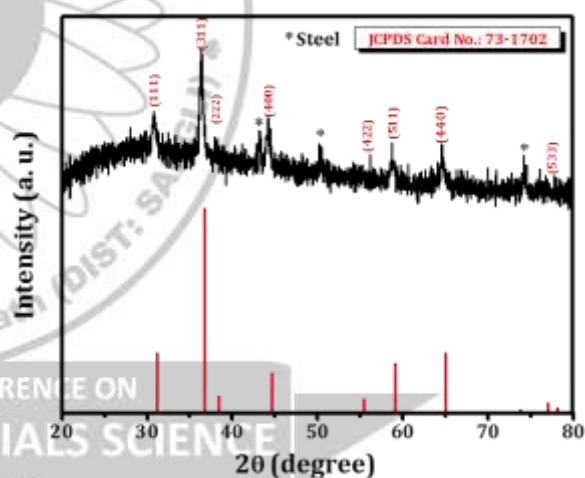
3.1. Structural analysis

The structural analysis of deposited thin films was carried out by using XRD pattern. Fig. 1. shows the XRD pattern of NiCo_2O_4 nanowalls after annealing at 400°C for 3 h on stainless steel substrate. It exhibit diffraction peaks at 2θ along

$31.1, 36.6, 38.3, 44.5, 55.3, 59, 64.9$ and 76.9 degree corresponding to the lattice planes (220), (311), (222), (400), (422), (511), (440) and (533) respectively. The diffraction peaks are in good agreement with those of the standard data card (JCPDS Card no. 73-1702) of the NiCo_2O_4 having cubic spinel crystal structure. No any characteristic impurity peak was observed, indicates the high purity of NiCo_2O_4 nanowalls. The * marked peaks are of stainless steel substrates. The crystallite size was determined by using Scherer's formula shown in equation (5) for high intense peak (311),

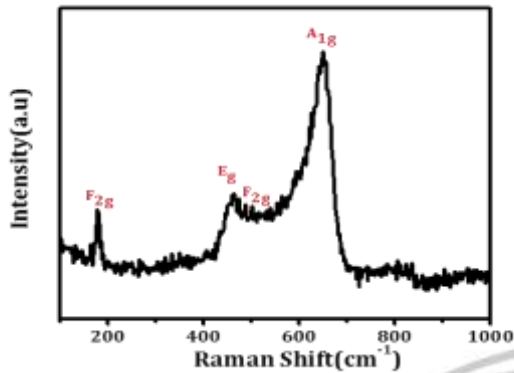
$$D = \frac{K\lambda}{\beta \cos \theta} \quad (1)$$

where 'D' is crystallite size, 'K' is constant (0.9), ' λ ' is wavelength of monochromatic X-ray (1.5418 \AA), ' β ' is full width at half maxima of the peak and ' θ ' is diffraction angle. The crystallite size for (311) plane was found 30.9 nm.



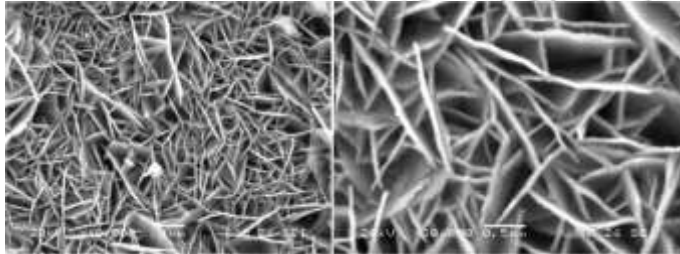
3.2 Raman Spectroscopy

In order to obtain the chemical composition and structure of annealed NiCo_2O_4 thin film, Raman analysis was performed. The Raman spectra recorded over $100\text{-}1000 \text{ cm}^{-1}$ for the samples T2, T3, T4, T5 and T6 are shown in Fig.2. The well-defined peaks at $186, 465.5, 507.2$ and 654.2 cm^{-1} corresponds to F_{2g}, E_g, F_{2g} and A_{1g} vibrational modes of spinel of NiCo_2O_4 , respectively. These results are well consistent with those the reported values in previous reports [19].



3.3. Surface morphological studies

Fig.3.shows the SEM images of NiCo₂O₄ nanostructure thin film on to a stainless steel substrate at different magnifications. The SEM images show formation of nanowalls structure of NiCo₂O₄. Due to presence of higher surface area, it is possible for electrolyte ions to diffuse in the nanoflowers to give maximum active contact with the material which will improve the supercapacitive performance. It can be seen that the film consists of a porous structure with nanowalls provides easy access for ions to access the electrode|electrolyte interface, which is a very important factor for the faradic surface reaction.

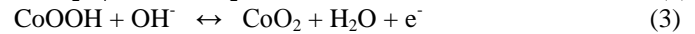


3.4. Supercapacitive properties

3.4.1. Cyclic voltammetry of NiCo₂O₄ thin films

The specific capacitance is determined by cyclic voltammetry (CV) measurements of the NiCo₂O₄ nanowalls in aqueous KOH electrolyte. Fig.4.(a) shows the CV curves of the electrode with different scan rates ranging from 5 to 100 mV s⁻¹ in the potential window of -0.2 to 0.6 V. Apparently, the shape of the CV curves clearly shows the pseudocapacitive characteristics of the active material and it also shows that the shape of redox peaks in the CV curves are prominent even at a

high scan rate of 100 mV /s indicating that the nanowalls structure is beneficial for diffusion of ions in solution and fast redox processes [20].The peak is mainly associated with the reversible Faradaic redox reaction related to M–O/ M–O–OH, where M represents Ni or Co ions[21]. The possible redox mechanism is as shown in equation (6) and (7) [22],



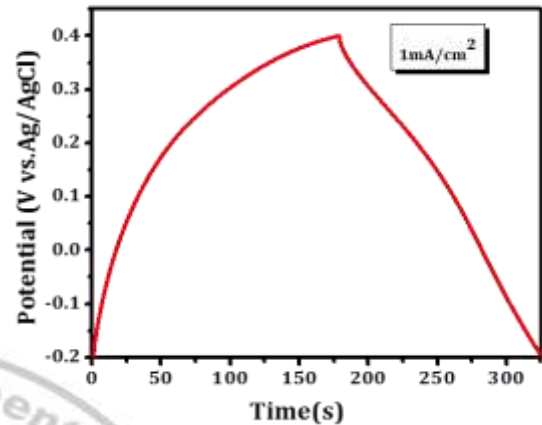
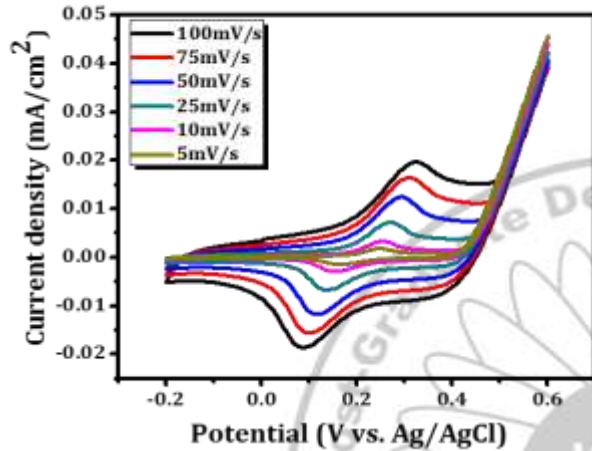
The corresponding peak current increases with increase in scan rate when the oxidation and reduction peak shift towards higher and lower potentials respectively; which shows that, the rapid transport of electrons and ions within the electrode [23]. The values of specific capacitance of the sample were calculated through the following equation:

$$C = \int \frac{I dv}{mv\Delta V} \quad (4)$$

where, ‘C’ is specific capacitance, ‘ΔV’ is the potential window, ‘I(V)’ is the current response (mA) of the NiCo₂O₄ electrode for unit area (1 cm²) dipped in 2 M KOH electrolyte and ‘m’ is deposited mass of NiCo₂O₄ on 1 cm² surface of substrate.

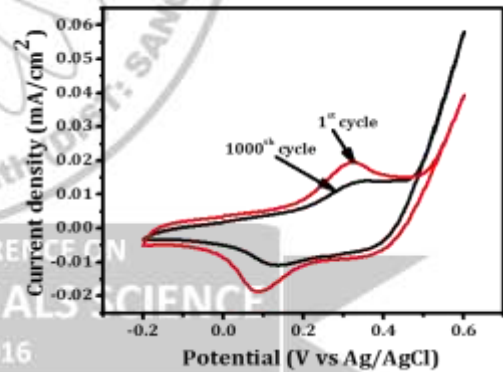
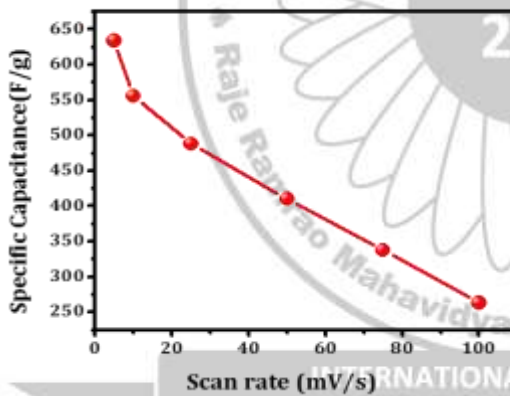
The specific capacitance of the sample is 634.2, 556.4, 488.1, 410.5, 338.6 and 263.7 F/g at scan rates of 5, 10, 25, 50, 75 and 100 mV/s respectively. Kuang et al.[1] prepared NiCo₂O₄ by hydrothermal method and reported specific capacitance of 372 F/g. Salunkhe et al.[24] prepared nickel-cobalt hydroxide by CBD method and reported capacitance 456 F/g. The specific capacitance value reported in the present work is much higher than these previous reports, which may be due to the porous nanowalls like structure. Dubal et al.[8] reported the value of capacitance of 672 F/g for Co-Ni mixed hydroxide by two step chemical method and which is larger than present work. The NiCo₂O₄ nanowalls electrode shows a decrease in specific capacitance from 634.2 to 263.7 F/g with increases in scan rate as shown in Fig. 4(b). The reduction in specific capacitance at high scan rate can be attributed to the low diffusion of the electrolyte ion. A relatively high Cs value at

5 mV/s scan rate suggests that the desired nanowalls structures with direct contact on stainless steel substrate leads to fast and efficient energy storage within the electrode [1, 25].



3.4.3 Stability Study

To evaluate the cyclic performance and electrochemical stability of the electrode, the material is performed at constant scan rate of 100 mV/s as shown in Fig. 6. It shows the initial (1st cycle) and final (1000th cycle) CV curves. From figure it is observed that the capacitance retention is 92.5 % after 1000 cycles. The NiCo₂O₄ nanowalls show excellent cycling stability.



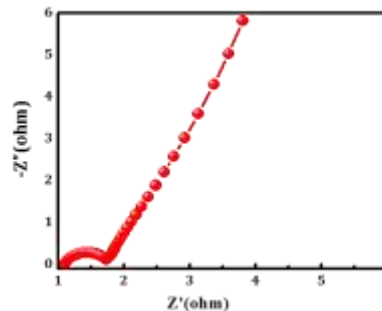
3.4.2. Galvanostatic charge discharge measurements

Fig.5.shows the galvanometric charge discharge behavior of electrode within the potential range of -0.2 to 0.4 V vs Ag/AgCl electrode at 1 mA/cm². The nearly triangular shape of the charge discharge curves for the sample shows the good pseudocapacitive behavior of the electrode material.

3.4.4. Electrochemical impedance spectroscopy measurements

Fig. 7.shows the Nyquist plot of NiCo₂O₄ nanowalls electrode tested in aqueous 3 M KOH with a frequency region of 0.1 Hz to 100 kHz at AC amplitude of 5 mV at open circuit potential. The impedance spectrum is composed of one semicircle at high frequency followed by a linear component at low frequency. In the low frequency region, the slope of the curve shows the Warburg resistance

(Zw) which shows that the electrolyte diffusion to the electrode surface. The X-intercept of the Nyquist plot corresponds to equivalent series resistance (R_s) and the charge transfer resistance (R_{ct}) is due to faradic reaction and double layer capacitance at the contact interface of electrode/electrolyte. The value of R_{ct} can be calculated from the diameter of semicircle arc. The value of R_s for the $NiCo_2O_4$ nanowalls is 0.99Ω and the value of R_{ct} is 1.79Ω .



Conclusions

In summary $NiCo_2O_4$ nanowalls thin films are directly deposited onto the stainless steel substrate surface by using simple CBD method. The XRD study confirms the formation of polycrystalline cubic spinel crystal structure. The SEM study shows formation of $NiCo_2O_4$ nanowalls uniformly dispersed on to stainless steel substrate. The $NiCo_2O_4$ nanowalls exhibited high Cs of 634 F/g at 5mV/s and excellent cycle life up to 1000 cycles. This manuscript represents the excellent electrochemical performance of $NiCo_2O_4$ nanowalls synthesized by facile synthesis method at relatively low cost and $NiCo_2O_4$ nanowalls believed to be a promising electrode material for supercapacitor application.

Acknowledgement

Both authors thankful to Department of Physics, Yashwantrao Chavan Institute of Science, Satara for providing laboratory facilities to complete this work.

References

1. Kuang M, Zhang W, Guo X L, et al. (2014) Template-free and large-scale synthesis of hierarchical dandelion-like $NiCo_2O_4$ microspheres for high-performance supercapacitors. *Ceram Int* 40:10005–10011.
2. Patil S J, Lokhande V C, Chodankar N R, Lokhande C D (2016) Chemically Prepared La_2Se_3 Nanocubes Film for Supercapacitor Application. *J Colloid Interface Sci.* doi: 10.1016/j.jcis.2016.02.003
3. Jiang L, Zou R, Li W, et al. (2013) $Ni(OH)_2/CoO$ /reduced graphene oxide composites with excellent electrochemical properties. *J Mater Chem A* 1:478–481
4. Jin Y, Chen H, Chen M, et al. (2013) Graphene-patched CNT/ MnO_2 nanocomposite papers for the electrode of high-performance flexible asymmetric supercapacitors. *ACS Appl Mater Interfaces* 5:3408–3416
5. Bhattacharjya D, Kim M S, Bae T S, Yu J S (2013) High performance supercapacitor prepared from hollow mesoporous carbon capsules with hierarchical nanoarchitecture. *J Power Sources* 244:799–805
6. Jiang H, Li C, Sun T, Ma J (2012) High-performance supercapacitor material based on $Ni(OH)_2$ nanowire- MnO_2 nanoflakes core-shell nanostructures. *Chem Commun* 48:2606–2608
7. Zhi M, Xiang C, Li J, et al. (2013) Nanostructured carbon-metal oxide composite electrodes for supercapacitors: a review. *Nanoscale* 5:72–88
8. Dubal D P, Jagdale A D, Patil S V, Lokhande C D (2012) Simple route for the synthesis of supercapacitive Co-Ni mixed hydroxide thin films. *Mater Res Bull* 47:1239–1245
9. Salunkhe R R, Jang K, Yu H, et al. (2011) Chemical synthesis and electrochemical analysis of nickel cobaltite nanostructures for supercapacitor applications. *J Alloys Compd* 509:6677–6682
10. Wu Z S, Wang D W, Ren W, et al. (2010) Anchoring hydrous RuO_2 on graphene sheets for high-performance electrochemical capacitors. *Adv Funct Mater* 20:3595–3602
11. Zhang G Q, Wu H Bin, Hoster H E, et al. (2012) Single-crystalline $NiCo_2O_4$ nanoneedle arrays grown on conductive substrates as binder-free electrodes for high-performance supercapacitors. *Energy Environ Sci* 5:9453–9456
12. Liu M-C, Kong L-B, Lu C, et al. (2012) A Sol-Gel Process for the Synthesis of $NiCo_2O_4$ Having Improved Specific Capacitance and Cycle Stability for Electrochemical Capacitors. *J Electrochem Soc* 159:A1262–A1266
13. Cui B, Lin H, Li J B, et al. (2008) Core-ring structured $NiCo_2O_4$ nanoplatelets: Synthesis, characterization, and electrocatalytic applications. *Adv Funct Mater* 18:1441–1447
14. Wei T Y, Chen C H, Chien H C, et al. (2010) A cost-effective supercapacitor material of ultrahigh specific capacitances: spinel nickel cobaltite aerogels from an epoxide-driven sol-gel process. *Adv Mater* 22:347–351
15. Wang H, Gao Q, Jiang L (2011) Facile approach to prepare nickel cobaltite nanowire materials for supercapacitors. *Small* 7:2454–2459.
16. Li L, Peng S, Cheah Y, et al. (2013) Electrospun porous $NiCo_2O_4$ nanotubes as advanced electrodes for electrochemical capacitors. *Chem - A Eur J* 19:5892–5898
17. Zhang G, Lou X W (2013) General solution growth of mesoporous $NiCo_2O_4$ nanosheets on various conductive substrates as high-performance electrodes for supercapacitors. *Adv Mater* 25:976–979
18. Waghmode R B, Torane A P (2016) Hierarchical 3D $NiCo_2O_4$ nanoflowers as electrode materials for high performance supercapacitors. *J Mater Sci Mater Electron* 27:6133–6139
19. Liu Z, Xiao K, et al (2013) Fabrication of hierarchical flower-like super-structures consisting of porous $NiCo_2O_4$ nanosheets and their electrochemical and magnetic properties. *RSC Advances* 3:4372–4380
20. Zhang C, Kuila T, Kim N H, et al. (2015) Facile preparation of flower-like $NiCo_2O_4$ /three dimensional graphene foam hybrid for high performance supercapacitor electrodes. *Carbon N Y* 89:328–339
21. Kong D, Ren W, Cheng C, et al. (2015) Three-Dimensional $NiCo_2O_4@Polypyrrole$ Coaxial Nanowire Arrays on Carbon Textiles for High-Performance Flexible Asymmetric Solid-State Supercapacitor. *ACS Appl Mater Interfaces* 7:21334–21346
22. Naveen A N, Selladurai S (2016) Novel synthesis of highly porous three-dimensional nickel cobaltite for supercapacitor application. *Ionic*. doi: 10.1007/s11581-016-1664-7
23. Zhang G, David Lou X W (2013) 186 Controlled growth of $NiCo_2O_4$ nanorods and ultrathin nanosheets on carbon nanofibers for high-performance supercapacitors. *Sci Rep* 3:1470–1475
24. Salunkhe R R, Jang K, Lee S, Ahn H (2012) Aligned nickel-cobalt hydroxide nanorod arrays for electrochemical pseudocapacitor applications. *RSC Adv* 2:3190–3193
25. Kuang M, Zhang Y X, Li T T, et al. (2015) Tunable synthesis of hierarchical $NiCo_2O_4$ nanosheets-decorated Cu/CuOx nanowires architectures for asymmetric electrochemical capacitors. *J Power Sources* 283:270–278

Synthesis of Superhydrophobic Silica Coatings on Different Substrates

Sandip Patil^a, M R Shedam^b

^aVijaysinh Yadav Arts, Commerce & Science college, Petvadagaon

^bShri Padmbhusan D.B.Patil Research center. The New College, Kolhapur.

*Corresponding Author: mahadev.shedam@yahoo.com

Abstract:

Superhydrophobic silica coatings were formed on three different metal substrates using sol-gel dip coating method. Surface morphological studies shows that the film involves both micro-nano scale hierarchical structures. Highest static contact angle was above 164° on alumina substrates. FESEM images of a top view of the coatings on different substrate shows that the surface is microscopically rough, which has a porous morphology. FTIR studies confirm formation of silica network. Such a transparent, adherent and super hydrophobic silica coating could find application in windshields of the cars as well as for the transparent coating on the solar cell panels.

Keywords. sol-gel growth; coatings; annealing; surfaces

1. Introduction:

Barthlott and Ehler discovered in 1990 that the self-cleaning property of the lotus leaf is because of the high density of minute surface protrusions. This phenomenon is known as “lotus leaf effect” [1]. The superhydrophobic surfaces inspired by lotus leaves, which has contact angle greater than 150° and sliding angle less than 10° attracted much interest from both industry and academia due to their usability in self cleaning surfaces[2], anti-icing systems [3], marine fouling [4], and so on.

The various methods for the preparation of superhydrophobic surfaces since last two decades have been reported, such as phase separation, solution immersion, template method, emulsion, wet chemical reaction, electrospinning, deposition. It has been demonstrated that sol-gel derived silica coatings exhibit comparable or even superior properties, such as homogeneity, purity, easy processing and ability to coat large and complex area substrate, compared to coatings prepared by other techniques [5]. The sol-gel processing gives a very wide flexibility in preparation of materials and control composition and optical properties of them. The sol-gel processing provides the novel route for the preparation of such hydrophobic coatings. The dip coating method to fabricate the superhydrophobic silica film on various substrates such as alumina, bronze and copper is studied.

2. Experimental:

The methyltrimethoxysilane (MTMS) based organically modified alcosol is used for the deposition on a different metal substrates. A coating sol was prepared by keeping the molar ratio of

MTMS: MeOH: H₂O constant at 1: 5.63: 1.58, respectively with PMMA 7 wt% and 0.5 M NH₄F as a catalyst for which we get maximum hydrophobicity. The cleaned metal substrates were slowly immersed into the beaker containing silica sol at a speed of 25 mm/min. The coated metal substrates were dried at room temperature and then annealed at 150 °C for 3 h to remove residual solvent.

The surface morphology of coating was examined by Field emission-Scanning electron microscopy (FE-SEM) (JEOL JSM- 7001F, Japan). Fourier Transform Infrared (FT-IR) spectra were recorded with a Perkin-Elmer, model no. 783. The sessile drop method was used for measurements of contact angle by double distilled water (>18 M_Ω cm), the experiments were performed with help of goniometer (Rame hart Instrument Co., Model 501F1, USA

3. Result and Discussion:

3.1 Surface morphological studies

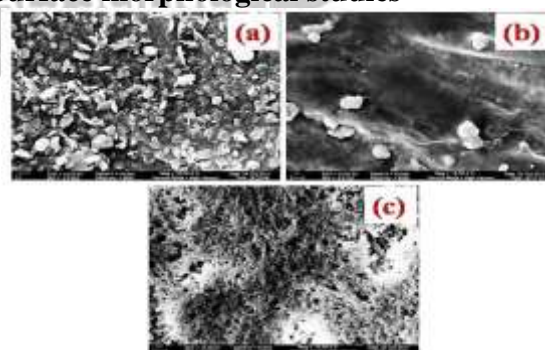


Fig. 1: SEM images of silica coating on different metallic substrates (a) aluminum substrate, (b) bronze substrate and (c) copper substrate

The two dimensional morphological studies of silica coatings have been carried out using FESEM micrographs as shown in Fig. 1.

FESEM images of the coatings on shows that the surface is microscopically rough, which has a porous morphology [6]. The morphology of the films involves both micro-nano scale hierarchical structures. Therefore, it can be expected to show superhydrophobicity. The water contact angle of films above 150° is indeed in the super hydrophobic range.

3.2 Fourier transforms infrared spectroscopy

The chemical composition of the films deposited on aluminum, copper and bronze substrates were investigated by the FT-IR spectroscopy using the KBr method in transmission mode. Several characteristic absorption peaks were observed in the range 450 to 4000 cm⁻¹ indicating formation of silica network. The FTIR spectra of the silica films prepared with different metal substrates are shown in Fig. 2. The peak at 1122 cm⁻¹ corresponded to the Si-O-Si asymmetric stretching vibration [7]. The absorption bands observed at around 2950 cm⁻¹ are due to stretching of C-H bonds, the peaks observed at 1274, and 782 cm⁻¹ are due to the Si-C bonds [8]. The broad absorption

band at around 3400 cm⁻¹ is due to the -OH due to the residual Si-OH groups.

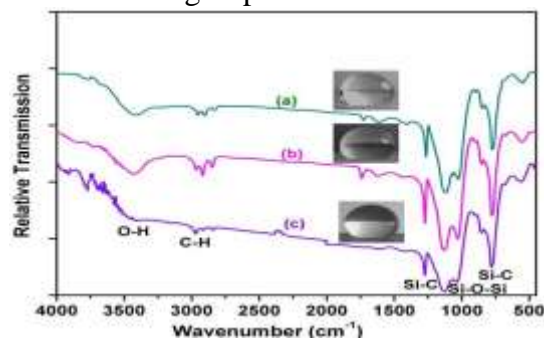


Fig. 2: FTIR spectra of silica coating on different metallic substrates (a) aluminum substrate, (b) bronze substrate and (c) copper substrate

3.2 Static and dynamic water contact angle measurements

The hydrophobicity of the resulting surfaces was assessed with water contact angle measurements. A low sliding angle renders the surface “nonsticky”, a property that is crucial for the fabrication of water-repellent and self-cleaning surfaces. The surface wettability for film prepared on various metal substrates was observed by CA and SA measurements before and after deposition, and a related CA and SA are listed in a Table 1.

Table 1. Comparisons of contact angle (CA) and sliding angle (SA) before and after deposition on of a various metal substrates with water

Metal	Contact angle		Sliding angle	
	Before deposition	After deposition	Before deposition	After deposition
Aluminum	69	164	36	7
Bronze	58	153	32	12
Copper	61	161	33	9

6. Conclusions

The sol-gel process offers many potential avenues for the conservation of art objects. Silica coatings, prepared by a single step sol-gel process using methyltrimethoxysilane as a precursor was found uniform and relatively dense. We have successfully fabricated superhydrophobic silica coating on aluminum, bronze and copper substrates without any surface modification agent. Having contact angle as high as 164° and SA as low as 7°. The selection of precursor and sol-gel composition yielded coatings was found to be adhesive, water-repellent, and effective at preventing corrosion of coated metal substrates. Such a transparent, adherent and superhydrophobic silica coating could find application in windshields of the cars as well as for the transparent coating on the solar cell panels.

Acknowledgement

This is great pleasure to thank The University Grant Commission, New Delhi for providing minor research project.

References

1. M Joshi, A Bhattacharyya, N. Agarwal, S Parmar, Bull. Mater. Sci., 35 (2012) 933–938.
2. R. Fuerstner, W, Barthlott, C, Neinhuis, Langmuir 21 (2005) 956–61

3. S. Farhadi, Farzaneh M Kulinich, Appl. Surf. Sci. 257 (2011) 6264–9
4. J. Genzer, K. Efimenko Biofouling 22 (2006) 339–60
5. Y. Huang, H. Zheng, I. Ball, Ceramic industry (2001) 17–20.
6. T. Yang, H. Tian and Y. Chen, J. Sol-Gel Sci. Tech. 49 (2009) 243-246.
7. S. S. Latthe, H. Imai, V. Ganesan, A. V. Rao, Applied Surface Science, 256 (2009) 217-222.

Effect of Polyaniline Film Thickness on Rectifying Characteristics of Polyaniline Based Heterojunction

V. S. Jamadade¹, D. S. Gaikwad^{*2}, C. J. Khilare¹, A. S. Burungale³

1. Dahiwadi College Dahiwadi, Tal-Man, Dist- Satara-415508

2. S. K. N. Sinhgad College of Engineering, Korti, Pandharpur- 413304

3. S. M. Joshi College Hadapsar, Pune-28.

Author email: vinayakjamadade@yahoo.com

Abstract

In the present work, effect of polyaniline film thickness on rectifying characteristics of NiFe₂O₄-polyaniline heterojunction film by cost effective electrochemical route on stainless steel substrate. NiFe₂O₄-polyaniline heterojunction were tested for rectifying behavior using linear sweep voltammetry technique in the voltage range ± 1 V.

Keywords: Effect of polyaniline film thickness, NiFe₂O₄, heterojunction

1. Introduction

Rectifying junctions are the basic elements of many electronic components. Since the discovery of the conducting polymers rectifying junction such as p-n junction and Schottky junction have been studied, so as to explore the possible application of conducting polymers [1]. Among the conducting polymers, polyaniline has attracted great deal of attention in the past two decades because of its potential applications [2] such as sensing by detecting vapour of variety of gases [3,4], lightweight batteries [5] Schottky diodes [6], field effect transistors [7] and light emitting diodes [8]. In this article, semiconducting polyaniline were prepared by cost effective electrochemical route on electrochemically deposited NiFe₂O₄ film electrode. This junction was tested by rectifying J-V characteristics at room temperatures.

2. Experimental details of n-NiFe₂O₄/p-polyaniline heterojunction

NiFe₂O₄ thin films formation using galvanostatic mode of electrodeposition at room temperature onto stainless steel substrate. Different preparative parameters were optimized to get good quality adherent films. For fabrication of n-NiFe₂O₄/p-polyaniline heterojunctions, a polyaniline was deposited onto a previously NiFe₂O₄ film by an electrodeposition method using a galvanostatic mode by applying a constant current range of 4.63 to 17.61 mA/cm². To deposit a polyaniline film, a solution containing 0.5 M H₂SO₄ + 0.45 M aniline (C₆H₅NH₂) was used. The thickness of the film was

calculated by a weight-difference method, employing a sensitive microbalance.

Structural characterization of the NiFe₂O₄ and polyaniline films was carried out using a X-ray diffractometer CrK α radiation ($\lambda = 2.28\text{\AA}$) in a 2θ range from 20 to 100°. The surface morphological study of the cross-sectional interface of n-NiFe₂O₄/p-polyaniline heterojunction was carried out using field emission scanning electron microscopy (FESEM-Model; JEOL-6360) [9].

3. Results and discussion

The J-V characteristics plot for different thicknesses of polyaniline films on NiFe₂O₄ film is shown in Fig. 1. The characteristics showed rectifying behavior of junction. The forward current density (J) for biasing voltage in the voltage range ± 1 V was found in the range 4.63 to 17.61 mA/cm² as polyaniline film thicknesses in the range 0.40 to 0.72 μm onto fixed 1.20 μm NiFe₂O₄ film thickness. The J-V curves was increased smoothly with thickness of polyaniline film. The maximum thickness of polyaniline over NiFe₂O₄ film was observed up to 0.72 μm , further the polyaniline film delimitation was observed.

Fig.2. shows ln J-V characteristics at various thicknesses of polyaniline films. The junction ideality factors are found to vary in range between 1.37 to 1.26 for thickness of polyaniline.

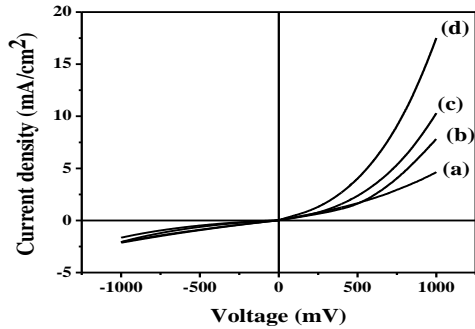


Fig.1. J – V characteristics plots of electrodeposited n-NiFe₂O₄/p polyaniline heterojunction at different thickness of polyaniline films a) 0.40, b) 0.55, c) 0.67 and d) 0.72 μ m.

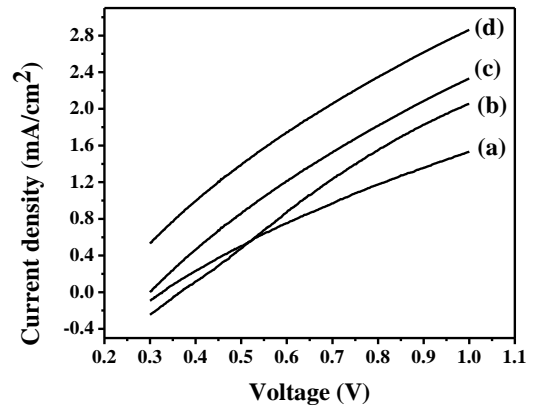


Fig. 2. ln J - V characteristics plots of n-NiFe₂O₄/p polyaniline at variable thickness of polyaniline films a) 0.40, b) 0.55, c) 0.67 and d) 0.72 μ m.

Table 1. Thickness polyaniline dependent electrical parameters of n-NiFe₂O₄/p-polyaniline Junction

Thickness of polyaniline film, (μ m)	Static Resistance, R_s (Ω)	Dynamic Resistance, R_d (Ω)	Rectification Ratio, R_R	Junction Ideality Factor, "n"
0.40	136	349	2.163	1.37
0.55	64	179	3.752	1.32
0.67	44	192	4.975	1.29
0.72	48	153	10.93	1.26

4. Conclusions

As a brief summary of this paper, studies on n-NiFe₂O₄/p polyaniline heterojunction has been successfully fabricated using cost effective electrochemical route and effect of p-polyaniline film thickness on fixed 1.20 μ m thickness of n-NiFe₂O₄ film electrode and studied their current (J)–voltage (V) characteristics.

References

1. D. Patidar, N. Jain, N.S. Saxena, Kananbala Sharma, and T.P. Sharma, Brazilian Journal of Physics, vol. 36, no. 4A, December, 2006.
2. P. K. Khanna, M. V. Kulkarni, Narendra Singh, S. P. Lonkar, V. V. S. Subbarao, A.Kasi Viswanath, Mater. Chem. Phys. 95 (2006) 24.
3. M.Wolszczak, J. Kroh, and M. M. Abdel-Hamid, Radiate Phys.Chem. 45, 71 (1995).
4. J. M. G. Iaranjeira, H. J. Khoury, W. M. de Azevedo, E. F. da Silva Jr., and E. A. da Vasconcelos, Braz. J. Phys. 32, 1 (2002)
5. E. Kalayclooglu, U. Akbulut, and L. Toppare, J. Appl. Polym.Sci. 61, 1067 (1996).
6. H. Koezuka, A. Tsumura, Synthetic Metals 28, C-753 (1989).
7. G. Gustafsson, G. M. Treacy, Y. Cao, and A. J. Heeger, SyntheticMetals 55-57, 4124 (1993).
8. J. C. Chiang, A. G. Macdiarmid, Synthetic Metals 13, 193(1986).
9. V. S. Jamadade, A. S. Burungale, C.D.Lokhande, IASR ISBN 978-81-907287-5-4 (2016)

Study the Structural, Optical and Morphological Properties of PbSe Thin Films prepared by Chemical Bath Deposition (CBD) method

Sujit A.Kadam¹, G.B. Devidas^{2*} and T.Sankarappa³

Solid State Physics Laboratory, Department of Physics, Yashwantrao Chavan Institute of Science, Satara

Department of Physics, Rani Channamma University, Belagavi-591156, India

Department of Physics, Gulbarga University, Kalaburagi-585106, India

Email: ksujit17@gmail.com, devidasgb@rediffmail.com

Abstract

Nanocrystalline PbSe thin films were prepared by Chemical Bath Deposition (CBD) method using lead nitrate, sodium selenate and sodium tart rate. The structural, morphological and optical properties were studied using X-ray diffraction (XRD), scanning electron microscopy (SEM), UV-VIS spectroscopy. From the X-ray diffraction results it has been confirmed that films were polycrystalline in nature. The maximum crystallite size was found to be 15.9 nm. The optical band gap was found to decrease from 2.12 eV to 1.72 eV with increase in deposition time. The atomic force microscopy results shows 22 nm minimum surface roughness of chemically deposited PbSe thin films.

Keywords: Chemical Bath Deposition, Optical Properties, Surface morphology, Thin Films.

INTRODUCTION:-

Metal chalcogenide compounds exhibit semiconducting properties and that is why they are of technological interest in the production of optoelectronic devices. Many authors have reported their research results on the fabrication and characterization of these compounds in the form of thin film. Lead Selenide thin films were investigated by many researchers due to their applications in solar cell technology. The PbSe thin films were deposited by number of methods and reported in the literature. These deposition methods can be grouped into two categories; chemical and physical deposition methods. Chemical deposition methods include solution growth technique, spin coating deposition and atomic layer deposition. While the physical deposition methods are sputtering, electro spray deposition and cathode arc deposition[8],[9]. In this paper, we present our results on optical and structural properties of three PbSe thin films that were prepared by chemical bath deposition method for deposition times 60 minutes, 120 minutes and 150 minutes, at the temperature of 50°C

II EXPERIMENTAL

Deposition of Films

Lead Selenide thin films were deposited on microscope glass slide using chemical bath deposition method. Prior to deposition, the glass slides were degreased in ethanol for 10 minutes followed by ultrasonic cleaning in distilled water for 15 minutes and finally dried in air. An aqueous

solution of lead nitrate [Pb(NO₃)₂] was used as lead source, sodium selenate [Na₂O₄Se] as sulfide source and sodium tartrate [C₄H₄Na₂O₆] as complexing agent for depositing PbSe thin films. All these chemicals were of analytical grade and all the three solutions were prepared in deionized water (Alpha-Q Millipore). For deposition, 30 ml of 0.2 M lead nitrate was complexed with 20 ml of 0.2 M sodium tartrate solution. Then, 30 ml of 0.2 M sodium selenate [10] was added slowly to the reaction mixture. The pH was adjusted to 5 by adding hydrochloric acid with constant stirring using pH meter. The clean glass slide was vertically immersed into the chemical bath. Three films were prepared by immersing glass slides separately in the same chemical bath for 60 minutes, 120 minutes and 150 minutes, at the temperature of 50°C and, labeled as samples a, b and c respectively. The films were taken out of the bath and rinsed with de-ionized water. The films were found to be homogenous, brownish and well adhered to the substrate. The films were annealed at 350°C for 4 hours. After the annealing, films were kept in vacuum desiccators for further characterization.

Characterization of Films

X-Ray Diffractometer Bruker D8 focus with CuK α radiation (1.5406Å) was used for crystallographic analysis of the film in the 2 θ range from 20° to 60°. Surface morphology studies were carried out using scanning electron microscope (SEM JOEL-JSM-5600) and atomic force

microscope (PARK SYSTEM XE 70). The optical properties of the PbSe thin films were studied using UV-VIS spectrophotometer (JASCO V630) at room temperature in the wavelength range from 200 nm to 1100 nm.

III. RESULTS AND DISCUSSIONS

Structural Analysis

Phase formation and crystallite sizes of the films have been determined by using X-ray diffraction measurements. XRD peaks indicate that the films is polycrystalline in nature. Sometimes a mixture of the two phases were also reported. Fig.1 shows XRD patterns of all the three annealed PbSe films. The presence of silicon oxide comes from the substrates during deposition process. The films were found to be in hexagonal phase. Three dominant peaks corresponding to (111), (200) and (220) planes were observed. All these peaks corresponding to cubic phase of PbSe and were well matched with the standard JCPDS (Reference code: 00-065-1040) data The (111) peak is the preferred orientation. On the other hand, the presences of the silicone dioxide (JCPDS ref. No. 01-074-0201) peaks in the XRD pattern are due to the glass substrate used. The structural parameters obtained are shown in Table 1.

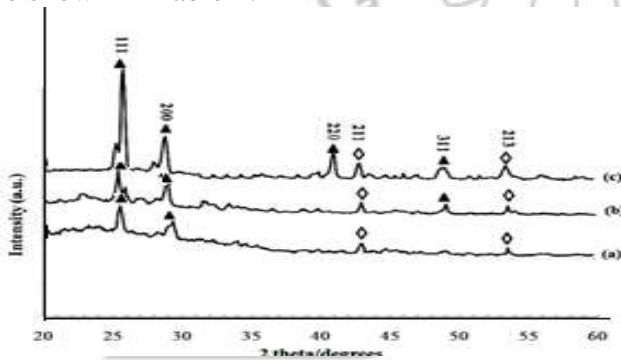


Figure1:-X-ray Diffraction Patterns of PbSe Thin Films Deposited at (a)60 min.,(b) 120min, (c)150min at 50°C. PbSe (▲), SiO2 (◇)

The average crystallite size was determined from peaks at $2\theta=25.5^\circ$ using the Debye Scherer formula.

$$D = \frac{0.94\lambda}{\beta \cos\theta}$$

Where β is FWHM in radians and λ the wavelength of x-rays. With increase in deposition time, the crystallite size increased from 14.4nm. to 15.9 nm. The crystallite size and FWHM are shown in Table 2.

Table 1: Structural Parameters determined from XRD patterns

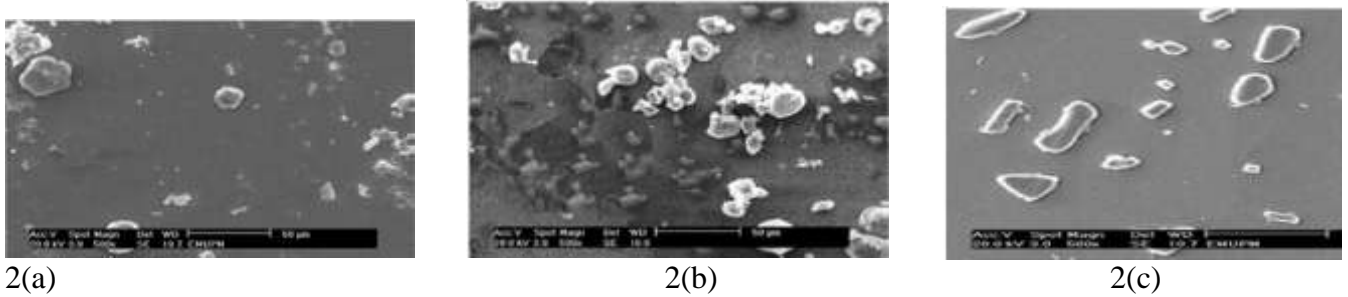
dst (Å) JCPDS	dobs (Å) Sample a	dobs (Å) Sample b	dobs (Å) Sample c	(hkl)
3.54	3.53	3.54	3.49	111
3.06	3.07	3.25	3.20	200
2.17	2.15	2.14	3.15	220

Table 2: FWHM, average crystallite size determined from XRD pattern and Optical band gap obtained from UV-VIS data

Film	FWHM (radians)	Average crystallite size(nm)	Band gap(E_g) (eV)
a	0.0302	14.4	2.129
b	0.0251	15.6	1.753
c	0.0241	15.9	1.727

SEM Analysis

Scanning electron microscopy (SEM) is useful for determining surface morphology of a film. It can give the grain size and structure. Fig.2 shows surface morphologies of all the three films. Changes in film morphology with the deposition temperature were observed. The SEM micrograph shown in Fig.(2a) indicates that film is not compact and do not have good coverage of glass substrate. This films revealed that grains are very small with no well defined grain boundaries. In Fig. 2b, well defined grains of 0.5 μm are observed. The cubic shaped PbSe crystal covered the glass substrate surfaces. As temperature increases, the surface morphology of the film becomes more homogeneous and grain sizes increase gradually. For film C, the small polycrystalline materials agglomerate together to form PbSe grains (Fig. 2c). The grains somehow formed compact and densely packed. This means that the temperature at which the film was deposited play a vital role on the quality of the films.



2(a) 2(b) 2(c)
Fig. 2: The SEM Micrographs of PbSe Films (2a) for film a, (2b) for film b & (2c) for film c. (2a)60 Minute (2b) 120 Minute and (2c) 150 Minutes.

Atomic Force Microscope Studies:-

The morphology of the film is influenced by the deposition parameters. To have a deeper insight into the structural features of PbSe thin films atomic force microscopy has been performed. This method provides information about the grain size, surface roughness and structure of the films. The AFM 3D images are shown in Figs. 3(a), 3(b), 3(c) for films *a*, *b* and *c* respectively. From 3D images it is clear that there is particle agglomeration, which led to the formation of islands of different sizes. They have elongated morphology. The average grain size and roughness are shown in Table 3. The average roughness for samples *a* and *c* is nearly the same where as for sample *b* the roughness is nearly three times of other samples. This can be clearly seen from the 3D images, the islands are very dense for films *a* and *c* in comparison to film *b*, which is the cause for large roughness. The average grain size by and large increases with increase in deposition time.

$$\alpha = \frac{A(h\nu - E_g)^n}{h\nu}$$

Table 3. Roughness and average grain size measured using atomic force microscopy

Film	Roughness (nm)	Average grain size (nm)
a	22	322
b	63	664
C	225	1994

Optical Studies

The fundamental absorption which corresponds to the transition from valence band to the conduction band can be used to determine the band gap of the material. The absorbance of all the three films was measured in the wavelength range from 200 nm to 1100 nm. The relation between α and incident photon energy $h\nu$ is

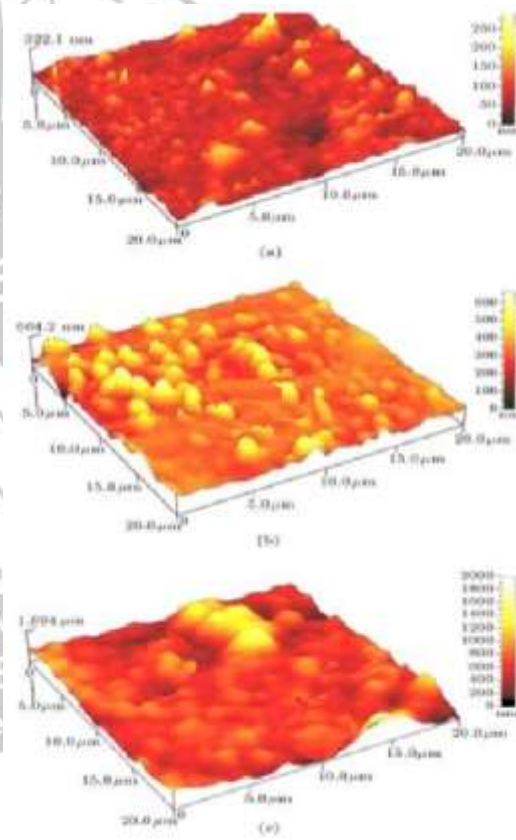


Fig. 3:- AFM Images of PbSe thin films deposited for (a)60 Minute (b) 120 Minute and (c) 150 Minutes.

where A is a constant, E_g the optical band gap, $n=1/2$ for direct band gap semiconductor . The value of E_g is obtained by extrapolating the straight line portion of $(\alpha h\nu)^2$ versus $h\nu$ (see Fig.4). The

optical band gap increased from 1.727 eV to 2.129 eV as the particle size decreased from 15.9 nm to 14.4 nm (Table 2). The observed values of E_g for these nanocrystalline PbSe thin films is higher than that of the bulk sample (1.74 eV) due to quantum confinement of carriers in the semiconductor nanocrystals. This increase of band gap is called blue shift.

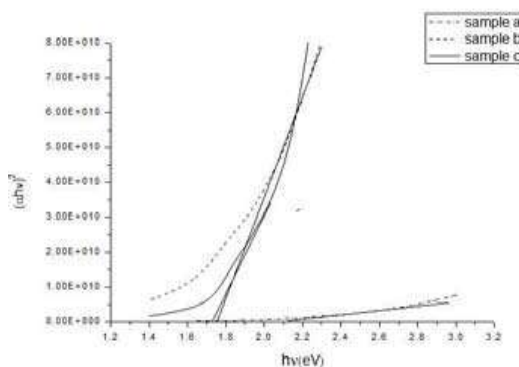


Fig.4 A Plot of $(\alpha h\nu)^2$ versus $h\nu$ for PbSe films.

IV Conclusions

PbSe thin films have been deposited using chemical bath deposition technique. Polycrystalline nature and cubic structure of the films have been established from the XRD studies. Most preferred orientation for growth was found to be along (111) direction. With increase in deposition time, the average crystallite size increased and optical band gap decreased. This result indicates decrease in size quantization. The SEM and AFM images revealed that each grain contains nanocrystals. AFM image also indicated strong agglomeration of particle.

References

1. Wang W., Geng Yan, Qian Y., Ji Mingrong and Liu X., A novel pathway to PbSe nanowires at room temperature, *Adv. Mater.*, **10**, 1479-1481 (1998).
2. Kawar S. S., Chalcogenide thin films having nanometer grain size for photovoltaic application, *Res. J. Chem. Sci.* **1(8)**, 31-35 (2011)
3. Ezenwa I.A., Effect of film thickness on the transitivity of chemical Bath Synthesized PbSe thin film. *Research Journal of engineering Sci.* **2(2)**, 23-25 (2013)
4. Okereke and Ekpunobi A.J., Structural and Optical studies of Chemical Bath deposited Lead Selenide (PbSe) thin films, *Journal of Physical Research*, **1(1)**, 37-40, (2010)
5. Ezenwa I.A., Synthesis and optical characterization of Zinc Oxide thin films, *Res. J. Chem. Sci.*, **2(3)**, 26-30 (2012)
6. R.B. Kale., S.D. Sartale, V. Ganessan, C.D. Lokhande, L. Yi-Feng and Shih-Yuan. Room temperature and Chemical synthesis of Selenide Thin films with preferred Orientation. *Appl. Surf. Sci.* **253**, (2006)930.
7. S. S. Oluyamo, M. S. Nyagba and A.S. Ojo. Optical Properties of Copper (I) Oxide Thin Films Synthesized by SILAR Technique. *IOSR Journal of Applied Physics (IOSR-JAP)*, **6**, (3), (2014)102-105.
8. P. A. Cox. The electronic structure and chemistry of solid, Oxford University Press Oxford. (1987).
9. Padam G.K., *Thin Solid film* **150**, L89-L9210(1987)
10. Ishiwu S. and M.N. Nnabuchi M.N., The Optical and Solid State properties of Lead Selenide thin films by Chemical Bath Deposition (CBD) Technique, *Journal of Ovanic Research*, **6(2)**, 81-86 (2010)
11. Zhu, J., Liao, X., Wang, J. and Chen, H.Y. Photochemical synthesis and Characterization of PbSe nanoparticles, *Materials Research Bulletin*, **36(7-8)**, pp. 1169-1176(2001).
12. Kumar, N., Sharma, V., Padha, N., Shah, N.M., Desai, M.S., Panchal, C.J. and Protsenko, I.Y. Influence of the substrate temperature on the structural, optical and electrical properties of tin selenide thin Films deposited by thermal evaporation method, *Crystal Research Technology*, **45**, pp. 53-5(2010).

Synthesis and Characterization of Fe₃O₄/PANI Nanocomposite

¹S A Kulkarni, ²P S Sawadh, ¹M G Gote, ¹K K. Kokate, ³S E Bhandarkar

¹Department of CEES, MIT College of Engineering, Pune-411038, Maharashtra, India

²Department of Physics, B.D. College of Engineering, Sevagram- 442102, Maharashtra, India

³Department of Chemistry, GVISH, Amravati, Maharashtra, India.

Abstract:

In the present work, the effect of magnetite nanoparticle concentration on the spectral, morphological, thermal properties of the Fe₃O₄/PANI nanocomposite has been investigated. Our aim was to obtain the magnetite /polyaniline nanocomposites with less agglomeration along with promising thermal stability. The Fe₃O₄/PANI nanocomposites were prepared by in-situ polymerization of aniline. The resulting nanocomposites were analyzed by, XRD, SEM, TEM, TGA.

Keywords: Fe₃O₄, nanocomposites, ultrasonication.

Corresponding Author's mail Id: kulkarnisachin42@gmail.com.

Introduction

Polyaniline (PANI) is one of the most studied conductive polymers due to its easy synthesis, environmental stability, simple doping/dedoping and high conductivity [1]. Polymer encapsulated magnetic nanoparticles are of great technological interest as the coating provides a matrix for binding of the particles and also prevents grain growth and agglomeration.

Experimental Procedure

Materials

For the synthesis of Fe₃O₄/PANI nanocomposite in this study, all chemicals were of analytical grade and were used without further purification purchased from Aldrich.

Synthesis of Fe₃O₄/PANI Nanocomposites:

Fe₃O₄/PANI nanocomposites were synthesized by in situ polymerization method. In this method, initially 0.1 g of Fe₃O₄ was added into a three necked flask (100 mL, capacity) containing 40 mL of 0.1 M HCl aqueous solution. Then the suspension was ultrasonically treated for 15 mins, and then kept at 5°C for 12 h. The HCl aqueous solution was decanted by applying an external magnet. Then 10 mL of anhydrous ethanol and 0.1 mL of redistilled AN were added into the flask. The mixture was ultrasonically treated for 10 min, and then kept at 5°C for 12 h in a nitrogen atmosphere. Thereafter, the flask was transferred into a thermostatic bath maintained at 5–7 °C, followed by addition of 0.17 mL of 12 M HCl and dropwise addition of precooled APS aqueous solution (0.04 M, 30 mL). The mixture was treated with constant stirring and intermittent

ultrasonication in a nitrogen atmosphere for 3 h. The resulting product was magnetically collected, washed with distilled water and ethanol several times, and finally dried in a vacuum oven. Further three more composites are prepared by varying the quantity of magnetite as 0.15 g, 0.2 g and 0.25 g.

Characterization

The resulting nanocomposites were analyzed by, XRD, SEM, TEM, TGA.

Results and Discussion

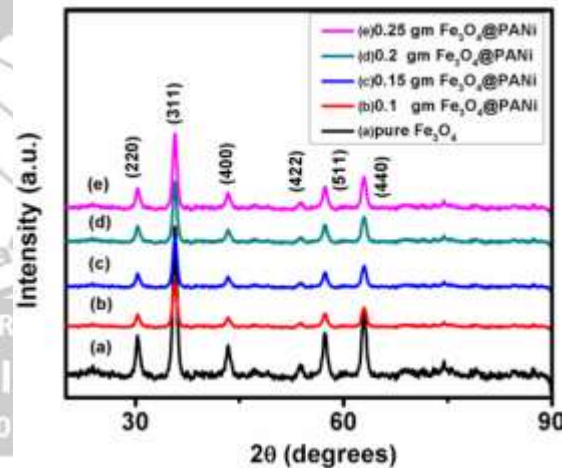


Fig. 1. XRD patterns of magnetite nanoparticles and Fe₃O₄/PANI Nanocomposites

Fig.1. shows the XRD patterns of pure Fe₃O₄ nanoparticles and PANI modified Fe₃O₄ nanocomposites. The single phase formation of Fe₃O₄ nanoparticle is confirmed by matching with standard JCPDS card no. 88-0315. The crystallite size of the Fe₃O₄ nanoparticles was calculated by using Scherer's formula and found to be ~ 39 nm. From XRD it has been observed that intensity of

(b) is reduced in comparison to (a) due to amorphous nature of PANI. While with further increase in magnetite content in composites rise in intensity is observed from (c) to (e). Presence of PANI in XRD pattern is not observed, which supports with the earlier literature.[2,3]

Fig.2 shows SEM micrographs of Fe₃O₄ nanoparticles. It is observed that particles are small

in size and agglomeration is evident. But Fig.2 (b) which is SEM of PANI coated Fe₃O₄ (0.25 g) nanoparticles clearly indicates large and agglomeration free nanocomposites suggesting that in the polymerization process PANI may be forming a polymeric matrix in which the magnetite nanoparticles are dispersed.

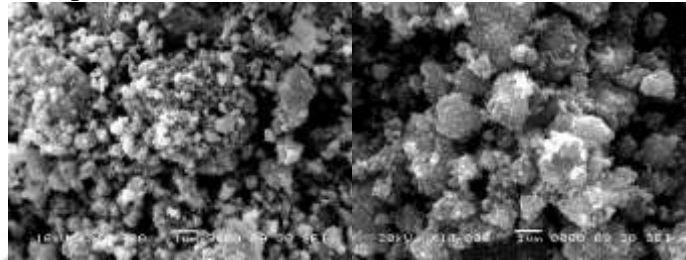


Fig. 2(a)SEM Micrograph of Fe₃O₄ nanoparticles & (b) Fe₃O₄/PANI nanocomposites

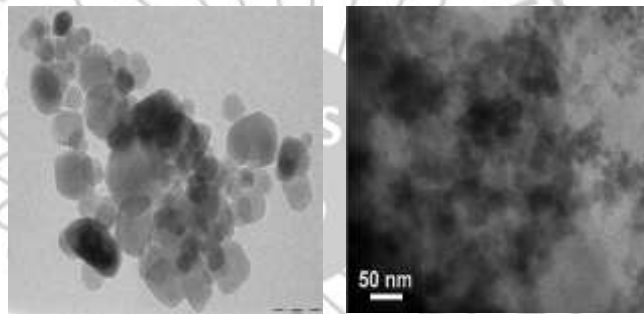
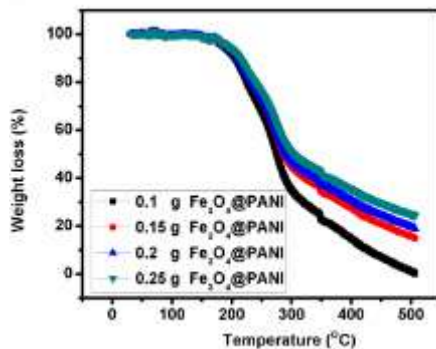


Fig.3(a) TEM micrograph of pure Fe₃O₄ & (b)Fe₃O₄/PANI nanocomposites

Fig.3(a) shows the TEM micrograph of pure Fe₃O₄ nanoparticles. The particles are observed to be almost spherical in nature with diameters ranging from 25–45 nm. These particles are polydisperse and some of them agglomerated due to magneto-dipole interactions between particles. Fig.3 (b) shows the TEM micrographs of Fe₃O₄/PANI nanoparticles, which is quite polydispersed.

Fig.4 TGA analysis of Fe₃O₄/PANI nanocomposites.

Fig.4 shows TGA results for the Fe₃O₄/PANI nanocomposites synthesized in HCl. The first step (50–100 °C) indicates the loss of water in the composite. The second weight loss, which occurs between 150 and 300 °C, may be attributed to the loss of more tightly bound water in the oxide matrix; in the case of the composites, this second step may also be related to loss of acid dopant or volatile elements bound to the PANI chain. Above 300 °C, the weight loss is assigned to the combustion of PANI. It can be observed that with the increase in magnetite content in the composite the thermal stability of composite has increased. For higher magnetite content in the composite, the weight loss of the composite was found to be less than the lower magnetite content composite [4]. TGA results clearly indicate that Fe₃O₄ improves



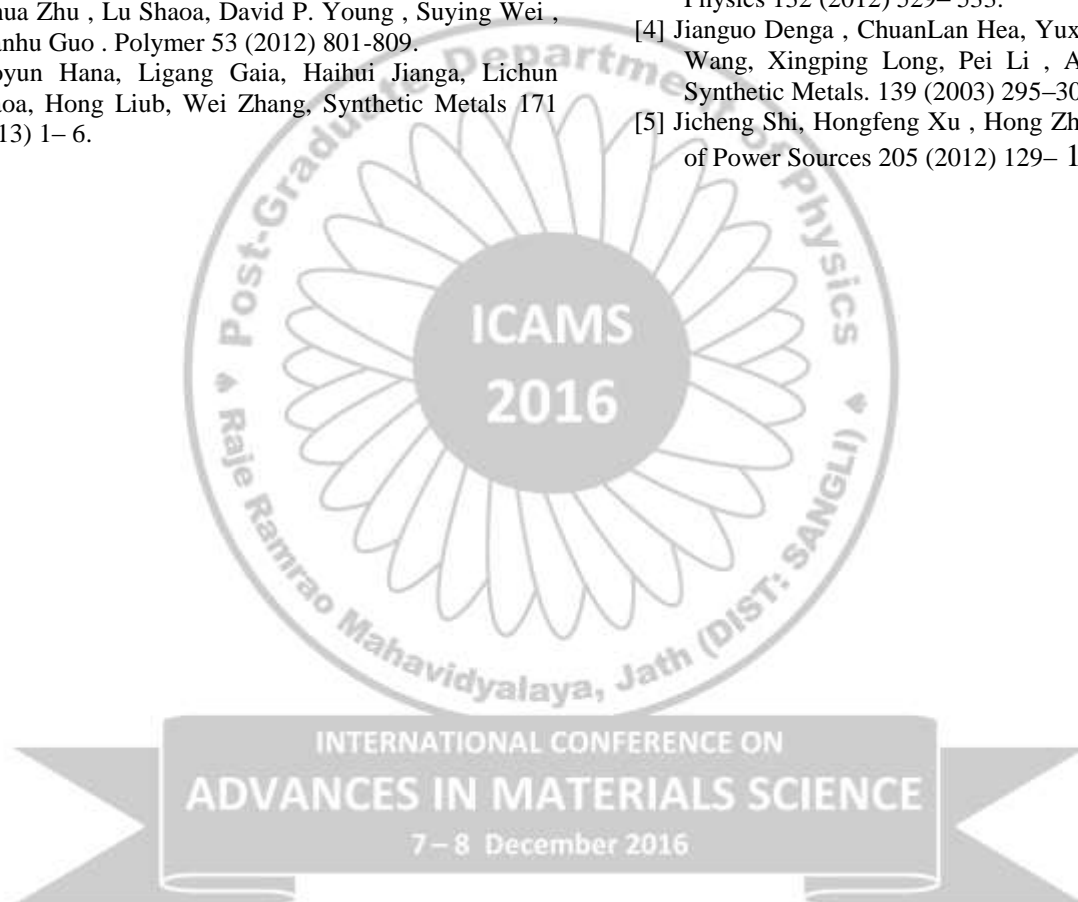
the thermal stability of PANI through aniline during in situ polymerization [5].

Conclusion:

Well-defined core-shell structured $\text{Fe}_3\text{O}_4/\text{PANI}$ microspheres are obtained by an in-situ polymerization method without using the surfactant. SEM micrographs of PANI coated Fe_3O_4 nanoparticles clearly indicate the development of large and agglomeration free particles suggesting that in the polymerization process PANI may be forming a polymeric matrix in which the magnetite nanoparticles are dispersed. From TGA it can be observed that with the increase in magnetite content in the composite the thermal stability of composite has increased. For higher magnetite content in the composite, the weight loss of the composite was found to be less than the lower magnetite content composite.

References

- [1] Hongbo Gu , Yudong Huang , Xi Zhang , Qiang Wang , Jiahua Zhu , Lu Shaoa, David P. Young , Suying Wei , Zhanhu Guo . Polymer 53 (2012) 801-809.
- [2] Xiaoyun Hana, Ligang Gaia, Haihui Jianga, Lichun Zhaoa, Hong Liub, Wei Zhang, Synthetic Metals 171 (2013) 1– 6.
- [3] Beatriz E. Jaramillo-Tabares, Franklin Jaramillo Isaza, Susana I. Córdoba de Torresi, Materials Chemistry and Physics 132 (2012) 529– 533.
- [4] Jianguo Denga , ChuanLan Hea, Yuxing Peng , Jianhua Wang, Xingping Long, Pei Li , Albert S.C. Chan , Synthetic Metals. 139 (2003) 295–301
- [5] Jicheng Shi, Hongfeng Xu , Hong Zhao, Lu Lu, Journal of Power Sources 205 (2012) 129– 135.



Synthesis and structural study of Al³⁺ substituted Cd ferrites

S R Bhitre

Jijamata college of Science and Arts, Bhende, Tal.- Newasa, Dist.-Ahmednagar

Abstract

The Cd₁Al_xFe_{2-x}O₄ ferrites systems were prepared by double sintered ceramic method. The structural characterization was carried out using X-ray diffraction method. The single phase spinel structure was confirmed from XRD patterns. Lattice parameter, X-ray density, porosity, particle size and intensities of diffracted lines were calculated. The intensity ratios of structure sensitive planes have been estimated and considered for cation distribution.

Introduction:-

The spinel ferrites have gained enormous importance because of their novel combined electric and magnetic properties. Ferrites are widely used in transformers, ultrasonic generators, modulators, phase shifters, isolators, memory devices, recording devices, sensors etc. The substitutions of magnetic and non-magnetic ions in spinel ferrites on tetrahedral A site and octahedral b site greatly influence the structural, magnetic and electrical properties of ferrites. The influence of substitution of non-magnetic cations on the magnetic properties has been investigated by many researchers [1-4]. It has been found that when A site is diluted by non-magnetic cation A-B interaction becomes weak and Neel's collinear structure gets perturbed and gives triangular or canted spin orientation [5-6].

The available literature shows that the addition of trivalent cations for Fe³⁺ influences the magnetic and electrical properties of the system [7-15]. The magnetic order can be controlled by proper cation substitution [16]. The distribution of cations among available A and

B sites decides the basic properties of ferrites [17]. The substitution of magnetic and non-magnetic cations can be done in order to get particular properties resulting from cation distribution in crystal lattice. The substitution for Fe³⁺ by another trivalent cation is one of the most effective means to control saturation magnetization. The effect of cadmium substitution on structural and magnetic properties of nickel ferrite has been studied by K. M. Jadhav et. al. [18]. Electrical Properties of Cadmium Substitution in Nickel Ferrites has been studied by Ande Ashok et. al. [19]. Effects of cadmium on physical and magnetic properties of Co-Cd ferrites has been studied by Saraut Noor et. al. [20]. In the survey of reported work so far, there is no information available to our knowledge about the systemic study of the structural and magnetic properties of mixed magnetic oxides CdFe_{2-x}Al_xO₄. Therefore, view of this fact, it is proposed in the present investigation to study the effect of substitution of non-magnetic cation Al³⁺ on the structural and magnetic properties of these mixed ferrites.

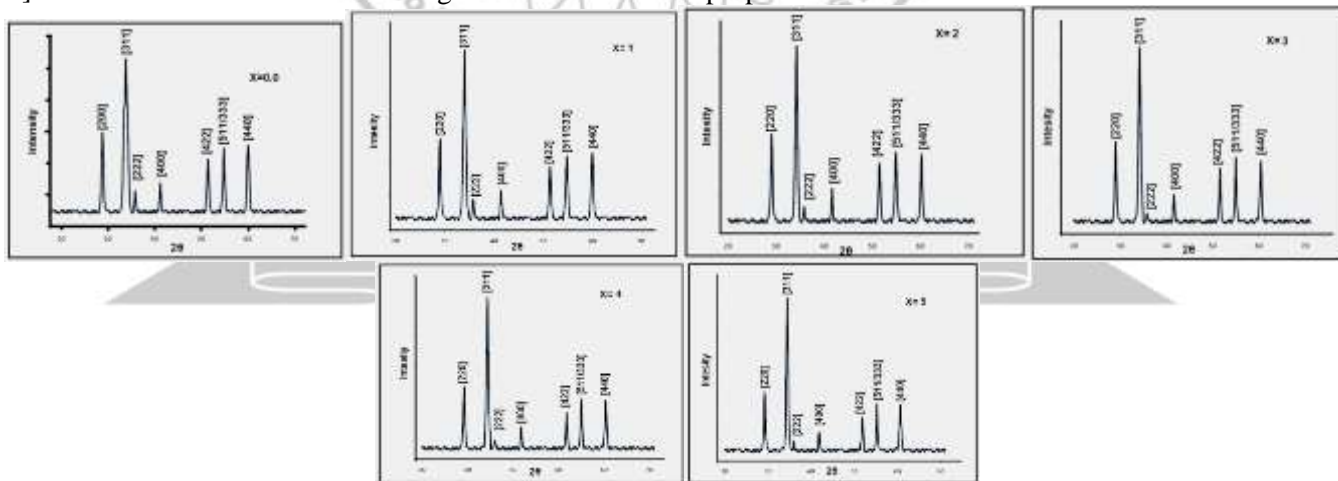


Fig. 1. Typical X-ray diffractograms of the Cd₁Al_xFe_{2-x}O₄ system.

Experimental:-

The spinel ferrite series of Cd₁Al_xFe_{2-x}O₄ where x varies from x=0.0 to 0.5 in the steps of 0.1 were prepared by the conventional ceramic method. The chemicals for ferrite systems were of analytical grade

high purity oxides CdO, Al₂O₃ & Fe₂O₃ were mixed in proper proportion so as to yield the desired stoichiometry composition. Each of these compositions was ground for half an hour in an agate mortar. This mixture was then presintered at 850 °C for 24 hours then

slowly cooled to room temperature. The presintered samples were gain milled to fine powder. The powder was then pressed at around 5 tones/square inch of pressure to form pellets of about 1 cm in diameter. The

pellets were finally sintered at 900°C for 24 hours and naturally cooled to room temperature. The X-Ray diffraction patterns for all the powdered samples were recorded on X-ray diffractometer.

Table 1. Variation of Lattice parameter and ionic radii r_A of A-site, r_B of B-site and r the average ionic radii with Al concentration.

Composition x	X-ray density dx (gm/cm ³)	Bulk density d (gm/cm ³)	Crystalline size t (A ⁰)	Porosity %
0.0	5.774	3.906	333.7	32
0.1	5.775	3.765	303.4	35
0.2	5.736	3.623	371	37
0.3	5.717	3.511	238.5	39
0.4	5.697	3.491	256.9	39
0.5	5.677	3.408	278.4	40

Results and discussion:-

The X-ray diffraction patterns of all the six samples of the Cd₁Al_xFe_{2-x}O₄ system are shown in figure (1). The X-ray diffraction patterns confirm the single phase spinel formation. The reflections from different planes in the XRD pattern indicate the cubic spinel structure of the samples. The Lattice parameter 'a_{cal}' of each of the sample was calculated using the X-ray data and the same is listed in table (1). The lattice parameter is found to decrease with increase in Al³⁺ concentration in the composition. The ionic radius is found to influences the lattice parameter. The ionic radii r_A & r_B (of the tetrahedral site & octahedral site respectively) have been calculated considering the cation distribution. Theoretical values of the lattice parameter 'a_{th}' have been determined using the following relation [21]

$$a_{th} = \frac{8}{3\sqrt{3}} [(r_A + R_0) + \sqrt{3}(r_B + R_0)] \text{ ----- 1}$$

The lattice parameter 'a_{th}' calculated using relation 1 is listed in table (1). The ionic radii r_A of tetrahedral site, r_B of octahedral site and the average ionic radii have been calculated and are listed in table (1). The decrease in r_B with increase in Al³⁺ is due to the replacement of larger Fe³⁺ (0.64 A⁰) by smaller Al³⁺(0.51 A⁰) on the B- site [22]. The octahedral site plays a dominant role in influencing the lattice parameter. The average ionic radius decreases with increase in Al³⁺ content. This accounts for the decrease in lattice parameter with (x). Thus the decrease in lattice parameter with increase in Al³⁺ content may be attributed to the replacement of larger Fe³⁺ (0.64 A⁰) by

smaller Al³⁺(0.51 A⁰) ions. The values of theoretical and observed lattice parameter are listed in table (1). These values are comparable with the values reported in literature [23,24].

The X-ray densities (dx) of all the samples were calculated by using the formula [25]

$$dx = \frac{ZM}{NV} \text{ gm/cm}^2 \text{ ----- 2}$$

The X-ray densities (dx) are tabulated in the table (2). It can be seen from the table that the X-ray density decreases with increasing Al³⁺. The bulk density also reflects the same behavior as X-ray density. This decrease in density with increase in Al³⁺ content can be ascribed to the atomic weight and density of Al³⁺ (27, 2.79 gm/cm⁺³), which is lower than that of Fe³⁺ (55.8, 7.87 gm/cm⁺³).

The crystalline size of all the samples was calculated by using Scherer's formula [26]

$$t = \frac{0.9\lambda}{BCos\theta} \text{ ----- 3}$$

The crystalline size of all the samples is given in table (2). It can be observed from the table that the crystalline size varies in the range of 225A⁰ to 375A⁰ with average crystalline size 297 A⁰ which is consistent with the crystalline size of ceramically prepared systems.

The percentage porosity (%P) of all the samples have been calculated by using the formula given by Standly K.J. [27]

$$\%P = [1 - \frac{d}{dx}] \times 100 \text{ ----- 4}$$

The values of percentage porosity (%P) are d listed in table (2). From the table it can be seen that porosity is found to be 30% to 40%, which is in good agreement with the values reported by R.G.Dorie etal. [28].

Table 2 Variation of X-ray density, Bulk density, Crystalline size and % porosity for Cd₁Al_xFe_{2-x}O₄ system.

Compos ition (x)	Lattice parameter		Ionic radii		
	a _{th.} Å	a _{cal.} Å	r _A (Å ⁰)	r _B (Å ⁰)	$r = \frac{r_A + r_B}{2}$ (Å ⁰)
0.0	8.74	8.73	0.97	0.64	0.805
0.1	8.73	8.71	0.97	0.634	0.802
0.2	8.71	8.69	0.97	0.627	0.799
0.3	8.69	8.67	0.97	0.621	0.796
0.4	8.67	8.65	0.97	0.614	0.792
0.5	8.65	8.63	0.97	0.608	0.789

Table 3. Cation distribution for Cd₁Al_xFe_{2-x}O₄ system.

Composition x	Cation distribution	
	A-Site	B-Site
0.0	(Cd ₁)	(Fe ₂)
0.1	(Cd ₁)	(Fe _{1.9} Al _{0.1})
0.2	(Cd ₁)	(Fe _{1.8} Al _{0.2})
0.3	(Cd ₁)	(Fe _{1.7} Al _{0.3})
0.4	(Cd ₁)	(Fe _{1.6} Al _{0.4})
0.5	(Cd ₁)	(Fe _{1.5} Al _{0.5})

The cation distribution was determined on the basis of X-ray intensities and the saturation magnetization. The X-ray intensities were calculated by using the formula given by Burger [29].

$$I_{hkl} = |F_{hkl}|^2 \cdot P \cdot L_p \text{ ----- } 5$$

Where, F_{hkl} is structure factor, P is multiplicity factor and L_p is Lorentz polarization factor.

The distribution of divalent and trivalent ions among the tetrahedral and octahedral sites in the Cd₁Al_xFe_{2-x}O₄ system are determined by considering the ratios of intensities for structure sensitive planes [30]. The intensity ratios of the planes : I(220)/(400), I(422)/I(400) and I(440)/I(422) are structure sensitive [31]. These ratios have been considered to determine cation distribution besides saturation magnetization. The estimated cation distributions are given in table (3). It is evident from the table that the trivalent Al³⁺ ion replaces Fe³⁺ ion in the octahedral B site. The divalent Cd²⁺ occupies the tetrahedral A site as it has strong preference for A site. The same trend is reported by number of researchers.

Conclusions

The system Cd₁Al_xFe_{2-x}O₄ with x = 0.0 to 0.5 (with step of 0.1) has a single phase spinel structure. The Lattice parameter decreases with increase in Al³⁺ content. The cation distribution indicates that Al³⁺ has preference for B-site.. Non-magnetic Al³⁺ ion replaces magnetic Fe³⁺ ion and the divalent Cd²⁺ occupies the tetrahedral A site as it has strong preference for A site.. The X-ray density decreases with increasing Al³⁺ and the bulk density also reflects the same behavior as X-ray density. The crystalline size varies in the range of 225Å⁰ to 375Å⁰ with average crystalline size 297 Å⁰ which is consistent with the crystalline size of ceramically prepared systems. The porosity is found to be 30% to 40%.

References

[1] C. B. Kolekar et. al. J.M.M. 138 (1994) 211.
 [2] O.G. Mundada et. al. Indian J. Pure and Appl. Phys. Vol. 35 (1997) 554.
 [3] H. Mohan et. al. Physica B 127 (1996) 292.
 [4] A.K. Ghatge et. al. J. Mater. Sci. Letter 15 (1996) 1548.
 [5] P. N. Kamble et. al. Indian J. Pure and Appl. Phys. Vol. 28 (1990) 542.
 [6] M. G. Patil et. al. Bull. Mater. Sci. Vol. 4 (1994) 399.
 [7] T. Tsushima, J. Phys. Soc. Japan 18 (1963) 1162.
 [8] J.J. Bara. et. al. Phys. Stat. Sol. A44 (1997) 325.
 [9] R. L. Maxwell and S. J. Pickart. Phys. Rev. 92 (1953) 1120.
 [10] A. haoet, J. Teillet et. al. Phys. Stat. Sol. A103 (1987) 1257.
 [11] J. Chappert and R. B. Frankel Phys. Rev. Lett. 19 (1967) 570.
 [12] V. I. Nikoloev et. al. Sov. Phy. Solid State 13 (1971) 317.
 [13] V. I. Nikoloev et. al. Sov. Phy. Solid State 14 (1972) 521.
 [14] T. A. Kaplan et. al. J. Appl. Phys. 32 919610 135.
 [15] N. N. Jani et. al. Mater. Sci. Vol. 21, No. 3 June (1998) 233-239
 [16] Yafet and C. Kittel Phys. Rev. 87 91952) 290.
 [17] J. Samuel Smart Phys. Rev. 94(40 (1954) 847.
 [18] K. M. Jadhav et. al. Chinese J. of Chem. Phys. Vol. 23, No. 4 Aug. 27 (2010)
 [19] Ande Ashok et. al. World J. of Condensed Matter Phys., 2 (2012) 257-266
 [20] Saroaut Noor et. al. J. of Ban. Acad. of Sci. Vol. 35, No. 2 (2011) 229-235.
 [21] S. A. Mazen et. al., Bull. For Sci. Zagazig Uni. 13 (1991) 344.
 [22] J. D. Dunitz, L. E. Orgel. J. Phys. Chem. Solids (1957).
 [23] B. K. Modi et. al., J. Mater. Sci. Lett. 17 (1998).
 [24] B. K. Modi et. al., J. Mater. Sci. Lett. 31 (1996) 1311.
 [25] B. D. Cullity Elem. of X-Ray Diff. Adison-Wesley Presss Reading M.A. (1959)
 [26] K. J. Standly, Oxide Magnetic Materials, Clarendon Press, Oxford (1972).
 [27] M. J. Buerger Crystal Structure Analysis, Wiley New York (1960).
 [28] R. G. Dorik, K.B. Modi, K.M. Jadhav, Ind. J. Pure Appl. Phys., 35 (1997) 594.
 [29] R. K. Datta, R. Roy, J. Am. Cerm. Soc., 56 (1967) 578.
 [30] R. W. G. Wyckoff, Crystal Structure, Vol.2, Interscience, New York, (1994) 75.
 [31] Ohinishi & T. Teranishi, J. Phys. Soc. Jpn., 16 (1961) 36.

Synthesis and Structural Study Of Cobalt Sulphide Thin Films By Chemical Bath Deposition

Shivani Gavande, Gouri Tuljalpurkar, Pooja Solapure
Abhijit Nivargikar, S.S.Gavande^{a*}

^{a*}Department of Physics, Sangameshwar College, Solapur 413003, M.S., India.

*Address to whom all correspondence can be addressed. E-mail: shubhangi.gavande15@gmail.com

Abstract

The cobalt sulphide thin films were prepared by simple chemical bath deposition technique. The prepared peacock green coloured thin film was characterized by XRD technique for structural study of prepared Cobalt sulphide thin films. XRD revealed the hexagonal crystal structure of Cobalt sulphide thin films.

Keywords: Chemical bath deposition, Cobalt sulphide, Thiourea, X-ray diffraction.

1. Introduction:

Cobalt sulphide is a chemical compound with formula Co_xS_y . Cobalt sulphide species include minerals with the formula CoS_2 and Co_3O_4 and also the synthetic mineral Co_9S_8 . The sulphides of cobalt are black, semiconducting and insoluble in water. They react with strong acids to release hydrogen sulphide gas. They are weak reducing agents and can be oxidized to Cobalt sulphate. Cobalt sulphides precipitate when aqueous solutions of cobalt (II) ions are treated with Hydrogen sulphide. This reaction is useful in the purification of cobalt from its ores as well as in qualitative inorganic analysis. In combination with molybdenum, the sulphides of cobalt are used as catalysts for the industrial process called hydrodesulphurization, which is implemented on a large scale in refineries. Cobalt sulphide thin films are of particular interest due to their unique catalytic, electrical, optical and magnetic properties and exhibit strong intrinsic absorption in the visible and near infrared regimes of the electromagnetic spectrum [2- 6].

There are number of physical and chemical techniques used for the deposition of thin films of the semiconducting material. The choice of technique depends on the material to be deposited, nature of substrate, required film thickness of thin film, application were the film used etc. The techniques used for the deposition of a semiconducting material are classified as physical and chemical techniques. Chemical techniques are relatively economical and easier as compared to physical methods.

Chemical bath deposition (CBD) is a solution growth process used for depositing thin films of compound materials. An aqueous solution of a metal complex, when mixed with a solution of chalcogen

bearing compound, precipitation of the chalcogenide occurs under certain condition. When the precipitation is controlled, compound gets deposited on the wall of the container and surface of the substrate. CBD method has been used successfully to deposit binary and ternary semiconductors. The parameters like temperature, pH value, concentration of ions, the nature of the substrate, nature of the complexing agents and salts used control the deposition process. CBD technique is very simple and low cost. In CBD method, thin films are deposited on the substrate from aqueous solution either by passing a current or by chemical reaction under appropriate conditions. CBD yields stable, adherent, uniform and thin films with good reproducibility by a relatively simple process. The growth of thin films strongly depends on growth conditions, such as duration of deposition, composition and temperature of the solution and topographical and chemical nature of the substrate.

2. Experimental Method:

The glass substrates were used for the deposition of Cobalt sulphide thin films. The glass substrates were cleaned by boiling for 1-2 hours in a solution of Chromium trioxide. The boiled substrates were washed using double distilled water and finally cleaned with acetone and then dried. Then 1M of 10 ml solution of Cobalt sulphate ($CoSO_4$) and 1M of 10 ml solution of Thiourea was mixed together. Then 2.2 ml of Triethylamine was added drop by drop to the reaction mixture with continuous stirring. Lastly 15ml of Ammonia was added to the reaction mixture to maintain pH at 10.5. The bath temperature was set to 65°C and was maintained constant. The glass substrates were mounted on the substrate holder and then immersed in the reaction mixture, which was

stirred at a rate of 70 rpm by a rotator for a deposition time of 90 mins. Then after 90 mins thin, uniform and adherent peacock green colored deposition was obtained on the glass substrates.

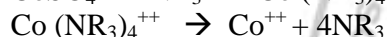
Weight of the deposited Cobalt sulphide SS-substrate per unit area (mg/cm^2) was measured by digital weight balance with a least count of $\sim 0.1\text{mg}/\text{cm}^2$. The internal structure of the Cobalt sulphide thin films was studied by using X-ray diffraction patterns carried out by X-ray diffractometer (XRD) (Rigaku D/max 2550Vb+18 kw with $\text{CuK}\alpha$ $\lambda=1.54056\text{\AA}$) in the range of diffraction angle 2θ from 20° – 80° .

3. Results and discussion:

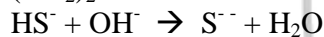
3.1 Film Formation mechanism:

Chemical Reaction:

The chemical reaction that occurs in the reaction mixture is as follows:-



where $\text{R} = \text{H}/\text{CH}_2\text{CH}_2\text{OH}$



3.2 Structural characterization

Fig.1 shows the XRD patterns of Cobalt sulphide thin film of 456 nm deposited at a temperature of 65°C . It is observed that deposited Cobalt sulphide sample was crystalline in nature. The peak orientation along (222) indicates the formation of Co_3S_4 . The observed 'd' values well matched with standard 'd' values taken from JCPDS data card no.47-1738. The peak orientation along (0010) indicates the formation of CoS . The observed 'd' values well matched with standard 'd' values taken from JCPDS data card no.19-0364. Both these phases have hexagonal crystal structure. The XRD pattern confirms the formation of crystalline Cobalt sulphide thin film.

The observed average value of the crystallite size 'D' is calculated for predominant (222) plane using Scherer's formula [1].

$$D = \frac{0.9\lambda}{\beta \cos \theta}$$

Where, 0.9 is the Scherer's constant, ' λ ' is the wavelength of X-ray, ' β ' is the full-width

at half-maximum and ' θ ' is the diffraction angle. The observed crystallite size for (222) plane is around 12.26 nm. The presence of broad crystal diffraction peaks indicate that the thin film deposited on the substrate is of nano-size [7, 8]. Nanocrystalline thin films are of significant interest for a large variety of electronic and optoelectronic devices [9, 10].

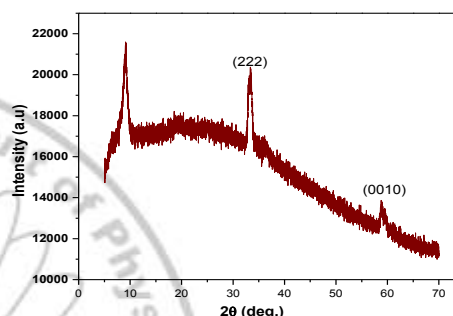


Fig. 1 XRD pattern of Cobalt sulphide thin film

4. Conclusion

Chemical bath deposition technique was suitable for the preparation of Cobalt sulphide thin film. The deposited peacock green coloured Cobalt sulphide thin film has hexagonal crystal structure.

Reference

1. B. D. Cullity, Elements of X-ray Diffraction, 2nd ed., Addison-Wesley Publishing Company, Reading, Massachusetts, USA (1978) 284.
2. F.C.Eze., C.E.Okeke, Mater Chem Phys. 47 (1997) 31-36.
3. F.Tao., Y.Q.Zhao., C.Q. Zhang., H.I. Li, Electrochem Commun.9 (2007) 1282.
4. C.N.R.Rao., K.P.R. Pisharody, Prog Solid State Chem 10 (1976) 2017.
5. A.Wold., K. Dwight (Eds), Solid State Chemistry, Chopman and Hall, New York (1993).
6. S.S.Gavande., A.L.Nivergikar., L.P.Deshmukh., Journal of Recent ant Innovation Trends in Computing and Communication 4 ,276-280 (2016).
7. Deshmukh L.P. and Mane S.T., Liquid Phase Chemical deposition of cobalt Sulphide Thin Films: Growth and properties, Digest J. Nano materials and Biostructures, 6, 931-936 (2011)
8. O.Oladeji and L.Chow., Thin Solid Film; 474, 77, (2005).
9. A.M.Popa., V.S.Lissa., M. Buda., E. Pentia, and T. Botila., J. Optoelectron. Adv Mater.8,(2006).
10. Deshmukh L.P. and Hollikatti S.G., A Cd:Sb photoelectrode for photoelectrochemical applications, J. Phys. D: Appl. Phys. 27, 1786-1790(1994).

Simple Co-precipitation Synthesis of Nanostructured Tin oxide as an Anode for Li-ion Rechargeable Batteries

Ramchandra S Kalubarme*, and Suresh Gosavi*

Centre for Advanced Studies in Material Science and Solid State Physics,
Department of Physics, Savitribai Phule Pune University, (Formerly University of Pune) Ganeshkhind, Pune -
411007, INDIA, Email: swg@physics.unipune.ac.in and ramkalubarme@yahoo.co.in

Abstract:

Transition metal oxides are widely used in energy storage applications. Nanostructured tin oxide particles are prepared by simple and controlled co-precipitation process. The microstructure of the prepared material confirms the formation of nanoparticles having tetragonal SnO₂ phase with cassiterite structure and size upto 10 nm. On testing, as anode for Li-ion battery, delivered reversible charge capacity of 957mAh g⁻¹ at applied current rate of 0.05 C. The tin oxide showed excellent rate performance displaying capacity of 527 mAh g⁻¹ at 10 C and capacity retention of 75 % after 50 cycles at applied current of 0.5C.

Introduction:

Increasing standards of living and rising population numbers are leading to inevitable increases in global energy consumption. Meeting our energy needs in an environmentally and geopolitically sustainable fashion is likely the most important technological challenge facing society today. However, the present technologies based on fossil fuel are either too limited in terms of resources, too inefficient and will deplete soon. On the other hand, renewable energy sources such as solar and wind have been widely used to generate electricity for green energy systems. These systems show huge potential for meeting the future energy demands [1-3]. However, the electricity generated from these renewable sources are intermittent, and efficient electrical energy storage (EES) devices are needed for effective delivery of uninterrupted electricity (power storage back up) and load leveling as well as grid energy storage [4-5].

Nowadays, Li-ion batteries have become a mainstay for EES [6-8]. To meet the requirements of these applications, further improvements in terms of energy power, densities and calendar life are required. In addition, increasing the specific capacity of Li-ion battery anodes is considered as an attractive route to improve energy density, reduced weight and volume with low cost. In recent years, metal oxides such as, SiO, GeO₂, Co₃O₄, Fe₂O₃, SnO₂, TiO₂, CuO and NiO have been explored as anode materials for Li-ion batteries due to their higher Li-ion storage capacities than commercial graphite anode [9]. However, conventional bulk electrode materials display their inherent limits in performance and unable to fully reach the increasing demands. Reaching such levels of performance will require the use of nanotechnology:

nanostructures enable efficient diffusion and efficient displacement reactions in batteries and can be used to produce multifunctional and hybrid materials that combine mixed electronic/ionic conduction. Hence in the present work, we report a simple and controlled approach to obtain fine tin oxide nanoparticles as anode for Li-ion batteries. The fine particles of tin oxide exhibited a high reversible capacity of 978mAh g⁻¹ at a 0.05 C rate and an excellent rate performance.

Experimental:

A facile and controlled co-precipitation process is employed to prepare fine tin oxide nanoparticles. In particular process, SnCl₄ and NaOH (Sigma Aldrich 99%) were used as received without further purification. The aqueous solutions of NaOH was added to the 0.5M solution of SnCl₄ and then stirred thoroughly to obtain white precipitate. The precipitate thus obtained was washed repeatedly for removal of Cl⁻ impurities and dried overnight in a vacuum oven at 80 °C.

The microstructure, surface morphology, and chemical composition of the synthesized materials were examined by a RIGAKU D/Max Ultima III high-resolution X-ray powder diffractometer (HR-XRD). The microstructure of the samples was observed using transmission electron microscopy (Tecnai G2, Philips). The test electrodes were prepared by casting a paste containing acetylene black, active material, and polyvinyl difluoride (PVDF) binder at 10:80:10 onto a Cu sheet current collector. A coin-type half cell (CR-2032) was assembled with Li metal as an anode, the test electrode containing the active material as a cathode, and 1M Lithium hexafluoride in Ethylene carbonate (EC)/ Dimethyl carbonate (1:1 v/v) as an electrolyte. The cyclic voltammograms for lithium

storage were obtained in the potential range of 0.05 V to 3.0 V versus Li/Li⁺ at a scan rate of 0.01 mV·s⁻¹. In addition, the galvanostatic discharge and charge test on the Li-ion half cells were conducted at an applied current of 0.05 C to 10 C.

Results and Discussion:

In the particular synthesis process, hydrolysis of the precursor used in the present work, i.e., SnCl₄·xH₂O, can easily occur in the presence of NaOH producing stannic hydroxide precipitate, further on annealing in air environment the decomposition of precipitate leading to the formation of stannic oxide (SnO₂). The morphology of the products was detected using TEM. Figure 1a-b shows a typical low and high magnification TEM image of the post-annealed sample. As illustrated, the sample consists of agglomerated uniform spherical particles with average diameters of 10 -20 nm. The particles observed by HR-

TEM for tin oxide sample was composed of numerous single crystals. Furthermore, from the HR-TEM images of the tin oxide sample, it can be seen that the uniform particle distribution is observed in the sample. Moreover, the crystal structure of the prepared powder was revealed by X-ray diffraction (XRD). Figure 1c shows XRD patterns of tin oxide sample prepared using co-precipitation followed by annealing process. For tin oxide powder samples the obtained high-intensity diffraction peaks were indexed to the tetragonal SnO₂ phase with a cassiterite structure (JCPDS 41-1445). No additional peak related to any other tin oxide phase or any other impurity, indicating the phase purity of the tin oxide powder sample. It is obvious that all of the typical peaks are broadened and are of low intensity, demonstrating that the size of the SnO₂ particles is very small.

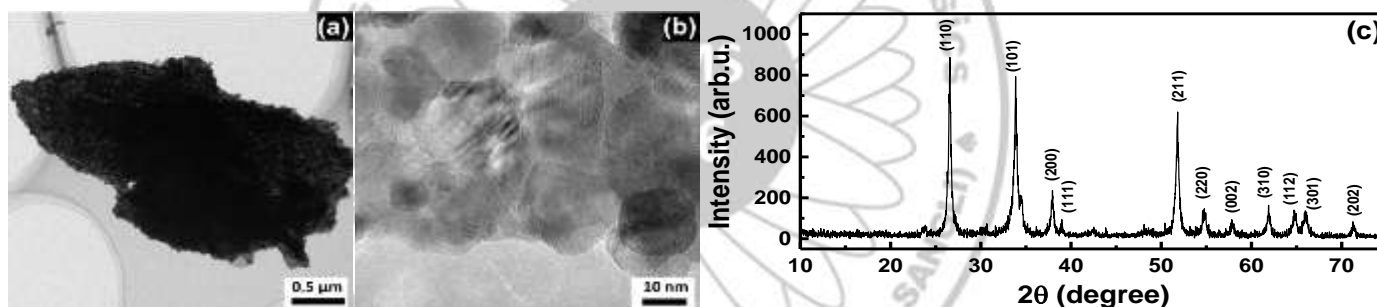


Figure 1. (a) TEM, (b) HR-TEM image and (c) XRD of tin oxide prepares using simple co-precipitation method.

The Lithium-storage capacity of the stannic oxide sample was estimated from galvanostatic discharge-charge measurements carried out at room temperature. The galvanostatic discharge-charge curves were recorded at the constant current rate of 0.05 C within the potential window of 0.01 – 3.0 V vs Li/Li⁺, as shown in Figure 2a. In the first discharge curve of stannic oxide, well-defined two slope regions were clearly observed: viz., region I, OCP to 0.9 V; region II and 0.9 to 0.01. A similar nature of the discharge curve was demonstrated by Zhou et al. for SnO₂ particles [10]. Accordingly, these two regions correspond to the following two different reactions. Region I is ascribed to the conversion reaction, in which reduction of SnO₂ to metallic Sn takes place forming Li₂O as shown in reaction (1) and region II can be assigned to the Li-Sn alloying reaction and the formation of a solid-

electrolyte interface (SEI) [11], as shown in reaction (2) [12].



In the consecutive charge curve two well defined regions were observed from 0.01 to 0.8 V and from 0.8 to 2.0 V. Herein, the low-potential region indicates the dealloying process of Li_xSn, while the reaction occurring at higher potential is ascribed to the reaction between Sn and Li₂O to regenerate SnO₂. Moreover, the discharge and charge capacities obtained for stannic oxide in the first cycle were 1511 and 957 mAh g⁻¹, respectively with conversion efficiency of 63%. The initial low Columbic efficiency could be attributed to the formation of a SEI layer in the first cycle.

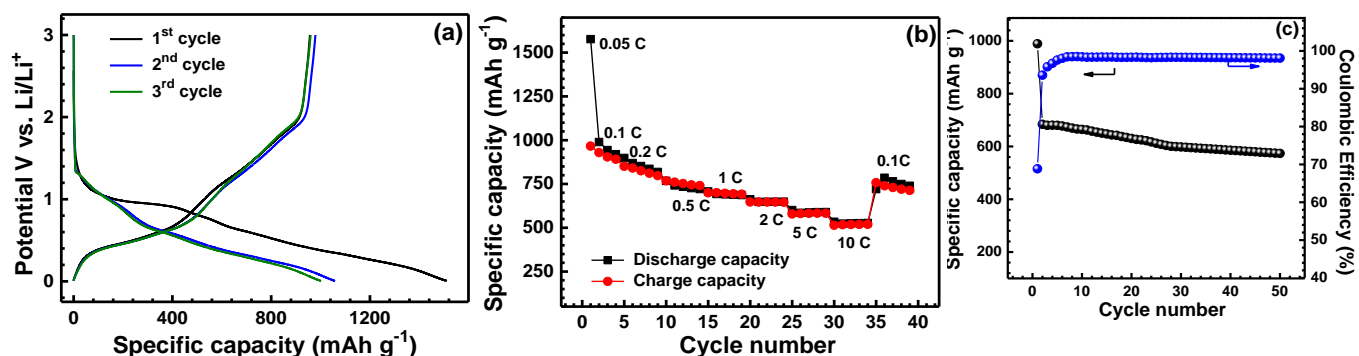


Figure 2. (a) Galvanostatic discharge-charge profile, (b) Rate performance and (c) Cycle- life of half-cell assembled using tin oxide powder.

To better understand the electrochemical behavior of stannic oxide sample under the various current rates, we also investigated their C-rate performances as shown in Figure 2b. The electrode was operated at various C-rates between 0.05 and 10 C. It can be clearly seen that the stannic oxide electrode shows excellent rate capability delivering a high reversible capacity of 527 mAh g^{-1} at 10 C. The capacity obtained for the stannic oxide electrode at a current rate of 10 C is higher than the theoretical capacity of currently used graphite electrode. More importantly, when the testing current returned to a lower current rate of 0.1 C, the discharge/charge capacities

recovered to the same levels that were initially shown at that particular rate. In order to further investigate the effect of high current rate on the long-range cyclability of the stannic oxide, we further evaluated the cyclability of the electrodes at a high current rate of 0.5 C for 50 cycles as shown in Figure 2c. It can be clearly seen that the prepared material show high reversible capacity of 684 mAh g^{-1} for first cycle and good cyclability up to 50 cycles with specific capacity 573 mAh g^{-1} , which is almost 75% of the specific capacity achieved at first cycle. This excellent electrochemical performance of stannic oxide shows its promising applications as an anode material for lithium ion batteries.

Conclusions:

This paper describes a simple co-precipitation method for synthesis of fine nanopartcles of stannic oxide as anode materials for lithium ion batteries. The as-prepared stannic oxide delivered high reversible lithium storage capacity of 957 mAh g^{-1} and displayed enhanced rate capacity of 527 mAh g^{-1} at a high current density of 10 C. Good capacity retention performance was also observed for the fine stannic oxide nanoparticles electrode after 50 cycles at the current density of 0.5 C, maintaining the specific capacity of 573 mAh g^{-1} .

Acknowledgement: RSK would like to thank the University Grants Commission, New Delhi, for the awarding of the D. S. Kothari Post-Doctoral Fellowship (F.4-2/2006 (BSR)/PH/14-15/0132)

References:

1. S. Linic, P. Christopher, D.B. Ingram, *Nat. Mater.* 2011, 10, 911.
2. Y. Zhou, P. Luckow, S.J. Smith, L. Clarke, *Environ. Sci. Technol.* 2012, 46, 7857.
3. M. Kaltenbrunner, M.S. White, E.D. Głowacki, T. Sekitani, T. Someya, N. Serdar Sariciftci, Siegfried Bauer, *Nat. Commun.* 2012, 3, 770.
4. G. Dennler, M.C. Scharber, C.J. Brabec, *Adv. Mater.* 2009, 21, 1323.
5. T. Ackermann, L. Soder, *Renew. Sust. Energ. Rev.* 2002, 6, 67.
6. J.M. Tarascon, M. Armand, *Nature* 2001, 414, 359.
7. K. Kang, Y.S. Meng, J. Bréger, C.P. Grey, G. Ceder, *Science* 2006, 311, 977.
8. M. Ge, J. Rong, X. Fang, C. Zhou, *NanoLett.* 2012, 12, 2318.
9. M. V. Reddy, G. V. Subba Rao, and B. V. R. Chowdari, *Chem. Rev.* 2013, 113, 5364.
10. J. Yang, L. Xi, J. Tang, F. Chen, L. Wu, X. Zhou, *Electrochim. Acta* 2016, 217, 274.
11. I.A. Courtney, J.R. Dahn, *J. Electrochem. Soc.* 1997, 144, 2045.
12. F. Wang, H. Jiao, E. He, S. Yang, Y. Chen, M. Zhao, X. Song, *J. Power Sources*, 2016, 326, 78.

Microstructural and Morphological study of SnO₂ nanoparticles

C. B. Mane^{a*}, R. P. Pawar^b, D. D. Gaikwad^c, R. V. Khobare^c, A. P. Tayade^c, K. D. Warad^c

^aDepartment of Chemistry, Shri. Vijaysinha Yadav College of Arts and Science, Peth Vadgaon, ^bDepartment of Chemistry, Govt. Vidarbha Institute of Science and Humanities, Amravati, ^cGovernment College of Arts and Science, Aurangabad, Maharashtra (India).

*Corresponding author-Chandrakant B. Mane, E-mail: cbmane007@gmail.com

Abstract

The present work involves the study of tin oxide nanoparticles by a simple micro wave assisted sol-gel method by studying growth, microstructure and morphology. The characterization of SnO₂ nanoparticles was carried out by X-ray Diffraction to investigate the phase structure. The optical study was carried out by using UV Visible absorption spectroscopy. The surface morphology and nanostructure properties of the same sample were observed by scanning electron microscopy (SEM) and transmission electron microscopy (TEM). Different parameters like pH of the solution, temperature of substrate, deposition time, annealing etc. were carefully monitor to decide the optimized growth condition of the tin oxide nanoparticles.

Key words: Microstructural, Morphological.

1. Introduction

In metal oxides, tin oxide is an important n-type semiconductor material with wide band gap ($E_g = 3.6$ eV). Because of its unique electronic, optical, electrochemical and catalytic properties, tin oxide were extensively used in number of applications such as catalytic agent [1,2], heat reflecting mirrors[3,4], gas sensors[5,6] solar cell, transparent conducting electrodes, soiled-state sensors, rechargeable Li batteries and optoelectronic devices [7] etc. Many methods have previously used for synthesis of tin oxide. Naze et al [8] have synthesized Tin Oxide (SnO₂) nanoparticles by chemical precipitation method. Tetragonal phase SnO₂ nanocrystals were synthesized via facile solvothermal process by using SnCl₄.5H₂O and HCl at different temperature. by Anandan et al.[9], Zhang et al [10] have synthesized nanostructured tin oxide using a sol-gel process based on tin tetrachloride and ethylene glycol. Furthermore Patil et al [11] also have previously reported Preparation and Characterization of SnO₂ Nanoparticles by Hydrothermal Route. Krishnakumar et.al [12] successfully prepared SnO₂ nanoparticle (39 nm) by simple chemical method. The nanocrystalline SnO₂ material was having better humidity sensing property towards moisture, when compared with bulk SnO₂ material. Thus, synthesis and applications of SnO₂ nanomaterials encourages researchers and can be exposed new accesses in the research and development.

Tin oxide nanoparticles have attracted considerable attention due to their unique properties, which are not present in bulk materials. In this investigation, we synthesize tin oxide nanoparticles by a simple micro wave assisted sol-gel method. The raw materials used for present study are very cheap and the SnO₂ particles obtained are in the nanometer scale with very high surface area. The particles have been characterized by means of XRD, UV-Vis, FTIR, SEM and TEM.

2. Experimental

All the chemicals are of analytical grade about 2.2565 g of SnCl₄ 2H₂O is dissolved in 100 ml Distilled water. 30 ml of above solution is taken in 250 ml Beaker and 45 ml 1M ammonia solution was added dropwise with constant stirring till precipitation completed and gel is formed. Then the solution was kept in (800 W EO-77 HORNO ELECTRICO, ORBIT) microwave oven at 80⁰c for 30 min. The resulting gel was filtered through Whatmann filter paper No. 40 then it is dried at 80⁰c for 24 Hrs in order to remove moisture or water molecule present in it. Then the precipitate obtained collected in silica crucible and calcination was carried out at 550⁰c for 2 hrs finally ash colored tin oxide nanoparticles were formed.

3. Result and Discussion

Fig. 1 shows that X-ray diffraction pattern of SnO₂ nanoparticles. The observed 'd' values of the film were in good agreement with those reported in the JCPDs data file for SnO₂ (88-0287), possessing tetragonal crystal structure. Furthermore it is

observed that presence of more than one peak shows polycrystalline nature of SnO₂ sample. It is seen from the figure that the SnO₂ film exhibited the orientations along (110), (101), (200), (211), (220), (002), (310), (112), (310), (202) and (321) planes corresponding to their diffraction angle. The XRD peak intensity of (110) plane was relatively higher than those of other reflections.

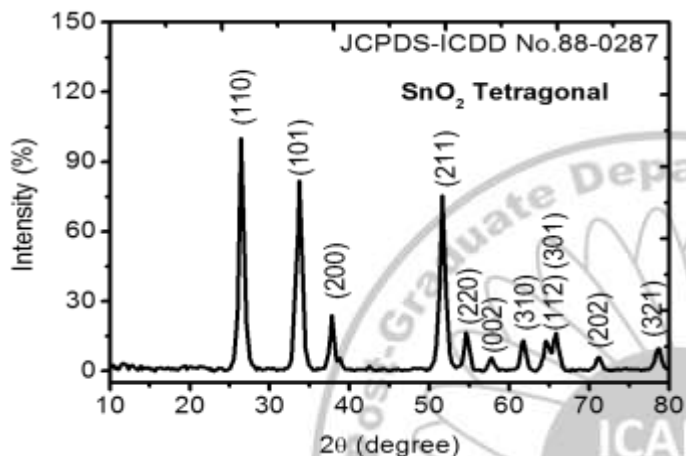


Fig. 1 X-ray diffraction pattern of SnO₂ nanoparticles.

The absorption spectra of the SnO₂ sample was studied at room temperature without taking into consideration reflection and transmission losses. The spectrum in figure 2 shows that SnO₂ sample has low absorbance in the IR region (275 nm = 4.51 eV) of the solar spectrum. The absorption data were analyzed and the band gap was estimated using Tauc's relationship between the absorption coefficient (α) and the photon energy ($h\nu$)

$$\alpha h\nu = E_D (h\nu - E_g)^{1/2}$$

Where E_g is the direct band gap, and E_D is a constant. The band gap can be determined by fitting the absorption data to the direct transition equation by extrapolating the linear portions of the curves to absorption equal to zero.

FT-IR study was performed to identify the presence of any water bending or stretching vibrations in the synthesized compound. Figure 3 shows that FT-IR spectrum of SnO₂ nanoparticles. The small broad absorption peak observed at 3100–3600 cm⁻¹ is assigned to the fundamental stretching vibrations of hydroxyl groups (free or bonded). The absorption band 1511 cm⁻¹ is caused by the bending vibration of

coordinated H₂O as well as Sn–OH [18]. The strong peak located at around 550–700 cm⁻¹ is likely due to the vibration of Sn–O bond [18] in SnO₂ lattice. Thus, the FT-IR spectrum confirmed the presence of Sn–O bonds and OH groups in the SnO₂ nanoparticles.

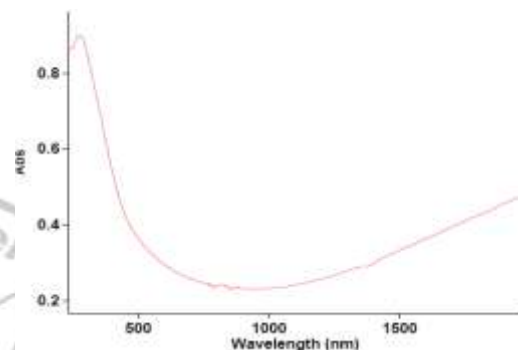


Fig. 2. UV-Vis absorption spectra of the SnO₂ nanoparticles

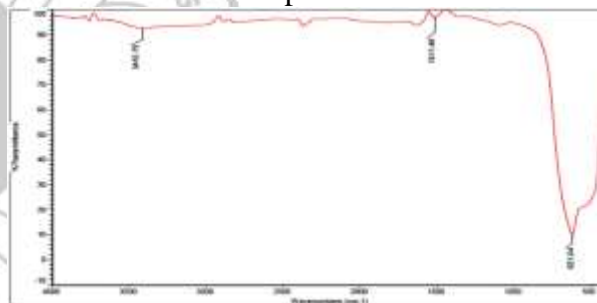


Fig. 3 shows that FT-IR spectrum of SnO₂ nanoparticles

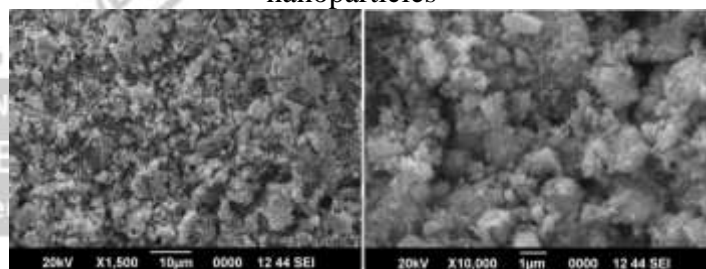


Fig. 4. SEM images of SnO₂ powder at different magnification

SEM analysis was performed to reveal morphological features of the sample. SEM micrograph of SnO₂ powder sample is shown in figure 4. It shows a homogeneous and uniform distribution of SnO₂ microparticles with good porous features. The well dispersed SnO₂ microparticles provides easy path for the gas absorption.

Fig. 5(a-c) shows that TEM, HRTEM and SAED images of SnO₂ sample. Fig. 5a displays the interconnected spherical nanoparticles with size in the range 20-60 nm. Spherical nanoparticles offer high surface area for gas interaction. Figure 5b shows HRTEM image of SnO₂ sample. It consist of a group of parallel fringes with d spacing of 0.324

nm and 0.264 which match well with d value of the (110) and (101) planes often tetragonal crystal structure of SnO₂ supported by two strong peaks given in the XRD. Thus result shows that the formation of SnO₂ with tetragonal crystal structure. Figure 5c shows SAED pattern of SnO₂ sample confirming polycrystalline structure.

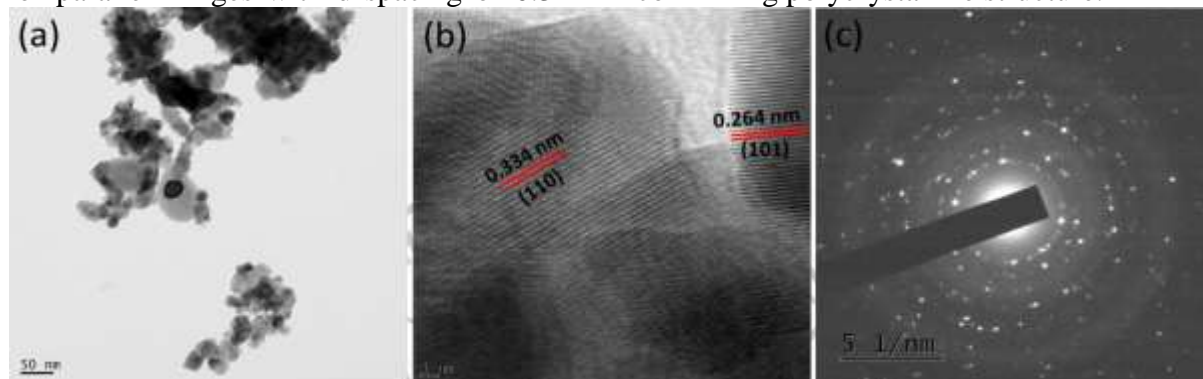


Fig. 5. (a) TEM image (b) HRTEM image of SnO₂ sample, (c) SAED pattern of SnO₂ sample

Conclusion

The well dispersed SnO₂ nanoparticles have been synthesized by microwave assisted sol-gel method annealed at 550⁰C. At high temperatures, small grains tend to agglomerate into large entities, decreasing both surface areas and catalytic properties of the material. The X-ray diffraction investigations showed that pure SnO₂ nanoparticles possessing tetragonal crystal structure. Furthermore it is observed that presence of more than one peak shows polycrystalline nature of SnO₂ sample. The FT-IR spectrum confirmed the presence of Sn-O bonds and OH groups in the SnO₂ nanoparticles. SEM micrograph of SnO₂ sample shows a homogeneous and uniform distribution of SnO₂ microparticles with good porous features. TEM image displays the interconnected spherical nanoparticles with size in the range 20-60 nm. HRTEM image of SnO₂ sample consist of a group of parallel fringes with d spacing of 0.324 nm and 0.264. SAED pattern of SnO₂ sample confirming polycrystalline structure. The well dispersed SnO₂ microparticles provide easy path for the gas absorption.

References

1. L. Chou, Y. Cai, B. Zhang, J. Niu, S. Ji, S. Li, Appl. Catal. A: Gen. 238 (2003) 185.
2. P.T. Wierzchowski, L.W. Zatorski, Appl. Catal. B: Environ. 1352 (2003) 1.
3. M. Kojima, F. Takahashi, K. Kinoshita, T. Nishibe, Ichidate, Thin Solid Films 392 (2001) 349
4. C.M. Lampert, Sol. Ener. Mater. 6 (1981) 1.
5. A.J. Moulson, J.M. Herbert, Electroceramics, Chapman & Hall, New York, (1990).
6. Y. Shimizu, M. Egashira, MRS Bull. 24 (1999) 18.
7. K. Anandan, S. Gnanam, J. Gajendiran, V. Rajendran "Effect of temperature on SnO₂ nanoparticles-facile solvothermal synthesis and characterization", (NCMNN)-49, pp. 26, 2010.
8. Asama. N. Naje, Azhar S.Norry, Abdulla. M. Suhail, Preparation and Characterization of SnO₂ Nanoparticles IJIRSET, Vol. 2, Issue 12, p-7068-7072, 2013.
9. K. Anandan, V. Rajendran, Size Controlled Synthesis of SnO₂ Nanoparticles facile solvothermal process, Journal of Non-Oxide Glasses Vol. 2, No 2, p. 83 – 89, 2010.
10. G. Zhang, M. Liu, Preparation of nanostructured tin oxide using a sol-gel process based on tin tetrachloride and ethylene glycol, Journal of Materials Science 34, p3213 – 3219, 1999
11. Ganesh E. Patil a, Dnyaneshwar D. Kajale a, Vishwas B. Gaikwad b, Gotan H. Jain, Preparation and Characterization of SnO₂ Nanoparticles by Hydrothermal Route Int. Nano Lett., Vol. 2, No. 1, pp. 46-51, 2012.
12. T.Krishnakumar1,a, R. Jayaprakash1,b, V.N. Singh2,c and B.R. Mehta2,d A. R. Phani Synthesis and characterization of tin oxide nanoparticle for humidity sensor applications, Journal of Nano Research Vol. 4 pp 91-101,2008.

Effect of sintering temperature on structural and dielectric properties of $\text{Ba}_{0.7}\text{Ca}_{0.3}\text{TiO}_3$ ceramic sintered by microwave technique

Sagar M. Mane^{1,2}, Chandrakant B. Kolekar², Shrinivas B. Kulkarni^{1*}

¹ Department Of Physics, The Institute Of Science, Mumbai-400032, India.

² Department Of Physics, Sahakar Maharshi Shankarrao Mohite-Patil Mahavidyalaya, Natepute, Solapur- 413109, India.

Abstract:

$(\text{Ba}_{0.7}\text{Ca}_{0.3})\text{TiO}_3$ lead free ceramics were synthesized by coprecipitation method and sintered by fast microwave sintering at 1100°C and 1200°C keeping different soaking time. After being sintered at two different temperatures for different time the material was characterized for structural, microstructural, frequency and temperature dependent dielectric properties, and ferroelectric measurements. X-ray diffraction confirms presence of the tetragonal and orthorhombic phases in as sintered ceramic sample. SEM images show the well structured grains with uniform grain size. Shifting in the transition temperature was observed in the ceramic sample.

Introduction:

Barium titanate (BaTiO_3 or BT)-based materials have been extensively studied for their interesting electrical properties like high dielectric constant, low dielectric loss, ferroelectric, piezoelectric and pyroelectric behavior. Among the dielectric ferroelectric perovskite oxides, BT was used most for electrical and electronic applications, in the years immediately after its discovery. Perovskite oxides derived from BT have a wide range of applications in electronic appliances, such as positive temperature coefficient devices, pulse generating devices, infrared detectors, voltage tunable devices in microwave electronics, multilayer ceramic capacitors, actuators, and lead-free piezoelectric transducers, and charge storage devices [1]. Doping is an effective way to improve the electrical performance of electroceramics [2]. For instance, barium zirconium titanate $\text{Ba}(\text{Zr,Ti})\text{O}_3$ [BZT], and barium calcium titanate $(\text{Ba,Ca})\text{TiO}_3$ [BCT] [3-4] are widely used in electrical material applications.

BCT solid solutions are specifically used in multilayer ceramic capacitor applications and in various other applications like: dielectric filters, antennas, resonators, duplexers and phase shifters, and piezoelectric actuators [4]. Ca^{2+} can occupy either Ba^{2+} site or Ti^{4+} site in BaTiO_3 lattice. Ca^{2+} substitution in the Ti^{4+} site requires charge compensation by creating oxygen vacancies in $\text{Ba}(\text{Ca}_x\text{Ti}_{1-x})\text{O}_3$. On the other hand the microwave sintering technique is superior than conventional sintering (CS) due to its unique characteristics, such as rapid heating, enhanced densification rate and

improved microstructure. In the microwave process, the heat is generated internally within the material instead of originating from external sources, and hence there is an inverse heating profile. The heating is very rapid as the material is heated by energy conversion rather than by energy transfer, which occurs in conventional techniques [5]. The present paper reports on the synthesis of $(\text{Ba}_{0.7}\text{Ca}_{0.3})\text{TiO}_3$ via hydroxide coprecipitation method following sintering with the fast microwave sintering technique. The effect of the fast microwave sintering technique with increasing temperature on the structural, microstructural, dielectric, ferroelectric and properties are investigated and reported in the present study.

Experimental:

Powder samples of $(\text{Ba}_{0.7}\text{Ca}_{0.3})\text{TiO}_3$ was synthesized by using coprecipitation method. For synthesizing this powders stoichiometric amounts of barium nitrate $\text{Ba}(\text{NO}_3)_2$, calcium nitrate $\text{Ca}(\text{NO}_3)_2 \cdot 4\text{H}_2\text{O}$, and potassium titanium oxalate $\text{K}_2\text{TiO}(\text{C}_2\text{O}_4)_4 \cdot 2\text{H}_2\text{O}$ of purity 99.9 % are used as starting materials. KOH is used as a precipitating agent for complete precipitation of $\text{Ba}(\text{OH})_2$ and $\text{TiO}(\text{OH})_2$, the procedure of synthesis is as reported earlier [5]. In each stage of precipitation the pH of solution was maintained above 10. The obtained precipitate of BCT was dried and grinded for 4–5 hours to make a fine powder, then calcinated at 1000°C for 4 hours. This calcinated powder sample was pressed by using hydraulic press; the pressure was maintained at about 5 tons to get the material in a disk shape of 1 cm diameter and about 2 mm thickness. Pressed disks (pellets) and remaining

powder sample were sintered at 1100°C and 1200°C using fast microwave sintering for 30 and 20 min respectively. Programmable microwave furnace with 1.3 KW, 2.45 GHz and thermally insulated chamber which prevent heat loss was used for this purpose.

Results and Discussion

Structural analysis of BCT

After sintering through the microwave sintering technique at 1100°C and 1200°C powder samples of BCT are characterized for structural analysis with x-ray diffraction. For structural analysis the sample was scanned at 2θ scale between 20° to 80° at room temperature while the scan rate was maintained at 3°/min. Figure 1 shows the diffraction pattern of Ba_{0.7}Ca_{0.3}TiO₃ (BCT) sintered at 1100°C and 1200°C. BCT is a perovskite ceramic, which is a solid solution of BaTiO₃ and CaTiO₃. At room temperature BaTiO₃ exhibits a tetragonal crystal structure while CaTiO₃ reveal orthorhombic structure [6]. Tetragonal peaks in the BCT ceramic are more and are in good agreement with JCPDS 81-1288, while orthorhombic peaks corresponding to CaTiO₃ are indexed according with Table 1. Lattice parameters, c/a ratio, unit cell volume and crystallite size of Ba_{0.7}Ca_{0.3}TiO₃ sintered at different temperature.

JCPDS data card 75-2100. Calculated lattice parameters, tetragonal distortion ratio and volume of unit cell with average crystallite size measured from the highest intense peak of both the ceramic samples sintered at different temperatures are listed in table 1.

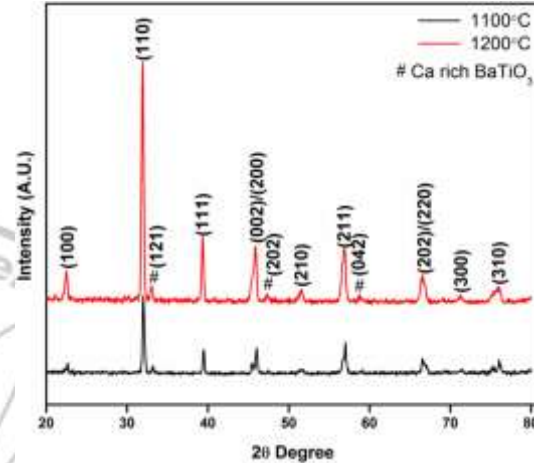


Figure 1 Room temperature x-ray diffraction pattern of Ba_{0.7}Ca_{0.3}TiO₃ sintered at 1100°C and 1200°C

Sintering Temperature and Time	Lattice parameters			Volume of Unit Cell (a ² c)	Crystallite size nm
	a(Å)	c(Å)	c/a ratio		
1100 deg 30 min	3.9256	4.001	1.0192	63.87	35.56
1200 deg 20 min	3.9487	4.002	1.0134	63.98	38.33

The highest intensity peak or most prominent peak of tetragonal side is 110 while peak indexed as 121 is the most prominent peak of the orthorhombic system and this peaks are almost coincide each other. Peak intensity of the ceramic sample sintered at 1200°C is more which confirms the well diffusion of Ca²⁺ ions in BT matrix. From the diffraction pattern the average crystallite size was estimated using the Debye-Scherrer equation as,

$$D = \frac{0.9\lambda}{\beta \cos \theta} \dots (1)$$

It could be seen that the crystallite size increases with increase in the temperature on the

other hand the tetragonal distortion ratio (c/a) slightly decreases. This may resulted as; with increase in temperature partial incorporation of Ca²⁺ ions occurs at barium site.

2. Morphological Analysis and EDAX

Figure 2 (a) and (b) show the scanning electron microscope images of Ba_{0.7}Ca_{0.3}TiO₃ sintered at 1100 deg and 1200 deg respectively. Backscattered microstructural images were collected by using scanning electron microscope with energy dispersive spectrometer (JEOL JSM 6390). Figures reveals that sintered ceramics at different temperatures are very dense, grains are uniform void free and with increase in temperature the grain size increases. Fast microwave sintering technique,

which heats the surface of the material body from inside and heats all the area in equal magnitude results in more uniformity of the grains. Uniform grain structure of microwave sintered ceramic sample results in enhancement of electrical and physical properties of ceramic material. The

presence of all the elements in stoichiometric proportion is confirmed by using Energy Dispersive Spectrometry (EDAX) study of $Ba_{0.7}Ca_{0.3}TiO_3$. Figure 2 (c) shows the EDAX spectra of BCT sintered at 1200°C.

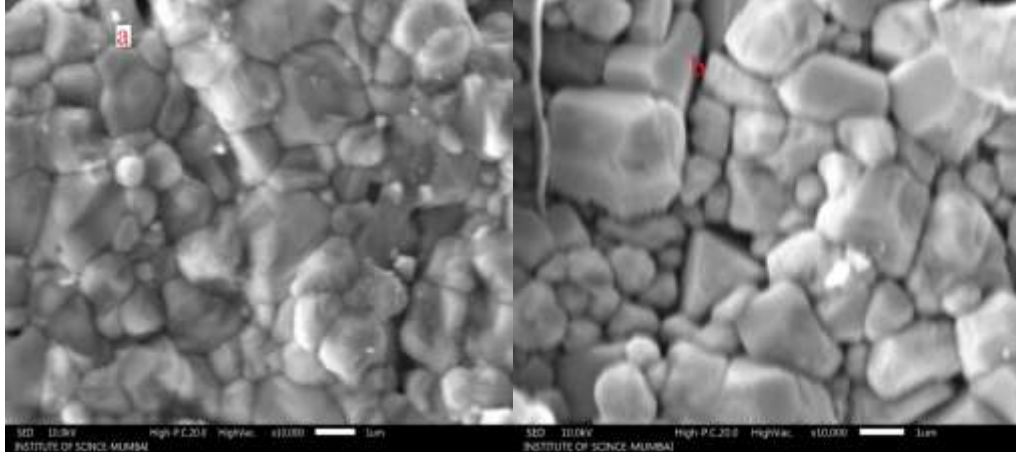


Figure 2 Scanning electron microscope images of $Ba_{0.7}Ca_{0.3}TiO_3$ ceramic sintered at different temperature (a) 1100°C and (b) 1200°C

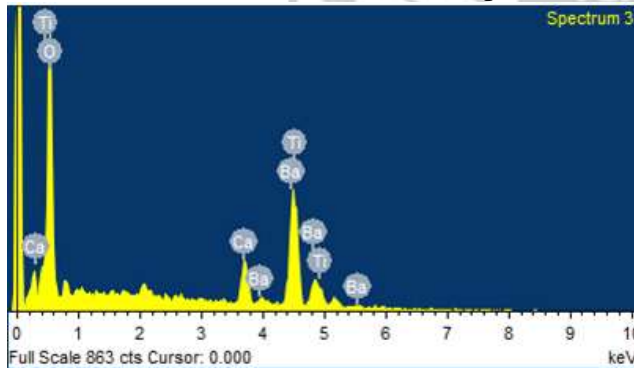


Figure 2 (c) Energy dispersive spectra (EDS) of $Ba_{0.7}Ca_{0.3}TiO_3$ ceramic sintered 1200°C

3. Frequency Dependant Dielectric Measurement

Room temperature variation of dielectric constant with varying frequency of $Ba_{0.7}Ca_{0.3}TiO_3$ sintered at 1100°C and 1200°C is shown in figure 3 (a) and (b) respectively, loss tangent with variation of frequency is also incorporated in figure. The dielectric constant and dielectric loss tangent was measured from frequency range between 100 Hz to 1 MHz Ceramic sintered at both temperatures shows the similar kind of variation with frequency. Both ceramic sample posses high dielectric constant at lower frequency and dielectric loss tangent is also has a high value. At lower frequency dielectric constant decreases

rapidly and remains constant at higher frequency, while the loss tangent also shows similar kind of nature analogous to dielectric constant. Contribution of the different types of polarization i.e. interfacial, space charge, dipolar, electronic, and ionic polarization leads to the dielectric dispersion of ferroelectric materials [5]. Rapid dielectric dispersion at lower frequency is due the contribution of interfacial polarization. This type of polarization is resulted due to the inhomogeneous structures of the materials. At higher frequency the dielectric constant does not follow the applied alternating field and results in constant behaviour. It could be seen that the value of dielectric constant of ceramic sample sintered at 1200°C is larger, and posses low dielectric loss value as compared to ceramic sample sintered at 1100°C. Sintering at higher temperature increases the more diffusion of Ca^{2+} ions which results in higher densification of sample, higher density results in more improved electrical properties. At lower frequency the loss is higher and loss tangent value decreases with increase in frequency, which normal characteristic property of ferroelectric material.

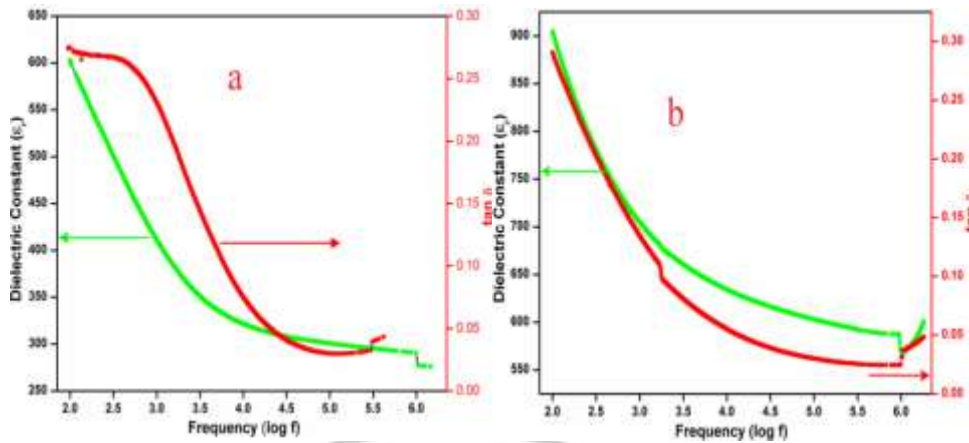


Figure 3 Variation of dielectric constant and loss tangent with frequency of $Ba_{0.7}Ca_{0.3}TiO_3$ sintered at (a) $1100^\circ C$ and (b) $1200^\circ C$

Conclusion

Lead free $Ba_{0.7}Ca_{0.3}TiO_3$ ceramic sample was synthesized by coprecipitation method. As synthesized, ceramic sample were sintered with the fast microwave sintering at different temperature. Microwave sintering technique found to be more important and effective technique over the conventional heating technique for the ceramic materials, where high sintering temperature is required for formation of required material. X-ray analysis confirms room temperature $BaTiO_3$ exhibits a tetragonal crystal structure while $CaTiO_3$ reveal orthorhombic structure. It could be seen that the value of dielectric constant of ceramic sample sintered at $1200^\circ C$ is larger, and possess low dielectric loss value as compared to ceramic sample sintered at $1100^\circ C$.

References

1. Venkata Sreenivas Puli, R. Martinez V, Ashok Kumar, J.F. Scott, Ram S. Katiyar, Mater. Res. Bull. 46 (2011) 2527–2530.
2. Z. Yu, C. Ang, R. Guo, A.S. Bhalla, J. Appl. Phys. 92 (2002) 1489.
3. A. Dixit, S.B. Majumder, A. Savvinov, R.S. Katiyar, R. Guo, A.S. Bhalla, Mater. Lett. 56 (2002) 933–940.
4. Liang-Yu Li, Xin-Gui Tang, Mater. Chem. Phys. 115 (2009) 507–511.
5. S.M. Mane, P.M. Tiramali, D. J. Salunkhe, P.B. Joshi, C.B. Kolekar, S.B. Kulkarni, J Mater Sci: Mater Electron 27(7) (2016) 7204-7210.
6. Venkata Sreenivas Puli, Dhiren K. Pradhan, Brian C. Riggs, Douglas B. Chrisey, Ram S. Katiyar Journal of Alloys and Compounds 584 (2014) 369–373.

INTERNATIONAL CONFERENCE ON
ADVANCES IN MATERIALS SCIENCE
7–8 December 2016

Ultrasonic Distance Measurement Using Microcontroller 8051

Ramesh M. Bandgar

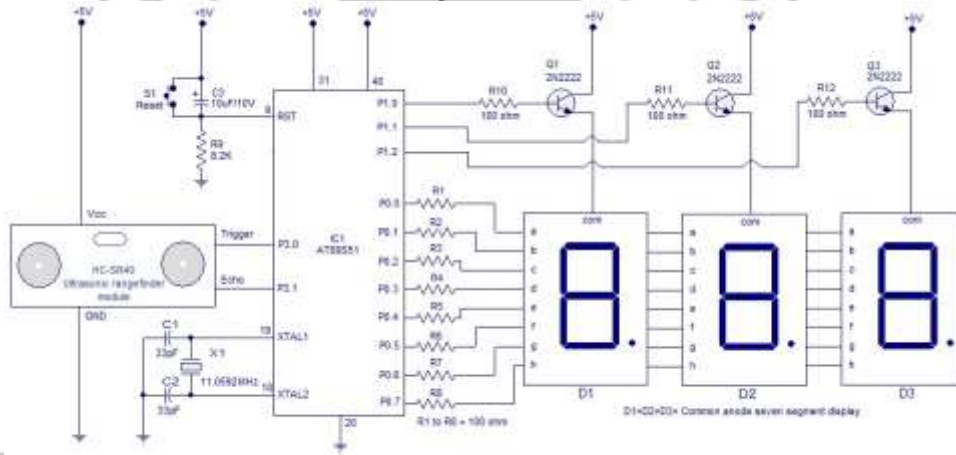
School of Physical Sciences, Solapur University, Solapur.

physicsstudentramesh@gmail.com

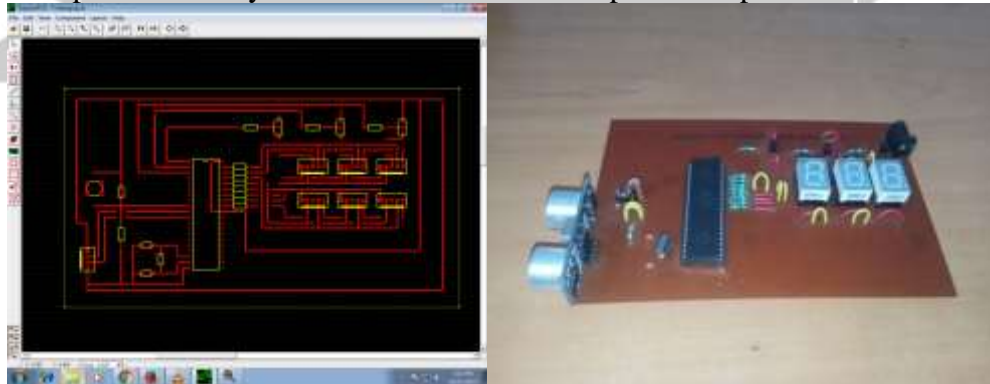
Abstract—

Now a day, we have some difficulties in obtaining the distance that we want to measure. Even though, measuring tape is an easy option, but this kind of tool will have a limitation of manual error. Before this, researcher have produced a range finder module but in the end, they find out the module have many disadvantages like limitation for distance, different result for different coloured obstacles, and need a calibration for every time before starts using it. Manual distance measuring is always done at the expense of human error. Precise and fix measurement of low range distance, is the main objective for this project. This device can measure distance in the range of 2cm to 400cm with the accuracy of 1cm. This project is used to measure the distance by using ultrasonic sensors. It works by transmitting ultrasonic waves at 40 kHz. Then, the transducers will measure the amount of time taken for a pulse of sound travel to a particular surfaces and return as the reflected echo. After that, the circuit that have been programmed with AT mega microcontroller will calculate the distance based on the speed of sound at room temperature which an atmospheric temperature and also the time taken. The distance then will be display on a 7 Segments LED. The importance of the project is calculating accurate distance from any obstacle that we want to measure. The device can be used in many different fields and categories like distance calculation in construction field, robots, car sensor to avoid obstacles and many other applications. The building process of the device was based on using as much as possible from the courses taken in the university, like Micro Processor, Basic Electrical Engineering, Multimedia and systems and Electronics Devices and also practical work in the laboratories.

Block Diagram of ultrasonic distance measurement using module & controller.



Express PCB Layout Screenshot and Component Implemented Circuit



Experimental Arrangement With Accurate Distance Measurement

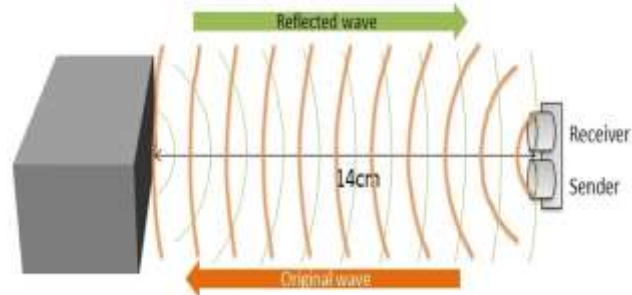


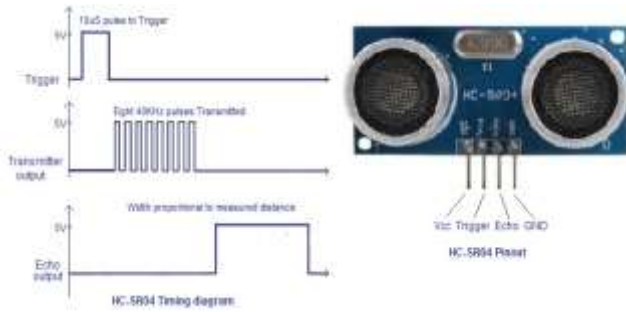
How does it works ?

The first part of the program sets the initial conditions. Port 0 and Port 1 are set as output ports for sending digit drive patterns and digit drive signals respectively. Port pin 3.0 is set as an output pin for sending the trigger signal to the ultrasonic module for starting transmission and port pin 3.1 is set as an input pin for receiving the echo. TMOD register of the microcontroller is so loaded that the Timer 1 operates in mode2, 8 bit auto-reload mode. Timer 0 of the microcontroller is not used here. In the next part of the program (loop MAIN) the TL1 and TH1 registers of Timer1 are loaded with the initial values. TL1 is loaded with the initial value to start counting from and TH1 is loaded with the reload value. This is how timer 1 in mode 2 works: When TR1 bit of the TCON register is set the TL1 starts counting from the initial value loaded into it and keeps counting until roll over (ie; 255D). When roll over occurs, TF1 flag is set and TL1 is automatically loaded with the reload value stored in TH1 and the sequence is repeated until TR1 is made low by the program. The TF1 goes high at the first roll over and if you want it as an indicator for each roll over, you have to clear it using the program after each roll over. In the next part of the MAIN loop P3.0 is set high for 10uS and then cleared to make 10uS triggering pulse. The ultrasonic module issues a 40Khz pulse wave form after receiving this trigger and the program waits until a valid echo is received at P3.1. The pulse width of the echo signal is proportional to the distance to the obstacle and so the next job of the program is to measure the pulse width. Whenever there is a valid echo pulse at P3.1, the Timer1 starts and it counts from the initial value to 255 ie: 255-

207= 48 counts. Then the counter restarts and accumulator increments by one for every restart. This sequence is repeated until the echo signal at P3.1 vanishes (ie; P3.1 goes low). Now the content in A will be equal to the number of Timer1 reloads which is in fact proportional to the distance. From the datasheet it is clear that 58uS echo pulse width indicates 1cm distance. When the processor is clocked by a 12MHz crystal, 58 counts of Timer1 indicates 1cm. That means 1 reload is equal to 1cm. But here we are letting the Timer1 to count only 48 times before reload and this is done in order to compensate for the time lags caused by the branching instructions used for checking the status of P3.0 and P3.1 pins. If this trick is not done, the individual time lags caused by the branching instructions will be cumulatively added to the observed pulse width and the range finder will show a reading higher than the original distance. Some trial and error was required for getting the correct Timer1 reload value and with the 207D (ie; 48 counts) used here the error was found to be less than half a Centi meter which is quite fine in this context. The next part of the program does necessary mathematics on the current content in A and displays it as 3 digit readout on the display.

How does works HC-SR04 Ultrasonic Module?





Ultrasonic sensor HC-SR04 is used here to measure distance in range of 2cm to 400cm with accuracy of 3mm. The sensor module consists of ultrasonic transmitter, receiver and control circuit. The calculation part of the ultrasonic module is as follows. The principle behind ultrasonic distance measurement is that the sensor sends an ultrasonic wave that reflects once it is met by an object on its path. As the wave bounces off, it travels back to the receiver end of the sensor. The sensor measures the time it takes for the emitted wave to travel from a sender to the object and back to the receiver. Knowing the round-trip travel times and the speeds of the wave in the medium, ultrasonic devices calculate the distance that the sound traveled. Use the following equation to calculate the speed of sound. High Level Signal is sent for 10µs using trigger. The module sends eight cycle of 40KHz signals automatically, and then detects whether pulse is received or not. If the signal is received, then it is through high level. Then the time of high duration is the Time gap between sending and receiving the signals. Distance = elapsed time x speed of sound/2

$$\text{Distance} = (\text{time} \times \text{speed of ultrasonic sound}) / 2$$

Hence, the distance between the sensor and the object is one-half the distance traveled by the sound wave.

Applications

1. This system can be used to measure the distance of target objects or material through the air using non contact technology.
2. They measure distance without damage and are easy to use reliable.

3. This project uses Ultrasound to measure distance. Measured distance is displayed on seven segments LED.

4. We can use this digital output data in making many interesting projects such as accident proof vehicles or robots, object identifier, **SONAR** (**SO**und **N**avigation **A**nd **R**anging) detection of objects under water. This system works similar to **RADAR** (**R**adio **D**etection **A**nd **R**anging)

Future Scopes

1. There is lot of scope for this system.
2. To detecting UFOs (Unidentified Flying Objects).
3. It can be large amount of use in medical research field.
4. To detect water level and under water some natural elements as well as measure sea depth, The system is known as SONAR.

Conclusions

1. It is a successfully working system. It can be used for the distance measurement.
2. It can be used in so many industrial and research as well as military purposes.
3. To detecting, locating position and counting its range.
4. The system is much advanced but it has limitation.

References:

- <http://www.8051projects.net>
- <http://www.electronicshub.com>
- <http://www.Engineersgarege.com>
- <http://www.Alldatasheet.com>

Acknowledgement:

I am deeply obligate to the people without whose sincere help and co-operation during the period of this project work would not have taken its present form.

I wish to thank our project guide **Dr. S.S. Suryavanshi**, Director, School Of Physical Science for his valuable suggestions and advices throughout the project that helped us a lot to sort out all the problems.

I would like to thank **Prof. L. P. Deshmukh**, Head of the Dept. of Applied Electronics(Physics). School of physical sciences, Solapur University, Solapur for his valuable suggestion and moral support to write this research paper.

Hydrothermally synthesized CZTS: A potential candidate for methylene blue dye degradation

S. A. Phaltane¹, S. S. Shinde¹, B. L. Kamble², P.S. Patil², L. D. Kadam¹

1. Solid State Physics Laboratory, Department of Physics, Yashwantrao Chavan Institute of Science, Satara,

2. Thin Film Materials Laboratory, Department of Physics, Shivaji University, Kolhapur, M.S.

Email: kdaxman_222@yahoo.co.in

Abstract:

In present work, eco friendly and cost effective hydrothermal method has been used for the synthesis copper zinc tin sulfide (CZTS) nanoparticles which shows kesterite crystal structure and a band gap of 1.53 eV with agglomeration morphology. CZTS powder has been used as a catalyst for the degradation of Methylene blue (MB) dye, shows 48 % of degradation in aqueous medium after 180 min of irradiation.

Key words: CZTS, hydrothermal, MB, dye degradation

Introduction: Copper zinc tin sulfide ($\text{Cu}_2\text{ZnSnS}_4$) is a quaternary semiconductor has attracted much more attention as a good absorber material in photovoltaic applications due to its important optical properties. More over its constituents are non toxic, inexpensive and eco friendly. CZTS is a p type semiconductor with direct band gap (1.4-1.5 eV) and high absorption coefficient of $10^4/\text{cm}$ [1, 2]. It is used in energy harvesting, thermoelectric as well as photocatalytic applications [3-6]. CZTS was reported by Katagiri for the first time [7]. Thereafter different methods were used for the synthesis of CZTS such as microwave [8], Sol-Gel [9], solvothermal [10], SILAR [11], Hot injection [12], Electro deposition [13], Sputtering [14], Pulse laser deposition [15], Hydrothermal [16]. Among these methods, hydrothermal has simpler procedure, eco friendly and economical nature. These specialties attract us for the synthesis of CZTS via hydrothermal route. In present work we synthesis CZTS powder and studied its use for photocatalytic degradation of methylene blue dye.

Experimental method: For synthesis of CZTS, Copper (I) chloride (CuCl), Zinc(II) chloride (ZnCl_2), tin (IV) chloride pentahydrate ($\text{SnCl}_4 \cdot 5\text{H}_2\text{O}$) and thiourea $\text{SC}(\text{NH}_2)_2$ were used as a precursors in the molar ratio (2:1:1:8). They were dissolved in 80 ml double distilled water under magnetic stirring at room temperature. Obtained solution was transferred into 100 ml Teflon-lined stainless steel autoclave, kept in muffle furnace at 210°C for 24 hours. After cooling to room temperature final product was centrifuged and washed with double distilled water several times for

removal of water soluble impurities. It finally dried at 60°C for 6 hours. To obtain pure phase and more crystalline nature of CZTS, as synthesized powder was annealed in presence of sulfur powder at 500°C under N_2 gas for 30 min in tubular furnace.

Characterizations: The XRD patterns of the films were recorded using X-ray powder diffractometer (Bruker AXS Analytical Instruments Pvt. Ltd., Germany, Model: D2 phaser) with $\text{Cu K}\alpha$ radiation. The surface morphology of the CZTS powder was recorded by a scanning electron microscope (SEM; S-4700, Hitachi). Raman spectra were recorded using Renishaw InVia micro-Raman spectrometer using an excitation source of 635 nm laser. The scattered light was analyzed by using charge coupled device (CCD) detector. The room temperature optical absorption measurements were performed in the wavelength range over 100–1000 nm by using a UV–Vis spectrophotometer (UV1800, Shimadzu, Japan).

Photocatalytic activity measurement: In typical photocatalytic experiment 100 ml of 2 mM Methylene Blue (MB) solution was prepared under magnetically stirring for one hour and it was kept in dark for overnight to achieve adsorption equilibrium. A sample of about 5 ml was taken to determine the initial concentration of MB prior to illumination. Under a magnetic stirring 25mg of CZTS was added as a catalyst. Whole system was irradiated from top with a visible light. After every 30 min, 5 ml of solution was pipette out, centrifuged and absorbance of the clear supernatants was determined. The catalytic degradation efficiency (%) for CZTS powder was calculated as:

$$\text{Efficiency of degradation (\%)} = 100 \left(\frac{A_0 - A_t}{A_0} \right) \text{ ---- Eq. (1)}$$

Eq. (1)

Where A_0 = dye solution absorbance in absence of catalyst, A_t = dye solution absorbance in presence of catalyst after time t . According to first order kinetics reaction, rate constant ‘kapp’ was determined by using the relation:

$$\ln \left(\frac{A_t}{A_0} \right) = -k_{app} t \text{ ----Eq. (2)}$$

Result and Discussion: Structural analysis (XRD):

The XRD pattern of annealed sample is shown in Fig. 1. It shows three major peaks at $2\theta = 28.65$, 47.58 and 56.37° can be attributed to the diffraction from (112), (220) and (312) planes respectively and some minor peaks at 23.10 , 33.11 , 69.30 and 76.69 attributed to the (110) (200), (008) and (332) [16, 19]. Diffraction peaks matches well with the JCPDS data card 26-0575 reveals that the synthesized power has kesterite CZTS phase [16]. The lattice parameters for the tetragonal structure can be calculated by the expression:

$$\frac{1}{d^2} = \frac{h^2 + k^2}{a^2} + \frac{l^2}{c^2} \text{ ----Eq. (3)}$$

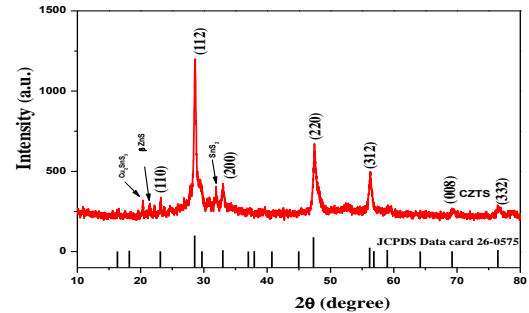


Fig. 1 XRD pattern of annealed CZTS powder. The fine line shows the simulated pattern of kesterite CZTS (JCPDS no. 26-0575)

The observed mean values of the lattice parameters are ($a=5.57 \text{ \AA}$, $c=10.33 \text{ \AA}$) matches well with the JCPDS card 26-0575 ($a= b=5.43 \text{ \AA}$, $c = 10.84 \text{ \AA}$). The standard and observed ‘ d_{hkl} ’ values with their respective planes of the annealed sample were calculated by using Bragg’s law: $2d_{hkl}\sin\theta = n\lambda$ are summarized in following table:

Sr. No.	2θ (in degree)		Plane (h k l)	‘d’ spacing (in Å)	
	Standard	Observed		Standard	Observed
1	23.10	23.10	(110)	3.8470	3.8470
2	28.53	28.65	(112)	3.1260	3.113
3	32.99	33.11	(200)	2.7130	2.703
4	47.33	47.58	(220)	1.9190	1.909
5	56.17	55.37	(312)	1.6360	1.658
6	69.22	69.30	(008)	1.356	1.355
7	76.43	76.69	(332)	1.2450	1.242

Using Scherer’s formula $d = \frac{0.9\lambda}{\beta \cos \theta}$,

average grain size can be calculated, where β is full width half maxima (FWHM), λ is the X-ray wavelength. The average grain size of annealed sample using the (112) planes reflection is 30 nm. Some secondary phases such as ZnS, Cu_2SnS_3 are detected in XRD pattern. But for the confirmation of CZTS phase, Raman analysis is performed because the secondary phases like ZnS and Cu_2SnS_3 have similar lattice parameters [11].

RAMAN Analysis: The room temperature micro Raman spectra of powder CZTS was carried out by the excitation by 532 nm laser in the range of 100 to 600 cm^{-1} , is shown in Fig.2. We observed a minor peak at 287 cm^{-1} and most intense peak at 333 cm^{-1} which matches well with the reported [16, 17]. Intense peak can be assign to A1 mode of vibration of sulfur atoms surrounded by motionless neighboring atoms [17].

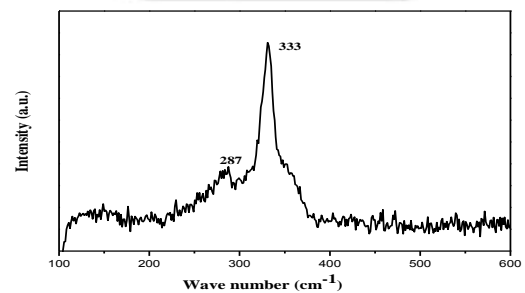


Fig. 2 Raman spectrum of CZTS powder.

SEM analysis: Surface morphology and microstructure plays very important role for photocatalytic applications. Fig.3 shows SEM image which reveals that CZTS powder is agglomeration of particles.

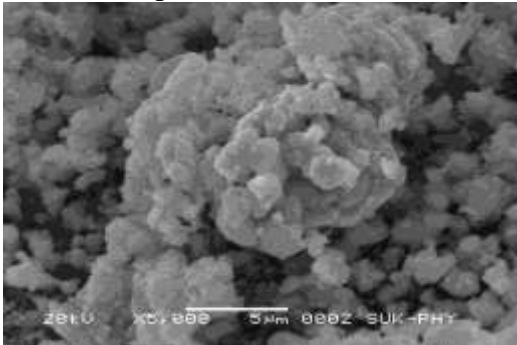


Fig. 3 SEM image of CZTS powder.

UV Visible spectroscopy: Optical absorbance measurement was used to determine the band gap of CZTS sample. Liquid phase method was used to determine the band gap. CZTS powder exhibit broad absorption in visible region whereas the tail of graph extends to the longer wavelength.

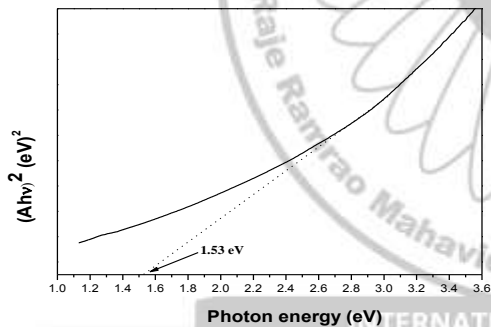


Fig. 4 Tauc plot for measurement of band gap

Tauc and Davis Mott model was used to obtain optical band gap by using equation:

$$(\alpha h\nu)^n = A (h\nu - E_g) \quad \text{-----Eq. (4)}$$

Where A is absorbance, E_g is band gap, $h\nu$ is the incident photon energy, α is absorption coefficient and n is index characterizing the type of optical transition. $n = 2$ for direct band gap. Fig.4 shows the UV-vis spectra powder sample. By extrapolating the linear part of the graph of $(Ah\nu)^2$ versus the photon energy gives the direct band gap of 1.53 eV. This value matches well with the

literature values [17-19] and indicate that material is efficient for photovoltaic application.

Photocatalytic degradation of MB dye: CZTS powder was used as a catalyst for the photocatalytic dye degradation. Degradation of Methylene blue has been studied at its characteristics wavelength at 664 nm with the help of UV-vis spectrometer. Fig.5 shows effect of addition of 25 mg of CZTS as a catalyst and characteristic peak of MB blank solution. Without catalyst MB shows maximum absorption intensity at $\lambda_{max} = 664$ nm. No degradation observed under a dark condition when solution was kept under dark overnight showing MB alone is stable and not degrade on its own. On addition of catalyst and exposure to visible light, 48 % reduction in characteristic peak within 180 min was observed which is calculated by using equation (1). [19]

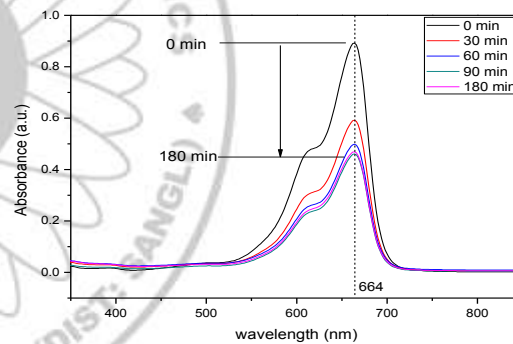


Fig. 5 UV-Vis absorption spectra of degradation of 2mM MB 100 ml MB solution under a visible light radiation in presence of 25 mg of CZTS

Fig. 6A demonstrates the degradation rate of MB without catalyst and with CZTS as a catalyst under the visible radiation. Without catalyst no significant degradation was observed while with catalyst degradation efficiency of MB clearly increased. First order rate constant that has been calculated from equation (2) is shown by Fig.6B. The apparent first order reaction rate constant (k_{app}) was found to be 0.0037 min^{-1} [19]

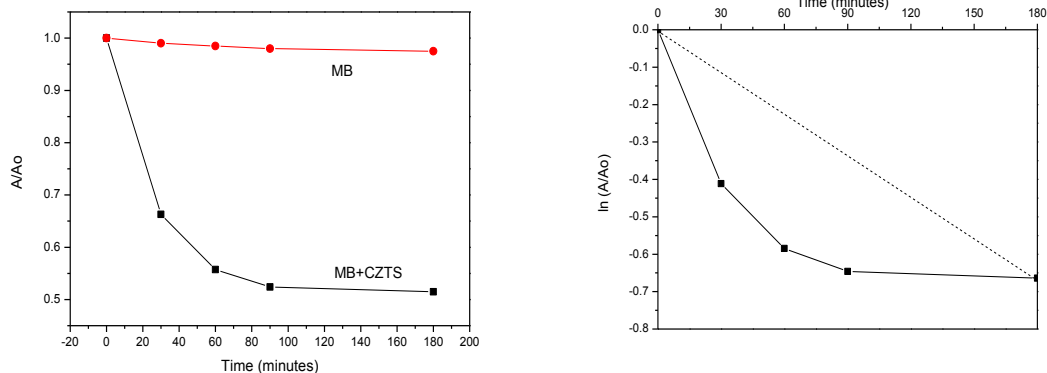


Fig. 6A: Plot of $[A_t]/[A_0]$ against reaction time t , **Fig.6B:**Plot of $\ln(A_t/A_0)$ against time t for evaluating rate constant k_{app} for MB

Conclusion:

Hydrothermal method has been used for the synthesis of CZTS. XRD analysis reveals its kesterite crystal structure and Raman analysis gives confirmation of CZTS phase. SEM image shows agglomeration of the particle with direct band gap of 1.53eV. As synthesized CZTS powder shows potential to degrade 48% of MB in 180 min with rate of reaction 0.0037 min^{-1} . We are currently studying the details of degradation of MB dye with CZTS as a catalyst.

References:

1. K.V. Gurav, Electrosynthesis of CZTS films by sulfurization of CZT precursor: Effect of soft annealing treatment, *Applied Surface Science* 283 (2013) 74– 80
2. U. Ghorpade, Towards environmentally benign approaches for the synthesis of CZTSSe nanocrystals by a hot injection method: a status review, *Chem. Commun.* 50 (2014) 11258
3. P. Kush, Efficient hydrogen/oxygen evolution and photocatalytic dye degradation and reduction of aqueous Cr(VI) by surfactant free hydrophilic $\text{Cu}_2\text{ZnSnS}_4$ nanoparticles, *J. Mater. Chem. A*, 3 (2015) 8098
4. X. Yu, $\text{Cu}_2\text{ZnSnS}_4$ -Pt and $\text{Cu}_2\text{ZnSnS}_4$ -Au Heterostructured Nanoparticles for Photocatalytic Water Splitting and Pollutant Degradation, *J. Am.Chem. Soc.* 136, (2014) 9236.
5. J. Wang, Surfactant-free Hydrothermal Synthesis of $\text{Cu}_2\text{ZnSnS}_4$ (CZTS) Nanocrystals and Photocatalytic Properties, *RSC Adv.* 4(2014), 27805.
6. L. Rovelli, Optimization and Stabilization of Electrodeposited $\text{Cu}_2\text{ZnSnS}_4$ Photocathodes for Solar Water Reduction, *ACS Appl. Mater. Interfaces*, 5 (2013) 8018.
7. K. Ito, Characterization of $\text{Cu}_2\text{ZnSnS}_4$ Thin Films Prepared by Vapor Phase Sulfurization, *Jpn. J. Appl. Phys.* 27, (1988) 2094
8. V. A. Madiraju, CZTS synthesis in aqueous media by microwave irradiation, *J Mater Sci: Mater Electron*, 27 (2016) 3152
9. G. L. Agawane, Synthesis of simple, low cost and benign sol-gel $\text{Cu}_2\text{ZnSnS}_4$ thin films: influence of different annealing atmospheres, *J Mater Sci: Mater Electron* 26 (2015) 1900
10. S. S. Mali, Polyvinylpyrrolidone (PVP) assisted single-step synthesis of kesterite $\text{Cu}_2\text{ZnSnS}_4$ nanoparticles by solvothermal process, *Phys. Status Solidi RRL* 7, 12 (2013) 1050
11. M. Suryawanshi, The synergistic influence of anionic bath immersion time on the photo electrochemical performance of CZTS thin films prepared by a modified SILAR sequence, *RSC Adv.* 4, (2014), 18537
12. D. Xia, Synthesis and characterization of $\text{Cu}_2\text{ZnSnS}_4$ nano crystals by hot-injection method, *J Mater Sci: Mater Electron*, 26 (2015) 5426
13. E. M. Mkawi, Influence of substrate temperature on the properties of electrodeposited kesterite $\text{Cu}_2\text{ZnSnS}_4$ (CZTS) thin films for photovoltaic applications, *J Mater Sci: Mater Electron* 26 (2015) 222
14. B.T. Jheng, Promising sputtering route for dense $\text{Cu}_2\text{ZnSnS}_4$ absorber films and their photovoltaic performance, *Solar Energy Materials & Solar Cells* 128 (2014) 275
15. S.A. Vanalakar, Effect of post annealing atmosphere on the grain-size and surface morphological properties of pulsed laser deposited CZTS thin films, doi.org/10.1016/j.ceramint.2014.06.121, *Ceramics International*
16. W. C. Liu, Facile hydrothermal synthesis of hydrotropic $\text{Cu}_2\text{ZnSnS}_4$ nanocrystal quantum dots: band-gap engineering and phonon confinement effect, *J. Mater. Chem. A*, 1, (2013)3182
17. G. Rajesh, Solution-based synthesis of high yield CZTS ($\text{Cu}_2\text{ZnSnS}_4$) spherical quantum dots, *Superlattices and Microstructures* 77 (2015) 305
18. Y. Zhao, Synthesis and characterization of $\text{Cu}_2\text{ZnSnS}_4$ nanocrystals prepared by microwave irradiation method, *J Mater Sci: Mater Electron*, 26 (2015) 5645
19. P. Kush, Anisotropic kesterite $\text{Cu}_2\text{ZnSnSe}_4$ colloidal nanoparticles: Photoelectrical and photocatalytic properties, *Materials Chemistry and Physics* 162 (2015) 608e616

Effect of sintering temperature on electrical and magnetic properties of

La_{0.7}Ca_{0.3}MnO₃
Shankar Kekade¹, S. I. Patil¹

¹ Department of Physics, S. P. Pune University, Pune-411007, India

Presenting author: skekade@physics.unipune.ac.in

Corresponding author: patil@physics.unipune.ac.in

Abstract

The single phase La_{0.7}Ca_{0.3}MnO₃ (LCMO) nanoparticles were synthesized by solution combustion method. These nanoparticles sintered at different temperatures from 600 - 1200 °C. The results shows the electric and magnetic properties of LCMO samples are strongly depend on sintering temperature. The grain size of nanoparticle was increase with increasing sintering temperature. As sintering temperature increase the insulator- metal transition temperature (T_{IM}) increase with decreasing the resistivity. The saturation magnetization was observed to increase in the sintering temperature.

Introduction

Mixed valance manganites exhibit variety of crystallographic, electronic and magnetic phases. This led to the formulation of new physical concepts such as zener double exchange and Jahn-Teller distortion. The field of manganites started with the paper of Jonker and Van Santen (1950) where the existence of ferromagnetism in mixed crystals of LaMnO₃, CaMnO₃, LaMnO₃/SrMnO₃, and LaMnO₃/BaMnO₃ was reported [1]. The general chemical formula for the manganese oxides described in Jonker and van Santen's paper (1950) and many other compounds investigated later on, is T_{1-x}D_xMnO₃, with T is a trivalent rare earth, and D a divalent alkaline earth element like (Sr, Ca or Ba) cation showing considerable interest [2, 3]. Depending on the composition; they show a variety of magnetic and electronic phenomena, including ferromagnetism, antiferromagnetism, charge and orbital ordering and magnetic-field driven metal insulator transitions. The physical properties of the manganites strongly depend on their crystal structure and they are sensitive to pressure, composition and strain.

In certain range of doping $x = 0.2$ to 0.4 ; the ground state is ferromagnetic and the paramagnetic to ferromagnetic transition is accompanied by a sharp drop in resistivity. Jonkar and Van santen introduced this phenomenon in 1950 [4]. Jonkar and Van santen showed that at temperature above the ferromagnetic Curie point T_C, the resistivity behaves like a semiconductor, $dp/dT < 0$, but that below T_C, not only there is a sharp reduction in resistivity, but also a transition to metallic behavior, $dp/dT > 0$ [4]. The results of electrical, magnetic and structural behavior of La_{1-x}Ca_xMnO₃, exhibiting large colossal magnetoresistance (CMR) were, published by Chahara *et al* [5]. This intrinsic compound is perovskite in nature

and shows very large magnetoresistance, at comparatively lower magnetic field and close to room temperature. This compound shows a transition from paramagnetic insulating to ferromagnetic metallic state, upon lowering of temperature. The magnetic transition temperature (T_C) is found to be close to metal insulator transition temperature (T_p). The observed physical behavior is well explained on the basis of Zener double exchange mechanism.

Now a day, the effect of particle size on the electrical as well as magnetic properties is an interesting topic for experimental and theoretical exploration. In literature survey, the hole doped magnetic nanoparticles try to investigate the change in electrical properties and the T_{IM} transition temperature [6-8]. People work out the changes in magnetic properties likes magnetic phase transition, CMR, hysteresis behavior when particle size is in the nanometer range. The Roy et al shows the coercivity of the La_{0.8}Sr_{0.2}MnO₃ nanoparticles increases as the particle size varies from 53nm to 21 nm [9].

The synthesis of perovskite LCMO via solution combustion method has been continuous interest [10-12]. The combustion method has potential advantages over other traditional processing techniques such as better homogeneities, low processing temperature and material properties [10].

Experiment:

Nanophasic polycrystalline La_{0.7}Ca_{0.3}MnO₃ is synthesized using solution combustion method. Initially the high purity powders of required acetates and citric acid were taken. Suitable proportions of Lanthanum nitrate (La(NO₃)₃.6H₂O), Calcium acetate [Ca(OOCCH₃)₂.9H₂O], Manganese acetate [C₄H₆MnO₄.4H₂O] and citric acid [C₆H₈O₇] were used as starting materials. All these chemicals were mixed together and dissolved in distilled water. Further these acetates were converted into their respective nitrates by

adding concentrated HNO_3 . Finally citric acid was added to it which would act as a surfactant. The resulting solution was heated on water bath at 96°C . This heating was continued for several hours, until a pale orange colored gel was formed. After that, heating was continued till formation of black powder. This powder was separated into parts. A part of the powder was investigated using powder X-ray diffraction (XRD) characterization technique and found secondary phase of oxides. When the powder was calcined at 600°C and X-ray diffraction pattern was obtained, it was found that phase formation has been started at this temperature. This was indicated by peaks which are very well matched with standard LCMO, JCPDS data. These peaks have very low intensity and are broad in nature, which shows that when the sample was calcined at 600°C grain growth has been just started. The samples were further calcined at different temperatures varying from 600°C to 1200°C in the steps of 100°C for 12 hours. The crystallite size of the samples was determined independently using Scherrer formula. The surface morphology and grain size study was done by using Scanning Electron Microscope (SEM). Magnetic measurements were carried out for these samples using Vibrating Sample Magnetometer (VSM). The effect of grain size on electrical properties was carried out using standard four probe resistivity method.

Results:

Powder x-ray diffraction (XRD) pattern, recorded at room temperature of synthesized samples using solution combustion method are shown in figure 1. The result indicates that the all samples correspond to the pure LCMO phase with no any detectable secondary or impurity phase. The as prepared shows LCMO phase with secondary phases. To remove the secondary phases we sintered the sample up to 1200°C . The sample sintered below 600°C observed the secondary phases, hence these samples not considered for further studies.

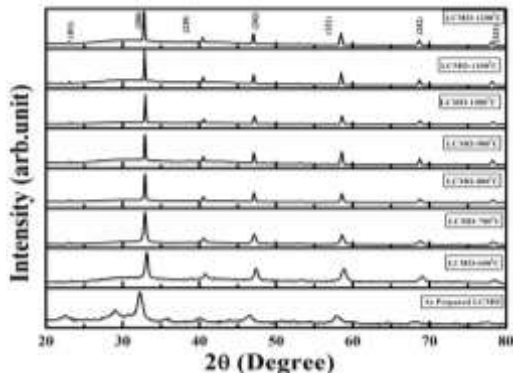


Figure 1: X-ray diffraction patterns of the LCMO samples.

Bragg reflections corresponding to different planes can be seen in figure 1. The Miller indices, corresponding to the perovskite structure (orthorhombic), have confirmed from (JCPDS-ICDD 49-0416). From the XRD patterns, it is clear that single phase LCMO with perovskite structure (orthorhombic) has been started to grow at 600°C after sintering the powder for 12 hours. Further heating helped in enhancing the grain growth of the samples, which is indicated by the reduction of the full width at half maximum of the diffraction peaks figure 1. It is found that the structure remains unchanged with the increase in grain size due to increased sintering temperature. FWHM of the peaks is used to calculate the average crystallite size of the samples.

The structural parameters determined using the XRD patterns are enlisted in table 1. The increase in grain size also leads to an increase in the unit cell volume, which may be due to the relaxation of strain. The average crystallite size of those samples are found to be 17nm to 43nm corresponding to sintering temperature 600°C to 1200°C , respectively shown in table 1. The intensity of diffraction peaks for the LCMO perovskite phase increase as the sintering temperature increase from 600°C to 1200°C , indicating that the crystallinity of LCMO becomes better and the particle size increases as the sintering temperature increases.

The figure 2 shows temperature dependence resistivity carried out using four probe resistivity method. The measurement is carried out from the room temperature to 30K. The value of resistivity increases with the decrease in sintering temperature shown in table 1, exhibits a pronounced peak at T_{MI} and then decreases as the temperature is further lowered below T_{MI} .

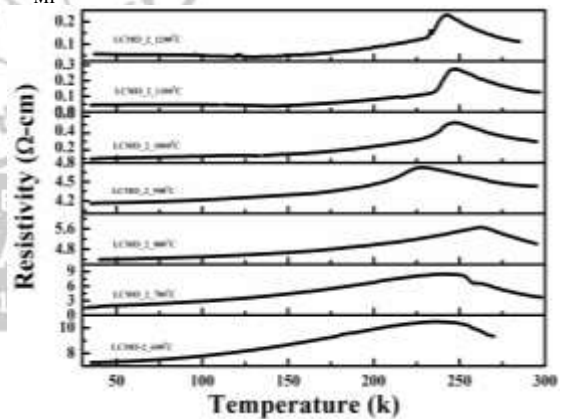


Figure 2: Temperature dependence resistivity of $\text{La}_{0.7}\text{Ca}_{0.3}\text{MnO}_3$

The compound was found to undergo a paramagnetic to ferromagnetic transition at temperature T_C . Thus, the evolution of the negative temperature coefficient of resistivity $d\rho/dT < 0$ above T_{MI} indicates an insulating nature, whereas the positive temperature coefficient $d\rho/dT > 0$ below this temperature displays a metallic behavior

of the sample thereby marking an insulator-metal transition at T_{MI} together with a paramagnetic to ferromagnetic transition in the vicinity. From the figure it is evident that the resistivity of the compound increases with decrease of the grain size, implying that the decrease of the grain size relatively increases the insulating regions due to the enhancement of the grain boundary effect [13].

The representative images of SEM samples are shown in figure 3a, b, c, and d showing the surface morphology of the LCMO nanoparticles sintered at 600°C, 800°C, 1000°C and 1200°C

respectively. It is seen that grain size increases with increase in sintering temperature. Increase in sintering temperature leads to grain growth, which indicates increase in grain size. Samples sintered at 600°C to 900°C show the agglomeration, all grains are agglomerated. For higher sintering temperature, the grains are well separated and the grain boundaries are clearly seen. The nominal presence of elements is determined by Energy Dispersive X-ray analysis Spectra. Confirm stoichiometric composition of the La, Ca, Mn and O present in the synthesized compound using EDAX.

Table 1: Lattice constants a , b and c (Å) along with the unit cell volume, resistivity and saturation magnetizations are indicated for the LCMO samples annealed at various temperatures.

Sample Name	a (Å) (±0.01)	b (Å) (±0.01)	c (Å) (±0.01)	Unit cell volume (Å ³)	D (nm)	ρ (Ω-cm)	M_s (emu/gm)
LCMO-600	5.41	7.68	5.41	225.36	17	10.23	36
LCMO-700	5.40	7.69	5.43	225.61	18	8.45	60
LCMO-800	5.40	7.69	5.44	226.49	22	6.12	72
LCMO-900	5.44	7.72	5.45	227.88	37	4.44	79
LCMO-1000	5.45	7.71	5.42	228.30	38	0.52	80
LCMO-1100	5.44	7.72	5.43	228.80	40	0.27	84
LCMO-1200	5.45	7.72	5.44	229.30	43	0.22	88

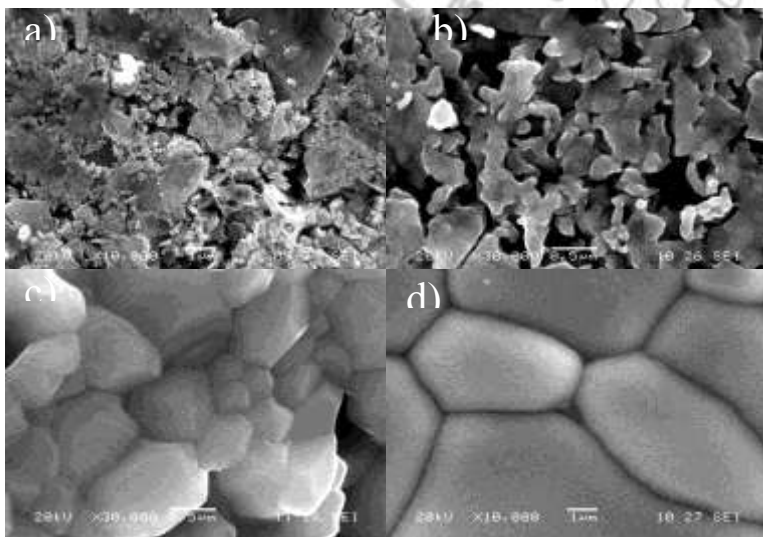


Figure 3: SEM images of LCMO samples sintered at different temperature; a) 600°C, b) 800°C, c) 1000°C and d) 1200°C.

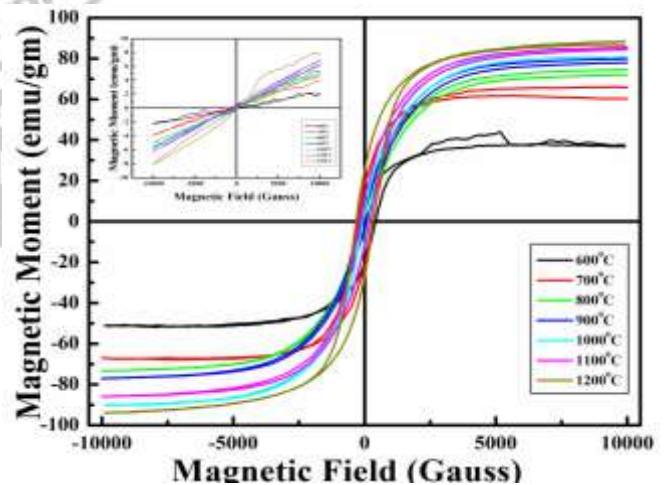


Figure 4: Field dependence of magnetization ($M-H$) curves at 20K of LCMO samples sintered at temperature ranging from 600°C to 1200°C. The inset et shows ($M-H$) curves at room temperature.

The room temperature as well as low temperature magnetization as a function of applied magnetic field was measured using VSM and is as shown in figure 4. At 20K i.e. at low temperature, all the samples show well defined hysteresis curve, which indicates ferromagnetic nature of the samples with low coercivity. Saturation magnetization (M_s) of LCMO-1200 sample is about 88 emu/gm; while samples with smaller grain sizes have weaker M_s (LCMO-600 sample is about 37 emu/gm.) The saturation magnetization (M_s) increases with increasing sintering temperature shown in table 1 [14-16]. In the figure inset shows the M-H curve at room temperature. At room temperature, M-H curve shows the paramagnetic behavior for all samples.

So hysteresis measurements suggest that saturation magnetization decreases with decrease in grain size. A. Gaur et al have attributed this observation to formation of extra grain boundaries

due to lower sintering temperature [8]. However this is the most general observation in the case of nanoparticles of manganite system. When size of material is reduced to nanometer scale the surface to volume ratio increases and surface effects become progressively more important. This can be attributed to the increase in the relation between the amounts of atoms that constitute the surface region to those in the bulk. Such a surface layer is known to exhibit spin glass behavior which can occur due to unavailability of exchange partners to the surface atoms, surface strains and surface disorder. In magnetic material the magnetic order in the surface of the particles is modified and the properties such as magnetization and transition temperature may get strongly affected. Especially in ferromagnetic systems the magnetic coupling in the surface region can become highly frustrated leading to decrease in ferromagnetism.

Conclusion:

In summary, we have successfully synthesized and studied the electrical as well as magnetic properties of nanophasic $\text{La}_{0.7}\text{Ca}_{0.3}\text{MnO}_3$ samples. All samples shows pure LCMO perovskite phase with orthorhombic unit cell. The grain size of nanoparticles increases with increasing sintering temperature. As sintering temperature increases, the value of resistivity decrease due to change grain boundary effect. The magnetic measurement shows that saturation magnetization decrease with decrease in grain size.

Reference

1. Jonker G H and Van Santen J H 1950 Physica 16 (1950) 337
2. Nagaev E L, Phys. Rep. 346 (2001) 387.
3. Rao C N R, Mahesh R, Raychaudhuri A K and Mahendiran R 1998 *J. Phys. Chem. Solids* 59 (1998) 487.
4. Van Santen J H and Jonker G H 1950 Physica 16 599.
5. K. Chahara, T. Ohno, M.Kasai and Y.Kosono, Appl. Phys. Lett 63 (1993) 1990
6. M. M. Savosta, V. N. Krivoruchko, I. A. Danilenko, V. Yu Tarekov, T. E. Konatantinova, A. V. Borodin, V. N. Varyukhin, Physical Review B 69 (2014) 024413.
7. Ning Zhang, Weiping Ding, Wei Zhong, Dingyu Xing, Youwei Du, Physical Review B 56 (1997) 8139-8142.
8. Anurag Gaur, G.D. Varma, Journal of Physics: Condensed Matter 18 (2006) 8837-8846.
9. Sujoy Roy, Igor Dubenko, Dossah D. Edoorh, Naushad Ali, Journal of Applied Physics 96 (2004) 1202-1208.
10. R. G. Shetkar and A. V. Salker, J. Mater. Sci. Technol., 26 (2010) 1098-1102.
11. Dragana Markovic, Vladan Kusignerski, Marin Tadic, Jovan Blanus, Marco vittori Antisari and Vojislav spasojevic, Scripta Materialia 59 (2008) 35-38.
12. S. Ponce, M. A. Pena, J. L. G. Fierro, Applied Catalysis B: Environmental 24 (2000) 193-205.
13. Andres A de, Garcia Hernandez M and Martinez J L, Appl Phys. Lett 74 (1999) 3884.
14. P. A. Yadav, A. V. Deshmukh, K. P. Adhi, B. B. Kale, N. Basavaih, S. I. Patil, JMMM 328 (2013) 86-90.
15. Balcels I. Fontcuberta J, Martinez B and Obradors X, Phys. Rev. B 58 (1998) R14697.
16. Rivas J, Hueso E, Fondado A, Rivadullo F and Lopez Quintela M. A. J Magn. Mater 221 (2000) 57.

Acknowledgment:

The Author would like to thanks UGC, BSR for financial assistance.

Fabrication and performance of the solar cell devices based on electrodeposited compact CZTS films

N.L. Tarwal^{1,2}, A.M. Nalawade³, S. A. Rasal¹, R.P.Bhosale¹, A.E.Korade¹, R.V.Shejwal³, P.S. Patil⁵, J.H. Jang^{2*}

¹Department of Physics, Lal Bahadur Shastri College, Satara-415002

²Research Institute for Solar and Sustainable Energies (RISE), Gwangju Institute of Science and Technology (GIST), Gwangju 500-712, Republic of Korea. ³Department of Chemistry, Lal Bahadur Shastri College, Satara-415002

⁴Thin Film Materials Laboratory, Department of Physics, Shivaji University, Kolhapur-416004

E-mail: tarwalnilesh@gmail.com

Abstract

Nowadays, copper based chalcogenides such as $\text{Cu}_2\text{ZnSnS}_4$, $\text{Cu}_2\text{ZnSnSe}_4$ are the promising candidates for production of low-cost thin film solar cells due to their tunable direct band gaps (~1.0-1.5 eV), large absorption coefficient and high natural abundance of all constituents. Herein we report the simple route to obtain a compact layer with average thickness of ~2 μm by a simple and low cost electrodeposition and their solar cell performance with efficiency of 1.41%. The deposition potential was kept at -1.1V (SCE). Also the preparative parameters of the electrodeposition were optimized for getting compact layer of the CZT precursor films. These precursor films were further sulfurized at 550 °C to obtain CZTS thin films. The prepared films were characterized by using the XRD, Cross-sectional SEM, Raman, etc. The solar cell devices were fabricated by using the optimized back hand processes. I-V characteristics of the fabricated CZTS solar cell devices were investigated and discussed.

Keywords: $\text{Cu}_2\text{ZnSnS}_4$ (CZTS) films; XPS; Electrodeposition; Solar cell devices

1. Introduction

Recently, $\text{Cu}_2\text{ZnSnS}_4$ (CZTS) thin film solar cells have attracted substantial interest as renewable energy devices and have shown potential as an alternative technology due to the use of earth abundant and its environmentally friendly elements. [1]

In addition, CZTS is a p-type semiconductor with a direct band gap energy of 1.5 eV and a large absorption coefficient over 10^4cm^{-1} , properties similar to those of $\text{Cu}(\text{In,Ga})\text{Se}_2$ (CIGS), which is regarded as one of the best absorber materials for sustainable and highly efficient solar cell [2–7] Thus, promising sunlight conversion efficiency (η) of more than 15% can be expected in the near future, indicating that a CZTS solar cells have potential for industrial production of the Solar cell devices.

Various synthesis techniques have been employed for the synthesis of CZTS films such as thermal co-evaporation [8], pulsed laser deposition [9], sputtering [10], solution processes [11] and electrochemical deposition [12,13], have been applied in the preparation of CZTS thin films. Among these methods, electrochemical deposition is more attractive process due to low equipment cost, low cost source materials, and scalable deposition with room temperature growth [12]. The

simplest route for CZTS electrodeposition is single step formation of CZTS precursors by using bath containing four elements at optimum deposition potential [8]. It is noteworthy that wide potential difference in reduction potentials of Cu, Zn, Sn and S with specific reversibility of S makes process complex. Furthermore, electrodeposition is a promising process due to its technical advantages for the fabrication of low-cost solar cells. For instance, electrodeposition of metallic precursor layers can usually be performed at room temperature without a heating or cooling environment using nontoxic and low-cost metallic salt solutions. These solutions can also be used for a long period and recycled, thus avoiding waste of resources.

Katagiri et al. reported η of 6.77% using a CZTS thin film fabricated by sputtering metallic precursors followed by annealing in H_2S . [14] Shin et al. obtained a CZTS-based solar cell with η of 8.4% using vacuum thermal evaporation at 150 °C and subsequent atmospheric pressure annealing at 570 °C. [15]

In the present study, we report on synthesis of CZT precursors with controlled compositions and then sulfurization in order to get the stoichiometric CZTS film with compact morphology simply by controlling sulfurization

times. The various properties of CZTS films is reported herewith.

2. Experimental

A three electrode assembly with Saturated Calomel Electrode (SCE) as a reference electrode, an inert anode (graphite) and a working electrode (Mo on glass substrate) was used. All the precursors were taken in the single bath for the deposition of the CZT precursor layer and then the as-deposited CZT precursor is being used for the further treatment and investigations.

In typical synthesis procedure, the bath compositions contains aqueous solutions of 0.01 M CuSO_4 , 0.02 M ZnSO_4 , 0.01 M SnSO_4 , 0.1M sodium citrate were taken along with 0.005M EDTA. 2 ml of the tartaric acid was added to the final solution. The electrodeposition of the CZT precursor layers have been carried out by using the chronoamperometry routes for various times (10 min to 30 min). For the CA route constant potentials (-1.1 and -1.2 V) were applied.

The prepared CZT precursors have been investigated by using the SEM and EDAX for examination of the compact morphology and the elemental confirmation. Further these precursor films were used for the various characterization such as XRD, SEM, Raman and Photovoltaic measurements. The structural properties of the annealed films were studied using high resolution X-ray diffraction (XRD) with $\text{Cu K}\alpha$ radiation [$\lambda = 1.54056 \text{ \AA}$] (X'pert PRO, Philips, Netherlands) operated at 40 kV and 30 mA. The surface morphology of films was observed by using FE-SEM (field emission scanning electron microscopy, Model: JSM-6701F, Japan) attached with an energy-dispersive X-ray analysis (EDAX) system. Raman investigations have been carried out by using the Laser Raman Spectrophotometer (laser wavelength: 532 nm). The photovoltaic I-V measurements have been done by using the Newport's Solar simulator.

3. Results and discussion

The CZT precursor films were prepared by using the earlier codeposition route. The as-deposited films were soft annealed at 250 °C for 30

min and used for sulfurization by using sulfurization system at 550 °C for 10 min.

3.1 XRD

The XRD patterns of the films sulfurized at 550 °C is shown in Fig.1 . All the peaks are corresponding to the CZTS phase. The main CZTS peak i. e. (112) stems at $\sim 28^\circ$. Also other peaks like (200), (220), (312) , (008) and (316) are present in the XRD patterns which are corresponding to the CZTS phases.

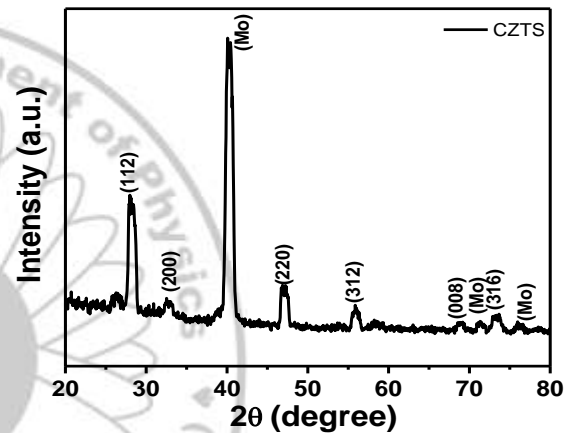


Fig. 1 XRD pattern of the sulfurized CZT films

3.2 SEM

The SEM investigations were carryout out and the obtained SEM images are shown in Fig. 2. It is seen that the sulfurized films are compact and uniformly distributed over the entire surface of the Mo substrates with excellent adhesion. The thicknesses of the films after sulfurization was achieved ~ 2 to 3 μm . The crystalline quality with compactness is improved after sulfurization. An excellent compact morphology is achieved for temperature of 550°C. The EDAX spectra confirm that the prepared samples are belongs to CZTS material. After looking the compositions of the sulfurized films it is clear that the films are Cu rich and Zn poor. This is due to the presence of secondary phases like Cu_2S . However, these peaks can easily eliminated by NaCN etching step.

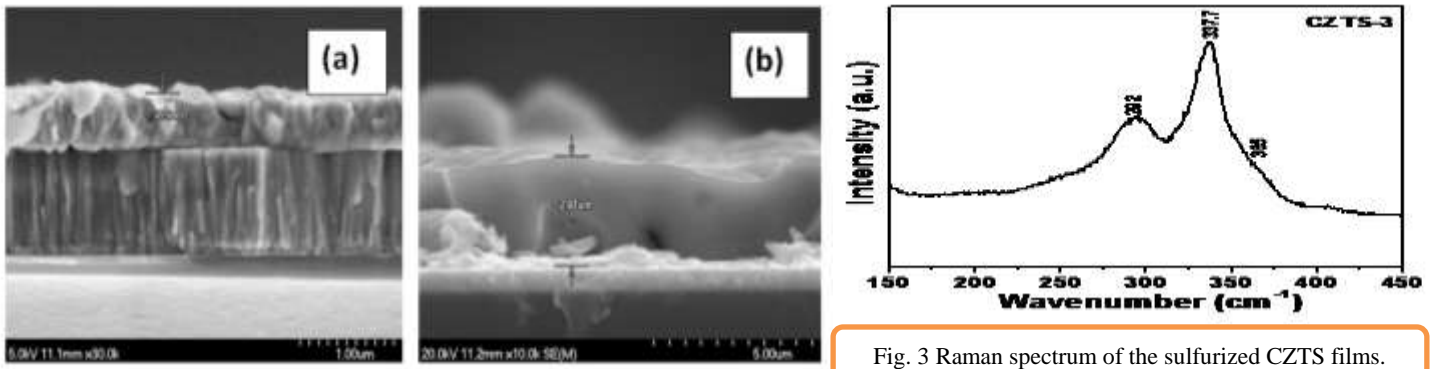


Fig. 3 Raman spectrum of the sulfurized CZTS films.

Fig. 2 shows the cross-sectional SEM images of the (a) CZT precursors and (b) CZTS films

3.3 Raman spectroscopy

The Raman spectra of the sulfurized CZTS films at 550 °C for 10 min were obtained and shown in the Fig.3. The CZTS phase formation is confirmed from Raman spectra. The sulfurized film shows three peaks at the wavenumbers of ~293, ~338 and ~365 cm^{-1} are corresponding to the CZTS phase. There is little deviations of these peaks are observed when films were sulfurized at various temperatures, as shown in the Fig. 3.

3.4 Solar cell performance of the CZTS films

The solar cell testing of the fabricated devices were carried out by using the Solar simulator. The two contact were made from the Mo and Al grid for the J-V curves measurements. The obtained J-V curves of the fabricated CZTS devices

CZTS device showed the current density (J_{sc}) value of ~ 13 mA/cm^2 and V_{oc} values of 0.38V with the efficiency value of 1.41%.

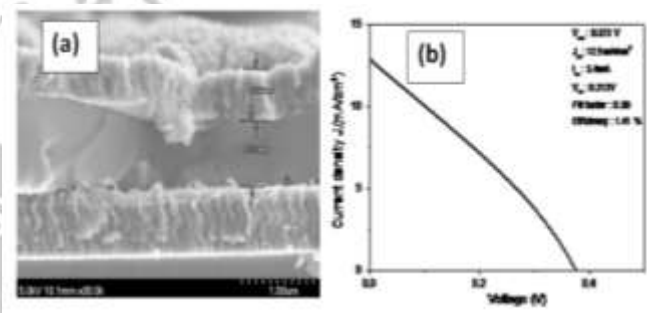


Fig. 4 (a) Cross-sectional image of the fabricated CZTS solar cell device and (b) obtained J-V curves of a fabricated CZTS device.

4. Conclusion

1.41% CZTS thin film solar cells were successfully fabricated by electrochemical deposition of a metallic precursor followed by sulfurization. The structural and Raman investigations confirms the CZTS phase formation. The overall picture of the CZTS solar cell is clearly seen from the cross-sectional SEM image. It is noticed that preheating treatment for a relatively long time just before the high-temperature sulfurization had a great effect on the quality of the final CZTS film. Therefore the present device still has a significant structural failure at the interface of the CZTS layer and the Mo back contact. Further experiments are required for tackling these issues and getting the higher efficiency. The present research work also suggests the possibility for improvements in solar cell properties of the CZTS solar cells fabricated by a simple and low cost electrodeposition.

References:

1. K.V. Gurav, Y.K. Kim, S.W. Shin, M.P. Suryawanshi, N.L. Tarwal, U.V. Ghorpade, S.M. Pawar, S.A. Vanalakar, I.Y. Kim, J.H. Yun, P.S. Patil, J.H. Kim, Appl. Surf. Sci. 334 (2015) 192
2. S. C. Riha, B. A. Parkinson, A. L. Prieto, J. Am. Chem. Soc. 131 (2009) 12054.
3. T. K. Todorov, K. B. Reuter, D. B. Mitzi, Adv. Mater. 22 (2010) E156.
4. H. Katagiri, K. Jimbo, W. S. Maw, K. Oishi, M. Yamazaki, H. Araki, A. Takeuchi, Thin Solid Films, 517 (2009) 2455.
5. K. Woo, Y. Kim, J. Moon, Energy Environ. Sci. 5 (2012) 5340.
6. J. J. Scragg, J. T. Watjen, M. Edoff, T. Ericson, T. Kubart, C. Platzer-Bjorkman, J. Am. Chem. Soc. 134 (2012) 19330.
7. B.-A. Schubert, B. Marsen, S. Cinque, T. Unold, R. Klenk, S. Schorr, H.-W. Schock, Prog. Photovoltaics 19 (2011) 93.
8. A. Redinger, M. Mousel, R. Djemour, L. Gutay, N. Valle, S. Siebentitt, Prog. Photovolt. Res. Appl. 22 (2014) 51.
9. M. Moriya, K. Tanaka, H. Uchiki, Jpn. J. Appl. Phys. 46 (2007) 5780.
10. J. He, L. Sun, K. Zhang, W. Wang, J. Jiang, Y. Chen, P. Yang, J. Chu, Appl. Surf. Sci. 264 (2013) 133.
11. W. Yang, H.S. Duan, B. Bob, H. Zhou, B. Lei, C.H. Chung, S.H. Li, W.W. Hou, Y. Yang, Adv. Mater. 24 (2012) 6323.
12. S.M. Pawar, B.S. Pawar, K.V. Gurav, D.W. Bae, S.H. Kwon, S.S. Kolekar, J.H. Kim, Jpn. J. Appl. Phys. 51 (2012), 10NC27.1.
13. K.V. Gurav, S.M. Pawar, S.W. Shin, M.P. Suryawanshi, G.L. Agawane, P.S. Patil, J.H. Moon, J.H. Yun, J.H. Kim, Appl. Surf. Sci. 283 (2014) 74.
14. H. Katagiri, K. Jimbo, W. S. Maw, K. Oishi, M. Yamazaki, Thin Solid Films 517, (2009) 2455.
15. B. Shin, O. Gunawan, Y. Zhu, N. A. Bojarczuk, S. J. Chey, S. Guha, Prog. Photovoltaics, 21, (2013) 72.

Study of Morphological Change in ZnO Nanoparticles by Capping Agents Using Sol-gel Method

D. A. Kumbhar^{1&2}, A. M. Nalawade², R. A. Nalawade², S. B. Raut³

¹Department of Chemistry, R.R. College, Jath, Maharashtra, 416404, India.

²Department of Chemistry, L.B. S. College, Satara, Maharashtra, 415002, India.

³Department of Chemistry, M. I. T. College of Engineering, Pune, Maharashtra, 411038, India.

Abstract:

Nanocrystalline Zinc Oxide (ZnO) powders with different morphology have been successfully synthesized by new capping agents such as Mannitol and Piperazine using sol-gel method. The products were characterized by powder X-ray diffraction (XRD) shows ZnO particles are in the range of 10 to 80nm and Scanning electron microscopy (SEM) shows the formation of nanoball and nano tube shaped morphologies.

Keywords: ZnO nanostructures, Nano oxides, Sol-Gel method, Structural studies.

I. Introduction

Among the different types of metal oxides, zinc oxide (ZnO) is a most commonly used metal oxide. In past decades, ZnO nanostructures have attracted a considerable attention due to their unique properties and various applications such as photo catalysts, conductivity, gas sensor, chemical sensors etc. ZnO is also a useful semiconductor material due to the wide direct band gap (3.3 eV) and large value of excitation binding energy (60 meV).

The variety of structures of nanometric zinc oxide means that ZnO can be classified among new materials with potential applications in many fields of nanotechnology. Zinc oxide can occur in one- (1D), two- (2D), and three-dimensional (3D) structures. One-dimensional structures make up the largest group, including nanorods, needles, helices, springs and rings, belts, combs etc. Zinc oxide can be obtained in 2D structures, such as nanoplate / nanosheet and nanopellets. Examples of 3D structures of zinc oxide include flower, dandelion, snowflakes, coniferous urchin-like, etc. That is ZnO provides one of the greatest assortments of varied particle structures among all known materials [1, 2].

The variety of methods for ZnO production, such as vapour deposition, precipitation in water solution, hydrothermal synthesis, the sol-gel process, precipitation from microemulsions and mechanochemical processes makes it possible to obtain products with particles differing in shape, size and spatial structure. [3, 4]

Among these methods sol-gel is one of the most common and promising method for the

synthesis of isometric zinc oxide crystals [5, 6, 7]. This method proven that it is very extremely versatile since it allows the formation of a large variety of metal oxides at relatively low temperatures. The structure and composition of nano oxides formed by sol-gel method depend on the preparation condition, the nature of the precursors, the ion source and pH [8, 9].

There are many studies in which different capping agents are applied to obtain appropriate size and shape [10, 11]. Here, ZnO nanostructures with the morphologies of nanoballs, nanotubes obtained in the presence of Mannitol and Piperazine via a sol-gel process.

II. Experimental procedures

A. Synthesis of ZnO nanoparticles

In 0.2 M zinc acetate solution add aqueous 1:1 ammonia slowly till pH should be 8 to get a gel with continuous stirring. After 4 h, the obtained white gel then is dried at 80⁰C for 6 h and the obtained dried product is calcinated at 400⁰C for 3 h in a muffle furnace.

B. Synthesis of Capped ZnO nanoparticles

To 0.2M zinc acetate solution add capping agent i.e. Mannitol or Pyperazine under continuous stirring for 30 min, aqueous ammonia (1:1) was added slowly till pH should be 8 to get a gel. After 6 h of stirring white gel was dried at 80⁰C for 6 h and the obtained dried product is calcinated at 400⁰C for 3 h in a muffle furnace.

The product obtained after calcinations is taken in tubes and seen their size under XRD and SEM.

III. Characterization of ZnO nanostructures

The X-ray powder diffraction (XRD) of the samples was examined using the principle of Bragg

Brantano Geometry, with Cu-Ka radiation ($\lambda = 1.54 \text{ \AA}$). Fig. 1, 2, 3 shows the XRD peaks of ZnO.

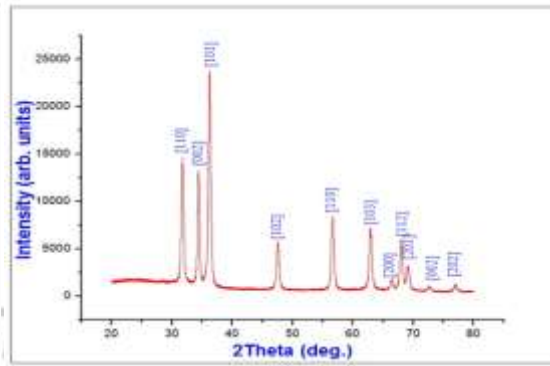
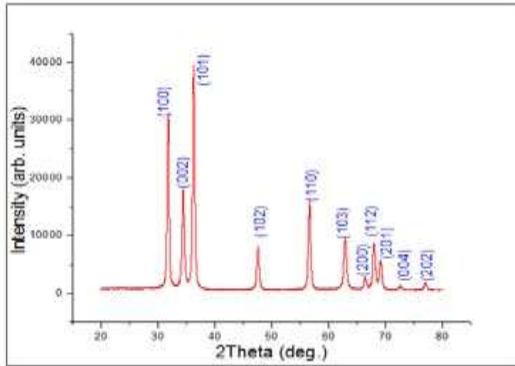


Fig 1. XRD pattern of ZnO nanoparticles

Fig 2. XRD pattern of Mannitol Capped ZnO nanoparticles

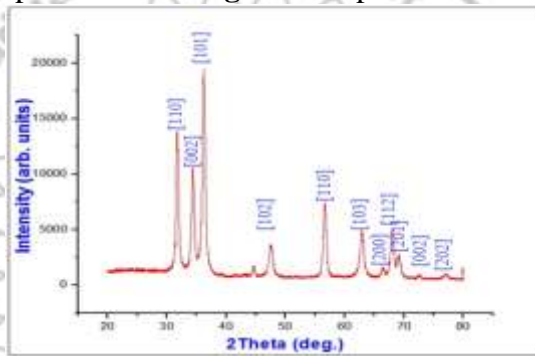


Fig 3. XRD pattern of Pyperrazine Capped ZnO nanoparticles

The morphology of the samples was inspected using a scanning electron microscope. Fig.4, 5, 6

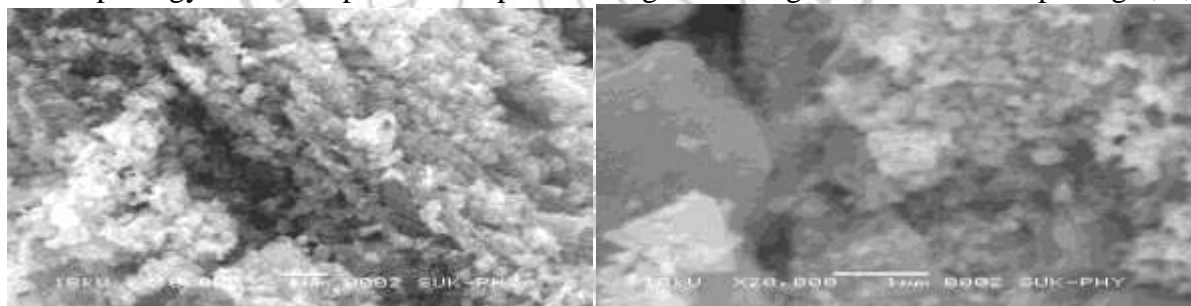


Fig.4. SEM images of pure ZnO nanoparticles

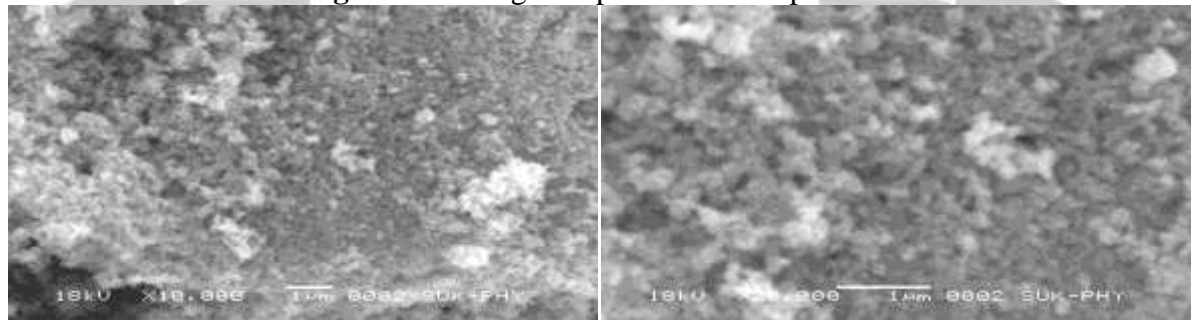


Fig. 5. SEM images of Mannitol Capped ZnO nanoparticles

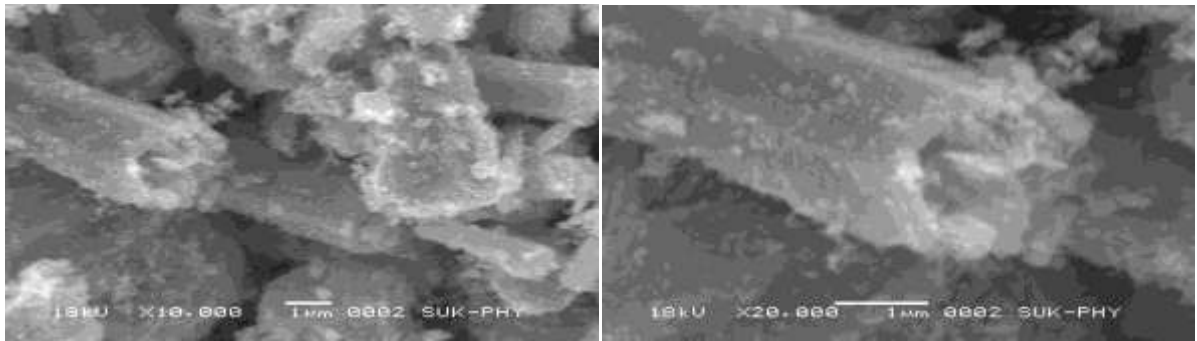


Fig 6. SEM images of Piperazine Capped ZnO nanoparticles

IV. Result and discussion

Capping agents used in synthesis of ZnO from zinc acetate precursor are Mannitol,

Piperazine, which are having following structures and operate through the general route given below.

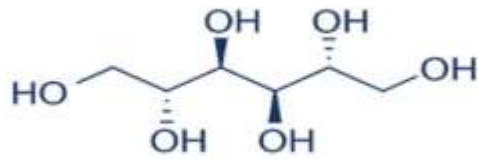


Fig.7 Mannitol

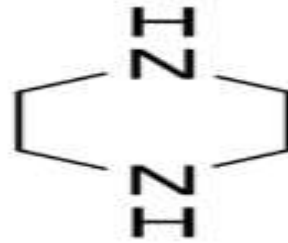


Fig.8 Piperazine

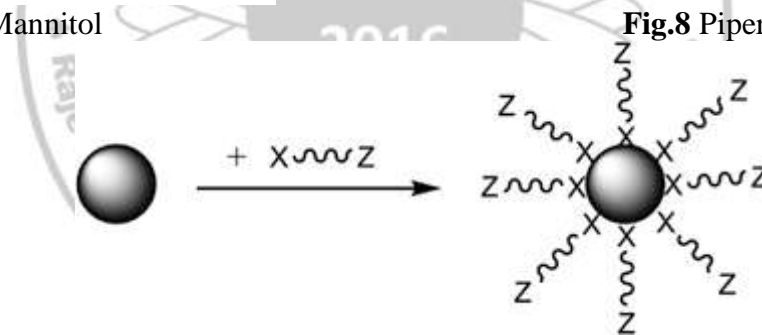


Fig.9 Schematic representation of capping

In all Schemes of crystalline size of the particles has been estimated from XRD. The pattern of the prepared Zinc oxide nanopowder is shown in fig. The observed diffraction peaks of ZnO at $2\theta = 31.72^\circ, 34.38^\circ, 36.26^\circ, 47.54^\circ$ and 56.58° are associated with (100), (002), (101), (102) and (110). All the reflections can be assigned to the standard powder pattern for the pure hexagonal phase of ZnO with lattice constants $a = 3.2516 \text{ \AA}$, $c = 5.2000 \text{ \AA}$. The (hkl) values are agreed well with the standard card of ZnO powder sample (JCPDS file No: 36-1451). The crystallite size (t) of the prepared nanopowder can be calculated by using Scherrer's formula, $t = 0.9\lambda/\beta \cos \theta$, Where λ is the

wavelength of X rays used (1.54060 \AA), β is the full width at half maximum (FWHM) and θ is the angle of diffraction. So, The XRD's of pure ZnO, Mannitol capped ZnO and Piperazine capped ZnO shows the average particle size in the range of 10 to 80 nm and are in hexagonal phase and wurtzite in structure which matches with JCPD File No. 36-1451.

The SEM image Fig. 4 of the uncapped ZnO sample displayed a rock – like agglomerated structure with a rough surface and lot of striations (uneven surfaces). No distinct morphology was observed for the uncapped ZnO sample. In Mannitol capped ZnO Fig.5 sample less agglomerated with a proper nano ball structures are

formed. Here hydrogen bonds associated with the Mannitol framework prevents the synthesized nanoparticles from agglomeration. Piperazine contain

“N” as heteroatom binds strongly to shows ordered pattern of capping and form nano tubes.

V. Conclusion

Using simple Sol-gel method we successfully synthesized different ZnO nanoparticles. The size of the particles were found between 10 nm to 80 nm studied by the XRD. SEM images of the pure ZnO nanoparticles show that agglomerations have been taken place in pure ZnO sample with irregular particle size. So, different capping agents give newer and regular morphologies. Mannitol and Piperazine plays an excellent role in eliminating the surface defects as well as in introducing a phase transition. Uniform biocompatible capping with Mannitol and heteroatomic capping with Piperazine results in nanoball, nanotube shaped morphologies. The nanoparticles are clearly well separated indicating effective capping on the nanoparticle surfaces. Such synthesized zinc oxides will be used for energy storage, sensing, data storage, optics, transmission, environmental protection, cosmetics, biology, and medicine for better results.

References

1. Feynman R. There's plenty of room at the bottom. J Sci. 1991; 254:1300e1301.
2. H. Duan, D. Wang and Y. Li., Chem. Soc. Rev., 2015, 44, 5778-5792.
3. D. Sornalatha, P. Murugakoothan', Int. J. Emerging Tech. and Adv. Eng., 2013, Vol.3(9).
4. J. Park, J. Joo, S. G. Kwon, Y. Jang and T. Hyeon, Angew. Chem., Int. Ed., , 46, 4630–4660, 2007
5. K. Vidhya, M. Saravanan, G. Bhoopathi, V. Devarajan, S. Subanya, Appl. Nanosci, 2015, 5:235–24.
6. Y.L. Wu et al, Applied Surface Science 2007,253, 5473–5479.
7. M. Umadevil, M.R. Bindhu, V. Sathe , Mater. Sci. Technol., 2013, 29(4), 317-322.
8. A. Deshpande, B. Gogte., Res. J. Chem. Sci. 2011, Vol. 1(6), 42-47.
9. Sharda, K. Jayanthi, S.Chawla., Applied Surface Science 2010, 256, 2630–2635,.
10. J. A. Lopez-Sanchez, N. Dimitratos, C. Hammond, G. L. Brett, L. Kesavan, S. White, P. Miedziak, R. Tiruvalam, R. L. Jenkins, A. F. Carley, D. Knight, C. J. Kiely and G. J. Hutchings, Nat. Chem., 2011,3, 551–555.
11. X. Pang, L. Zhao, W. Han, X. Xin and Z. Lin, Nat. Nanotechnol., 2013, 8, 426



X-Ray Crystallography- A Tool for Material Characterisation

Shriyog Kokare[#], Shrikant Kokare and Ashok Shinde

Department of Physics, Abasaheb Garware College, pune

Email : kokareshriyog@yahoo.com

Abstract:

X- rays are used in medical and many industrial applications. Not only can this but it be also used in material characterisation. The structural characterisation along with its crystal structure can be determined using the X- rays. For this purpose the principle of brags condition ($2d \sin\theta = n\lambda$) is used and the brags spectrometer heaths to characterize the material. Further this X- ray crystallography is used to identify the quality of drugs. The paper gives the details of material characterisation and identifying quality of drugs through the X- ray crystallography.

1. Introduction

The German physicist Wilhelm Rontgen discovered the X-ray in 1895. He is known to be the father of X-ray, because he first studied the X-rays systematically. Due to the high intensity of X-ray, they are used in medical sciences, especially to identify the bone structure. X-rays are also used to detect the fake drugs. Not only this they are also used for cutting the metal in heavy industry. X- ray crystallography is a tool used for identifying the atomic and molecular structure of a crystal. Crystals are regular arrays of atoms, and X-ray can be considered waves of electromagnetic radiation. Along with all these application X-rays are

Brag's law is $2d \sin\theta = n\lambda$. Figure 1 shows geometry of brags condition. In this case we have used $Ba_{0.7}Sr_{0.3}TiO_3$ (1) citrate gel. For thin film $SiO_2/n-Si(100)$ was used as a substrate. The citrate gel was used for thin film making use of spin coating technique with rpm at 4000 and for 1 min duration. Then after deposition of thin film was subjected to heating under the IR lamp for 10 minute. After the required thickness is achieved, the films were annealed at $900^{\circ}C$ for 2 hour. The citrate gel of above was synthesized using modified pichini method.

For crystallography study x-rays are allowed to incident on material under test (MUT). The reflected ray's from MUT is collected in a ionisation chamber on a photographic plate. The intensity of reflected X-rays is measured by changing the angle of incidence Verses intensity. Gives the X-ray spectrograph which will helps to analyse the material. The schematic of X-ray spectrometer used for material characterization is given in figure.

Through this X-ray spectrograph we can obtain the nature, purity, lattice parameter and crustal structure of that crystallized molecule. Using the method of half width principle of maxima we can obtain the particle size also. This $Ba_{0.7}Sr_{0.3}TiO_3$ crystallized molecule nature is crystalline, purity is pure, lattice parameter is $c=a=b=3.970$ AU and crystal structure is cubic.

The nature of X rays whether they were particles or electromagnetic radiation was a topic of debate until 1992. If the wave was correct, researchers knew that the wavelength of this light would need to be on the order of 1 angstrom (10^{-8}

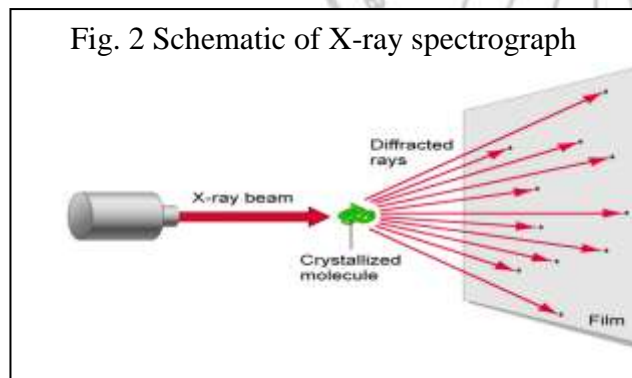


Fig. 2 Schematic of X-ray spectrograph

extensively used in material characterization and material identification

2. Experimental

In case of the Principle of diffraction X ray beam is inserted on the crystallized molecule and then give the diffracted rays on the screen called as film. Means it is called as preparation of thin film. Also one more thing is that the principle of diffraction is depends on the brags condition. The

cm). Diffraction and measurement of such small wavelengths would require a gradient with spacing on the same order of magnitude as length.

3. Result and Discussion

The x-ray spectrograph observed for above synthesized material as shown in figure 3. The

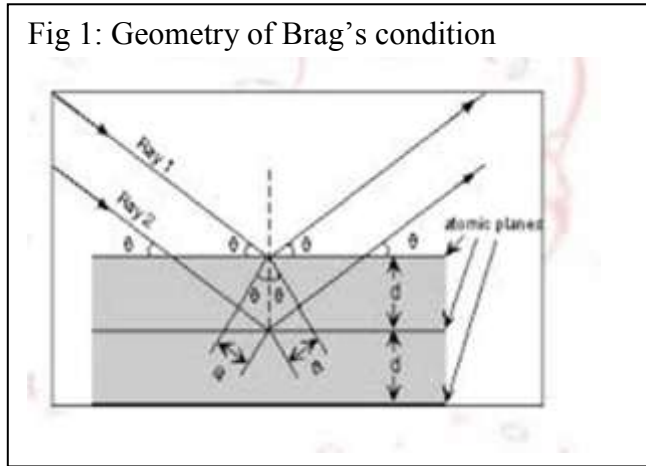


Fig 1: Geometry of Brag's condition

various parameters measured from the X-ray spectrograph are discussed below.

3.1 Nature of material

As we know the materials are either crystalline or amorphous. In case of amorphous material the reflection intensity doesn't change drastically. That is the graph shows more or less constant intensity. Here sharp increase in intensity are quick fall indicates that the material is crystalline.

3.2 Purity

To decide the purity of material the x-ray crystallography helps a lot. If we compare the X-ray spectrograph of synthesized material with the standard JCPDs data, then we can analyze the purity of material. Larger the unindexed peaks in the X-ray spectrograph are the indication of greater impurity. The pure material gives an indexing of all peaks. Here in the case of $Ba_{0.7}Sr_{0.3}TiO_3$ three peaks of intensity at angle (2θ) 33, 63 and 70 could not be indexed with the help of JCPDs data. The literature review suggests that these peaks could be due to the silicon substrate.

3.3 Millar indices

Any of a set of three numbers or letters used to indicate the position of a face or internal plane of a crystal and determined on the basis of the reciprocal of the intercept of the face or plane on the crystallographic axes. In case of crystalline material Millar indices are important which gives the prominent planes (h k l) in the crystal. The material synthesized above clearly gives that the planes like (100), (110), (111), (200), (210), (211), (220) are prominent.

3.4 Lattice parameter

We know that the crystalline material has seven types of crystalline material have seven types of crystal structure depending upon the parameters of unit cell. That is the lattice distance a,b,c and angle α, β, γ . The material synthesized here gives the cubic structure and its parameter can be calculated using Hull and Deavy method (2) The parameters observed are $c=a=b=3.970$ AU and $\alpha=\beta=\gamma=90^\circ$. The above observed parameter suggest that the crystal is of cubic in nature.

3.5 Particle size

While synthesizing any material the particle size is important parameter to be tailored because most of the physico-chemical properties of the materials are particle size dependent. To determine the particle size the method of full width half maxima is used (3). According to this method we got the average size of particle to be 96 nm. This

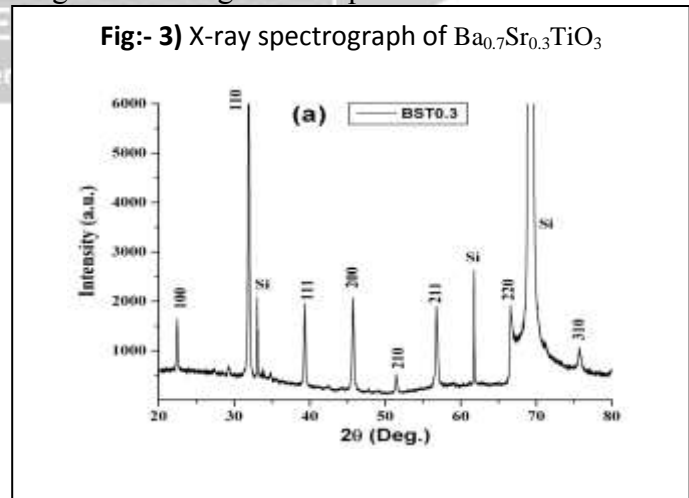


Fig:- 3) X-ray spectrograph of $Ba_{0.7}Sr_{0.3}TiO_3$

size is in good agreement with the size determined with the help of SEM. In other word XRD could be used as a tool for identification of nanomaterial.

4. Conclusion

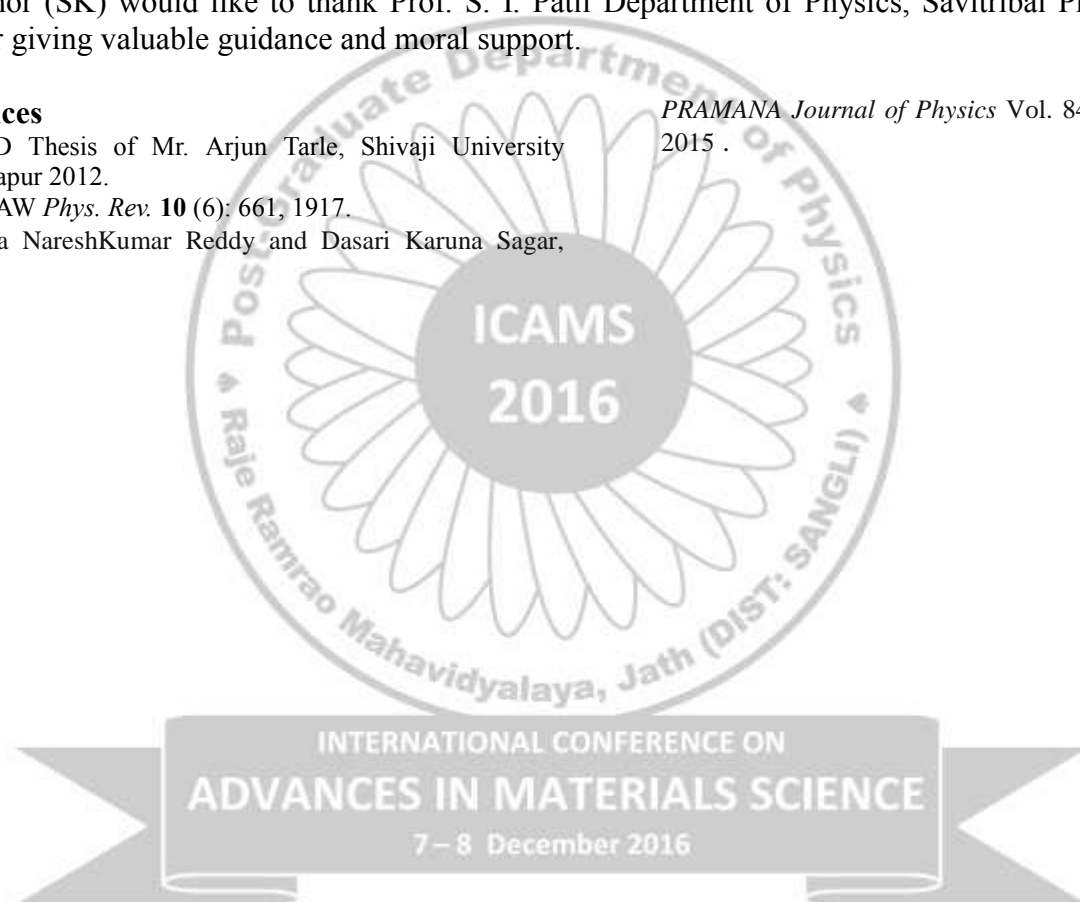
X-rays has many fold application in industry, medicine, research and defence. But from the discussion above we may conclude that X-rays are best and primary tool to character the material. Further excess exposers of human body to the X rays are also dangerous.

5. Acknowledgement

Author (SK) would like to thank Prof. S. I. Patil Department of Physics, Savitribai Phule University, Pune for giving valuable guidance and moral support.

References

1. Ph. D Thesis of Mr. Arjun Tarle, Shivaji University Kolhapur 2012.
2. Hull AW *Phys. Rev.* **10** (6): 661, 1917.
3. Andra NareshKumar Reddy and Dasari Karuna Sagar, *PRAMANA Journal of Physics* Vol. 84, No. 1, 117–126, 2015 .



Investigation to reveal the nature of interaction of human hemoglobin with Gibberillic acid

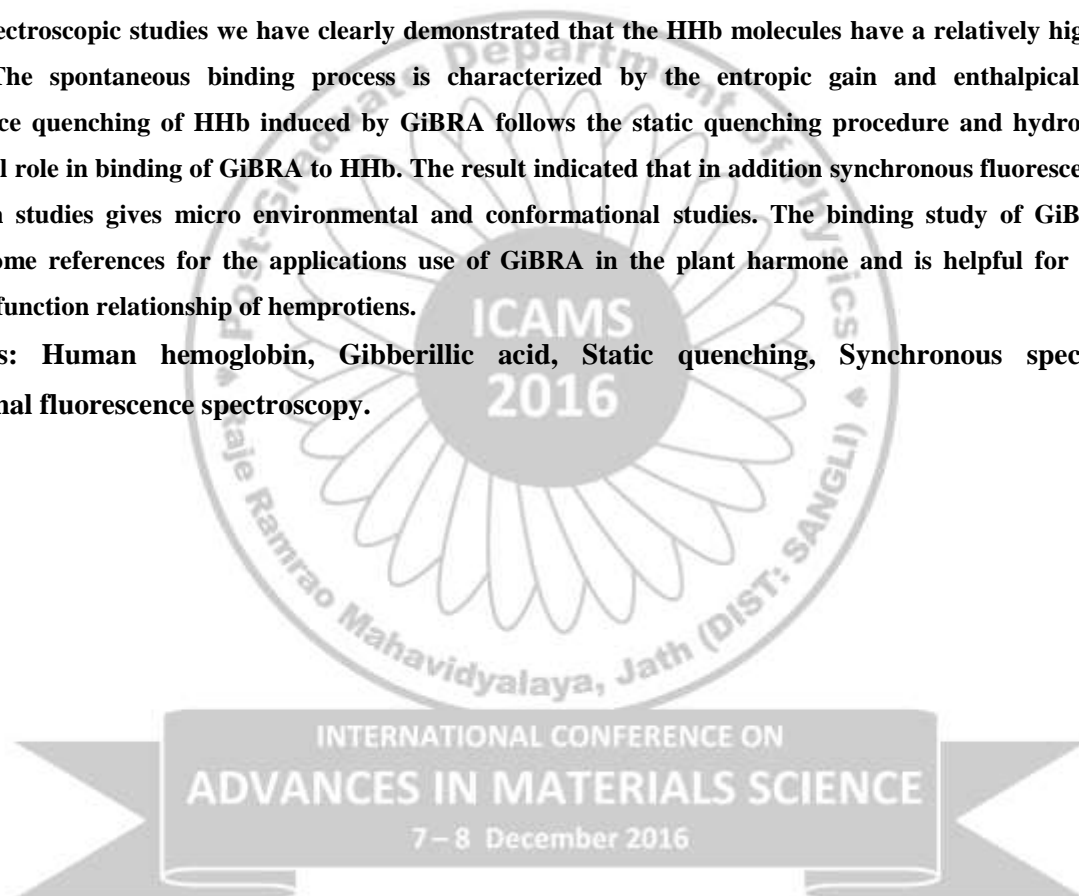
Minakshi V. Patil^a, Laxman S. Walekar^a, Uttam R. Kondekar^a, Prashant V. Anbhule^a, Shivajirao R. Patil^a, Govind B. Kolekar^{a,*}

^aFluorescence Spectroscopy Research Laboratory, Department of Chemistry, Shivaji University, Kolhapur - 416 004, Maharashtra, India.

Abstract:

We have investigated the binding interaction between hemoglobin and gibberillic acid by using multispectroscopic techniques. The binding were confirmed through quenching of the intrinsic fluorescence of the protein. In summary, from critical spectroscopic studies we have clearly demonstrated that the HHb molecules have a relatively high affinity with the GiBRA. The spontaneous binding process is characterized by the entropic gain and enthalpically favorable. The fluorescence quenching of HHb induced by GiBRA follows the static quenching procedure and hydrophobic interaction play a vital role in binding of GiBRA to HHb. The result indicated that in addition synchronous fluorescence and Uv-visible absorption studies gives micro environmental and conformational studies. The binding study of GiBRA and HHb can provide some references for the applications use of GiBRA in the plant hormone and is helpful for understanding the structure-function relationship of hemprotiens.

Keywords: Human hemoglobin, Gibberillic acid, Static quenching, Synchronous spectroscopy, three-dimensional fluorescence spectroscopy.



Chemical Bath Deposition of Cd-Zn-S Thin Film of Solar Cell Application

T.M. Khot, A.N. Pasale, M.S. Ankalagi

Department of physics, Raje ramrao college, Jath. (Maharashtra), India 416404

Email: akashpasle1995@gmail.com

Abstracts:

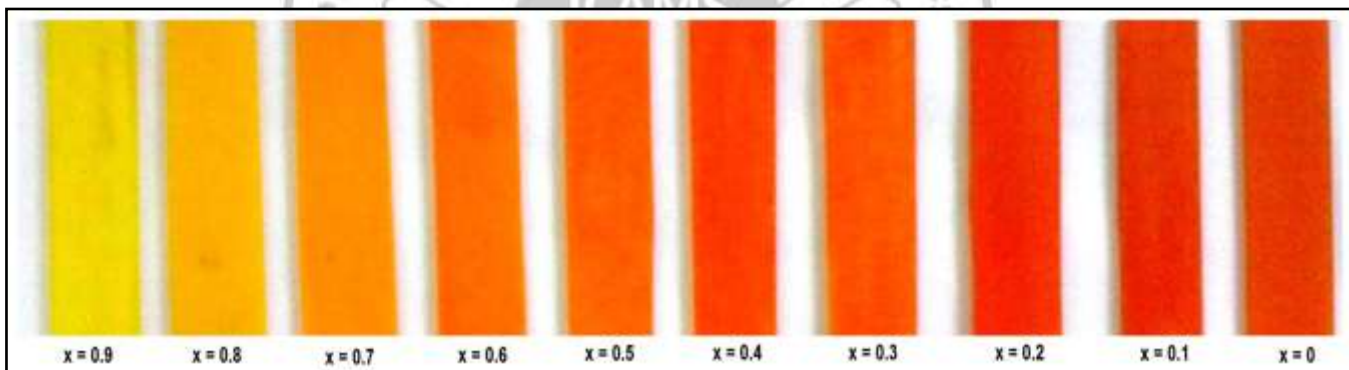
The optical parameter such as absorption coefficient, energy band gap, type of optical transition and refractive index for $Cd_{1-x}Zn_xS$ thin film were estimated using the optical absorption measurements. The optical absorptions measurements were recorded using UV-VIS spectrophotometer (BIO-AGE UV=VIS 2800 PC), in the 300-1500 nm wavelength range.

Introduction:-

Among the various chemical deposition techniques, chemical bath deposition (also referred as solution growth or controlled precipitation or electroless plating) has attracted a great deal of attention, because of its overriding advantages over the conventional methods.

Usually, CBD refers to deposition from an aqueous solution, where the required deposit is both chemically generated and deposited in the same bath.

The chemical deposition method is low cost process and the film is found to be comparable quality to those obtained by more sophisticated and expensive physical deposition process. A chemical deposition has been used to deposit film of metal sulphides, selenide, tellurides and oxides, together with miscellaneous compounds. The range of materials deposited by CBD is extremely wide and there are several possible mechanisms for CBD and often the size of the crystals in the films may depend on the mechanism.



2. Experimental Procedure

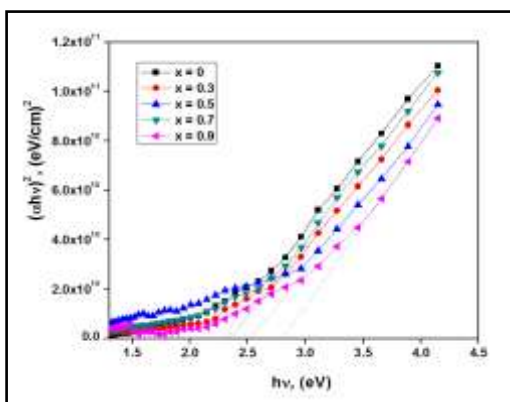
2.1 Sample preparation:

$Cd_xZn_{1-x}S$ ($0 \leq X \leq 1$) thin films were obtained onto the optically plane and throughly cleaned glass substrate using aqueous alkaline chemical bath deposition.

The actual deposition of $Cd_{1-x}Zn_xS$ was carried out in an alkaline medium. Initially the precursor for Cd^{+2} , Zn^{+2} & s^{-2} were prepared in double distilled water. For each of materials out of this series, the film deposition stiochiometry was maintained by adjusting the ion concentration volumes of the Cadmium sulfate and Zinc sulfate.

2.2 Characterization:

The optical parameter such as absorption coefficient, energy band gap, type of optical transition and refractive index for CdS and $Cd_{1-x}Zn_xS$ thin film were estimated using the optical absorption measurements. The optical absorptions measurements were recorded using UV-VIS spectrophotometer (BIO-AGE UV=VIS 2800 PC), in the 300-1500 nm wavelength range.



3 Result and discussion:-

3.1 Physical Observations:

Optical Measurements:

The $Cd_{1-x}Zn_xS$ thin film must exhibit intermediate optical band gap energy values between the two energy gap limits. The nature of the variation in the optical to gap may be useful to design a suitable top or absorber material depending on Zinc concentration.

Composition Parameter (X)	Energy Bandgap (eV)
0	2.27
0.3	2.32
0.5	2.52
0.7	2.36
0.9	2.80

Conclusions

In this project report, we have presented our studies on chemical bath deposition (CBD) of Cd-Zn-S thin films. State-of-the-Art CBD method is simple, inexpensive and capable of yielding nano-crystalline thin films, such metals chalcogenide films are technologically important in devices such as solar cell, photo-electrochemical cells, solar selective coatings, dye sensitized cells, gas sensor, etc. where large sample area is desirable.

References

1. S T Mane, Ph.D. Thesis, Thin film & Solar Studies Research Laboratory, Department of Physics, Solapur University, Solapur (2012).
2. S T Mane, S S Kamble, L P Deshmukh, Materials Letters, (2011), 65, pp. 2639-2641.
3. V S Karande, S H Mane, V B Pujari, L P Deshmukh, J. Mater. Sci. Mat in Electronics, (2004), 15, pp. 419.
4. Ramadan, A M El-Shabiny, A Ashour, Egypt. J. Solids 1986. 8:p. 110.
5. C W Huang, H M Weng, Y L Jiang, H Y Ueng, Vacuum, 83 (2008), 313-318.
6. J M Fatah, T Piorek, P Harrison, T Stirner, W E Hangston, Phys Rev B 49 (1994), 10341-4.



Coersivity, Magnetic moment, Remnent and Saturation magnetization of nanoparticle sized Aluminium substituted copper cobalt ferrites

S.S. Karande¹, S. A. Masti², M.S. Kavale¹, B.R.Karche³

¹Department of Physics, Sangameshwar college, Solapur.(M. S.)

²Dr. Ghali College, Gadhinglaj (M.S.)

³Material Science and Thin Film Laboratory, Shankarrao Mohite Mahavidyalaya, Akluj.Dist: Solapur (M.S)

Abstract:

The polycrystalline aluminium substituted nano-particle sized copper cobalt ferrite samples $\text{Cu}_x\text{Co}_{1-x}\text{Fe}_{2-2y}\text{Al}_{2y}\text{O}_4$ (where $x=0.0, 0.2, 0.4, 0.6, 0.8, 1.0$; $y = 0.05, 0.15$ and 0.25) have been prepared by standard ceramic technique. Phase formation is investigated using X-ray diffraction, Infrared absorption technique and Scanning electron microscope technique. Magnetic properties of the samples are investigated by using Vibrating Sample Magnetometer (VSM) and Helmholtz's double coil apparatus. The lattice constants of the all samples are evaluated from x-ray diffraction data. A universal testing machine as well as Archimedes's method was applied for determining the physical properties of the samples. Ionic radii R_A and bond lengths (A-O) on both sites are found decreases with Al^{3+} and copper content. The Lattice constant 'a', physical density as well as X-ray density of samples goes on increasing with Al^{3+} and copper content. The ratio c/a is found increasing when addition of copper content and decreases with aluminum content. It means that Al^{3+} and copper acquire the tetragonal prolate type distortions on B site and hence (c/a) ratio increases and automatically crystal lattice turned from tetragonal spinel to cubic spinel. Addition of Al^{3+} replaces Fe^{3+} on A-site and hence magnetic moment per unit values decreases. Copper cobalt ferrite exhibits canting of spins of magnetic moments on B-site. The canting angle α_{yk} is found decreasing with Al^{3+} content in the host lattice.

KEY WORDS:-polycrystalline, standard ceramic technique, magnetic moment, canting angle

Introduction:

In a way, every material utilized today is a composite. Composite materials are a physical mixture of two or more compatible micro or macro constituent particles which differ in form and chemical composition and are essentially insoluble in each other. Composite materials are best suited for scientific applications which could not be achieved by any one component acting on its own properties. Ferrite / ferroelectric composites are termed as magneto electric (ME) composites due to the coupling between the electric and magnetic fields in the materials. The conversion of magnetic to electric fields in such ME composite originates from the elastic interaction between ferrite and ferroelectric subsystems [1]. In the presence of the magnetic field, the magnetostriction in the ferrite phase gives rise to mechanical stresses that are transferred to the ferroelectric phase, resulting in electric polarization of the ferroelectric phase owing to its magneto electric effect. ME materials find applications as smart materials in actuators, sensors, magnetic probes, phase inverters, rectifiers, modulators, and transducers in solid state microelectronics and microwave devices [2,3].

Spinel ferrite nanoparticles are being intensively investigated in recent years because of their remarkable electrical and magnetic properties and wide practical applications in information storage system, ferro-fluid technology, magnetocaloric refrigeration and medical diagnosis [4]. Among the spinels, mixed Zn ferrites and especially Ni-Zn ferrites are widely used in applications like transformer cores, chokes, coils, noise filters recording heads etc. [5]. While Ni-Zn ferrite possesses higher resistivity and saturation magnetization, cobalt ferrite possess high cubic magneto crystalline anisotropy and hence high coercivity. The high coercivity is driven by large anisotropy of the cobalt ions due to its important spin orbit coupling. It is ferromagnetic with a Curie temperature (T_c) around 520°C , [6] and shows a relatively large magnetic hysteresis which distinguishes it from rest of the spinels. The synthesis of ultra fine magnetic particles has been extensively investigated in recent years because of their potential applications in high density magnetic recording and magnetic fluids [7]. Among the current methods for synthesis of mixed ferrite the combustion reaction method stands out as an alternative and highly promising method for the synthesis of these ferrites [8]. Magnetic properties

measured at room temperature by vibrating sample magnetometer (VSM) reveal an increase in saturation magnetization with increase in cobalt concentration [9].

Experimental:

The ferrites with general chemical formula $Cu_xCo_{1-x}Fe_{2-2y}Al_{2y}O_4$ (where $x = 0.0, 0.2, 0.4, 0.6, 0.8, 1.0$; $y = 0.05, 0.15$ and 0.25) were prepared by the standard ceramic technique using AR grade cobalt oxide, copper oxide, ferric oxide and aluminium oxide. The compositional weights of powders were mixed physically and blended in agate mortar in acetone medium. The final sintering process was carried at $1000^{\circ}C$ for 48 hours. The slow cooled samples were heated at rate of $80^{\circ}C$ per hour. The pellets and toroids were formed by using respective steel die. A universal testing machine as well as Archimedes's method was applied for determining the physical properties of the samples. The formation of the cubic spinel structure of the samples prepared is confirmed by X- ray diffraction analysis. Saturation

magnetization of each was carried out using high-field hysteresis loop tracer and presented in fig.2. The saturation magnetization (σ_s), magnetic moment (n_B) were determined from the magnetization study and presented by graphs (Fig.3)

Results and discussion:

The lattice constants 'a' and 'c' for all prepared samples are calculated by using prominent (311) XRD peak [10]. The calculated and observed values of inter planer distance (d) are found in good agreement with each other for all reflections. The particle size (D) for all the ferrite samples is calculated by Debye Scherer formula, ionic site radii (R_A, R_B) and ionic bond lengths (A-O, B-O) are calculated from the formulae given by Gadkari et.al [11]. From the calculations of lattice constants 'a' and 'c' for all the prepared ferrites; it is observed that $c > a$; tetragonality ratio (c/a) is found in the range of 1.03 to 1.07. This result is in good agreement with previous report [12-13].

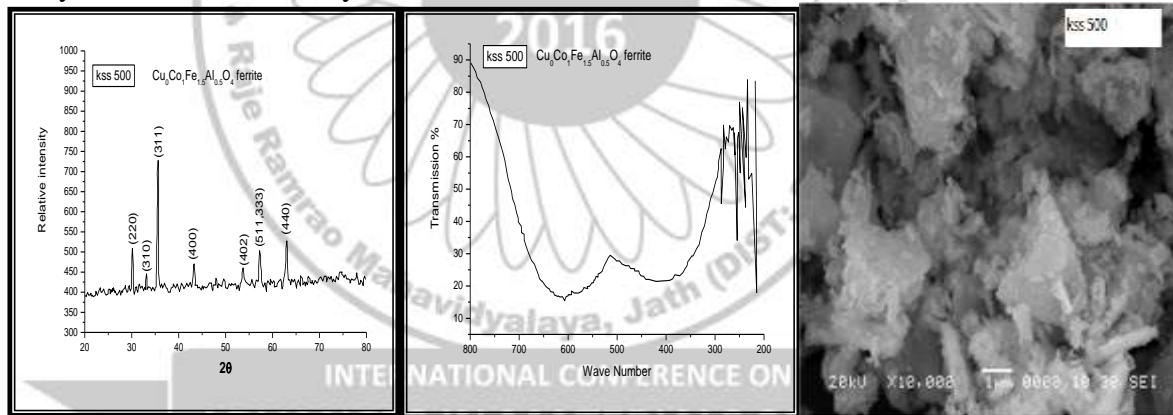
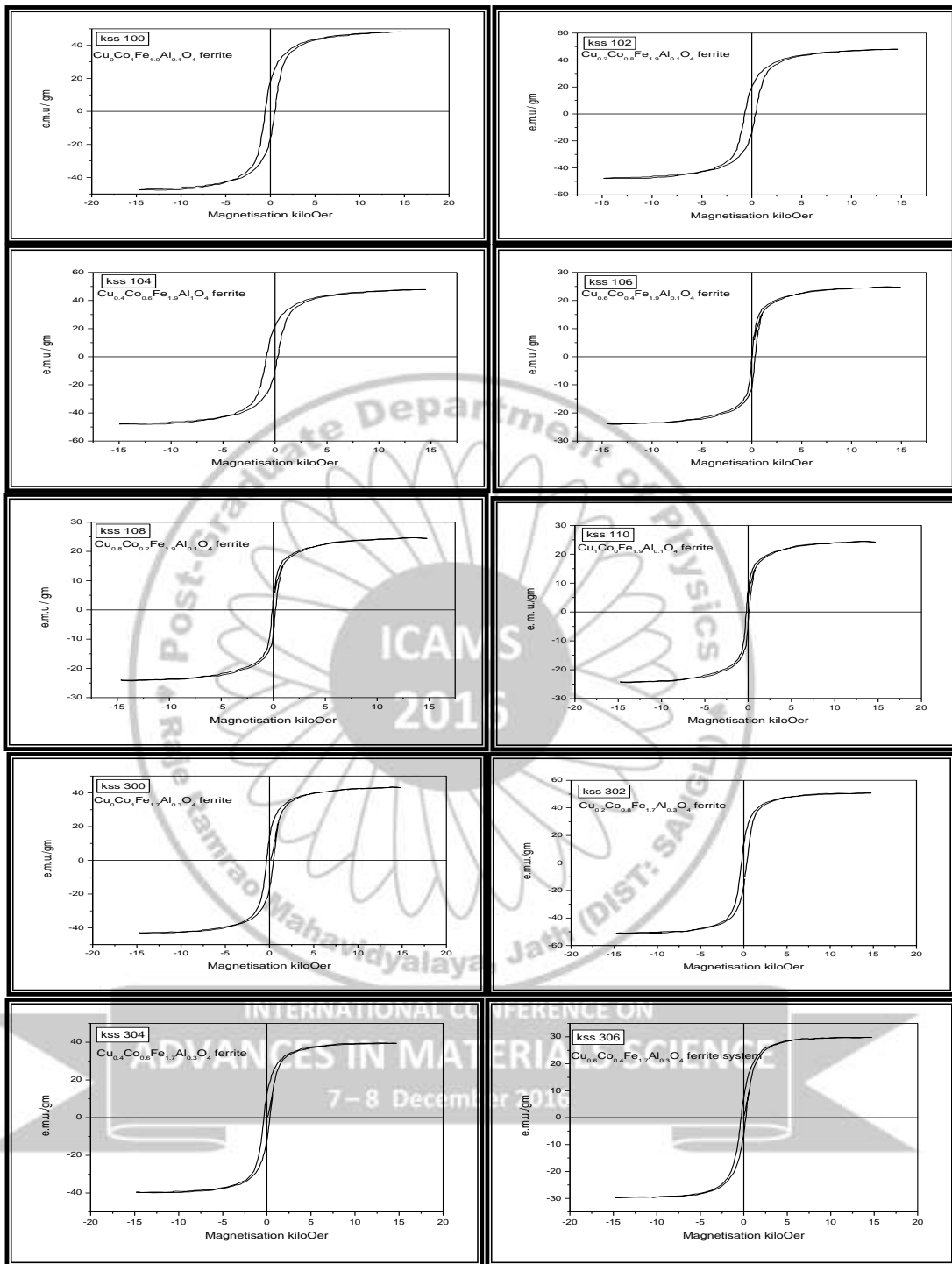


Fig: 1 Characterisation of ferrite samples by XRD,IR, SEM

The infrared absorption spectra showing two distinct absorption band ν_1 due to tetrahedral (A) site interstitial voids near 600 cm^{-1} and other ν_2 due to octahedral (B) site interstitials voids near 400 cm^{-1} . Our results in this present communication are well supported by previous reports [14, 15].

The close inspection of all micrographs revealed that there is continuous grain growth with well defined grain boundaries formed. The present system shows multi domain behaviour. No exaggerated grain growth is observed in any of this composition. The average grain size is found to

decrease with increase in Al content in copper cobalt ferrite. However in the present system the grain growth shows generally a decreasing trend with aluminum content, which is rather expected because of multi-domain behavior of these compositions in copper cobalt ferrite. Grain growth is almost accompanied with grain size, which is increasing with copper and aluminum content. So it appears that copper and aluminum content favours the grain growth. The scanning electron micrograph was shown above.



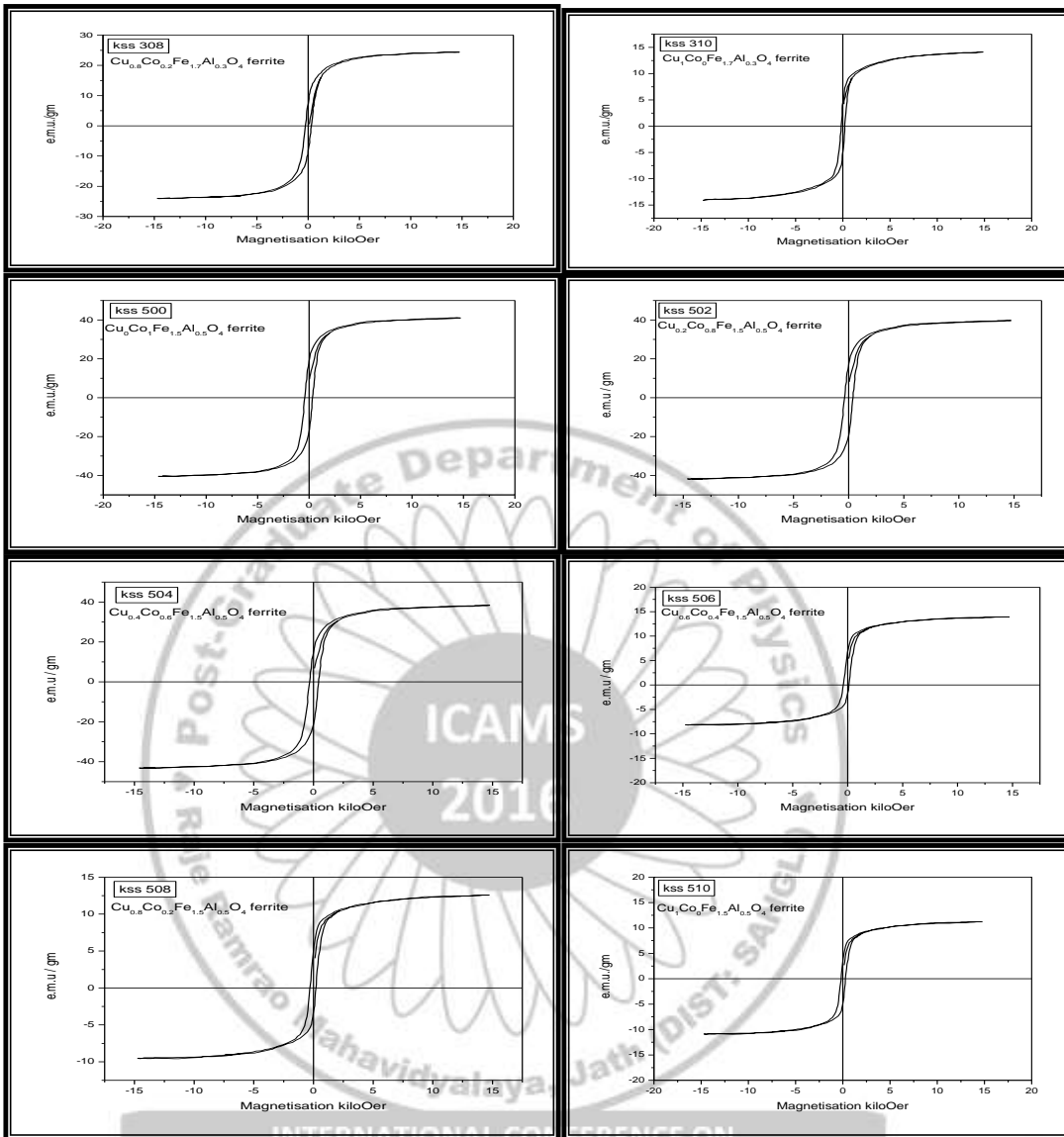
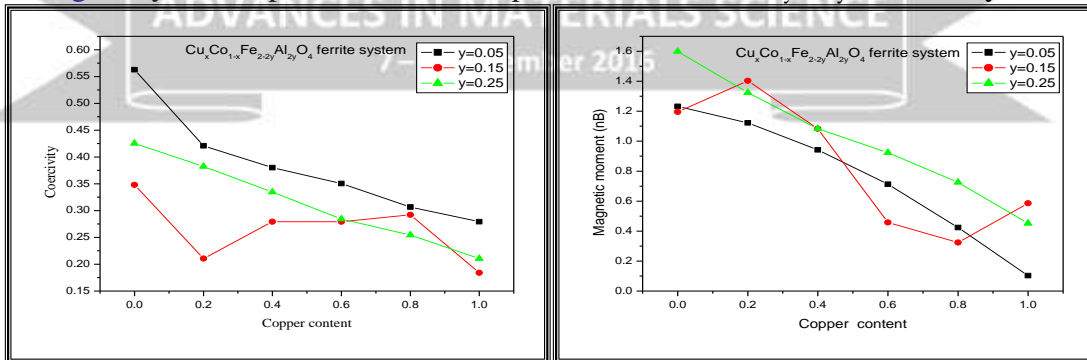


Fig. 2. Hysteresis patterns of the samples for $\text{Cu}_x\text{Co}_{1-x}\text{Fe}_{2-2y}\text{Al}_{2y}\text{O}_4$ ferrite system



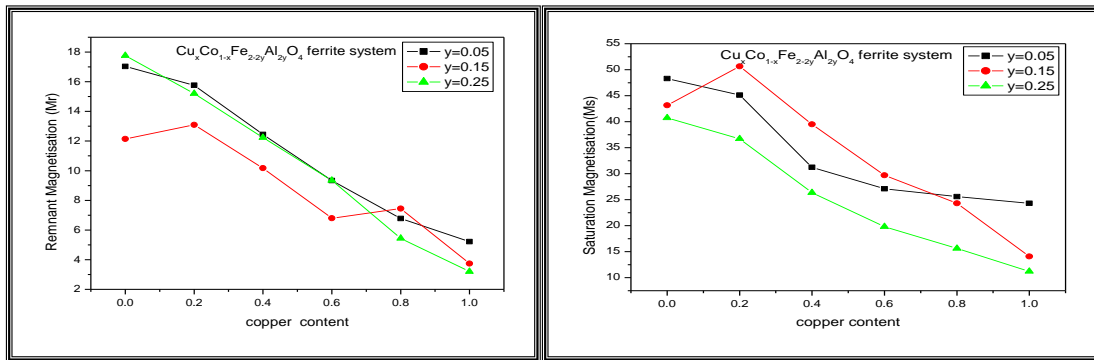


Fig 3: Variation of coersivity, magnetic moment, Remnent magnetization and saturation magnetization with copper and aluminium content for $Cu_xCo_{1-x}Fe_{2-2y}Al_{2y}O_4$ ferrite system

The value of n_B was observed which goes on decreasing for aluminium doped copper cobalt ferrite with increasing aluminium and copper content. Addition of Cu^{2+} content replaces Fe^{3+} from A to B site which produces canting of the magnetic spins and results in the decrease in both magnetic moments on A and B sites. This clearly indicates the decrease in A-B interaction.

Saturation magnetization is found increasing upto 20 % of copper content and thereafter decreases. The increasing trend of saturation magnetisation with Cu^{2+} content up to $x=0.2$ suggest that the Neels two sub-lattice model is predominating up to $x = 0.2$ and thereafter Y-K three sub lattice predominant. The decrease in saturation magnetization (Ms) can also be explained in the light of Yafet-Kittle model of triangular spins.[16]

The coercivity decreases with particle size as suggested by Liu et al. The large value of coercivity essentially originates from the anisotropy of the copper ions at the octahedral (B) site due to its important spin orbit

coupling. The coercive field (H_c) in Al doped copper cobalt ferrite is found to decrease with increasing Aluminium content in the doped copper cobalt ferrites, which may be attributed to the loss of anisotropy due to the migration of Cu^{2+} ions to the tetrahedral site and also due to the decrease in the ferrous content in doped copper cobalt ferrite. The decrease in coercivity of samples is accompanied by the reduction of saturation magnetization and remnant magnetization. The reason for the decrease in coercivity of copper cobalt ferrite is the decrease in magneto-crystalline anisotropy by lowering the concentration of Fe^{2+} ions at the octahedral sites in the spinel lattice because Fe^{2+} ions are also a source of the magnetic anisotropy in ferrites.

The remnant magnetization (Mr) of Al^{3+} doped copper cobalt ferrite shows a decreasing behaviour with increase in copper and Al content from $x = 0.00$ to $x = 0.1$ and $y=0.05, 0.15, 0.25$. The decrease in Mr is due to lower magnetic moment of Al^{3+} as compared to Fe^{3+} .

Conclusion:

Copper cobalt ferrite is partially inverse spinel ferrite. addition of al^{3+} ions replaces fe^{3+} on (b) site resulting in increase of lattice constant a, decrease in ionic radii(r_a) and bond length(o-a). the lattice constant obtained from xrd data shows increases. the coersivity (hc), magnetic moment(n_b), remnent magnetization (mr) and saturation magnetization (ms) with copper and aluminium content goes on decreasing.

References:

1. R. S. Devan, S. A. Lokare, S. S. Chougule, D. R. Patil, Y. D. Kolekar, and B. K. Chougule, J. Phys. Chem. Solids **67**, 1524 (2006).
2. K. Zhao, K. Chen, Y. R. Dai, J. G. Wan, and J. S. Zhu, Appl. Phys. Lett. **87**, 162901 (2005).
3. S. R. Kulkarni, C. M. Kanamadi, and B. K. Chougule, Mater. Res. Bull. **40**, 2064 (2005).
4. Zhao L, Yang H, Yu L, Cui Y, Zhao X, Zou B, Feng SJ. MagnMagn Mater2006;301:445-51.
5. Rath C, Sahu KK, Anand S, Date SK, Mishra NC, Das RP. J MagnMagn Mater 1999;202:77-84.
6. Rajendran M, Pullar RC, Bhattacharya AK, Das D, Chintalapudi SN, Majumdar CK. J MagnMagn Mater 2001;232:71-83.
7. Ozaki M. Mater Res Bull 1989;12:35-43.
8. Costa ACM, Tortella E, Morelli MR, Kaufman M, Kiminami RHGA. J Mater Sci2002;37:3569-72.
9. M.M. Mallapur, B.K. Chougule; Materials Letters; Vol. 64 (2010); P. 231-234.
10. H. P. Klug, L. E. Alexander, X-ray diffraction procedure for polycrystalline and amorphous materials,(Wiley N.Y 1997)637.
11. A. B. Gadkari, T. J. Shinde, P. N. Vasambekar, J. Mater Sci: Mater Electron 21 (2010) 96-103.
12. A. T. Raghavender, R. G. Kulkarni and K.M. Jadhav; Chinese J. of Phys.vol.48 No.4 (2010) 512-522.
13. A.T. Raghvendra et al. magn. Mater. 316 (2007) 1
14. Waldron R.D, Phy.Rev.; 99(6) (1955)1727.
15. K. V. S. Badarinath, Phys. Stat. Solidi (a) 91(1985)K-19-23.
16. Yafet Y, Kittel C, (1952), Antiferromagnetic arrangements in ferrites, Phys. Rev.; Vol. 87; P. 290.

Column Chromatographic Separation of Iron and copper from Immobilization of Cation Exchanger Resin with derivatives of Phosphine Oxide

S. H. Burungale; A.N. Bhingare

Department of Chemistry, Yashwantrao Chavan College of Science, Karad-415124 (India)

Email: shivajiburungale777@gmail.com

Abstract:

Column chromatography is versatile technique and has been applied successfully to the separation of Fe (III) ion from stationary phases. In Trioctylphosphine oxide has been used for the extraction chromatographic separation of other metal ions. The investigation of the extraction chromatographic separation of Iron and copper on a Cation exchanger resin column with triethylphosphine oxide as the stationary phase. Method is presented for the separation of iron with copper and a large number of elements in multi- component mixtures. The method has been extended to the determination of Iron in various samples.

Keywords: Synthesis of immobilization of TOPO with cation exchanger resin separation of Fe (III) and Cu (II); Analysis of ore & Pharmaceutical samples

1. Introduction

The interest in the separation and determination of trace metals in natural water has increased in the last decades because of the environmental problems and public health studies. Iron in small amounts is essential for humans and animals. Iron deficiency caused anemia and much may cause several health problems (cancer, heart disease, arthritis, diabetes and liver diseases. Iron was restricted to 2 mg L^{-1} by World Health Organization and $200 \text{ } \mu\text{g L}^{-1}$ by European Legislation. Due to the very low concentration of iron and the interfering effect of the matrix, its determination demand very sensitive analytical techniques [1-6]. Separation and pre concentration were applied to overcome these difficulties. Many procedures are well characterized for such a purpose [7-8]. Of all, solid phase extraction (SPE) has attracted a great attention owing to its simple operation, rapid phase separation, no emulsification, high enrichment factor and for easily automation. Organic chelating resins [9], polymer inclusion sorbents [10], modified nanometer-sized alumina [11], C18-bonded silica gel [12], controlled-pore glass [13], activated carbon [14], ion exchange resins [15], thermal modified kaolinite polymeric resin [16].

2. Experimental

2.1. Apparatus

Graduated apparatus of standard calibration were used for measurements. All glassware's were washed with nitric acid (5% v/v) new glassware's were allowed to stand for several hours in nitric acid.

After three rinses with distilled water, and the glassware's were stored under dust free conditions.

2.2. Equipments

Spectrophotometer: Systronic India Ltd. Model No pH meter, Digital Balance

2.3. Reagents

All reagents used were of analytical grade. Double distilled water was used for solution preparation. The reagents used in this study were immobilization of baker yeast with trioctyl phosphine oxide polymeric resin, Ferric Chloride (99.5%, hydrochloric acid (37%).

2.4. Stock solution

Ferric nitrate solution: Dissolve 3.62 grams of reagent grade $\text{Fe}(\text{NO}_3)_3 \cdot 9\text{H}_2\text{O}$ in 500 ml of one per cent HNO_3 to prepare a solution that contains approximately 1 mg of iron(III) per ml. Standardize the solution versus potassium dichromate after reducing the iron(III) to iron(II) with stannous chloride and mercuric chloride. Working solutions for trace analysis were prepared daily by appropriate dilutions. Weigh exactly approximately 39 mg of $\text{CuSO}_4 \cdot 5\text{H}_2\text{O}$ (not dried, formula weight 249.68) into a 100 mL volumetric flask. Dissolve in water and dilute to 100 mL.

2.5. Preparation of column extractant.

The chromatographic column was made of a borosilicate glass tube, bore 8mm, length 25 cm, fitted with glass – wool plug at the bottom. 0.1 M TOPO solution was prepared by dissolving 1.94 g of reagent in 25 ml of water. Dowex-50 resin (BDH) (60 – 120 mesh) was dried at 120°C for 2-3 hours

and stored in desiccators. Some of the Dowex -50 resin and Trioctyl phosphine oxide is mixed with each other and packed in a U-tube through which is passed a stream of dry nitrogen that had been bubbled through a 20 ml of dimethyldichloro silane (DMCS) vapour was continued for 3-4 h. Dowex -50 resin containing Trioctyl phosphine was then washed with water and dried. A slurry of the coated Dowex -50 resin in distilled water was prepared by centrifugation at 2000 rpm and be the coated resin was packed into the chromatographic column to given a bed height of 6 cm. The bed was then covered with a glass wool plug and the column extractant

2.6. General procedure:

100 µg of Fe (III) was mixed with Hydrochloric acid in the concentration range of 0.05M to 2.4M in a total volume of 10 mL. The solution was then passed through Immobilized TOPO resin column pre-conditioning with same concentration of hydrochloric acid as that of the sample solution at flow rate of 0.5 mL/min. The column was then washed with the same concentration of hydrochloric acid. The sorbed Fe (III) was then eluted with different eluting agents at the flow rate of 0.5 mL/min. The fractions of 25 mL were collected and the Fe (III) content was determined spectrophotometrically with potassium thiocyanate [17, 18] at 490 nm.

3. Results And Discussion

Adsorption of Fe (III) on Immobilized TOPO resin as a function of Hydrochloric acid concentration. Sorption studies of Fe (III) were carried out from hydrochloric acid medium. The concentration of Hydrochloric acid varied from 0.05 M to 2.4 M. After sorption, Fe (III) was eluted with 2.0 M hydrochloric acid. It was found that there is quantitative (100%) sorption of Fe (III) from 0.5 M to 2M hydrochloric acid concentration. Further decrease in hydrochloric acid concentration there is decrease in sorption of Fe (III) shown in Table 1, Figure 1. The subsequent sorption studies of Fe (III) were carried out with 1.4M hydrochloric acid.

3.1. Elution study of Fe (III) with various eluting agents:

100 µg of Fe (III) in 0.05M to 2.4 M hydrochloric acid was sorbed on cation exchange resin with TOPO resin. After sorption, Fe(III) was eluted from column with various eluents such as hydrochloric acid, hydrobromic acid, sulfuric acid, perchloric acid and acetic acid. The concentration of eluting agent varied from 0.05 M to 4.0 M. Various elution studies revealed that, there is quantitative elution of Fe(III) with 25 mL of 4.0 to 8.0 M hydrobromic acid and 1.0 to 4.0 M sulfuric acid whereas perchloric acid and acetic acid were found to be inefficient eluents. Further elution studies of Fe(III) in this work were carried out with 4.0 M hydrochloric acid.

3.2. Sorption of Fe (III) on Immobilized TOPO resin as a Function of hydrochloric acid concentration:

Sorption studies of Fe (III) were carried out from hydrochloric acid medium. The concentration of hydrochloric acid varied from 0.05M to 2.4M. After sorption, Fe(III) was eluted with 4.0 M hydrochloric acid. It was found that there is quantitative (100%) sorption of Fe(III) from 0.5M to 2 M. hydrochloric acid concentration. Further decrease in hydrochloric acid concentration with decrease in sorption of Fe (III). The subsequent sorption studies of Fe(III) were carried out with 1.4 M. hydrochloric acid

Table 1. Sorption of Fe (III) as a function of hydrochloric acid concentration

Concentration of Iron µg	Adsorption of Fe (III).
100	100
200	100
400	100
600	100
800	100
1000	100
1200	80
1400	65
1600	45
1800	30

Hydrochloric acid Concentration M	Adsorption of Fe (III) %
0.05	90
0.06	97
0.07	99
0.08	99
0.1	100
0.2	100
0.4	100
0.6	100
0.8	100
1.0	100
1.2	98
1.4	78
1.6	54
1.8	12
2.00	00

Table:2 Effect of varying concentration of Fe(III):.

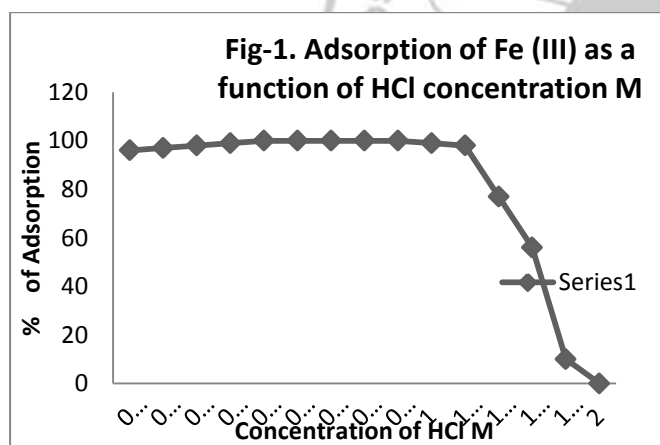


Fig-1. Adsorption of Fe (III) as a function of Hydrochloric acid concentration M

3.3. Effect of varying concentration of Fe (III) :

The capacity of the Immobilized TOPO resin for Fe (III) was evaluated by using 4.0 g of Immobilized TOPO resin and sorption studies were carried out from 1.4 M hydrochloric acid and 4.0 M hydrochloric acid as an eluent. The volume of Fe (III) sample solution was 10mL. The concentration of Fe(III) was varied from 100-2000 µg of Fe(III) Per10 mL of solution. The result shows that sorption of Fe (III) is quantitative up to 1500 µg/10 mL. Further decrease in percentage sorption ion with increase in concentration of Fe (III) ion as shown in

Table 2, the capacity of the Immobilized TOPO resin for Fe (III) was found to be 0.87 ±0.01 mmol/g Immobilized TOPO resin.

3.4. Multicomponent separation:

Separation of Fe(III) was carried out from number of associated elements in multicomponent mixture. The mixture containing Mg(II), Cu(II) and Fe(III) was passed through the Immobilized TOPO resin at 1.5 M HCl. The Mg(II) was not sorbed and hence passed through the column. The Cu(II) and Fe(III) remains on the column. The sorbed Fe(III) was first eluted with 25 mL of 2 M HCl after which Cu(II) was eluted with 0.5 M nitric acid. Using this method other multicomponent mixtures were separated and the results are shown in Table 3.

Table 3. Multicomponent mixture separation (Sorption)

Sr.No.	Mixture	Taken µg	Found µg	Recovery %	Eluent
1	Mg(II),	100	99	99	NSPC
	Fe(III)	100	98	98	2 M HCl
	Cu(II)	100	99	99	0.5 M HNO ₃
2	Ca(II),	100	99	99	NSPC
	Fe(III)	100	98	98	2 M HCl
	Cu(II)	100	99	99	0.5 M HNO ₃

3.5. Determination of Iron in real sample

Geological sample: 0.550 g of Hematite ore was heated up to 700 0C for 2 hrs to remove organic matter and was treated with concentrated HNO₃, the mixture was heated to moist dryness. The procedure was repeated for thrice and extracted with distilled deionized water. The hot solution was filtered, diluted and Fe (III) Content was determined by proposed method. The obtained results are shown in Table 4.

Table 4. Determination of Fe (III). From geological samples

Sample	Amount of Fe(III). found By		
	AAS	Proposed Method	Standard deviation (± 2 %)
Hematite ore	43%	42.5%	0.2%

3.6. Determination of Fe (III) in pharmaceutical samples

A tablet of drug or vitamin was digested using 5 mL of concentrated HNO₃ and dryness. After cooling, the residue was dissolved with another 5 mL of the acid. The solution was gently evaporated on a water bath till a residue was again left. It was heated with 50 mL of doubly distilled water, filtered off and completed to 100 mL in a calibrated flask. After adjusting the pH, the procedure for the determination of Fe (III) was applied (column mode). The recovered amount of Fe (III) was determined and the results are listed in Table 5.

Pharmaceutical tablets	Mineral Composition mg/tablet	Recovery % Fe(III)
Gerimax	Mg(II) 150 mg ,Fe(II) 14mg Mn(II)2.5 mg ,Zn (II)15 mg Cr(III) 0.05 mg	13.5 ± 0.02 100%
Centrum	Ca(II) 162 mg, Mg(II) 100 mg ,Fe(II) 27mg, Mn(II)7.5mg ,Zn (II)22.5 mg K 7.5mg, Cu 3.00 mg.	26.70± 0.02 99.15 %
Totavit	Cr 25 mg, Mn 2.5 mg, Fe 18 mg, Cu 2.00 mg Zn 15 mg	17.88± 0.02 99.65 %

4. Conclusion

A simple, rapid and selective column chromatographic method for the separation and determination of Fe (III) from other toxic metal ions using Immobilized TOPO resin in hydrochloric acid medium has been developed. In addition to adopting a simple method, the method extends for the determination of Fe (III) from real samples. The results obtained by this method were in good agreement with AAS results.

References

- Mondal, B.C.; Das, D.; Das, A.K. *Talanta* 2002, 56, 145-152.
- Scindia, Y.M.; Pandey, A.K.; Reddy, A.V.R.; Manohar, S.B. *Anal. Chem.* 2002, 74, 4204-4212.
- Pu, X.L.; Jang, Z.C.; Hu, B.; Wang, H.BJ. *Anal. At. Spectrom.* 2004, 19, 984.
- Mahmoud, M.E.; Gohar, G.A. *Talanta* 2000, 51, 77-87.
- Bruhn, C.G.; Pino, F.E.; Campos, V.H.; N'obrega, J.A. *Anal. Bioanal. Chem.* 2002, 374, 131.
- Cerutti, S.; Silva, M.F.; G'asquez, J.A.; Olsina, R.A.; Martinez, L.D. *Spectrochim. Acta Part B* 2003, 58, 43-50.
- Hassanien, M.M.; Hassan, A.M.; Mortada, W.I., El-Asmy A.A. *Am. J. Anal. Chem.* 2011, 2, 697-709.
- Afzali, D.; Taher, M.A.; Mostafavi, A.; Mobarakeh, S.Z.M. *Talanta* 2005, 65, 476-480.
- Taher, M. A. *Talanta* 2000, 52, 301-309.
- Taher, M.A. *Analyst* 2000, 125, 1865-1868.
- Mortada, W.I.; Hassanien, M.M.; El-Asmy A.A. *J. Trace Elements in Medicine and Biology*, 2013, 27, 267-272.
- Huang, W.H.; Hu, B.; Xiong, H.C.; Jiang, Z.C.. *J. Anal. Chem.* 2000, 367, 254.
- Xiong, H.C.; Hu, B.; Peng, T.Y.; Chen, S.Z.; Jiang, Z.C. *Anal. Sci.* 1999, 15, 737.
- B. S. Mohite, B. E. Mahadik & S. H. Burungale, *Res. J. Chem. & Environment*, 1998, 2, 43-45.
- B. S. Mohite, S. H. Burungale, B. E. Mahadik & D. N. Zambare, *Ind. J. Chem.*, 1998, 37A, 1035-37.
- B. S. Mohite & S. H. Burungale, *J. Chemical & Environ. Research*, 1998, 7(3-4), 205-212.
- S. H. Burungale, *International Journal of Analytical and Bioanalytical Chemistry* 2015; 5(2): 48-52

Comparative study of TiO₂, ZnO and hybrid TiO₂-ZnO thin film composites prepared by hydrothermal technique

Dadaso B. Shinde¹, Popatrao N. Bhosale³, Uday Patil, Raghunath K. Mane²,

¹Shri Pancham Khemraj Mahavidyalaya, Sawantwadi. Dist. Sindhudurg.

²Smt.K.R.P. Kanya Mahavidyalaya, Islampur-415 409, Tal. Walwa, Dist. Sangli,

E-mail: rmane.1970@gmail.com

³Materials Research Laboratory, Department of Chemistry, Shivaji University, Kolhapur

Abstract:

In the present investigation, we have used simple, hydrothermal reflux technique to deposit TiO₂, ZnO and hybrid TiO₂-ZnO thin films. As deposited films were studied for its structural, morphological, optical, and compositional analysis by XRD, SEM, UV-Vis-NIR spectrophotometer and EDS analysis techniques respectively. XRD study revealed that the films are nanocrystalline in nature and exhibit TiO₂ is rutile and ZnO in hexagonal crystal structure. The SEM micrograph shows the formation of nanorods and 3D nanorod flowers on the surface morphology. EDS results confirm the presence of Ti, Zn and O elements in the synthesized thin film. The band gap values of thin film were calculated from the absorption spectra which are found to be 2.95, 3.24 and 3.05 eV respectively.

1. Introduction

ZnO and TiO₂ are an important semiconducting materials used for variety of technological applications due to their unique properties such as high chemical stability, wide band gap, high refractive index, optical transparency in UV and visible range, semiconducting behavior, photocatalytic activities, high PEC efficiency, biocompatibility, long term photostability, non-toxicity and low cost etc and fabricated as nanowires, nanoribbons, nanobelts, nanocombs, nanoflowers, nanospheres, nanofibers etc [1-3].

2. Experimental Details

All chemical reagents used are AR grade. Zinc acetate dehydrate, hexamethylenetetraamine (HMTA) used as the

Zn precursor and Titanium tetraisopropoxide (TTIP), hydrochloric acid (HCl) used for the Ti precursors [4].

3. Results and Discussion

The growth mechanism for the formation of well aligned ZnO, TiO₂ and TiO₂-ZnO nanorod morphology can be explained in Ref.[4]. The UV-Vis-NIR absorption spectra of the deposited ZnO, TiO₂ and TiO₂-ZnO film were recorded in the range of 300-800 nm. The plot of $(\alpha h\nu)^2$ vs. $h\nu$ gives straight line at higher energies indicating direct type of transition. The intercept of the extrapolation to zero absorption with the photon energy axis is taken as the value of band gap (E_g) as shown in Fig.1 (a-c). The band gap of deposited ZnO, TiO₂ and TiO₂-ZnO thin films were found 3.3, 2.9 and 3.06 eV respectively.

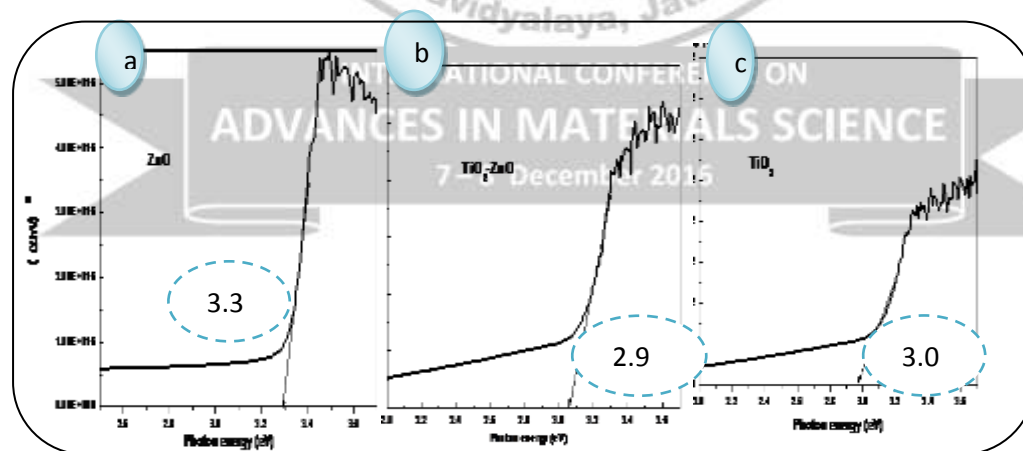


Fig. 1 (a - c) Shows plot of $(\alpha h\nu)^2$ vs. $h\nu$ of the ZnO, TiO₂ & TiO₂-ZnO films

Fig.2 shows XRD pattern of all the samples. XRD patterns exhibited strong diffraction peaks at 27.55°, 36.79° and 55.40° indicating formation of pure hexagonal wurtzite phase ZnO and tetragonal rutile phase of TiO₂

material. The intense peak at 27.55° is the representative peak for (110) plane of rutile TiO₂. All other peaks observed at 36.79°, 39.12°, 41.42°, 44.29°, 55.40°, 62.72° and 64.29°, represents (101), (200), (111), (210), (220),

(002) and (310) planes respectively which confirms the hexagonal wurtzite phase ZnO and tetragonal rutile structure of TiO₂. The samples are well crystallized in rutile TiO₂ single crystals and hexagonal wurtzite ZnO single crystal, where the growth direction is along (002) facets for ZnO and (001) orientation and the side surfaces exhibit (110) facets for TiO₂. All peaks are in good agreement with the standard JCPDS data (Card no. 80-0078 and Card No. 00 001-0562) [5-6]. The calculated crystallite size of ZnO, TiO₂ and TiO₂-ZnO for (110) planes are found to be 20, 16.47 and 16.68 nm respectively [7].

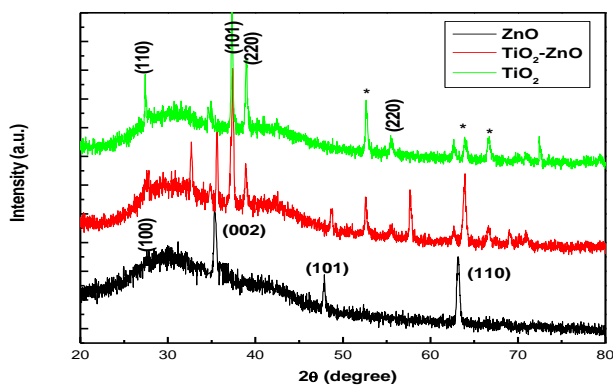


Fig. 2 Shows XRD pattern of ZnO, TiO₂ and TiO₂-ZnO thin films.

Fig.3(a, b) shows SEM images of the ZnO nanorods in uniform overall substrate surface. The average length and diameter of ZnO nanorods is found to be 50 nm and 10 nm respectively. Fig.3(c, d) shows SEM images of the TiO₂ nanorods in uniform, compact arranged and well aligned on the overall substrate surface. Fig.3(e, f) shows SEM images of the composite TiO₂-ZnO nanorods in uniform and 3D

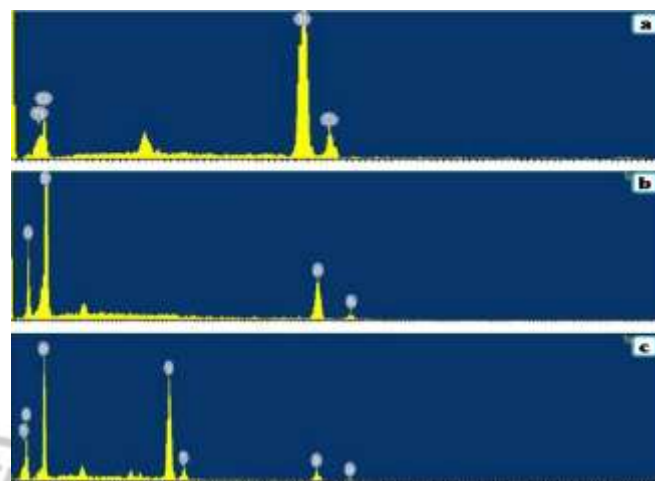


Fig.4(a - c) Shows Energy Dispersive X-ray (EDX) spectrum of ZnO, TiO₂ and TiO₂-ZnO thin films respectively

nanorod flowers. This kind of nanorods and flowers on the top surface of nanorods are densely and uniformly covered the whole surface of the substrate [8].

An elemental composition of ZnO, TiO₂ and TiO₂-ZnO thin films was analyzed by EDS. Fig.4 (a to c) shows an EDS pattern of ZnO, TiO₂ and hybrid TiO₂-ZnO samples respectively. There is no trace of any other impurities could be seen within the detection limit of the EDS. The corresponding EDS result confirms the formation of ZnO, TiO₂ and TiO₂-ZnO thin films [9].

Conclusions

We have successfully demonstrated a simple and low cost hydrothermal synthesis method for deposition of ZnO, TiO₂ and composite TiO₂-ZnO thin films having well aligned nanorod morphology using hydrothermal and low temperature chemical reflux method. Optical measurements allowed us to evaluate the energy gap values and to appreciate the occurrence of scattering effects due to the high surface area of the different structures coupled with their characteristic dimensions. XRD study revealed that the films are nanocrystalline in nature and exhibit TiO₂ is rutile and ZnO in hexagonal crystal structure. SEM and TEM analysis evidenced the structural differences and the high degree of crystallinity of these materials. An EDS analysis of the samples confirms the formation of pure TiO₂, ZnO and mixed TiO₂-ZnO material.

References

1. C. H. Wang, K. W. Cheng, C. J. Tseng, Sol. Energy. Mater. Sol. Cells., 95 (2011) 453.
2. G. Wang, L. Zhang, J. Zhang, Chem. Soc. Rev., 41, (2012), 797.
3. N. S. Patil, A. M. Sargar, S. R. Mane, P. N. Bhosale, 2008, Appl. Surf. Sci., 254 5261, 16
4. D. B. Shinde et J. of Nanomedicine and Nanotechn. (2015)
5. H. Perron, J. Vandenborre, C. Domain, R. Drot, J. Roques, E. Simoni, Surf. Sci., 601, (2007), 518
6. J. Li, W. Wan, H. Zhou, J. Liand, D. Xu, Chem. Commun., 48, (2012) 389.
7. A. Jahagirdar, N. Dhere, Sol. Energy Mater. Sol. Cells, 91, (2007) 1488.
8. M. Mekhnachea, A. Drici, L. S. Hamideche, H. Benzarouk, A. Amara, L. Cattin, J. C. Bernede, M. Guerioune, S.I. & Microstr. 49, (2011) 510.
9. S. S. Mali, C. A. Betty, P. N. Bhosale, P. S. Patil, J. Cryst. Eng. Comm, 13, (2011) 6349.

Cyclic voltammetric study of Fe₃O₄ flexible electrodes in different electrolytes

A. V. Thakur, Y. S. Kokare, S. R. mane, B. J. Lokhande*

*School of Physical Sciences, Solapur University, Solapur 413 255, M.S., India.

Abstract

Present work is a comparative study of the cyclic voltammetric performance of the Fe₃O₄ flexible electrodes (FEs) in different electrolytes viz. KCl, KOH and NaOH. The synthesis was carried out using successive ionic layer adsorption and reaction (SILAR) technique. For aqueous route SILAR synthesis, 0.2 M FeCl₃ and 0.1 M NaOH solutions were used as cationic and anionic sources respectively. X-ray diffraction (XRD) patterns of the FEs show peaks at $2\theta = 43.46^\circ$ and 44.54° indicating the formation of orthorhombic Fe₃O₄. The scanning electron microscopic (SEM) image of FE shows nano-clusters with interconnected nanograins of approximate size 10 nm. Cyclic voltammetric analyses substantiate that the electrochemical performance of FE is different in different electrolytes. It was found that, the FE shows maximum area under the curve and hence the maximum specific capacitance for NaOH. The observed maximum specific capacitance (SC) in 1 M NaOH at 100 mVs^{-1} was 444.44 Fg^{-1} .

Keywords: Thin films, electron microscopy, cyclic voltammetry, Fe₃O₄.

1. Introduction

Various transition-metal oxides, such as RuO₂, Co₃O₄, NiO, Fe₂O₃, IrO₂, SnO₂, MnO₂, etc., are being studied for the supercapacitor applications. RuO₂ is the most preferable material for supercapacitors because of its high specific capacitance, excellent reversibility, and long cycle life. High cost, less abundance and toxic nature have limited the commercial use of RuO₂. Accordingly, there is a strong incentive to find alternative electrode materials, which are inexpensive and exhibit pseudocapacitance similar to that of hydrous amorphous RuO₂. The researchers have been trying to use oxides of manganese [2], nickel [3], cobalt [4], vanadium [5] and copper [6] as electrode materials. Iron oxide can be the good choice as an electrode material for supercapacitors. Iron oxide thin films have been prepared by various methods, such as the sol-gel [7], chemical vapour deposition [8] and electrodeposition [9], spray pyrolysis [10]. Among these chemical methods, successive ionic layer absorption and reaction (SILAR) is low cost and low temperature soft chemical solution method. The SILAR method is relatively a new and less investigated method, which is based on sequential reaction on the substrate surface. Rinsing follows each reaction, which enables heterogeneous reaction between the solid phase and the solvated ions in the solution. SILAR method has its own advantages such as layer-by-layer growing mode, excellent material utilization efficiency, and good control over the deposition process along with the film thickness

and large-scale deposition capability on any type of substrate [11,12]. Electrolyte is one of the major factors that affect the morphology and the electrochemical behaviour of the electrodes. Thus, it will be interesting to study electrochemical behaviour of Fe₃O₄ flexible electrodes in different electrolytes using cyclic voltammetry. Hence in the present work, it was decided to study the effect different electrolytes on the cyclic voltammetric performance of Fe₃O₄ flexible electrodes.

2. Experimental

2.1 Materials

In the synthesis work, FeCl₃ and NaOH purchased from SD fine chemicals were used as source materials without further purifications. Double distilled water was used solvent for all the experiments.

2.2 Electrode preparation

Stainless steel (SS) strips of 304 grade (size = 1cm X 5cm) were used as a conducting substrate material. SS Strips were mirror polished using polish paper (grade 600) to get the rough finish. To allow the proper deposition of the electrode material by adsorption, the strips were ultrasonicated for 20 minutes to make them free from the dirt, oil, stains etc. 0.2 M FeCl₃ was used as cationic precursor and 0.1 M NaOH was used as anionic precursor. SS strips were immersed in cationic precursor for 10 s and anionic precursors for 10 s. These strips were pressure cleaned by the jets of double distilled water after each immersion. This is done to remove loosely bound, un-oxidized, partially oxidized radical. This

completes one SILAR deposition cycle. For every molar variation of cationic source, 120 such SILAR cycles were carried out.

2.3 Characterization

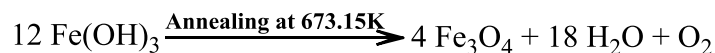
The structural characterizations of all uniformly deposited FEs were taken by using X ray diffraction (XRD) patterns given by X-ray diffractometer (Ultima IV Rigaku D/max2550Vb +18 kw with CuK α , $\lambda = 1.54056 \text{ \AA}$, Japan) in the range of diffraction angle (2θ) between 10° – 90° to study the nature of formed material, scanning electron microscopic (SEM) analyses were carried out by using scanning electron microscope (SEM S4300 HITACHI, Japan) to check the surface morphology of FE. Weight of the deposited material was measured by weight difference method using high accuracy analytical microbalance (Tapson-100TS, USA) with least count 10^{-5} g.

Electrochemical characterization of the deposited FEs were carried out using Electrochemical analyzer (CHI 408C, USA) with standard three electrodes cell in which along with working electrode, platinum wire as a counter electrode and saturated Ag/AgCl as a reference electrode were used.

3. Results and discussion

3.1 Film formation mechanism

In the cationic bath the compound FeCl $_3$ splits up into Fe $^{3+}$ cations and Cl $^-$ anions. In anionic bath, the NaOH splits up to give Na $^+$ and OH $^-$ ions respectively. The double displacement reaction occurs to give Ferric hydroxide films Fe(OH) $_3$ which on annealing at 673.15 K gives stable magnetite phase (Fe $_3$ O $_4$). Reaction mechanism is given below.



3.2 Structural elucidation

The XRD analysis of FE was carried to check the effect of molar concentration of the precursors on the crystallinity and lattice plane arrangement during the nucleation and growth of the material (Figure 1). The XRD pattern of the optimized sample shows peaks

corresponding to the formation of orthorhombic Fe $_3$ O $_4$ (magnetite) crystals. The details of diffraction angle (2θ), plane orientation (miller indices), and interplanar spacing (d) as per the JCPDS data card no. 760956 are given in the table1.

Table 1. Different parameters from XRD patterns of FE

JCPDS card no	Standar rd 2θ	Observed 2θ	Standard 'd'	Observed 'd'	h k l
760956	43.467	43.640	2.0802	2.0724	2
					2
					7
	44.500	44.547	2.0343	2.3600	1
				2	
					7

Scanning electron microscopy (SEM) was carried out to check the surface morphology of the FE. SEM exhibits nano-clusters with interconnected nanograins of approximate size 10 nm. This morphology is advantageous for the pseudocapacitive applications.

3.3 Cyclic voltammetric study

FES were subjected to the cyclic voltammetric (CV) analysis at 100 mV s^{-1} in 1M concentration of different electrolytes viz. KCl, KOH and NaOH respectively. Figure 3 shows the CV curves of FE in different electrolytes. Following formula was used to calculate the specific capacitance (SC) of the prepared FEs from the CV curves.

$$\text{SC} = \frac{c}{w} = \frac{\int_{V_1}^{V_2} I dv}{W(V) \frac{dV}{dt}} \quad 1$$

It was observed that, area under curve hence the current integral is largest in NaOH among all electrolytes. The variations in the values of specific capacitance may be due to the difference in mobility of Cl $^-$ and OH $^-$ ions. Further, the strength of ionic bond plays important role. Less strong ionic bond is responsible for low ionization potential of compound hence NaOH dissociates readily than KOH. Thus ionization takes less energy. Hence the current integral and SC were found larger for NaOH. The observed maximum SC of FE in 1 M of KCl, KOH and NaOH at 100 mV s^{-1} were 157, 229 and 444.44 F g $^{-1}$, respectively.

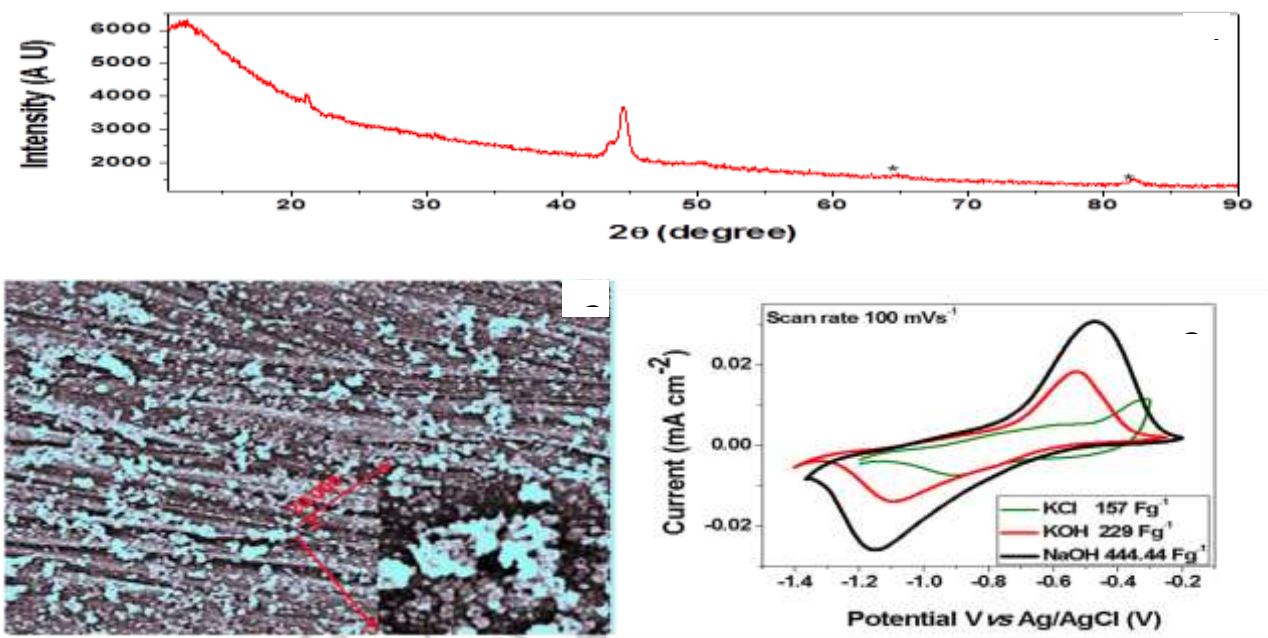


Fig.1. XRD pattern of prepared FE, **Fig.2.** SEM of FE prepared with 0.2M FeCl₃ and 0.1M NaOH, **Fig. 3.** Cyclic Voltammograms of samples in different electrolytes at 100mV/S

4. Conclusion

SILAR synthesized Fe₃O₄ FEs show variation in specific capacitance in different electrolytes. The electrolyte with low ionization potential and high mobility are most suitable. NaOH was found to be a suitable electrolyte producing highest specific capacitance of 444.44 F g⁻¹ at 100.mV s⁻¹.

References

1. B.E. Conway, Electrochemical Supercapacitors, Scientific Fundamentals and Technological Applications, Kluwer Academic/Plenum Press, New York, 1999.
2. D.P. Dubal, D.S. Dhawale, R.R. Salunkhe, V.J. Fulari, C.D. Lokhande, J. Alloys Compd. 497 (2010) 166.
3. K.W. Nam, K.B. Kim, J. Electrochem. Soc. 149 (2002) 346.
4. C. Lin, J.A. Ritter, B.N. Popov, J. Electrochem. Soc. 145 (1998) 4097.
5. H.Y. Lee, J.B. Goodenough, J. Solid State Chem. 148 (1999) 81.
6. D.P. Dubal, D.S. Dhawale, R.R. Salunkhe, V.S. Jamdade, C.D. Lokhande, J. Alloys Compd. 492 (2010) 26.
7. S. Duhan, S. Devi, Int. J. Electron. Eng. 2 (2010) 89.
8. T. Maruyama, Y. Shinyashiki, Thin Solid Films 333 (1998) 203.
9. N. Nagarajan, I. Zhitomirsky, J. Appl. Electrochem. 36 (2006) 1399.
10. J.D. Desai, H.M. Pathan, S.K. Min, K.D. Jung, O.S. Joo, Appl. Surf. Sci. 252 (2005) 1870.
11. H.M. Pathan, C.D. Lokhande, Bull. Mater. Sci. 27 (2004) 85.
12. A. V. Thakur, B. J. Lokhande, e-polymers 2016 aop. DOI 1515/2016-0160.

Enhanced Magnetodielectric Properties of Nickel Doped Ba_{0.7}Pb_{0.3}TiO₃ Single Phase Multiferroic Compounds

S.G. Dhumal^a, D. S. Ghadage^a, S. M. Todlari^c, S. B. Kulkarni^b D.J. Salunkhe^{a*}

^a Nano-Composite Research laboratory, Department of Physics, K.B.P. Mahavidyalaya, Pandharpur, 413 304, India.

^b Department of Physics, Institute of Science Mumbai, India.

^c Department of Electronics, Sangameshwar College, Solapur, India

Email- salunkhedj@rediffmail.com

Abstract:

We have synthesized Ni doped Ba_{0.7}Pb_{0.3}TiO₃ (BPT) samples by hydroxide co-precipitation method. X-ray diffraction reveals that the system exhibits the single phase tetragonal crystal structure. Scanning Electron Microscopy (SEM) image was also employed to observe surface morphology. There is uniform and spherical shaped grains are observed in case of pure BPT, while needle/ elongated shaped grains are observed in Ni doped BPT. Temperature variations of dielectric constant, dielectric loss were measured. The curie temperature T_c shifts to lower value with increasing nickel doping content and loss factor is shifted to higher values with increasing the concentration of Ni. The values of the P_{max} and P_r increases as the level of substitution increases.

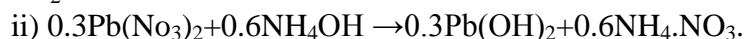
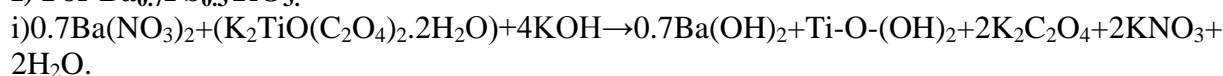
Keywords: Ceramics; X-ray techniques; Crystal structure; Dielectric properties.

1. Introduction:

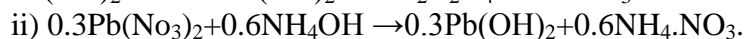
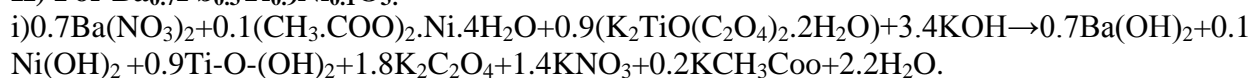
Barium titanate (BT) is a ferroelectric ceramic material used by the electronic industry for various applications such as capacitors, nonlinear PTCRs, piezoelectric transducers, sensors etc. [1-4]. However, pure BT exists in four forms of crystal structures (rhombohedral, orthorhombic, tetragonal and cubic) between -100 and 135 °C, so BT can not be used for all of these different applications in its pure form. Consequently, the phase transitions induces large variations in permittivity and dielectric loss. In order to avoid these disadvantages, only doped materials are used. The effect of addition of (30%) of lead on the dielectric properties of BT was investigated, where the ferroelectric Curie temperature was observed to increase from 120 °C to 135 °C [5]. This is the new work where we have doped Ni in BPT by hydroxide co-precipitation method.

Dielectric properties of the ceramics belonging to the BT family can be influenced by

I) For Ba_{0.7}Pb_{0.3}TiO₃:



II) For Ba_{0.7}Pb_{0.3}Ti_{0.9}Ni_{0.1}O₃:

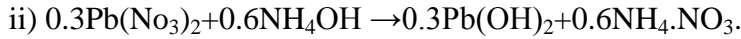
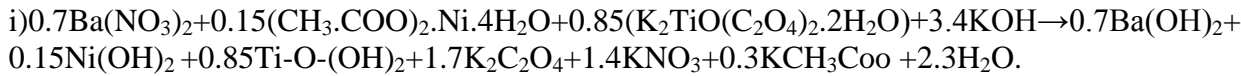


III) For Ba_{0.7}Pb_{0.3}Ti_{0.85}Fe_{0.15}O₃:

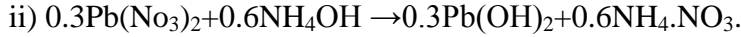
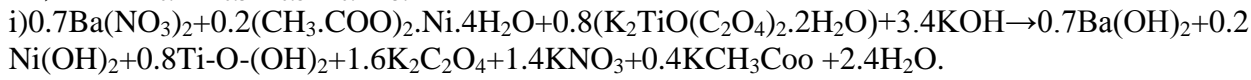
doping with the transition-metal ions. It has been found that ions with the valences smaller than 4 substituting the Ti sites exhibit acceptor character with charge deficiency compensated by doubly ionized oxygen vacancies [2, 6,].

2. Experimental:

The compositions Ba_{0.7}Pb_{0.3}Ti_(1-x)Ni_xO₃, where x = 0, 0.1, 0.15 and 0.2, were synthesized via hydroxide co-precipitation of synthesis. The stoichiometric amounts of high purity Ba(NO₃)₂, Pb(NO₃)₂, K₂TiO(C₂O₄)₂·2H₂O and (CH₃COO)₂Ni·4H₂O were used as starting chemicals. A mixture of NH₄OH and KOH is used as precipitants. Co-precipitation involves a stoichiometric mixture of soluble salts of the metal and precipitating them as hydroxides, citrates, oxalates etc. The mixture is filtered, dried, and then heated to give the final product. The chemical reaction takes place in this procedure is:



IV) For $\text{Ba}_{0.7}\text{Pb}_{0.3}\text{Ti}_{0.8}\text{Fe}_{0.2}\text{O}_3$:



Hydroxide co-precipitation method is one of the best method to gain better control on chemical homogeneity and stoichiometry. $\text{Ba}(\text{NO}_3)_2$ and $\text{Pb}(\text{NO}_3)_2$ are fractionally soluble in water but insoluble in KOH and NH_4OH . As lead hydroxide is dissolved in dilute KOH if its pH value is higher than 10, so precipitates are washed in dilute KOH solution maintaining $\text{pH} \leq 10$ [7]. The calcination was carried out at 1000°C for 8 hr. and the final sintering was carried out at 1200°C for 10 hr. Here, after the process of intermediate grinding, the powder was pressed in the form of disc shaped samples for the purpose of the measurements of the dielectric, magnetodielectric properties.

The prepared bulk samples were then characterized using various techniques. To determine the X-ray diffractograms Bruker (D8 advance) XRD diffractometer was used. Scanning Electron Microscope image by JEOL-JSM 6360 A-Analytical Scanning Electron Microscope. The measurements of dielectric constant for different temperature and different magnetic field were carried out using (HP4284A) LCR- Q meter, a custom designed tubular furnace and an electromagnet from Scientific Instruments Company, Ruraki (PS-75). P-E hysteresis loops were determined using a hysteresis loop tracer by M/S. Marin India.

3. Results and Discussions:

3.1. Structural Properties:

The fig. 1a, b, c, d shows the x-ray diffractograms of $\text{Ba}_{0.7}\text{Pb}_{0.3}\text{TiO}_3$ (BPT), $\text{Ba}_{0.7}\text{Pb}_{0.3}\text{Ti}_{0.9}\text{Ni}_{0.1}\text{O}_3$ (BPTNi0.1), $\text{Ba}_{0.7}\text{Pb}_{0.3}\text{Ti}_{0.85}\text{Ni}_{0.15}\text{O}_3$ (BPTNi0.15) and $\text{Ba}_{0.7}\text{Pb}_{0.3}\text{Ti}_{0.8}\text{Ni}_{0.2}\text{O}_3$ (BPTNi0.2) respectively. In this case the prominent peaks in the X-ray diffractograms could be associated with the reference number 01-074-2492 (ICSD). Here, parent as well as all Ni doped samples exhibits a single

phase tetragonal crystal structure with large lattice distortion. The result clearly shows that there are no diffraction peaks from impurity phases, indicating that the ferroelectric has a high degree of purity and crystallinity for BPTNi0.1. However, impurity peaks corresponding to the pyrochlore phase $(\text{BaPb})_2\text{Ti}_2\text{O}_6$ are seen in the x-ray diffractograms of the highly doped Ni samples. These reflections are marked with ‘*’ in the fig. 1c, d. Similar results are also reported earlier for the Fe doped PbTiO_3 compositions [8, 9].

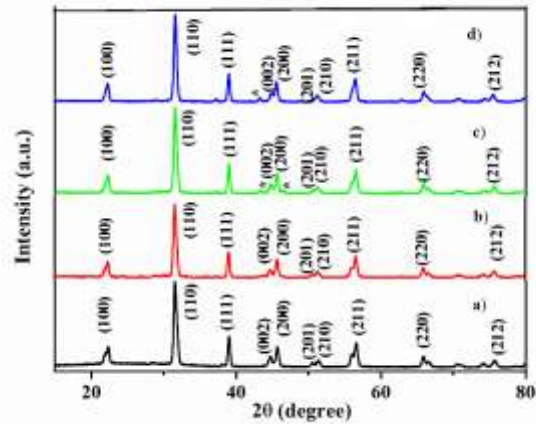


Fig. 1 a, b, c, d shows the x-ray diffractograms of (a)BPT, (b)BPNT0.1 (c)BPNT).2 (d)BPNT0.2

However, PbTiO_3 is well known for its very large lattice distortion ($c/a \sim 1.064$). If we add 30% Pb in Ba sites, lattice distortion reduces ($c/a \sim 1.016$) where as if we substitute transition metal element like Ni at Ti site then c/a ratio again decreases. This is expected according to Hill et al [10] in the reduction of lattice distortion after doping with transition metal element at Ti site. Also, it can be inferred that the lattice constants of BPT are $a = 3.9795\text{\AA}$ and $c = 4.0459\text{\AA}$ and the c/a ratio is 1.0166.

Table 1 shows variation of a , c , c/a for the BPT, BPTNi0.1, BPTNi0.15, BPTNi0.2. Using the Scherer’s formula the crystallite size of the above compositions are also determined and are shown in

table 1. It could be seen that the samples possess crystallites of nearly in between 50- 60 nm.

Table 1 Values of a, c, c/a and crystallite size for the BPT, BPTNi0.1, BPTNi0.15, BPTNi0.2 compositions.

Composition	'a' (A0)	'c' (A0)	c/a	D (nm)
BPT	4.0459	1.0166	52	3.9795
BPTNi0.1	3.9844	4.0404	1.0140	56
BPTNi0.15	3.9823	4.0707	1.0221	56
BPTNi0.2	3.9907	4.0475	1.0142	61

Figure 2a, b, c, d shows that SEM image of BPT, BPTNi0.1, BPTNi0.15, BPTNi0.2 respectively. From fig. 2 it is clear that grain distribution was

homogeneously uniform with clear grain boundaries and average grain size is nearly in between 300-485 μm . From SEM images, it is observed that pure BPT has grain particles uniform and spherical. On the other hand, if we doped Ni in BPT, most of the grains are 'needle/ elongated' shaped. The needle shaped or elongated grains are due to the inadequate inhibition of grain growth. [11]

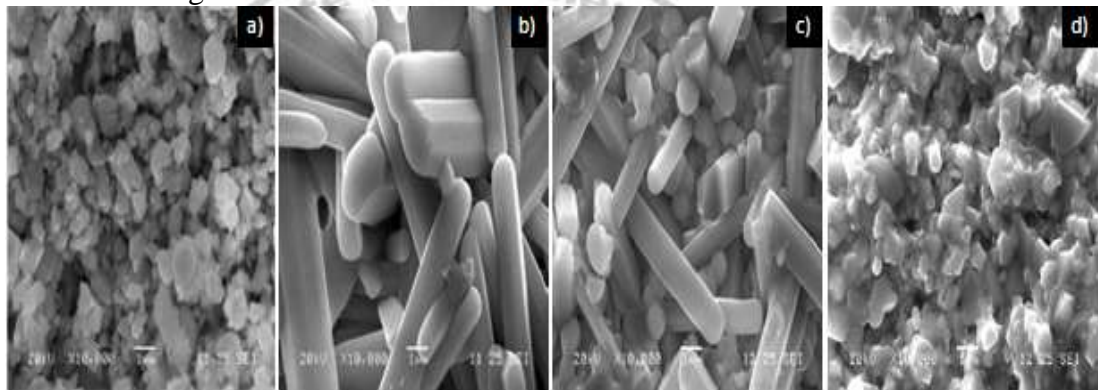


Fig. 2. Scanning Electron Microscope (SEM) images of BPT, BPTNi0.1, BPTNi0.15 and BPTNi0.2 compositions.

3.2 Dielectric Properties:

Figure 3a show variation of the dielectric constant (ϵ) as a function of temperature (T) for frequencies $F= 1$ kHz for BPT and all Ni doped compositions. From the fig. 3a it is seen that the ϵ passes through a peak in the vicinity of 350 $^{\circ}\text{C}$ i.e. T_c of parent composition. It is seen that the ϵ passes through a diffused phase transition at T_c and the T_c decreases with increasing Ni concentration. This feature is expected because of the chemical inhomogeneity induced by the substitution of Ni at very low concentration. This is one of the required features for a multiferroic system to exhibit magnetodielectric properties [12, 13].

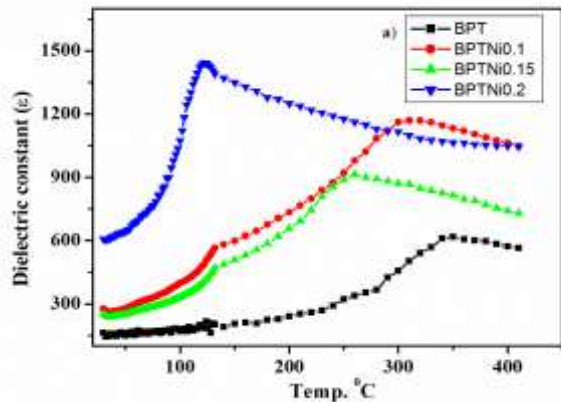


Fig. 3 Variation of the dielectric constant (ϵ) as a function of temperature (T).

3.3 Magnetodielectric properties:

Figure 4 shows variation of magnitude of magnetocapacitance ($M_c\%$) as a function of logarithmic frequency $\text{Log}(F)$ for BPTNi0.1, BPTNi0.15, BPTNi0.2 compositions and it is observed that value of $M_c\%$ is -10.32 which is highest at 100 Hz for BPTNi0.1 and then increases with increase in the frequency and beyond 1 kHz it saturates. However, M_c increases from negative to positive and beyond 1 kHz it saturates for all Ni doped compositions. Further, table 4 shows maximum values of magnetocapacitance M_c for all the Ni doped compositions studied. The samples studied in present case possess the concentration of Ni at very low values and therefore the multiferroic coupling parameters γ significant only at lower frequencies.

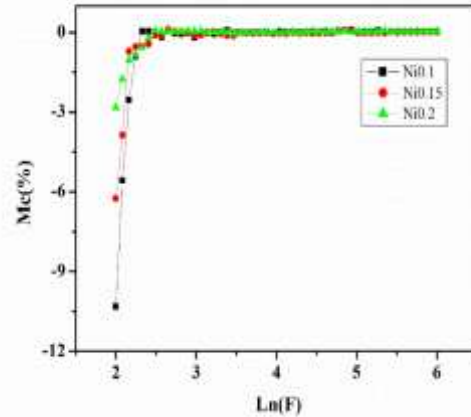


Fig. 4. Variation of magnetocapacitance M_c versus $\text{Log}(F)$ for BPTNi0.1, BPTNi0.15 and BPTNi0.2 compositions

4. Conclusion:

From the present observations it is seen that the $\text{Ba}_{0.7}\text{Pb}_{0.3}\text{Ti}_{(1-x)}\text{Ni}_x\text{O}_3$, where $x = 0, 0.1, 0.15$ and 0.2 , were synthesized via hydroxide co-precipitation of synthesis and all the compositions exhibit a single phase tetragonal crystal structure. SEM shows that all grains are homogeneously uniform with least porosity. It is observed that the value of the $(P_{\text{max}}) = 0.6761 \mu\text{C}/\text{cm}^2$, $(P_r) = 0.2089 \mu\text{C}/\text{cm}^2$, $(E_c) = 1.5357 \text{KV}/\text{cm}$ for BPT sample. The magnetoresistance increases due to the applied field and increase of frequency, which show the maximum value of M_c -10.32% for the sample BPTNi0.1.

Acknowledgement:

All authors are thankful to DRDO-NRB, New Delhi, India for financial support. DRDO-NRB, New Delhi, India ((NRB/MAT/288/13))

References

1. Sheppard L Ceram. Bull. 72 (1993) 45.
2. H.J. Hagemann, H. Ihring, Phys. Rev. B 20 (1979) 3871–3878.
3. B.L. Cheng, M. Gabbay, W. Jr Duffy, G. Fantozzi, J. Mater. Sci. 31 (1996) 4951–4955.
4. K. Uchino, Ferroelectric Devices (Marcell Dekker, Inc., New York – Basel) (2000) 105–118.
5. Ramamanohar Reddy N, Rajagopal E, Siva Kumar K V and Murthy V R K J. Electroceram. 11 (2003) 167.
6. R. A. Serway, W. Berlinger, K. A. Müller, R. W. Collins. Phys Rev B 16 (1977) 4761–4768.
7. Gang Xu, WenjianWeng, Jianxi Yao, Piya Du, Gaorong Han, Microelectronic Engineering 66 (2003) 568-573.
8. [V.R. Palkar, S.K. Malik](#). solid state communication 134 11 (2005) 783-786.
9. K. C. Verma, M. Ram, R. K. Kotnala, S. S. Bhatt & N. S. Negi. Indian Journal of Pure & Applied Physics 48 (2010) 593-599.
10. N A Hill. J Phys Chem. B 104 (200) 6694.
11. Shoumya Nandy Shuvo, Sujit Saha, Md. Miftaur Rahman, IJISME 3 (2015).
12. M. M. Sutar, A. N. Tarale, S. R. Jigajeni, S. B Kulkarni. V. R. Reddy, P. B.Joshi, Solid State Sciences, 14 (2012) 1064-1070.
13. T. Bonaedy, K.M. Song, K.D. Sang, Solid State Commun., 148 (2008) 424.
14. A. Ianculescu, D. Berger, L. Mitoşeriu, C.E. Ciomaga, G. Voicu, N. Dragan, D. Crişan and E. Vasile, Ferroelectrics, 22 (2008) 369.
15. J.S. Kim, S.Y. Cho, M.S. Jang, J. Korean Phys. Soc. 51(2) (2007) 692–696.

Enhanced NO₂ gas sensing properties of flower-like ZnO microstructure

V. L. Patil^{a,c}, P. M. Kadam^b, S. S. Kumbhar^c, S. A. Vanalakar^a, S.S.Shendage^d,
J.H. Kim^e, P. S. Patil^{d*}

^aDepartment of Physics, Karmaveer Hire Arts, Commerce, Science and Education College Gargoti, Dist: Kolhapur, 416 209, India

^bDepartment of Electronics, Smt.Kasturbai Walchand College, Sangli-416416, India

^cSchool of Nanoscience and Biotechnology, Shivaji University,
Kolhapur-416 004, India

^dThin Film Materials Laboratory, Department of Physics, Shivaji University,
Kolhapur-416 004, India

^eDepartment of Materials Science, Chonnam National University, Gwangju Republic of Korea

Abstract

In present study, we report rapid NO₂ gas sensor has been developed based on microstructure of zinc oxide (ZnO) thin film deposited on a glass substrate by using aqueous chemical route. In typical experiment, 0.05M Zinc acetate and 0.075 gm of Urea are dissolved in double distilled water and pH adjusted around 10. The deposition of ZnO thin films carried out at the temperature 90 °C for 2h. As synthesized ZnO thin films are characterized with different characterization techniques such as XRD, SEM, PL, electrical resistivity and Optical properties. The XRD pattern exhibit polycrystalline nature with hexagonal (wurtzite) crystal structure. Formation of ZnO flower is reveals from SEM micrograph. From SEM image it can be seen that the growth of ZnO flower is composed of no. of nanorods originating from the same core in symmetric fashion with average diameter around 200-220 nm. The deposited ZnO thin films were employed for gas sensing applications. The ZnO thin films deposited at 0.3 M solution concentration showed maximum sensor sensitivity (Rg-Ra/Ra) x100 ~ 1440 % at 150°C for 100ppm of NO₂ gas.

Keywords: Zinc oxide; Flower; Micro-structure; XRD; NO₂ gas sensor

Introduction:

Metal oxide gas sensors function according to the control of the electrical conductivity upon exposure to gases, and a number of physically and chemically stable metal oxides (such as ZnO, SnO₂, TiO₂, Fe₂O₃, WO₃, etc.) Have been developed for use in gas sensing Applications (1). In the field of chemical gas sensing, a huge effort was made worldwide to overcome the major drawbacks of metal oxide sensors, i.e. improving Sensitivity, Selectivity and Stability. Since performance of gas sensors depends on size, morphology and structure, many efforts have been taken to prepare different structures.

Semiconductor metal oxide gas sensors have got much attention since last decades due to their low cost, small size, simple synthesizing methods etc Among different metal oxide semiconductor (MOS) based gas sensing materials studied so far, ZnO as a nontoxic, inexpensive and wide-band-gap II-VI compound semiconductor, has been proved to be one of the promising materials for gas sensors [2]. ZnO is one of the versatile and technologically

important semiconducting materials which have a direct wide band gap (3.3eV). It has attracted considerable attention due to its optical, electrical, and piezoelectric properties. Recently, 1D structures of ZnO, such as nanowires, nanorods and nanobelts, were widely used in various applications such as gas sensors, hydrogen storage, solar cells, etc.[3] Films with well aligned ZnO nanorods or nanowires exhibit much larger surface areas than ZnO films prepared from randomly oriented nanoparticles. However, it still remains a big challenge to develop simple and reliable synthetic methods for 1D ZnO nanostructure. ZnO films have been prepared by several techniques, but, the aqueous chemical route are especially attractive because of the low-growth temperatures, potential for scaling up, and cost effectiveness. In recent years many research group have been investigated the highly controlled ZnO microstructures.

Nowadays environment pollution, volatilization of hazardous gases has become an important issue because of the rapid development of industrialization and urbanization in the past few decades. So it's requiring the use of gas sensors to

detect harmful gases or hazardous gases including oxides of carbon and nitrogen. Nitrogen dioxide (NO_2) is a dangerous gas that is generated during combustion in factories and thermal power plants, and it plays a major role in the atmospheric reactions that produce ground-level ozone, a major component of smog and the main cause of acid rain. NO_2 is a reddish-brown toxic gas with pungent odor and can be detected in the environment by using gas sensing devices, and the American Conference of Government Industrial Hygienists has determined the threshold value of NO_2 gas to be 3 ppm [4].

In this paper, ZnO flower like microstructure assembled by ZnO nanorods is prepared by a simple aqueous chemical route in the absence of surfactant and template and their sensor response towards various concentrations of NO_2 gas was investigated. Meanwhile, the structural, morphological, optical and electrical properties of ZnO films were studied using X-ray diffraction (XRD), scanning electron microscopy (FESEM), photoluminescence spectra and electrical resistivity measurements, respectively. ZnO films exhibit good sensor sensitivity towards NO_2 at relatively low operating temperature.

Experimental procedure:

For the synthesis of ZnO microflower zinc acetate dehydrate ($\text{Zn}(\text{O}_2\text{CCH}_3)_2(\text{H}_2\text{O})_2$, 98%), ammonia (NH_3) and Urea ($\text{CH}_4\text{N}_2\text{O}$) as a zinc source, a base and a complex-agent, respectively were purchased from Sigma-Aldrich. Double distilled water (DDW) was used as the solvent during the synthesis. The synthesis protocol was from this reference [5]

In a typical synthesis, Cleaning of the substrates prior to the actual deposition is an important parameter in order to grow uniform thin film over the entire substrate surface. Commercially available glass microslides were dipped in preheated (363 K) chromic acid for 15 min, washed with laboline, rinsed in acetone and finally ultrasonically cleaned with double distilled water for 15 min. prior to the actual deposition Briefly, 0.05 M of $\text{Zn}(\text{O}_2\text{CCH}_3)_2(\text{H}_2\text{O})_2$ were mixed with DDW this solution was then added to 0.075 gm of urea concentration with continuous stirring then the

solution was white precipitate. Then NH_3 dissolved in double distilled water, was added drop wise to this precipitate with constant magnetic stirring for 5 min. to get clear transparent solution with pH value 10. A cleaned soda-lime glass substrate was immersed vertically into the reaction solution. The chemical bath deposition was maintained the bath temperature 90°C for reaction periods over 2 h and allowed to cool down to room temperature naturally. The whitish film was formed on the surface of the glass substrate, which was washed with with DDW for several times to remove ions, possibly remnant in the products and finally dried in an oven at 300°C for 1h. Then it is used for further characterization.

Characterization techniques:

The structural and morphological characterizations were studied by Bruker D2 phaser diffractometer with $\text{Cu K}\alpha$ radiations of wavelength 1.5406 \AA and scanning electron microscope (JEOL JSM-6360 model) respectively. The photoluminescence spectra of the samples were recorded using a PL spectrophotometer (Model: PI-Max3, Make: Prince-ton Instruments, U.S.A.). The emission from the ZnO nano-structured thin films was investigated using micro-photoluminescence, carried out using a He-Cd laser as a continuous wave excitation source with a wavelength of 325 nm. Optical absorption study of the SnO_2 thin film samples was carried out in the wavelength range of 200–800 nm using UV-Vis-NIR spectrophotometer (UV-Vis 1800 spectrophotometer, Shimadzu, Japan). The electrical resistivity measurements were taken by conventional two probe method.

The gas sensing measurements were studied by laboratory made computer controlled static gas sensing unit. The unit consists of airtight stainless steel test chamber having volume capacity of 250cc with provision of gas inlet-outlet, and a flat heating plate with temperature controller. A Keithely 4200-SCS electrometer with data acquisition system controlled by computer was connected to the external leads of the thin film sensor. A thin film sensor of dimensions 10mm x10mm with silver contacts was fabricated and placed on the heating

plate in the test chamber where it is preheated at required temperature using temperature controller. At first, the sensor was heated until its base resistance was stabilized. After that the thin film sensor was exposed to the target gas of desired concentration in the gas chamber and change in resistance with respect to time was measured with Keithely 4200-SCS electrometer. After each successive measurement, the film sensor was recovered by opening the top lead of test chamber and purging the fresh air through the outlet of the system. The sensor responses were measured to various NO₂ concentrations ranging from 1-100 ppm with respect to the operating temperature ranging from 348-523K.

The sensor response (S) is defined as,

$$S = R_g/R_a \text{ for oxidizing gases and}$$

$$S = R_a/R_g \text{ for reducing gases,}$$

Where, the resistance R_g is the electrical resistance in target gas and R_a to that in air.

Results and Discussion:

3.1 X-ray diffraction studies

The X-ray diffraction spectrum of ZnO microflower thin films deposited are shown in Fig. 1. Both deposited thin films were found to be crystalline with hexagonal wurtzite structure and in well matches with JCPDS card no. 36-1451. The prominent characteristic peak of (100), (002), (101), (102), (110) and (103) was appearing in the patterns for the sample. The peak (002) was attributed to the vertically alignment of nanorods along c-axis of the crystal plane [6]. The XRD results confirm highly crystalline nature of ZnO microstructure arrays thin films. Furthermore, the intensity of (002) plane was found to be maximum for the films deposited for 2 h, which indicates that the nanorods are aligned along the (002) preferred orientation.

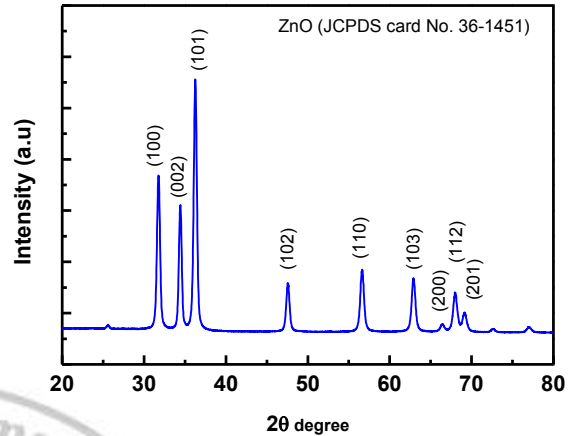


Fig.2 XRD spectrum of ZnO sample

The full width at half maximum (FWHM) was found to be decreased with increase in deposition time. The calculated crystalline size using Scherrer's formula was found to be 36 nm for the sample deposited for 2 h.

3.2 Scanning electron microscopy:

The morphologies of the ZnO thin films were investigated by SEM. Fig.2. Reveals SEM images of different magnification of the ZnO thin films synthesized by chemical route. The SEM images clearly show the well-defined nanorod over the entire substrate irrespective of molar concentration; however their size changes with molar concentration. From the fig shows the nanorod are well defined hexagonal shape also central rod appear the number of rod growing and finally we can see the flower like morphology is studied of the fixed concentration of precursor. The mean thickness and length of these nanorod are found to be about 2-4 μm respectively.

The flower like morphology of ZnO can also affect their sensing. It is well known that the higher the length of the flower arms with increase the surface-to-volume ratio. It can be noticed that with increase the surface area and it is beneficial for gas sensing application

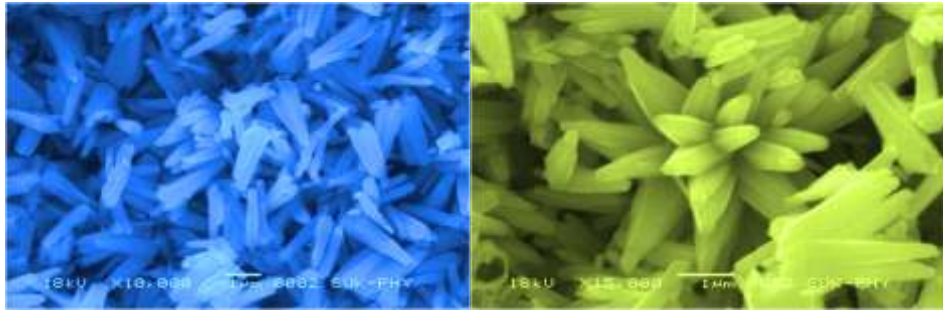


Fig.2 SEM images of ZnO sample with different magnification

3.3 Photoluminescence's studies :

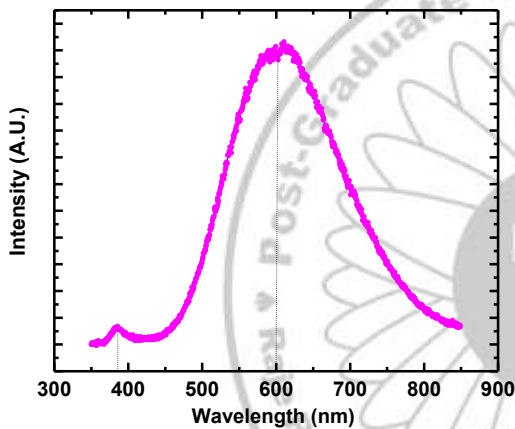


Fig.3 PL spectra of ZnO sample with different magnification

Fig. 3 shows the photoluminescence (PL) spectra of ZnO thin film samples recorded at room temperature. The PL spectrum of the sample show two peaks- one in ultraviolet (UV) and another in red in the visible region. The PL peak in UV region appears at 390 nm which is attributed to the near-band-edge emission from ZnO, due to the near band-edge free exciton transition from the localized level below the conduction band to the valance band [7]. The intensity of the UV region emission depends on the degree of alignment. The Z1 sample shows the strong emission at 390 nm as compared to the rest of ZnO samples. This strong absorption is generally attributed to the excitonic emission. The PL peak at 600 nm in the visible region is attributed the deep level emissions in all ZnO thin films are due to the presence of oxygen vacancies [8-9]. Moreover, the deep-level emission is mainly related

to point defects, such as Zn interstitial. The ratio of intensity of PL peaks of UV and visible regions for ZnO sample is as 0.83. The higher ratio suggests the presence of defects such as oxygen vacancies. The higher amount of defects and vacancies are beneficial for gas sensing applications. Oxygen vacancies induce a large number of electron donors on the surface of ZnO structures. The large number of electrons was captured from the conduction band of ZnO forming a thicker electron depletion layer, which is an indication of the better sensitivity of the sensor [10].

4. Gas sensing properties

The gas-sensing test was performed on the ZnO flower thin film sample. In general, the gas sensing mechanism of the metal oxide gas sensor is based on a variation in the electrical resistance due to the gas adsorption and desorption on the active surface. It is observed that the resistivity of ZnO based gas sensor devices increases after exposing to oxidizing gas such as NO₂. The sensitivity of nanorod based metal oxide thin films were believed due to the effect of their aspect ratio, porosity and appropriate interspace distance between the nanorods. However, the chemical reactions occurring at the surface of gas sensors are the basis of sensors [11]. In general the regularly spaced flower provides maximum surface and numerous channels for gas diffusion. Furthermore, increase of operating temperature improves chemisorptive amount of gas molecules, which enhances the gas response of thin film sensors.

Fig. (4) Shows the variation of gas sensitivity of ZnO flower sample as function of operating temperature for 100 ppm NO₂ gas . The ZnO sample exhibit gradual increment in gas sensitivity and reached a maximum response at

around 150⁰C for 100 ppm before it decreased. When the operating temperature is beyond 200⁰C, the gas response to NO₂ is reduced. The reduction in gas response at higher temperature is due to decrease of the amount of NO₂ adsorbed on the ZnO surface [12-13]. Fig. (4) Confirm the operating temperature of ZnO flower sample at around 150⁰C.

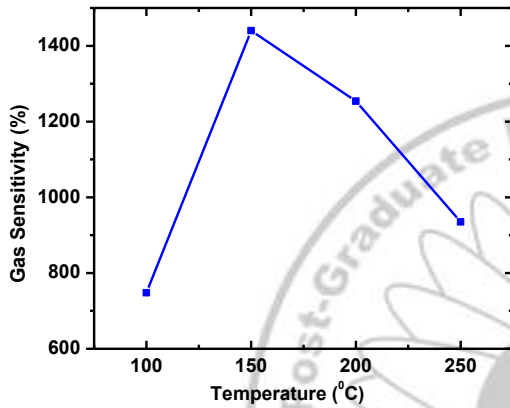


Fig. 4 Gas sensitivity of ZnO thin film sample at different operating Temperatures

Fig.5 shows the dynamic response of ZnO thin film sensor at different NO₂ concentrations ranging from 10 to 100 ppm. The gas response increases with increase in NO₂ concentration. It can be seen that the sensor is sensitive even at 10 ppm of NO₂. The response transient curve of the sensor shows that the resistances almost recover to its initial values after the removal of NO₂ gas, which indicates good reversibility of the sensor.

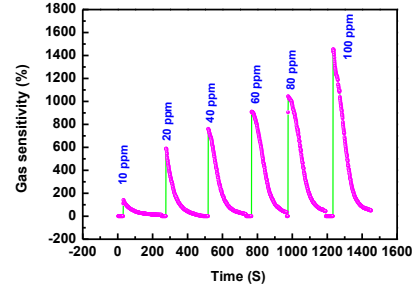


Fig.5 Gas sensitivity of ZnO thin film sample as function of different concentration of NO₂ gas

Fig. (6) shows the resistance versus time graphs and gas response of the ZnO nanorod arrays gas sensor for 100 ppm at 150⁰C. The resistance of the ZnO sample was measured under dry air flow to obtain baseline, then the measurement chamber was closed and NO₂ gas was injected into the chamber. After the sample was exposed to NO₂, the resistance of ZnO sample was found to increase. When the experimental gas was removed with dry air flow, the resistance of the sample was decreased slowly and recovers the baseline. The ZnO sample shows the 90% sensitivity at moderate temperature.

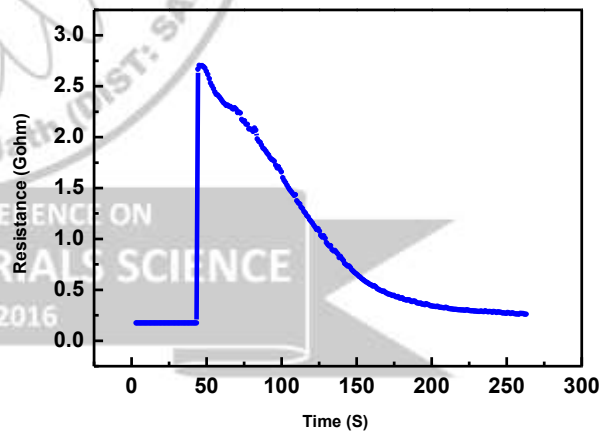


Fig. 6. The resistance versus time graphs for sample ZnO thin film

5. Conclusion:

In summary ZnO thin films have been deposited by a simple and cost effective wet chemical route at low temperature. The XRD pattern confirms the polycrystalline nature of ZnO nanorods with a c-axis orientation perpendicular to the substrate surface. The reported ZnO flower could be suitable candidates with high and quick sensitivity to NO₂ sensing. The sensitivity of ZnO thin films increased with increasing gas concentration. The linear relationship between sensitivity and gas concentration reported in the present study, before reaching the saturation of gas sensing, is helpful for the application

of digitized gas sensors. The surface morphology, density of the sensing materials, presence of defects in the materials are the important factors which influence the performance of ZnO based gas sensors.

Acknowledgement

Authors VLP and SAV are thankful to Science and Engineering Research Board (SERB), Department of Science and Technology (DST), New Delhi, India (No.SR/FTP/PS-083/2012) for the financial support. This work is supported by the Human Resources Development program (No. 20124010203180) of the Korea Institute of Energy Technology Evaluation and Planning (KETEP) grant funded by the Korea government Ministry of Trade, Industry and Energy.

References:

1. Controlled growth of ZnO nanorod arrays via wet chemical route for NO₂ gas sensor applications Sharadrao A. Vanalakar, Vithoba L. Patil, Namdev S. Harale, Sagar A. Vhanalakar, Myeng Gil Gang, Jin Young Kim, Pramod S. Patil, Jin Hyeok Kim *Sensors and Actuators B* 221 (2015) 1195–1201
2. Sharad A. Vanalakar, Sagar A. Vhanalakar, Vithoba L. Patil, Namdev S. Harale, Bharat B. Kale, Jin H. Kim, Pramod S. Patil Synthesis and Characterization of Chemically Deposited ZnO Nanorods for NO₂ Gas Sensing Applications Proceedings of the 2015²nd International Symposium on Physics and Technology of Sensors, 8-10th March, 2015, Pune, India
3. Cheng Peng, Jiaojiao Guo, Wenke Yang, Chunkai Shi, Mingrui Liu, Yixiong Zheng, Jing Xu, Peiqin Chen, Tingting Huang, Yuqian Yang Synthesis of three-dimensional flower-like hierarchical ZnO Nanostructure and its enhanced acetone gas sensing properties *Journal of Alloys and Compounds* 654 (2016) 371-378
4. S.A. Vanalakar, R.C. Pawar, M.P. Suryawanshi, S.S. Mali, D.S. Dalavi, A.V. Moholkar, K.U. Sim, Y.B. Kown, J.H. Kim, and P.S. Patil, "Low temperature aqueous chemical synthesis of CdS sensitized ZnO nanorods", *Mater. Lett.*, vol 65, pp. 548-551, Feb. 2011.
5. Kurniawan Foe, Gon Namkoong, Tarek M. Abdel-Fattah, Helmut Baumgart Mun Seok Jeong,, Dong-Seon Lee Controlled synthesis of ZnO spheres using structure directing agents *Thin Solid Films* 534 (2013) 76–82
6. Vithoba L. Patil, Sharadrao A. Vanalakar, Pramod S. Patil, Jin H. Kim Fabrication of nanostructured ZnO thin films based NO₂ gas sensor via SILAR technique *Sensors and Actuators B* 239 (2017) 1185–1193
7. S.A. Vanalakar, S.S. Mali, M.P. Suryawanshi, N.L. Tarwal, P.R. Jadhav, G.L. Agawane, K.V. Gurav, A.S. Kamble, S.W. Shin, A.V. Moholkar, J.Y. Kim, J.H. Kim, P.S. Patil, Photoluminescence quenching of a CdS nanoparticles/ZnO nanorods core-shell heterogeneous film and its improved photovoltaic performance, *Opt. Mater.*, 37 (2014) 766-772.
8. B. Liu, J. Xu, S. Ran, Z. Wang, D. Chen, G. Shen, High-performance photodetectors, photocatalysts, and gas sensors based on polyol reflux synthesized porous ZnO nanosheets, *CrystEngComm*, 14 (2012) 4582–4588
9. J. A. Alvarado, A. Maldonado, H. Juarez, M. Pacio, R. Perez, Characterization of nanostructured ZnO thin films deposited through vacuum evaporation, *Beilstein J. Nanotechnol.* 6 (2015) 971–975].
10. M. R. Alenezi, S. J. Henley, N. G. Emerson, S. Ravi, P. Silva, From 1D and 2D ZnO nanostructures to 3D hierarchical structures with enhanced gas sensing properties, *Nanoscale*, 6 (2014) 235-238.
11. Farming of maize-like zinc oxide via a modified SILAR technique as a selective and sensitive nitrogen dioxide gas sensor V. L. Patil, S. A. Vanalakar, A. S. Kamble, S. S. Shendage, J. H. Kim and P. S. Patil. *RSC Adv.*, 2016, 6, 90916
12. Sarita P. Patil, Vithoba L. Patil, Sambhaji S. Shendage, Namdev S. Harale, Sharad A. Vanalakar, Jin Hyeok Kim, Pramod S. Patil Spray Pyrolyzed Indium Oxide Thick Films as NO₂ Gas Sensor *Ceramics International* 42(14) July 2016 DOI: 10.1016/j.ceramint.2016.07.135
13. S. S. Shendage, V. L. Patil, S. A. Vanalakar, S. P. Patil, N. S. Harale, J. L. Bhosale, J. H. Kim, P. S. Patil Sensitive and selective NO₂ gas sensor based on WO₃ nanoplates *Sensors and Actuators B* 240 (2017) 426–433

Glycine Nitrate Mediated Convenient Synthesis of Erlenmeyer Azalactone

D. M. Pore*, S. N. Korade

Department of Chemistry, Shivaji University, Kolhapur-416 004 (India)

E-mail: p_dattaprasad@rediffmail.com

Introduction:

Heterocycles have played important role in the development of modern society. They have a wide range of applications in pharmaceuticals, agrochemicals and in veterinary products. The core skeleton of important natural products such as penicillins, cephalosporin, vinblastine, morphine, reserpine, etc. is heterocyclic in nature. They are also utilized as sanitizers, developers, antioxidants, corrosion inhibitors, copolymers, dye stuff, etc. Heterocycles are fundamental building blocks in synthetic organic chemistry.¹

In 1893, Friedrich Gustav Carl Emil Erlenmeyer² discovered the reaction between benzaldehyde with N-acetylglycine in the presence of acetic anhydride and sodium acetate. The reaction proceeds *via* a Perkin condensation following the initial cyclisation of the N-acetylglycine³ yielding the important class of heterocycles, 2-oxazolin-5-ones also called as Erlenmeyer azlactones.

Erlenmeyer azlactones have attracted much attention of modern researchers on account of their wide range of applications. They have been used as precursors in a variety of reactions to synthesize biologically active peptides, herbicides, fungicides, drugs, pesticides and agrochemical intermediates. Oxazol-5-ones inhibit the activity of tyrosinase enzyme with a maximum inhibition by the derivative which bears a cinnamoyl residue at C-4 of oxazolone moiety. Some prepared 3,4- diaryloxazolones displayed inhibition of cyclooxygenase-2 (COX-2) *in vivo* anti-inflammatory and excellent activities of arthritis and hyperalgesia.⁴⁻⁸

Moreover, they have been used in active site titrations of enzymes⁹, as antihypertensives¹⁰ and in the asymmetric synthesis of amino acids¹¹. Azlactones, anhydrides of N-acyl- α -aminoacids, are interesting intermediates for the synthesis of a variety of bioactive compounds, some of their activities are anticancer, antitumor, and inhibition of the central nervous system¹². Azlactones are also

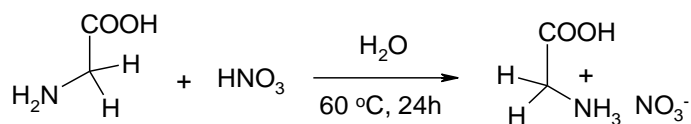
utilized in asymmetric synthesis of aminoacids¹³⁻¹⁴ and for the homologation of carboxylic acids¹⁵.

Ionic liquids (ILs) have marched far beyond the border as a solvent¹⁶ showing their significant role in controlling the reaction as catalysts due to their high polarity and the ability to solubilize both inorganic and organic compounds, which can result in the enhancement of the rate of the reaction¹⁷. Impressed by these properties of ILs and in continuation with our work for the development of green methodologies, herein we reported glycine nitrate mediated an efficient and green synthesis of Erlenmeyer azalactone using reaction between benzaldehyde, 2-phenyloxazol-5-one.

Result and discussion:

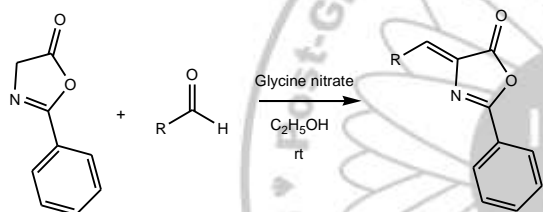
The catalyst plays a vital role in reactions. The catalyst should be eco-benign, efficient and task specific that should not catalyze side reactions. Literature reports revealed that Erlenmeyer azalactones can be synthesized by both acid as well as base catalysis. However, most of the times use of basic catalysts leads to self-condensation of the aldehydes. Hence we envisaged that acid catalysis would be suitable for the model reaction to avoid formation of byproduct.

In this perspective, initially we focused our attention towards synthesis of acidic ionic liquid which could be obtained by commercially available precursors and should be synthesized in convenient way. Amino acids have become precursors of choice due to their biodegradable nature and easy availability. Hence we have synthesized glycine nitrate by following a reported procedure from glycine and nitric acid¹⁸ [Scheme 1]. Synthesized ionic liquid was characterized with ¹H and ¹³C NMR. The ¹H-NMR spectrum exhibits the singlet for three protons of -NH₃ at δ 8.16 and another singlet appearing at δ 3.72 for two protons of ethylene group. ¹³C-NMR spectra shows signals at δ 169.20 and δ 40.29 with respect to acidic carbonyl carbon and ethylene carbon of ionic liquid, respectively.



Scheme 1: Synthesis of glycine nitrate ionic liquid

Initially, the model reaction between benzaldehyde (1 mmol), 2-phenyloxazol-5-one (1 mmol) using 50 mol % glycine nitrate in ethanol at room temperature (10 mL) was carried out (Scheme 2). Gratifyingly, the reaction was completed within 15 minutes which was monitored by TLC. The reaction mixture was then poured into ice-water and the precipitate formed was filtered and washed with hexane and recrystallized with hot ethanol. The formation of Erlenmeyer azalactone was confirmed by ¹H NMR, ¹³C NMR, IR and Mass spectroscopic methods.



Scheme 2: Glycine nitrate catalyzed synthesis of Erlenmeyer azalactones at ambient temperature

IR spectrum of the (4Z)-4-benzylidene-2-phenyl-1,3-oxazol-5(4H)-one (Table 2, entry 3a) exhibited the absorption bands at 3322, 2930 cm⁻¹ for aromatic stretching, 1795 cm⁻¹ for lactone functionality, 1655 and 1165 cm⁻¹ for exocyclic –C=C– and –C–O– stretching respectively. In PMR spectrum, singlet at δ 7.26 depicted the presence of olefinic proton while six aromatic protons appeared at δ 7.46-7.66 ppm as a broad multiplet. Remaining four aromatic protons emerged at δ 8.19-8.23 ppm in the form of multiplet.

In order to investigate catalytic efficiency of glycine nitrate, screening of catalyst for model reaction was carried out. Various acidic catalysts viz PEG 6000-SO₃H, *p*-TSA, acetic acid, Gly.-Cl⁻, Gly-PF₆⁻, Gly-NO₃⁻ were investigated for the reaction under optimized conditions (Table 1, entry 2-7). The best overall yield (88 %) was obtained in glycine nitrate (Table 1, entry 7) which might be due to both cationic and anionic moiety govern the electrostatic interaction and take part in reaction

resulting into higher percentage of the desired product.

To optimize the quantity of catalyst, varied proportion of catalyst viz. 10, 20, 30, 40 and 50 mol % were employed for model reaction (Table 2). Lower yields of product were obtained for 10, 20 and 30 mol% quantity (Table 2, entry 3-5). It was observed that 40 mol% catalyst furnished the same yield of product that was obtained with 50 mol%. (Table 2, Entry 2) Hence, 40 mol % glycine nitrate was found enough to catalyze the reaction.

Table 1: Screening of catalysts in the formation of 3a

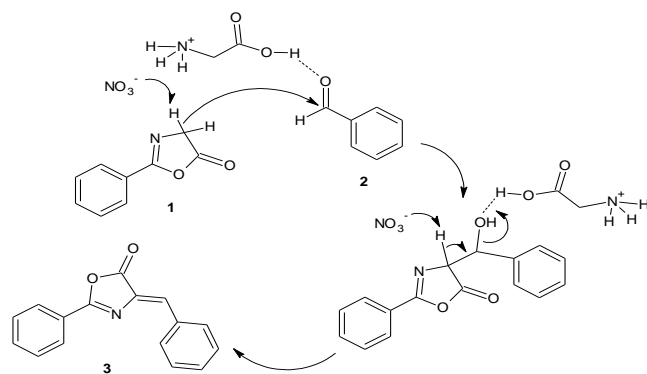
Sr. No	Catalyst	Time (h)	Yield (%) ^a
1	-----	4	65
2	PEG 6000-SO ₃ H	4	78
3	<i>p</i> -TSA	4	77
4	Acetic Acid	4	71
5	Gly-Cl ⁻	4	83
6	Gly-PF ₆ ⁻	4	82
7	Gly-NO ₃ ⁻	4	87

Reaction conditions: benzaldehyde (1 mmol), 2-phenyloxazol-5-one (1 mmol), catalyst (50 mol %), temp.= rt ^a isolated yield

Table 2: Optimisation of quantity of catalyst for synthesis of 3a

Entry	Catalyst Mol (%)	Time (min)	Yield (%)
1	50	15	87
2	40	15	87
3	30	15	80
4	20	15	73
5	10	15	70

This result encouraged us to investigate the plausible mechanism of the reaction shown in Scheme 3. The carboxylic group of glycine nitrate increases the electrophilicity of carbonyl carbon of aldehyde by hydrogen bonding whereas nitrate anion abstracts the acidic proton from 2-phenyloxazol-5-one leading to conjugate anion which then attacks on carbonyl carbon of aldehyde followed by catalyst assisted dehydration to furnish Erlenmeyer azalactone.



Scheme 3: Plausible mechanism for glycine nitrate mediated synthesis of Erlenmeyer azalactone

Thereafter to investigate the generality of the method, the reaction was carried out with different substrates having electron withdrawing and donating functionalities. Pleasingly, it was observed that the reaction underwent smoothly with all aldehydes

Experimental:

General

All chemicals (Sigma-Aldrich) were used as received. Melting points were determined and are uncorrected. IR spectra were recorded on Perkin-Elmer [FT-IR-783] spectrophotometer. NMR spectra were recorded on Bruker AC-300 (300 MHz for ^1H NMR and 75 MHz for ^{13}C NMR) spectrometer in DMSO- d_6 or CDCl_3 using TMS as an internal standard and δ values are expressed in ppm.

Typical Procedure

To a stirred mixture of aldehyde (1 mmol) in 10 mL ethanol, 2-phenyloxazol-5-one (1 mmol) was added. The reaction mixture was allowed to stir at room temperature for time as mentioned in table-2. The precipitated solid was filtered, washed with water and then with 5 mL of hexane. The product obtained was purified by simple recrystallization from ethanol.

Spectroscopic Data:

(4Z)-4-benzylidene-2-phenyl-1,3-oxazol-5(4H)-one (Table 2, entry 3a) : Mp.162-165 °C; IR (KBr): 3322, 2930, 1795, 1655, 1165 cm^{-1} ; ^1H NMR (300 MHz, CDCl_3): δ = 7.26 (s, 1H, -CH=), 7.46-7.66 (m, 6H, Ar-H), 8.19-8.23 (m, 4H, Ar-H)

furnishing excellent yield of products. (Table 3, entry 3b to 3k)

Table 2: Synthesis of library of Erlenmeyer azalactones

Entry	Product 3	Time Yield (min) (%) ^a
a	R = H	15 87
b	R = 4-OMe	15 79
c	R = 3-Cl	20 90
d	R = 4-CH ₃	10 78
e	R = 4-NO ₂	10 88
f	R=3-NO ₂	20 87
g	R = 4-isopropyl	15 85
h	R = 4-OH	10 86
i	R=3,4-OMe	10 80
j	R= 2,5-di-Me	15 84
k	R = 3-OMe, 4-OH, 5-NO ₂	15 83

^aYields refer to pure, isolated products

(4Z)-4-(3-chlorobenzylidene)-2-phenyl-1,3-oxazol-5(4H)-one (Table 2, entry 3c): Mp.160-162 °C; IR (KBr): 3322, 2930, 1799, 1657, 1165 cm^{-1} ; ^1H NMR (300 MHz, CDCl_3): δ = 7.16 (s, 1H, -CH=), 7.40-7.64 (m, 5H, Ar-H), 7.85 (d, 1H, Ar-H), 8.00 (d, 1H, Ar-H), 8.19 (d, 1H, Ar-H), 8.30 (s, 1H, Ar-H); ^{13}C NMR (75 MHz, CDCl_3): δ 125.39, 128.06, 128.58, 129.01, 129.87, 131.12, 131.25, 131.70, 134.02, 134.42, 135.84, 190.25.

(4Z)-4-(2,5-dimethylbenzylidene)-2-phenyl-1,3-oxazol-5(4H)-one (Table 2, entry 3j): Mp. 114-116 °C; IR (KBr): 3321, 2925, 1789, 1651, 1177 cm^{-1} ; ^1H NMR (300 MHz, CDCl_3): δ = 2.43 (s, 3H, Ar-CH₃), 2.48 (s, 3H, Ar-CH₃), 7.15 (s, 1H, -CH=), 7.43-7.53 (m, 5H, Ar-H), 7.77 (d, 1H, Ar-H), 8.17 (d, 1H, Ar-H), 8.61 (s, 1H, Ar-H).

(4Z)-4-(4-hydroxy-3-methoxy-5-nitrobenzylidene)-2-phenyl-1,3-oxazol-5(4H)-one (Table 2, entry 3k): Mp.165-167 °C; IR (KBr): 3208, 2935, 1791, 1680, 1106 cm^{-1} ; ^1H NMR (300 MHz, CDCl_3): δ 4.02 (s, 3H, Ar-OMe), 7.14 (s, 1H, -CH=), 7.55-7.63 (m, 5H, Ar-H), 8.13 (s, 1H, Ar-H), 8.37 (s, 1H, Ar-H), 9.88 (s, 1H, Ar-OH); ^{13}C NMR (75 MHz, DMSO- d_6): δ 57.20, 112.80, 121.53, 126.94, 127.66, 128.32, 129.79, 129.87, 137.49, 148.67, 150.68, 190.7

Conclusion:

In conclusion, we have developed an eco-benign and efficient method for synthesis of Erlenmeyer azalactones in ethanol at room temperature using glycine nitrate as a catalyst. The interesting feature of this catalyst is that it does not bring about the self-condensation of aldehyde. A variety of aldehydes undergo Erlenmeyer reaction smoothly in short time duration in high yields. The additional advantages are energy efficiency, operational simplicity, use of nonhazardous ethanol as a solvent, easy isolation as well as purification of product making this method superior.

Acknowledgement:

Author DMP thanks DST/SERB, New Delhi, India for financial assistance [No. SB/FT/CS-154/2012]

References:

1. Arora et al., IJPSR, **2012**; Vol. 3(9), 2947.
2. Erlenmeyer, E. *Annalen*. **1893**, 275, 1.
3. Baltazzi, E. *Q. Rev. Chem. Soc.* **1955**, (9), 150.
4. Ladva, K.; Dave, U.; Parekh, H., *J. Inst. Chem.* **1992**, (64), 80.
5. Latitha, N.; Bhalerac, U. T.; Iyengar, D. S., *J Chem. Soc., Perkin Trans I.* **1993**: 737.
6. Descas, P.; Jarry, C. *Eur. pat.*, 392 929, 17 OCT 1990. C.A. **1991**, (114), 143.
7. Benedlt, D.; Daniel, V., *J. Med. Chem.* **1994**, (37), 710.
8. Pereira, E. R.; Sancelme, M.; Voldoire, A.; Prudhomme, M., *Bioorg. Med. Chem. Lett.* **1997**, (7) 2503.
9. Bacse, H. J.; Havsteen, B. *Anal. Biochem.* **1989**, (181), 321.
10. Urano, K.; Torioka, Y.; Okubo, K.; Yarnazaki, K.; Nagamatsu, A. *Jpn. Kokai Tokkyo Koho JP 01 29369 189 29, 3691*, **1989**.
11. a) Gillespie, H. B.; Snyder, H. R. *Org. Synth. Coll. Vol.* **1943**, 2, 489; *Org. Synth., Coll. Vol.* **1939**, (19), 67.
b) Chandrasekhar, S.; Karri, P. *Tetrahedron Lett.* **2006**, (47), 5763.
12. Boruah, A.; Baruah, P.; Sandhu, J. *J. Chem. Res.(S)* **1998**, 614.
13. Liubeznova, M.; Karpeiskaya, E.; Klavunovskii, E. *Bull. Acad. Sci. USSR* **1990**, 39 (4.1), 731
14. Steglich, W.; Gruber, P. *Angew. Chem. Int. Ed.* **1971**, 10 (9), 655.
15. Zimmermann, J.; Bittner, K.; Stark, B.; Mulhaupt, R. *Biomaterials* **2002**, (23), 2127.
16. a) Welton, T. *Chem. Rev.* **1999**, (99), 2071;
b) Hallett, J. P.; Welton, T. *Chem. Rev.* **2011**, (111), 3508.
17. a) Meshram, H. M.; Ramesh, P.; Kumar, G. S.; Reddy, B. C. *Tetrahedron Lett.* **2010**, (51), 4313
b) Bhattacharyya, K. *J. Phys. Chem. Lett.*, **2010**, (1), 3254.
18. Tao, G.; He, L.; Sun, N.; Kou, Y. *Chem. Commun.* **2005**, 3562.

ADVANCES IN MATERIALS SCIENCE

7-8 December 2016

Green Synthesis of Silver Nanoparticles from Plants

Vidya C. Mali, Krinsha. K. Rangar, Rajendra A. Lavate, Dipak A. Kumbhar, Sanjay S. Sathe, and B. N. Kokare*

Raje Ramrao Mahavidyalaya, Jath, Maharashtra, India

*Meenalben Meheta Arts Commerce and Science College, Panchagani, Maharashtra, India.

Abstract

The present paper briefly describes the biosynthesis of silver nanoparticles and their application in different fields. Biosynthesis is a novel way to synthesize nanoparticles by using biological sources. It is gaining much attention due to its cost effective, eco friendly and large scale production possibilities. Generally physical, mechanical and chemical methods are involved for the synthesis of such important nanoparticles. But these methods are very expensive and some methods involve harmful chemicals. With the aim of developing clean, nontoxic and eco-friendly technologies, a wide range of biological sources has been used for the formation of nanoparticles. The importance of this study includes a precise and specific analysis of silver nanoparticles from biological systems that may support and revolutionize the art of synthesis. Nanotechnology is a modern field of science which plays a significant role in day to day life aspects.

Keywords: *Green Synthesis, Nanoparticles, Plants.*

1. Introduction

Nanotechnology is a modern field of science which plays a significant role in day to day life aspects. Nanotechnology is the study and application of small object which can be used across all fields such as physics, chemistry, biology, material science and engineering. Nanotechnology deals with production, manipulation and use of material ranging in nanometers¹. Nanotechnology has got direct impact on human life². Nanotechnology mainly deals with the nanoparticle synthesis having a size of 1-100 nm in one dimension used significantly concerning medicinal chemistry, atomic physics, and all other known fields too³. Nanomaterials are the atomic and molecular building blocks (~0.2 nm) of matter. Nanoparticles belong to a wider group of nanomaterials having amorphous or crystalline form and their surfaces can act as carriers for liquid droplets or gases⁴. Richard Feynman was the first person who gave a talk on Nanoparticles in the year 1959. It later on inspired the conceptual foundations of nanotechnology. Nanoparticles have been in use in pottery and medicine since ancient times. Since last decade the most effectively studied nanoparticles are those made from the noble metals such as silver, gold and platinum. Due to excellent physico-chemical properties, nanoparticles have potential applications in all fields of science and technology. Since ancient times human society use medicines, from gold, silver, mercury, sulphur, mica, arsenic, zinc, other minerals, gems, shells, horns treated with indigenous herbs as

bhasmas (a fine ash obtained through Incineration) and chendurams (prepared by the process of sublimation and they are much more potent than bhasmas). Hippocrates explained the beneficial healing and anti-disease properties of silver. Ancestors used silver bottles for storing water, wine and milk to prevent spoiling. Siddha medicine is a form of South Indian medicine which is believed to have been developed by the Siddhars⁵. Silver nanoparticles were developed as a potent antibacterial, antifungal, anti-viral and anti-inflammatory agent. The biomedical applications of silver nanoparticle can be effective by the use of biologically synthesized nanoparticles which minimize the factors such as toxicity, cost and are found to be exceptionally stable. The targeting of cancer cells using silver nanoparticles has proven to be effective⁶.

2. Methods used to synthesize nanoparticles

Traditionally Nanoparticles were produced only by physical and chemical methods. Some of the commonly used physical and chemical methods are ion sputtering, solvothermal synthesis, and sol gel technique. Basically there are two approaches for Nanoparticles synthesis namely the Bottom up approach and the Top down approach⁷. The Nanoparticles are synthesis by Physical and chemical methods like Sol-gel technique, Solvothermal synthesis, Chemical reduction, Laser ablation, Inert gas condensation and Biosynthesis of nanoparticles⁸.

Green syntheses of silver nanoparticles using plant extracts

Biosynthesis of nanoparticles using plant extracts is the latest most favorite method of green, eco-friendly production of nanoparticles as it offers one step. Currently it is exploited to a vast extent because the plants are widely distributed, easily available, safe to handle and with a range of metabolites⁹. The use of plants as the production assembly of Silver nanoparticles has drawn attention, because of its rapid, eco -friendly, non-pathogenic, economical protocol and providing a single step technique for the biosynthetic processes¹⁰. Silver nanoparticles have also gained significance due to their broad-spectrum activity against bacterial infections. Flavonone and terpenoid components of leaf broth are being predicted to stabilize the formation of Nanoparticles in comparison to high molecular weight proteins of fungal biomass¹¹. Nanoparticles produced by plants are more stable and the rate of synthesis is faster than that in other case of other organism. The reduction and stabilization of silver ions by combination of biomolecules such as proteins, amino acids, enzymes, polysaccharides, alkaloids, tannins, phenolics, saponins, terpenoids and vitamins which are already established in the plant extracts having medicinal values and are environmental benign, yet chemically complex structures.

In each and every steps of the experiment, sterility conditions were maintained for the effectiveness and accuracy in results without contamination¹². Silver nitrate ($AgNO_3$) was used as received without further purification. 5mL leaf broth was added to 100mL 10^{-3} M silver nitrate and allowed to react at ambient conditions. The observed colour change of reaction mixture from transparent yellow to dark brown indicates the formation of Silver nanoparticles. The suspension of Silver nanoparticles was allowed to settle and the excess liquid was removed. The particles were then rinsed to remove any organic residue and re-suspended in 95% ethanol for further characterization¹³.

Characterization of Silver nanoparticles

The characterization study of silver nanoparticle was done by the examining size, shape and quantity of particles. Number of technique is used for this purpose, including UV-visible spectroscopy, Scanning Electron Microscopy (SEM), Fourier Transmission Infrared

Spectroscopy (FTIR), X-Ray Diffraction (XRD), and Dynamic Light Scattering (DLS)¹⁹.

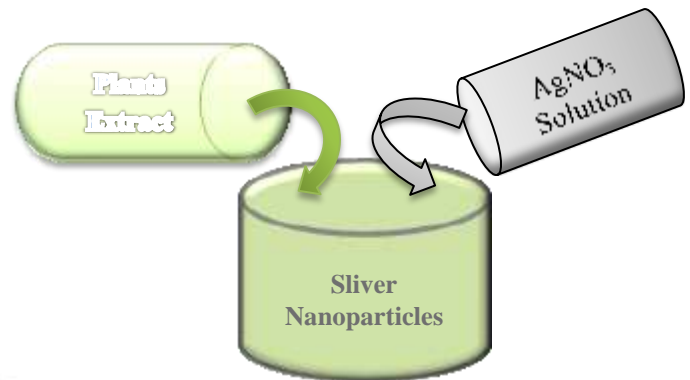


Table: The synthesized Nanoparticles from different Plants

Name of the Plants	Size (nm)	Pharmacological Applications	References
<i>Aloe vera</i>	50-350	Antimicrobial	14
<i>Allium sativum</i>	4-22	Antibacterial	15
<i>Azadirachta indica</i>	50-100	Antibacterial	15
<i>Argemone mexicana</i>	20-50	Antimicrobial	16
<i>Caria papaya</i>	20-25	Antimicrobial	16
<i>Cassia fistula</i>	55-98	Antihypoglycemic	17
<i>Catharanthus roseus</i>	48-67	Antibacterial	15
<i>Calotropis procera</i>	150-1000	Antimicrobial	15
<i>Citrullus colocynthis</i>	31	Antihypoglycemic	16
<i>Datura metel</i>	16-40	Antimicrobial	15
<i>Emblica officinalis</i>	10-20	Anticancer	18
<i>Ocimum sanctum</i>	~10	Antimicrobial	14
<i>Zingiber officinale Rosc.</i>	10	Drug delivery	17
<i>Melia azedarach</i>	78	Anticancer	18
<i>Moringa oleifera</i>	57	Antimicrobial	14
<i>Tinospora cordifolia</i>	34	Antimicrobial	16

<i>Withania somnifera</i>	5-40	Antimicrobial	14
<i>Coccinia indica</i>	10-20	Antimicrobial	16
<i>Vitex negundo</i>	10-30	Antiproliferative	16
<i>Thevetia peruviana</i>	10-30	Antimicrobial	16
<i>Vitis vinifera</i>	30-40	Antimicrobial	16
<i>Musa balbisiana</i>	20-40	Antibacterial	15
<i>Oscimum tenuiflorum</i>	10-30	Antibacterial	15

Applications of nanoparticles

The main application involved in use of Nanoparticles for biomedical applications, such as drug and gene delivery, cancer treatment and diagnostic tools, food etc. has been extensively studied throughout the past decade. The Nanoparticles created a huge interest due to their very small size and large surface-to-volume ratio, and they display absolutely novel uniqueness contrast to the large particles of bulk material. Very recently, Nanoparticles have gained significance in the field of biomedicine and bioremediation. Nanoparticles have potential application in medical field including diagnostics and therapeutics.

1. Anti-microbial, Anti-bacterial and Anti-Fungal Action^{15,16}

The antimicrobial properties of Silver nanoparticles have also been exploited both in the medicine and at home. Silver sulfadiazine creams use sometimes to prevent infection at the burn site and at least one appliance company has incorporated silver into their washing machines. Currently silver is used and appears in many consumer products likes that include baby pacifiers, acne creams, and computer's keyboard, clothing (e.g. socks and athletic wear) that protects from emitting body odour in addition to deodorizing sprays. The Silver nanoparticles exhibited antifungal action against various fungi. Actual mechanism behind the antifungal activity is not fully. The disrupting the structure of the cell membrane by destructing the membrane integrity, thereby the inhibition of the budding process has been attributed to be responsible for the antifungal

action of Silver nanoparticles against *C. albicans* species.

2. Drug delivery¹⁷

Nanoparticle involved in drug delivery. The Nanoparticles get entrapment of drugs are either enhanced delivery to, or uptake by target cells and/or a reduction in the toxicity of the free drug to non-target organs.

3. Food²⁰

There are several purposes for the development of nanofood. These include improvement of food safety, enhancement of nutrition and flavor, and cutting production and consumer costs. In addition, nanofood provides various benefits by which include health promoting additives, longer shelf lives and new flavor varieties. The application of nanotechnology in food is rapidly emerging and is involving all areas of the food chain from agricultural applications to food processing and enhancing bioavailability of nutrients.

4. Gene delivery²¹

Gene delivery it is a technique that plays a vital role that can efficiently introduce a gene of interest in order to express its encoded protein in a suitable host or host cell. Now a day, there are different types of primary gene delivery systems that mainly employ viral vectors like retroviruses and adenoviruses, nucleic acid electroporation, and nucleic acid transfection.

5. Cancer treatment¹⁸

There are a variety of Nanoparticles systems currently under investigation to be applied in biomedical with the emphasis on cancer therapeutics. The unique up conversion process of UC Nanoparticles may be utilized to activate photosensitive therapeutic agents for applications in cancer treatment.

6. Biosensor²¹

Metal Nanoparticles are feasible in different biological and electrochemical sensing system due to its chemical and physical property. Nanoparticles are coated with biological or molecular materials such as antibodies and collagen which act as bioinorganic interface. By controlling Nanoparticles size efficient fluorescent probe can be created that release fine illumination in broad array of wavelength. DNA and protein can be immobilized on surface of Nanoparticles after that intensity and wavelength

of Nanoparticles are observed and acts as a DNA and protein biosensor respectively. The shape of the Silver nanoparticles has a significant effect on the anti-microbial activity.

7. **Anti-Parasitic Action**²²

The Silver nanoparticles have been found to be effective larvicidal agents against dengue vector *Aedes aegypti* and *Culex quinquefasciatus*, filariasis vector *C. quinquefasciatus* and malarial vector *A. subpictus*, *Aedes aegypti*, *A. subpictus* and other parasites.

8. **Anti-Fouling Action**²²

The Silver nanoparticles synthesized from *Rhizopus oryzae* fungal species have been used for treating contaminated water and adsorption of pesticides and that from *Lactobacillus fermentum* cells have been used as anti-bio fouling agent. The Silver nanoparticles are being used to treat many environmental concerns like; air disinfection, water disinfection, ground water and biological water disinfection and surface disinfection.

9. **Other applications of nanoparticles**²³

In recent years Nanoparticles are involved with new applications in areas like information and communication technology, power engineering, industrial engineering, environmental engineering etc. For decades some nanoscale materials have been involved whereas others are newly discovered are used as sunscreens and cosmetics, textiles, coatings, sports goods, explosives, propellants and pyrotechnics or their applications are currently under development. All in all, the number of nano products and methods of their use increase continually. This paper has reviewed recent knowledge and built a data base of Nanoparticles. This review provides an overview of nanoparticle based upon the characterization methods, types, protocols based upon Strategies used to synthesize Nanoparticles and wide range of applications. Our study concludes that Nanoparticles has a tremendous growth in recent years. A wide range of opportunities or upcoming

projects are available some of the Nanoparticles get synthesized are cost effectiveness. For example Nanoparticles synthesis using plant sources is largely adopted due to its eco-friendly nature and cost effectiveness etc.,

Future Perspective

Nanoscale technologies can be improved and brought about new area towards revolutionizing the fundamentals of disease diagnosis, treatment, therapy and prevention by innovating nanomedicines. Because of its small size, have the potential to alter molecular discoveries arising from genomics and proteomics which can be benefit for patients. The advantage of biological production systems is in the controlled production at a molecular level. Nanoparticles are formed in highly defined structures, complex morphologies and narrow particle size distribution²⁵. As nanotechnology has gained interest in the last few years, and is expected to develop more in the future, the foremost challenge is to expand experimental protocols for the synthesis of silver nanoparticle by microbial sources, Fungal Sources and Plant sources. In addition, an enhanced understanding of the mechanism of the formation of nanoparticles and the bioreduction phenomenon of metal ions is needed. Today, with the help of modern technologies of impregnation of silver nanoparticles can solve the burning problem of resistance against antibiotics. Microbes are not able to develop resistance against silver, because they can develop against conventional and narrow target antibiotics. Metallic silver in the form of silver nanoparticles has made a beneficial comeback as a potential antimicrobial agent and has developed into diverse medical applications ranging from silver based dressings, silver coated medicinal devices, e.g. nanogels and nanolotions among others²⁶.

Conclusion

This paper has reviewed recent knowledge and built a data base of bioreductive approaches to formation of silver nanoparticles using different plant derivatives. The exact mechanism for the formation of nanoparticle by using biological resources is still being investigated and several possible ways have been proposed²⁴. Current aspects of process which includes plant sources should focus towards the use of highly structured physical and biosynthetic activities of plant cells to achieve better controlled manipulation of the size and shape of the particles. Furthermore effect is needed in order to develop more productive process for metallic nanoparticle production. In addition, improvements on biogenesis process are needed for the development of cheaper processes. It can be concluded that in

plants where carboxylic groups, amino groups, proteins and carbohydrates are present in the source extract, believed to play a key role in the biosorption and bioreduction process for the formation of nanoparticles. There is great need for further investigation to understand the effect of time, temperature, light and other parameters regarding the green synthesis of silver nanoparticles. The Silver nanoparticles synthesis using plant sources is largely adopted due to its eco-friendly nature and cost effectiveness. The synthesized Silver nanoparticles are very much important in different disciplines of life and are widely used for the benefit of mankind.

Acknowledgement

The authors are thankful to Principal Raje Ramrao Mahavidyalaya, Jath for encouragement and providing necessary facilities to complete the article.

References

1. Kavitha, K.S.et.al. (2013). Plants as green source towards synthesis of nanoparticles. *Int. Res. J. Biol. Sci.*,2(6): 66-76.
2. Jannathul Firdhouse et.al 2012. Novel synthesis of silver nanoparticles using leaf ethanol extract of *Pisonia grandis* (R. Br). *Der Pharma Chemica*, 4(6):2320-2326.
3. Amudha Murugan et.al 92014). Biosynthesis and characterization of silver nanoparticles using the aqueous extract of *Vitex negundo*. *World J. Pharm. Pharm. Sci.*, 3(8): 1385-1393.
4. Buzea, C. et.al (2007). Nanomaterials and nanoparticles: Sources and toxicity. *Biointerphases*, 2(4): 17-71
5. Arun Sudha. et.al (2009). Standardization of Metal-Based Herbal Medicines. *American Journal of Infectious Diseases* 5 (3): 193-199, 2009.
6. R.Vaidyanathan. (2009). *Biotechnology Advances*, 27:924-937.
7. Sepeur S. (2008) *Nanotechnology: technical basics and applications*.
8. Jitendra Mittal et.al (2014). Phytofabrication of nanoparticles through plant as nanofactories. *Adv. Natural Sci. Nanosci. Nanotechnol.*, 5:10.
9. Kulkarni N et.al (2014) Biosynthesis of metal nanoparticles: a review. *J Nanotechnol.* 1-8.
10. Huang J. et.al (2007) Biosynthesis of silver and gold nanoparticles by novel sundried *Cinnamomum camphora* leaf. *Nanotechnology* 18: 105104-105115.
11. Shankar SS. (2004). Rapid synthesis of Au, Ag, and bimetallic Au core-Ag shell nanoparticles using *Neem* (*Azadirachta indica*) leaf broth. *Journal of Colloid and Interface Science* 275: 496-502.
12. Sahayaraj K et.al. Bionanoparticles: synthesis and antimicrobial applications, science against microbial pathogens: communicating current research and technological advances. In: Mendez-Vilas, editor, *FORMATEX*; 2011. P. 228-44.
13. Kasthuri, J et.al (2009). Biological synthesis of silver and gold nanoparticles using *apiin* as reducing agent. *Colloids Surf. B: Biointerf.* 68, 55-60.
14. Raghunandan, et.al.(2011). Anti-cancer studies of noble metal nanoparticles synthesized using different plant extracts. *Cancer Nanotechnol.* 2, 57-65.
15. MubarakAli et.al (2011). Plant extract mediated synthesis of silver and gold nanoparticles and its antibacterial activity against clinically isolated pathogens. *Colloid Surf. B* 85, 360-365.
16. Sondi, I et.al, (2004). Silver nanoparticles as antimicrobial agent: a case study on *E. coli* as a model for Gram-negative bacteria. *J. Colloids Interface Sci.* 275, 177-182.
17. Nelson Durán (2005) Mechanistic aspects of biosynthesis of silver nanoparticles by several *Fusarium oxysporum* strains, *Journal of Nanobiotechnology* 3:8,
18. Balprasad Ankamwar, Biosynthesis of Gold Nanoparticles (Green-Gold) Using Leaf Extract of *Terminalia catappa*, *E-Journal of Chemistry*, 7(4), 1334-1339, (2010) 3.
19. Z. L.Wang, (2000) "Transmission electron microscopy and spectroscopy of nanoparticles," in *Characterization of Nanophase Materials*, Z. L. Wang, Ed., chapter 3, pp. 37-80, Wiley-VCH, Weinheim, Germany,
20. Nsongkla N et.al (2006) Multifunctional polymeric micelles as cancer-targeted, MRI-ultrasensitive drug delivery systems, *Nano Lett*, 6 (11): 2427-2430
21. Bozhevolnyi SI et.al (2006) Silver Nanoparticles, Project Group N344, P3 Project, Institute of Physics and Technology, Aalborg University.
22. A.A.Haleemkhan et.al(2015) Synthesis of Nanoparticles from Plant Extracts *International Journal of Modern Chemistry and Applied Science*, 2(3),195-203
23. Siavash Iravani et.al (2013). Green synthesis of silver nanoparticles using *Pinus eldarica* bark extract. *Hindawi Publishing Corporation, Biomed. Res. Int.*, doi: 10.1155/2013/639725.
24. Rai M, Yadav et.al (2008). Current trends in photosynthesis of metal nanoparticles *Critical Reviews in Biotechnology* 28: 277-284.
25. Sharma NC. Et.al (2007). Synthesis of plant-mediated gold nanoparticles and catalytic role of biomatrix-embedded nanomaterials. *Environmental Science and Technology* 41: 5137-5142.
26. Rai M, Yadav. et.al (2009). Silver nanoparticles as a new generation of antimicrobials. *Biotechnology Advances* 27: 76-83.

Heteropoly acid catalyzed synthesis of amidoalkyl naphthols

A. R. Supale^a and G. S. Gokavi^b

^aDepartment of Chemistry, Bharati Vidyapeeth's, Dr. Patangrao Kadam Mahavidyalaya, Sangli.416416

^bKinetics and Catalysis Laboratory, Department of Chemistry, Shivaji University, Kolhapur-416004.

Email: amitsupale@gmail.com

Abstract:

One pot synthesis of amidoalkyl naphthol by condensation of aromatic aldehydes, 2-naphthol and amide using heteropoly acids as a catalyst is reported. The reaction was carried out by using Ritter type methods. The method gave excellent yields of amidoalkyl naphthols.

Keywords: Catalytic material, Heteropoly acid, amidoalkyl naphthols, multicomponent reaction, heterogeneous catalyst.

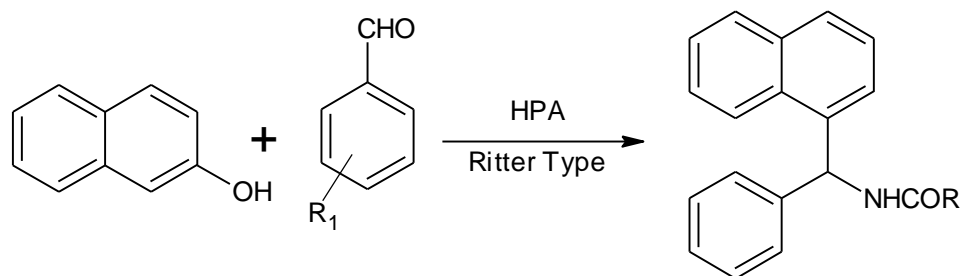
Introduction:

One pot multicomponent reactions (MCR's), sometimes also called as zipper reactions, links several transformations in a single step. In recent decades, MCR's have gain wide applicability in the field of synthetic organic chemistry as they increase the efficiency of the reaction and decrease the number of laboratory operations along with quantities of solvent and chemicals used. These methods also considerably reduce the reaction time and facilitate the yield of products than the normal multiple step methods. MCR's are an important tool in reactions such as Biginelli [1], Ugi [2] and Mannich [3]. Therefore, due to increased environmental responsibility and develop more efficient catalytic systems in synthetic organic chemistry attempts have always been made by the scientists to improve the known protocols. Such developments leads to prevail over one or more difficulties encountered in already reported systems. In continuation of our efforts to apply the properties of polyoxometalates in various organic transformations[4] we report herein the use silicotungstic acids for condensation of aldehyde, 2-naphthol and amide to synthesize amidoalkyl naphthols.

These 1-amidoalkyl-2-naphthols are important intermediates which can be easily converted into biologically active 1-aminoalkyl-2-naphthols derivatives by amide hydrolysis. The hypertensive and bradycardiac effects of these compounds have been evaluated[5]. Various Bronsted or Lewis acid catalysts such as Iodine[6], $K_5CoW_{12}O_{40}.3H_2O$ [7], *p*-TSA[8], Sulfamic acid[9],

K10 clay[10], $Ce(SO_4)_2$ [11], Cation exchange resins[12], $FeCl_3.SiO_2$ [13], $Fe(HSO_4)_3$ [14], $HClO_4.SiO_2$ [15] have been utilized for the preparation of 1-amidoalkyl-2-naphthols. However some of the catalysts used suffer from drawbacks such as long reaction time, toxicity, cost, unavailability and reusability of the catalyst. Therefore, there is still need for a green catalyst which can overcome one or more drawbacks and also an environmentally benign procedure to synthesize amidoalkyl naphthols.

Heteropoly acids due to their unique physicochemical properties are widely used as homogeneous and heterogeneous catalysts[16] for redox and acid catalyzed processes. The catalytic properties of heteropoly compounds have been associated with the characteristics of anionic units and the nature of elements contained in them. Among them, compounds of Keggin structure are known for their good thermal stability, high acidity and high oxidizing capability and are used in various organic transformations[17]. Their significantly higher Bronsted acidity of as compared with that of other traditional solid acids increased their importance in catalytic applications[18]. On the utilitarian front, among the heteropoly acids silicotungstic, phosphotungstic and molybdophosphoric acid are most well known. These are also easily available commercially. In the present investigation we report catalytic activity of silicotungstic acid for three component condensation of aldehyde, 2-naphthols and amide to form 1-amidoalkyl-2-naphthols. The condensation is carried out in acetonitrile medium (Ritter type) as shown in scheme 1.



Scheme 1

Experimental

All the products have been reported previously and were characterized by comparison of their physical and spectral data. ^1H NMR was recorded on Bruker Avance 300 MHz spectrometer. Mass spectra were recorded on Shimadzu GCMS-QP2010. Melting points were determined on an open capillary and are uncorrected. IR was recorded on Perkin Elmer-spectra one. Heteropoly acids and aldehydes, acetonitrile, dichloromethane, ethyl acetate were purchased from SD Fine chemicals (Mumbai, India) and used without further purification. All yields refer to isolated yields.

General procedure for synthesis of amidoalkyl naphthols:

2-naphthol (1 mmol, 0.144 g), aldehyde (1mmol) and catalyst (5 mol%) were taken in 5 ml acetonitrile (reactant as well as solvent) in round bottom flask. The reaction mixture was stirred at 85°C in an oil bath. The progress of the reaction was

monitored by TLC. After completion of the reaction, mixture was filtered off to separate catalyst. Then, the mixture was concentrated to get solid product which was further recrystallized from 15% ethanol.

Results and Discussion

The synthesis of amidoalkyl naphthols, catalyzed by heteropolyacid, were achieved by Ritter type reaction using acetonitrile as substrate and solvent. To optimize reaction conditions benzaldehyde and acetamide were chosen as model compounds. The various concentrations of catalyst silicotungstic acid (HSiW) were employed and reaction was carried out. The results (Table 1) indicate as the catalyst concentration increases there is an increase in the product yield and decrease in the time required with maximum yield at 5 mol% of catalyst. Further increase in the concentration of catalyst up to 10 mol% decreases the yield within the same time period. The formation side products like dibenzoxanthenes was not observed.

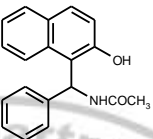
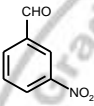
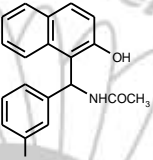
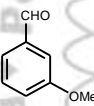
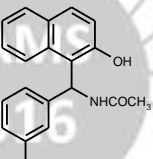
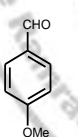
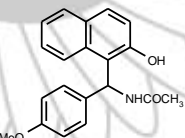
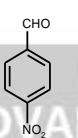
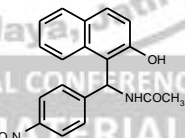
Table 1: Effect of catalyst concentration on the reaction^a:

Sr. No.	Catalyst (mol %)	Time (h)	Yield (%)
1	0.1	24	Trace
2	1	24	50
3	2	24	54
4	3	20	60
5	4	20	65
6	5	18	80
7	10	18	78

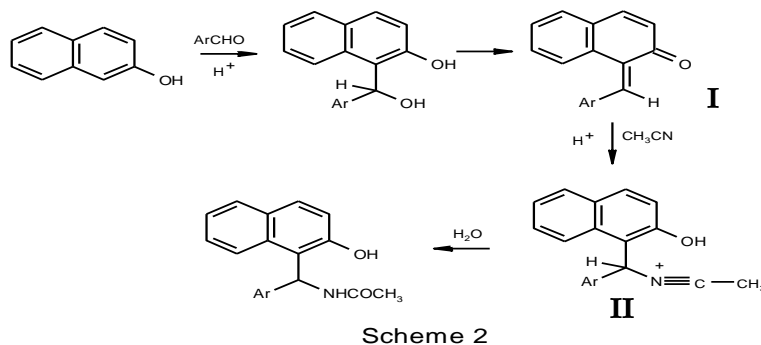
The reaction was carried out by using acetonitrile as substrate as well as solvent. The reaction affords product via Ritter type reaction after 18 hours in good yield than previously reported methods. The scope of the reaction was verified by

taking various aldehydes and subjected to the reaction along with acetamide as their counterparts in the reaction. The results of preparation of various amidoalkyl naphthols are tabulated in Table 2.

Table No: 2 Preparation of amidoalkyl naphthols:

Entry	Aldehyde	Amide	Product	Time (h)	Yield ^a (%)
1		H ₃ CCONH ₂		18	80
2		H ₃ CCONH ₂		18	90
3		H ₃ CCONH ₂		18	76
4		H ₃ CCONH ₂		18	75
5		H ₃ CCONH ₂		18	75

The probable mechanism for Method is as shown in Scheme 2.



Acetonitrile forms intermediate II with *o*-QMs which on hydrolysis gave 1-amidoalkyl-2-naphthols. After completion of the reaction the reaction mixture was filtered off to get catalyst back. It was recycled for five times without loss in its activity (Table 3).

Table 3: Recyclability of Catalyst:

Cycles	(%) Yield ^a
Initial	80
1	80
2	78
3	78
4	76
5	74

a – pure isolated yield

To show the importance of our method it is compared with previous literature and the use of silicotungstic acid as an acid catalyst is advantageous due to short reaction time and high yield.

Spectral data of selected compounds:

- Table 4, Entry 1-** M.p.242-244⁰C. IR(KBr, ν_{\max})3400, 3249, 2924, 1640, 1583, 1515, 1437, 1373, 1338, 1278, 1210, 1160, 1029, 987, 932, 875, 839, 808, 743 ¹H NMR (300 MHz, DMSO-*d*₆) δ 9.98 (s, 1H), 8.45-8.42 (d, 1H), 7.84-7.74(m, 3H), 7.37-7.11 (m, 9H), 1.97(s, 3H). MS m/z : 292 M⁺(17%), 248(3%), 231(100%), 202(15%), 127(3%), 115(7%), 104(6%), 77(4%), 43(8%).
- Table 4, Entry 2-** M.p.241-243⁰C. IR(KBr, ν_{\max})3375, 3222, 2924, 2849, 1648, 1578, 1524, 1438, 1374, 1350, 1317, 1205, 1167, 1110, 1065, 1035, 1001, 925, 807, 741, 710. ¹H NMR (300 MHz, DMSO-*d*₆) δ 10.13 (s, 1H), 8.63-8.60 (d, 1H), 8.05-8.001 (m, 2H), 7.83-7.78 (m, 3H), 7.56-7.40(m, 2H), 7.30-7.25(m, 1H), 7.19-7.15(m, 3H), 2.01(s, 3H). MS m/z : 337 M⁺(5%), 336(23%), 319(69%), 293(5%), 276(46%), 260(45%), 247(13%), 230(100%), 218(5%), 202(44%), 189(7%), 172(7%), 145(8%), 127(10%), 115(9%), 101(7%), 43(3%).
- Table 4, Entry 4-** M.p.183-185⁰C. IR(KBr, ν_{\max}) 3396, 3062, 3002, 2967, 2832, 2787, 2704, 2614, 1627, 1581, 1515, 1438, 1378, 1334, 1304, 1279, 1255, 1177, 1088, 1065, 1043, 983, 930, 880, 848, 822, 814, 8020, 745. ¹H NMR (300 MHz, DMSO-*d*₆) δ 10 (s, 1H), 8.4 (d, 1H), 7.80-7.73 (m, 4H), 7.35-7.04 (m, 6H), 2.5(s, 3H), 1.953(s, 3H). MS m/z : 322 M⁺(5%), 321(20%), 278(6%), 261(98%), 247(35%), 231(100%), 218(14%), 202(5%), 189(10%), 192(7%), 144(24%), 134(19%), 115(16%), 77(6%), 43(21%).
- Table 4, Entry 5-** M.p.248-250⁰C. IR(KBr, ν_{\max}) 3391, 3072, 1640, 1602, 1524, 1439, 1352, 1281, 1246, 1167, 1066, 1093, 983, 935, 883, 855, 825, 734,750. ¹H NMR (300 MHz, DMSO-*d*₆) δ 10.11 (s, 1H), 8.59-8.56(d, 1H), 8.14-8.12 (m, 2H), 7.83-7.79 (m, 3H), 7.41-7.38(m, 3H), 7.28-7.16(m, 2H), 2.02(s, 3H). MS m/z : 337 M⁺(8%), 336(31%), 293(8%), 276(19%), 260(72%), 247(8%), 230(100%), 202(28%), 189(6%), 145(7%), 115(13%), 43(23%).

Conclusion:

In summary, we have found that silicotungstic acid (HSiW) is an extremely good heterogeneous acid catalyst for synthesis of amidoalkyl naphthols by condensation of aromatic aldehyde, 2-naphthol and amide. The reaction was carried out by using acetonitrile as a solvent and substrate. The method is environmentally benign gives high yields of products. The catalyst, silicotungstic acid, used was recycled without loss in activity.

References:

- S. P. Maradur, G. S. Gokavi, *Catal. Commun.* 8 (2007) 279.
- I. Ugi, A. Demharter, W. Horl, T. Schmid, *Tetrahedron* 52 (1996) 11657.
- G. Zhao, T. Jiang, H. Gao, B. Han, J. Huang, D. Sun, *Green Chem.* 6 (2004) 75.
- a) S. D. Kadam, A. R. Supale, G. S. Gokavi, *Z. Phys. Chem.* 222 (2008) 635; b) S. P. Maradur, S. B. Halligudi, G. S. Gokavi, *Catal. Lett.* 96 (2004) 165.
- T. Dinermann, D. Steinhilber, G. Folkers, In *Molecular Biology in Medicinal Chemistry*; Wiley-VCH, 2004; b) A. Y. Shen, C. T. Tsai, C. L. Chen, *Eur. J. Med. Chem.* 34 (1999) 877.
- B. Das, K. Laxminarayana, B. Ravikant, B. R. Rao, *J. Mol. Catal. A: Chem.* 261 (2007) 180.
- L. Nagarapu, M. Baseeruddin, S. Apuri, S. Kantevari, *Catal. Commun.* 8 (2007) 1729.
- M. M. Khodaei, A. R. Khosropour, H. Moghanian, *Synlett* (2006) 916.
- S. B. Patil, P. R. Singh, M. P. Surpur, S. D. Samant, *Ultrason. Sonochem.* 14 (2007) 515.
- S. Kantevari, S. V. N. Vuppalapati, L. Nagarapu, *Catal. Commun.* 8 (2007) 1857.
- N. P. Selvam, P. T. Perumal, *Tetrahedron Lett.* 47 (2006) 7481.
- S. B. Patil, P. R. Singh, M. P. Surpur, S. D. Samant, *Synth. Commun.* 37 (2007) 1659.
- H. R. Shaterian, H. Yarahmadi, *Tetrahedron Lett.* 49 (2008) 1297.
- H. R. Shaterian, H. Yarahmadi, M. Ghashang, *Bioorg. Med. Chem. Lett.* 18 (2008) 788.
- H. R. Shaterian, H. Yarahmadi, M. Ghashang, *Tetrahedron* 64 (2008) 1263.
- I. V. Kozhevnikov, *Chem. Rev.* 98 (1998) 178.
- G. Li, Y. Ding, J. Wang, X. Wang, J. Suo, *J. Mol. Catal. A*, 262 (2007) 67.
- a) I. V. Kozhevnikov, *Russ. Chem. Rev.* 62 (1993) 473; b) T. Okuhara, M. Mizuno, *Adv. Catal.* 41 (1996) 13.

Hydrothermal synthesis and characterization of CNFO-BZT composites

S.G. Chavan^a, P. M. Kharade^a, S. N. tambe^a, D. S. Ghadage^a, S. B. Kulkarni^b, D. J. Salunkhe^{a*}

a. Nano-composite Research laboratory, Department of Physics, Karmaveer Bhaurao Patil Mahavidyalaya, Pandharpur, Solapur, 413 304, India.

b. Institute of Science, Mumbai, India.

Email: salunkhedj@rediffmail.com

Abstract:

The present paper reports the synthesis of $\text{Co}_{0.9}\text{Ni}_{0.1}\text{Fe}_2\text{O}_4$ (CNFO) and $\text{BaZr}_{0.05}\text{Ti}_{0.95}\text{O}_3$ (BZT0.05) composite via Hydrothermal route. The present work reports that the hydrothermal synthesis of BZT and CNFO nanoparticles followed by microwave sintering. The composites are formed by using solid state reaction of $x\text{CNFO} + (1-x)\text{BZT0.05} = x\text{CNFO-BZT0.05}$ where $x = 0.2, 0.3$ and 0.4 and investigated for their Structural, Morphological, Ferroelectric and Magnetolectric properties of Multiferric Composites.

Keywords: Hydrothermal Synthesis, Crystal Structure, Magnetolectric Effect.

Introduction:

In the last few years, many of researchers are interested in the field of Multiferric materials, because of their attractive practical application of such as transducer, actuators, phase shifter and magnetolectric sensors [1-3]. The BZT based materials have been attention for their practical applications in Dynamics Random Access Memories (DRAM) and tunable devices [4]. The ferrite CoFe_2O_4 has received a Magnetostriction materials with high resistivity, moderate saturation magnetization and excellent thermal stability [3,5].

In the present work, we report the hydrothermal synthesis of BZT and CNFO nanoparticles followed by microwave sintering. The composites are formed by using solid state reaction of $x\text{CNFO} + (1-x)\text{BZT0.05} = x\text{CNFO-BZT0.05}$ where $x = 0.2, 0.3$ and 0.4 and investigated for their structural, morphological, ferroelectric and magnetolectric properties of composites.

Experimental:

Hydrothermal Synthesis of $\text{BaTi}_{1-x}\text{Zr}_x\text{O}_3$ (BZT)/ $\text{Co}_{0.90}\text{Ni}_{0.10}\text{Fe}_2\text{O}_4$ (CNFO) Nanoparticles:

The composites consist ferroelectric and ferromagnetic was prepared by a conventional hydrothermal route. For the synthesis of $\text{BaTi}_{1-x}\text{Zr}_x\text{O}_3$ (BZT) Nanoparticles, the barium acetate (AR grade), Zirconium nitrate (AR grade) and potassium titanium oxalate (Loba Make 98.5%) are used as a precursors and potassium hydroxide was used as mineralizer. The obtained products were washed using dilute ammonia solution for several times and transferred to an autoclave filled up to 60% its volume. The reaction was carried in a

conventional furnace at 300°C for 2 hr. The product of hydrothermal reaction was again washed using dilute ammonia solution. The product is filtered and dried. Finally obtained product was annealed at 800°C for 1hr in a microwave furnace. The same method was used to synthesize the $\text{Co}_{0.90}\text{Ni}_{0.10}\text{Fe}_2\text{O}_4$ (CNFO) ferromagnetic phase taking suitable amounts of high purity of AR grade cobalt nitrate, nickel acetate and ferric nitrate were used as precursors in stoichiometric proportion.

Formation of composites:

The CNFO and BZT composites are formed using the formula:



Where $x = 0.2, 0.3$ and 0.4 . The sintered powder of CNFO and BZT was grounded together thoroughly in an Agate Mortar and pestol. The pellets are formed with diameter 1.2 cm and thickness 1.5 mm and then pellets are sintered using microwave furnace (m/s VB Ceramics) at 1200°C for 25 min in microwave furnace.

Results and discussion

Structural analysis:

Fig.1 a) and b) show the X-ray diffractogram of BZT-CNFO composite microwave sintered at 1200°C for 25 min. No impurity peaks are seen in the X-ray spectra. The peaks corresponding to (200) and (002) reflections could be attributed to the tetragonal distortion of perovskite structure of ferroelectric and spinel cubic structure of ferrite respectively in the composite samples.

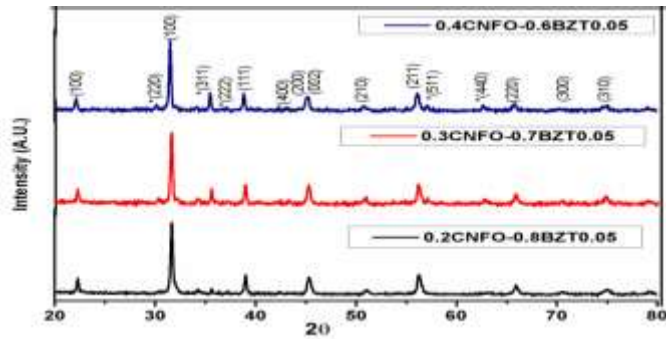


Figure1: X-ray diffractogram for xCNFO-(1-x)BZT0.05 where x=0.20,0.30 and 0.40.

Table 1: Value of maximum polarization (P_{max}),

Compositio n (x)	α (mV/Oe.cm)	$\beta \times 10^{-4}$ (mV/Oe ² .c m)
0.2	1.7	4.4
0.3	2.5	9.1
0.4	3.9	4.8

remnant polarization (P_r), coercive field (E_c) and P_r/P_{max} for xCNFO-(1-x)BZT0.05 where x=0.20,0.30 and 0.40.

Microstructure properties:

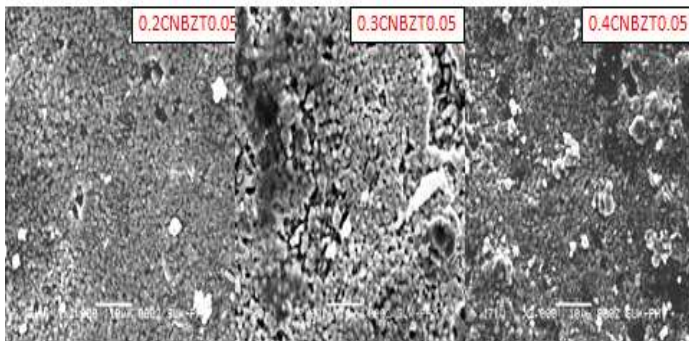


Fig. 2.SEM images of xCNFO-(1-x)BZT0.05 where x=0.20,0.30 and 0.40.

Fig. 2 show SEM images of xCNFO-(1-x)BZT0.05 for x=0.20,0.30 and 0.40 sintered at 1200°C for 25 min. SEM picture shows composite is homogeneous, more compact, lesser pores and fine grained. The grain size of xCNFO-(1-x)BZT0.05 where x=0.20,0.30 and 0.40 are 1.31, 1.75 and 1.32 μ m respectively

Ferroelectric studies:

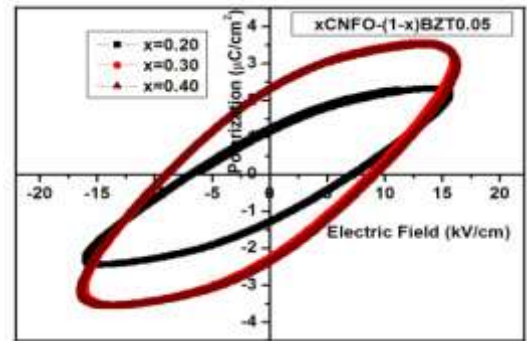


Figure 3. P-E hysteresis loops of xCNFO-(1-x)BZT0.05 for x = 0.2, 0.3 and 0.4.

Fig. 3 shows the ferroelectric hysteresis (P-E) measurements of xCNFO-(1-x)BZT0.05 composites at room temperature which show the ferroelectric behaviour of the composites. Further, if the % of concentration of ferrite contents increases, the P-E loops becomes narrow, which indicates the disrupted ferroelectric order of BZT due to addition of more percentage of CNFO in BZT[6, 7].

Magnetolectric properties:

The magnetolectric (ME) effect is defined as the dielectric polarization of a material in an applied magnetic field or vice versa. The linear and quadratic magnetolectric coefficients α and β are given by:

$$\alpha = dv / (dh \times t) \dots\dots\dots(1)$$

$$\beta = dv / (dH \times 2h_0t) \dots\dots\dots(2)$$

Here v is r.m.s value of ac voltage developed across the sample in response to an ac magnetic field with r.m.s value h, H is the applied DC magnetic field and t is the thickness of sample. The linear and quadratic magnetolectric coefficients α and β was determined at 4 KHz using a custom designed instrumentation setup.

Table 2. The linear magnetolectric coefficient α and quadratic magnetolectric coefficient β for x(CNFO-BZT0.05) for x=0.2 to 0.4.

Sr	P_{max} (μ C/cm ²)	P_r (μ C/cm ²)	E_c (kV/cm)	P_r/P_{max}
0.2	2.28	1.2	6.61	0.526316
0.3	3.34	2.31	8.77	0.691617
0.4	3.04	2.31	8.77	0.759868

Table 2 shows variations in magnetolectric coefficient α and quadratic magnetolectric

coefficient β for $x\text{CNFO}-(1-x)\text{BZT}0.05$ and $x\text{CNFO}-(1-x)\text{BZT}0.05$. The maximum value of magnetoelectric coefficients α is 3.9 mv/Oe.cm for the 0.4CNFO-BZT0.05 while the maximum value

of quadratic magnetoelectric coefficients β is 9.1 mv/Oe².cm for the 0.3CNFO-BZT0.05.

Conclusions:

The $\text{BaTi}_{1-x}\text{Zr}_x\text{O}_3$ (BZT) / $\text{Co}_{0.90}\text{Ni}_{0.10}\text{Fe}_2\text{O}_4$ (CNFO) composite consisting of two individual phases of ferroelectric and ferromagnetic was prepared by a conventional hydrothermal route. The XRD spectra shows mixed spinel perovskite phase for all compositions. The SEM micrographs show dense microstructure. P-E hysteresis of $x\text{CNFO}-(1-x)\text{BZT}0.05$ composites which show the ferroelectric behaviour of the composites The maximum value of magnetoelectric coefficients α is 3.9 mv/Oe.cm for the 0.4CNFO-BZT0.05.

Acknowledgements:

Authors are thankful to Defense Research and Development Organization-Naval Research Board for their financial support.

References:

1. C.-W. Nan, M. I. Bichurin, S. Dong, D. Viehland, and G. Srinivasan, J. Appl. Phys. 103, 031101 (2008).
2. J. van den Boogaard, D. R. Terrell, R. A. J. Born, and H. F. J. I. Giller, J. Mater. Sci. 9, 1705 (1974).
3. T. Zhao, A. Scholl, F. Zavaliche, H. Zheng, M. Barry, A. Doran, K. Lee, M. P. Cruz, and R. Ramesh, Appl. Phys. Lett. 90, 123104 (2007).
4. S. S. Mane, A N Tarale, S G Chavan, V R Reddy, P B Joshi and D J Salunkhe Indian J Phys DOI 10.1007/s12648-015-0755-z.
5. S. G. Chavan S. M. Mane S. B. Kulkarni M. E. Jayasingh P. B. Joshi, D. J. Salunkhe, J Mater Sci: Mater Electron DOI 10.1007/s10854-016-4672-5.
6. Anshu Sharma , R.K. Kotnala , N.S. Negi Journal of Alloys and Compounds 582 (2014) 628– 634.
7. R.Y. Zheng, J. Wang, S. Ramakrishna, J. Appl. Phys. 104 (2008) 034106.



Hydrothermal synthesis of CobaltOxide/ Reduced Graphene Oxide Composite and their Electrochemical Investigations

Sarika Jadhav, Ramchandra S. Kalubarme, and S.W. Gosavi*

Centre for Advanced Studies in Material Science and Solid State Physics,
Department of Physics, Savitribai Phule Pune University, (Formerly University of Pune) Ganeshkhind, Pune
- 411007, INDIA

Author to whom correspondence should be address Email: swg@physics.unipune.ac.in

Abstract:

A composite Co_3O_4 -reduced graphene oxide nanosheet (Co_3O_4 -rGO) is synthesized by facile hydrothermal method. It has been found that the Co_3O_4 particles with anurchin-like spherical microstructure are decorated on rGO nanosheet with the average size of about ~ 50 nm. The crystallinity of the rGO- Co_3O_4 composites is examined by X-ray diffraction. Raman spectroscopy confirm the successful reduction of GO to rGO and the effective interaction between Co_3O_4 and rGO matrix. Electrochemical properties are investigated by using cyclic voltammetry and galvanostatic charge/discharge in 1 M KOH electrolyte solution. Maximum specific capacitance 688 F/g is observed at 3A/g current density due to effective ion transfer and less agglomeration of Co_3O_4 nanoparticles on the surface of reduced graphene oxide.

Introduction:

In recent years, rapidly increased energy consumption is responsible for environmental problem which inspire us to develop an environment friendly, sustainable, highly efficient alternative of energy source and energy storage devices like supercapacitor and batteries [1]. Major part of current research on supercapacitor is concentrated on synthesis of better electrode material in easily process-able way having high energy storage capacity with lessened fabrication cost [2]. In supercapacitor, electrode material is a most crucial part for electrochemical performance, therefore various approaches have been explored to form desirable electrode with different structures [3]. It has been confirmed that the carbon-inorganic nanocomposites are effectively improved the electrochemical performance of metal oxide and carbon materials hence it attracted the interest of many researchers [4]. Among the available transition metal oxide, cobalt oxide (Co_3O_4) is one of most perspective material on the horizon of the metal oxide due to its high theoretical specific capacitance (~ 3560 F g⁻¹) and quite ordered structure, high surface to volume ratio, high ratio of surface atoms, high redox activity, relatively low cost, simple preparation method, high chemical durability and its high reversibility [5,6]. However, poor electrochemical stability and low electronic conductivity of Co_3O_4 limits its practical application in electrochemical storage capacitor. Hence to improve the conductivity and electrochemical performance, Co_3O_4 is combined with the carbon

based material which is electronically conductive to form a hybrid nanocomposite through growth mechanism method with different treatment [7, 8]. There are different techniques used to synthesizes and fabricate cobalt oxide nanostructure and also proposed several methods to improve the electrical conductivity of Co_3O_4 -based materials. Among all these techniques hydrothermal method is most favourable chemical route for synthesis and fabrication of nanostructured metal oxides. Taking advantage of this simplicity, there is choice to synthesis of the nanomaterials by tuning various parameters such as temperature, pH, time and concentration of the reagent or procures [9]. In this work, we report synthesis of cobalt oxide nanoparticles decorated on reduced graphene oxide (rGO) matrix by hydrothermal route for energy storage application.

Experimental Section:

Graphene oxide is synthesized from graphite powder by using modified Hummers and Offmens method reported elsewhere [10]. Synthesized graphene oxide powder (100 mg) was added in 100 ml distilled water and sonicated for an hour. The suspension was heated to 80°C for 4 h followed by addition of 3 ml of hydrazine hydrate into it. A synthesized product was collected by filtration and washing by distilled water, resultant product called reduced graphene oxide (rGO) is used for further analysis and experiment.

For Co_3O_4 -rGO synthesis, 0.1 g of rGO powder was added in 100 mL of deionized water and sonicated. Then a fresh 0.1M solution of CoCl_2 was prepared in

DI water and further sonicated for 20 min. The formed solution of Co-precursor was added in rGO suspension followed by addition of 2M urea solution under constant stirring for 60 min. Subsequently, the suspension was transferred to 200 mL teflon-lined stainless steel pressure vessel, maintained at 150°C for 4 hr. After completion of reaction the reactor is allowed to cool naturally at room temperature. After cooling precipitate was collected by filtering and washing with distilled water and absolute ethanol for several times then dried over night in oven at 60° C. Finally, Co₃O₄-rGO nanocomposite was obtained by annealing above product at 450° C temp for two hours.

Result and Discussion:

From the diffraction pattern of reduced graphene oxide, Fig. 1(a), highly intense peak at ($2\theta = 23^\circ$) is observed indicating the formation of reduced graphene. The analysis shows face centered cubic (FCC) crystal structure, having interplanar distance 1.97 Å. Fig. 1(b) shows XRD pattern for Co₃O₄-rGO composite. The diffraction pattern of Co₃O₄/rGO represents strong crystalline peaks at $2\theta = 19.0^\circ, 31.1^\circ, 36.8^\circ, 44.8^\circ, 58.9^\circ, 65.9^\circ$ corresponds to (111),(220),(311),(400),(511),(440) planes of standard cubic phase for Co₃O₄ (JCPDS NO. 42-1467). No other characteristic peak was observed indicating the purity of Co₃O₄ embedded in rGO matrix [11].

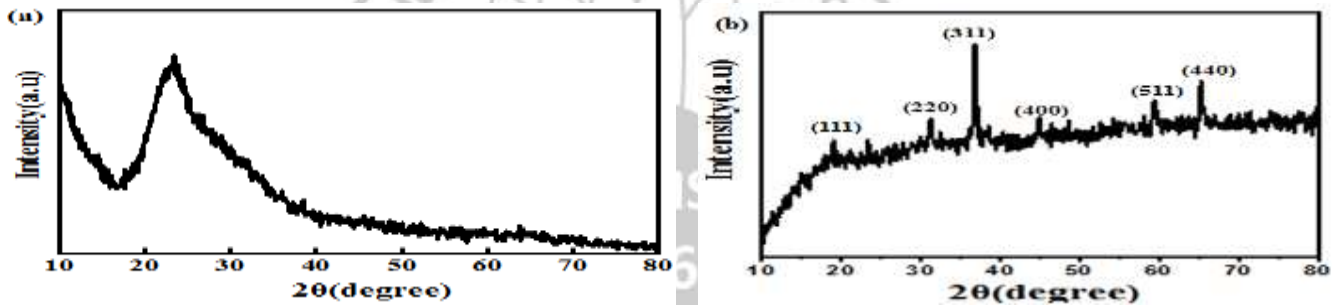


Fig.1 XRD pattern of (a) Reduced Graphene Oxide (rGO)(b) Co₃O₄-RGO

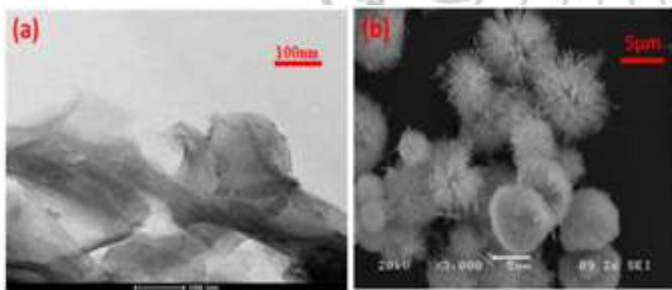


Fig.2 SEM images of (a) Reduced Graphene Oxide (b)Co₃O₄-RGO

The surface morphologies of synthesised reduced graphene oxide and Co₃O₄-rGO were investigated by scanning electron microscopy and transmission electron microscopy. Fig.2 (a) clearly shows the stacking of graphene sheets, urchin structured cobalt oxide (Co₃O₄) nanospheres with rGO nanocomposite are shown in Fig.2(b).Urchin structured 3D Co₃O₄ diameter ranges in between 10 -50µm.The urchin-like spheres are composed with lots of nanorods resulting from oxidation and decomposition of initial precursor. Growth of nanorod is outward from core and become hyper-

branched, uniform and unidirectional with length of micrometer is observed.

To investigate electrochemical performance of Co₃O₄-rGO nanocomposite, three electrode cell comprising Co₃O₄-rGO electrode as working, Pt as counter and Ag/AgCl₂ as reference electrode in 1M KOH electrolyte is used to record cyclic voltammogram (CV). Fig.3 (a) shows CV plot of Co₃O₄-rGO, in this plot a well define redox peak shows the pseudo capacitive behaviour of composite which was due to the hydroxyl ions with respective electrode [12]. Calculated specific capacitance value for Co₃O₄-rGO nanocomposite is 688 Fg⁻¹ at 10 mVs⁻¹ scan rate. Fig. 3(b) shows CV curves for Co₃O₄-rGO electrode at different scan rate, from this it is observed that, while increasing the scan rates, redox peak intensities increases with slight peak shift towards higher potential, which was evidence of fast redox reactions occur at the

interface between the active material and electrolyte. Generally, the rate capability was mainly dependent on three processes such as (i) the charge transfer in the electrode, (ii) the adsorption of ions on the electrode surface and (iii) the diffusion of electrolyte ions. Any of these processes is relatively slow at higher scan rate which reduces the specific capacitance of the composite. In case of Co_3O_4 -rGO nanocomposite reduced graphene oxide sheets provided highly conductive platform for the Co_3O_4 hierarchical structures due to the uniform dispersion

and intercalation on rGO nanosheet. This led to increase the electrochemical surface areas via enhancing the active sites of cobalt oxides on rGO nanosheet. The characteristic shape of the CV curve was not significantly changed, which was an indication that the Co_3O_4 -rGO composites have an outstanding rate capability. Well defined redox peak is observed at lower potential which confirms non-aggregation of Co_3O_4 nanoparticles on rGO nanosheets.

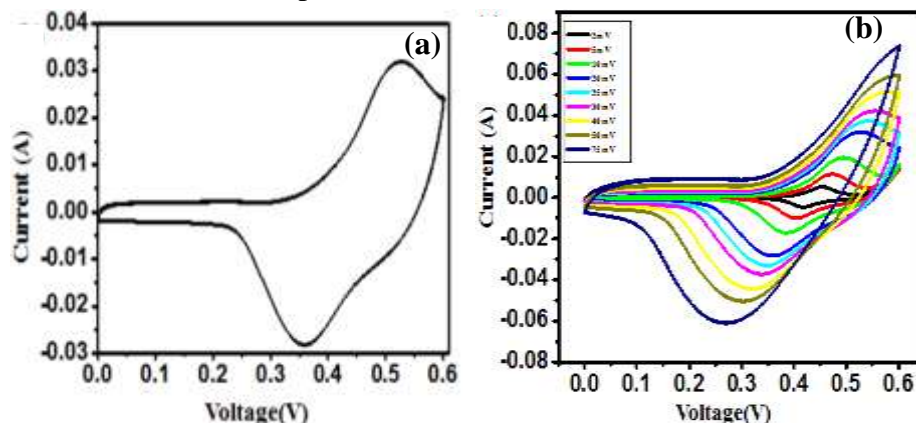


Fig.3 CV curves of (a) At scan rate of 10 mV s^{-1} (b) at different scan rate for Co_3O_4 -rGO composite electrodes in 1M KOH electrolyte

Conclusion:

A cost effective and simple hydrothermal method is successfully employed to fabricate Co_3O_4 -rGO nanocomposites as electrode materials for electrochemical supercapacitors. Urchin-like Co_3O_4 spheres having diameter ranging from $10\text{-}50\mu\text{m}$ composed with lots of nanorods is confirmed in SEM analysis. The Co_3O_4 /rGO composite exhibited specific capacitance of 688 F g^{-1} at 10 mV s^{-1} scan rate. This composites possess good electrochemical behaviour that are useful as electrode material for supercapacitors. In addition, the prepared materials are expected to have potential applications as catalysts, absorbents, and electrodes for other electronic devices.

Acknowledgement: SJ would like to thank University Grant Commission, UPE Phase II for financial support. RSK would like to thank the University Grants Commission, New Delhi, for the awarding of the D. S. Kothari Post-Doctoral Fellowship (F.4-2/2006 (BSR)/PH/14-15/0132)

References:

1. C. Yu, J. Yang, G. Wang, C. Zhao, X. Fan, J. Qui, *Nanoscale*, 2014, 6, 3097..
2. D.A.C.Brownson, D.K Kampouris, C.E. Banks, *J. Power Sources*, 2011, 196, 4873.
3. X. Tian, M. Shi, X. Xu, M. Yan, A. M. Khan, C. Han, L. He, L. Mai, *Adv. Mater.* 2015, 27, 7476.
4. D. Eder, *Chem. Rev.* 2010, 110, 1348.
5. C.Z. Yuan, L. Yang, L.R. Hou, L.F. Shan, X.G. Zhang, X.W. Lou, *Energy Environ.Sci.* 2012, 5, 7883
6. S.K.Meher, G.R.Rao, *J.Phys. Chem.C* 2011, 115, 15646.
7. G.Y. He, J. H. Le, H. Q. Chen, J. Shi, X. Q. Sun, X. Chen, X. Wang, *Mater. Letter* 2012, 82, 61.
8. S. Park, S. Kim, *Electrochim. Acta*, 2013, 89, 513.
9. M.M. Rahmana, J. Z. Wanga, X. L. Deng, Y. Li, H. K. Liu, *Electrochim. Acta*, 2009, 55, 504.
10. N.A. Kumar, S. Gambarelli, F. Duclairoir, G. Bidan, L. Dubois, *J. Mater. Chem. A*, 2013, 1, 2789.
11. Y. Kim, Y. Noh, E. J. Lim, S. Lee, S. M. Choi, W. B. Kim, *J. Mater. Chem. A*, 2014, 2, 6976.
12. N. Duraisamy, A. Numan, K. Ramesh, K. H. Choi, S. Ramesh, S. Ramesh *J. Mater. Lett.*, 2015, 161, 694.

Identification of Bacterial Blight Disease on Pomegranate Fruit

D.S. Gaikwad¹ and V. S. Jamadade^{2*}

1. Department of Electronics Sinhgad College of Engineering, Pandharpur, India
2. Department of Physics, Dahiwadi College Dahiwadi, Tal-Man, Dist- Satara, India

Author email: dhanshri712@gmail.com

Abstract

The main objective of this paper is to identify the bacterial blight disease on pomegranate fruits collected from farms in Natepute region of solapur district. In this image processing is used as tool for identification of diseases on Pomegranate fruit. The present system has efficiency and simplicity which will help in automation of agriculture. We develop a system which basically use of K-means clustering and SVM techniques. SVM is used to classify the diseases on pomegranate fruit. Feature extraction is used to extract the different feature form the diseased pomegranate image. The features Mean, Variance, Entropy, Standard Deviation etc are extracted. From these feature values the range of dataset for each disease is decided.

Keyword- Pomegranate, Bacterial Blight Disease, K-means, SVM(support vector machine)

1. Introduction

Pomegranate (*punica granatum*), so called "fruit of paradise" is one of the major fruit crops of arid region. It is popular in Eastern as well as in western parts of the world. In India it is cultivated over an area of 130.77 thousand hectare with a production of 1345.72 thousand MT (NHB, 2014). Amongst different states growing pomegranate, Maharashtra is the largest producer with a total area of 90 thousand hectare and production of 945 thousand MT followed by Karnataka, Andhra Pradesh, Gujarat and Rajasthan.

Area under pomegranate is increasing worldwide because of its hardy nature, wider adaptability, drought tolerance, higher yields, excellent keeping quality and remunerative prices in domestic as well as export markets. It thrives well in dry tropics and sub-tropics and performs up very well in soils of low fertility status, adding to that it is salt tolerant too.

The fruit has a wide consumer preference for its attractive, juicy, sweet, acidic and refreshing arils. Pomegranate fruits are good source of carbohydrates and minerals such as calcium, iron and sulphur possess pharmaceutical and therapeutic properties. It is rich in vitamin C and citric acid is the predominant organic acid in pomegranate. Glucose (5.46%) and fructose (6.14%) are the main sugars with no sucrose in fruits. Sweet varieties are mildly laxative, whereas sour types are good against inflammation of stomach and heartache. Flower buds are very useful in Ayurveda for managing bronchitis.

2. Methodology

The images of pomegranate fruits are collected from pomegranate farms in Natepute region of solapur

district. In this region, we found pomegranate fruits are majorly affected by bacterial blight disease. At first, collected images of pomegranate fruit given as input to the system. These images are pre-processed and then segmented by using K-means clustering algorithm. Features are extracted from segmented cluster containing disease part. I) Image Acquisition- The first phase of any vision system is the image acquisition stage. After collecting the images, different methods of processing can be applied to the image to achieve proposed tasks. II) Pre-processing- Preprocessing is the important step in any vision system. In preprocessing images are analyzed is such a way that images becomes more meaningful for farther use. III) Image Segmentation - In image segmentation the K-means clustering technique is used. K-means clustering method forms the cluster of processed image. These clusters give the information about the healthy part of the image, diseased part of the image and the back ground image. IV) Feature extraction- Feature extraction is the procedure to choose for the important characteristics of an image. Transforming the input data into the set of features is called Feature extraction. Thirteen helpful features are extracted from the pomegranate fruit image are Mean, Variance, Entropy, RMS value, Standard deviation, Smoothness, Kurtosis, Skewness, IDM, Contrast, orrelation, Energy, Homoginity. V) Classification- Support vector machine (SVM) concept is used for classification. Support vector machines (SVMs) were initially intended for binary classification. A number of methods have been projected where usually we create a multiclass classifier by combining some binary classifiers. Some authors

also wished-for methods that consider all classes at once. A support vector machine constructs a set of hyper planes in a high or infinite dimensional space, which can be used for classification. In this work SVM classify the pomegranate disease images into the respective disease category.

3. Experimental Results



Fig.1 Sample 1: Result of Bacterial blight disease.



Fig.2. Sample 2: Result of Bacterial blight disease.

Results show that the Bacterial Blight disease is identified correctly and the affected region is 3.187% and 3.18712% respectively.

The disease is characterized by appearance of small, irregular and water-soaked spots on fruit. If cracks are passing through the spots then the disease identified would be Bacterial blight.

4. Conclusions

From the above results, we can conclude that, the image processing technique is able to identify the Bacterial Blight disease on pomegranate fruit. The main motive of this system is to improve the efficiency and productivity. This work is very useful for farmers. In this paper, we are successfully identified Bacterial Blight disease on pomegranate fruits collected from farms in Natepute region of solapur district. The K-means clustering algorithm, Feature Extraction, and multiclass SVM is the important steps in our work.

References

1. Tejal Deshpande, Sharmila Sengupta, K. S. Raghuvanshi , "Grading & Identification of Disease in Pomegranate Leaf and Fruit," Vol.5(3), 2014, 4638-4645.
2. Monika Jhuria, Ashwani Kumar, Rushikesh Borse, "Image Processing For Smart Farming: Detection of Diseases and Fruit Grading," IEEE ICIIP, pp.521-526, 2013.
3. Sindhuja Sankarana, Ashish Mishra Reza Ehsania, Cristina Davisb,"A review of advanced techniques for detecting plant diseases,"Computers and Electronics in Agriculture, vol. 72, pp.1-13, 2010.
4. Usmaïl Kavdir,Daniel E. Guyer, "Apple Grading Using Fuzzy Logic", Turk J Agric (2003), 375-382 .
5. C.C.Teoh and A.R Mohd Syaifudin,"image processing and analysis techniques for estimating weights of Chikanan mangoes "J.Trop.Agric.and fd. Sc., vol35 (1), pp.183-190, 2007.
6. Sanjeev S Sannakki, Vijay S Rajpurohit, V B Nargund, ArunKumar, R, Prema S Yallur , "Leaf Disease Grading by MachineVision and Fuzzy Logic", Int. J. Comp. Tech. Appl., Vol 2 (5),1709-1716, 2011.
7. Boaz lerner, Hugo Guterman, mayer Aladjem,Its'hak Dinstein," A comparative study of neural network based feature extraction paradigm," pattern Recognition Letters, vol.20, pp.7-14, 1999.
8. Rafael C, Gonzalez, Richard E. Woods, "Digital Image Processing", second edition, 2005.
9. H.D. Cheng, X.H. Jiang, Y. Sun, Jingli Wang," Color image segmentation: advances and prospects," Pattern Recognition 34, PP.2259-2281, 2001.
10. Anand.H.Kulkarni, Ashwin Patil R. K.," Applying image processing technique to detect plant diseases "Vol.2, Issue.5, Sep-Oct. 2012 pp-3661-3664 .

Magnetic Behavior Of (X) $\text{Co}_{0.8}\text{Mn}_{0.2}\text{Fe}_2\text{O}_4$ And (1-X) $\text{PbZr}_{0.52}\text{Ti}_{0.48}\text{O}_3$ Magnetoelectric Composites

S. P. Yadav^a, K.Y. Rajpure^{b*}

^aKaramaveer Bhaurao Patil College, Vashi, Navi Mumbai 400703 (M.S), India.

^b Electrochemical Materials Laboratory, Department of Physics, Shivaji University, Kolhapur 416004 (M.S), India, *Corresponding Author: rajpure@yahoo.com, Tel: +91-231-2609227, Fax: +91-231-2691533

Abstract

The magnetoelectric composites namely (x) $[\text{Co}_{0.8}\text{Mn}_{0.2}\text{Fe}_2\text{O}_4]$ and (1-x) $[\text{PbZr}_{0.52}\text{Ti}_{0.48}\text{O}_3]$ (x= 0.25, 0.50 and 0.75) were prepared by standard ceramic method. The prepared samples were characterized by X-ray diffraction technique. The SEM micrographs of composites were recorded to determine the average grain size and also to study the surface morphology. The hysteresis measurements were carried out to determine saturation magnetization (M_s) and coercivity (H_c) of the samples. The variation of saturation magnetization and magnetic moment (μ_B) is interpreted in terms of composition.

Keywords Composite materials, Magnetic measurements, XRD

1. Introduction

Composite materials consisting of piezomagnetic and piezoelectric phases are known as magnetoelectric (ME) composites. A ME effect is the variation of dielectric polarization in a system as a response to an applied magnetic field or an induced magnetization by an external electric field. It occurs due to interaction between the magnetic and electric dipoles and it is absent in the constituent phases [1-3]. ME effect in composites totally depends on the chemical equilibrium of individual phases, magnetostriction coefficient of ferrite phase and piezoelectric coefficient of ferroelectric phase and mechanical coupling between grains.[4,5]. Also the resistivity of both phases should be high in order to avoid the leakage of accumulated charges through the magnetostrictive phase. The PZT ($\text{PbZr}_{0.52}\text{Ti}_{0.48}\text{O}_3$) has great piezoelectric properties with high dielectric constant and a better mechanical property. The ME composites consisting of these two phases are expected to yield better ME output [6,7]. A suitable combination of piezoelectric and piezomagnetic phases gives rise to this property. From literature survey it is observed that researchers have studied the ME effect in various composites [8,9]. We report here our results on measurements of structural and magnetic behaviour of the composites consisting of Mn substituted cobalt ferrite and PZT.

2.1 Preparation of ME composites

ME composites having the general formula (x) $\text{Co}_{0.8}\text{Mn}_{0.2}\text{Fe}_2\text{O}_4$ and (1-x) $\text{PbZr}_{0.52}\text{Ti}_{0.48}\text{O}_3$ were prepared by using the conventional ceramic method. The ferrite phase $\text{Co}_{0.8}\text{Mn}_{0.2}\text{Fe}_2\text{O}_4$ was prepared by

using combustion of aqueous solution of redox mixture of cobalt nitrate, manganese nitrate and ferric nitrate in stoichiometric molar proportions taken in a pyrex dish. The whole mixture of solution of nitrates was heated at about 80°C. Glycine was added to the melt and the slurry was introduced into a furnace preheated to 400 °C. After evaporation of the water content, the mixture ignited to combust with a flame and produces a fine powder. The powder was finally sintered at 1000 °C for 5h in the air. The ferroelectric phase $\text{PbZr}_{0.52}\text{Ti}_{0.48}\text{O}_3$ (PZT) was synthesized by using ceramic method. PbO , ZrO_2 and TiO_2 in molar proportions were milled for 2-3 h and pre-sintered at 500 °C for 10 h in air. After pre-sintering the composites were prepared with constituent phases with $x = 0.25, 0.5$ and 0.75 . The composites were again ground for 3 h to mix them thoroughly. The powders were then pressed into pellets and final sintering was carried at 1200 °C for 12 h and naturally cooled to room temperature.

2.2 Characterization

The crystal structure of the composites as well as their constituent phases was identified by powder X-ray diffraction measurements (XRD) performed with a Siemens D5000 X-ray diffractometer using $\text{Cu K}\alpha$ radiation ($\lambda=1.5406\text{\AA}$). The magnetization measurements of the samples were carried out by using high field hysteresis loop tracer, designed by Tata Institute of Fundamental research, Mumbai, connected to the computerized system. The magnetic moment was calculated using the relation

$$\mu = \frac{M\sigma_s}{5585} \quad (1)$$

where M is molecular weight and σ_s is the magnetization per gram of the sample[10,11].

3. Results and Discussion

3.1. Structural analysis

Fig.1 shows the X-ray diffraction patterns of (x) $\text{Co}_{0.8}\text{Mn}_{0.2}\text{Fe}_2\text{O}_4$ and (1-x) $\text{PbZr}_{0.52}\text{Ti}_{0.48}\text{O}_3$ composites with $x = 0.25, 0.5$ and 0.75 , respectively. Observed XRD patterns are characteristics of ferrite and ferroelectric phases. The indexing of patterns confirms that ferrite has cubic spinel structure and ferroelectric has tetragonal perovskite structure, because in ferrite (311) and in ferroelectric (101) reflection is more intense [12,13]. The intensity as well as the number of ferrite peaks increases with increasing ferrite content in the composites. The lattice parameters for ferrite phase, ferroelectric phase and their ratio (c/a) are listed in Table 1. The lattice parameters match well with the lattice parameters of the composites when present as single phase.

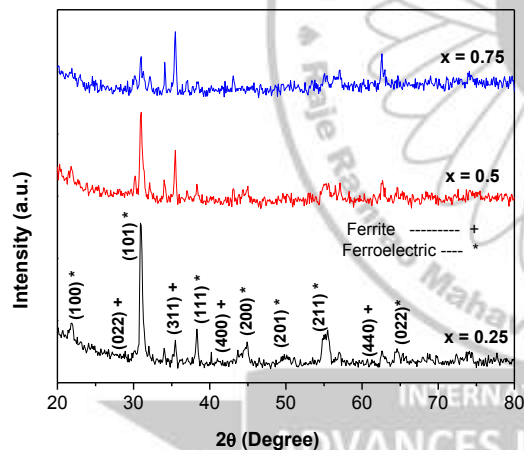


Figure 1: XRD patterns of (x) $[\text{Co}_{0.8}\text{Mn}_{0.2}\text{Fe}_2\text{O}_4]$ and (1-x) $[\text{PbZr}_{0.52}\text{Ti}_{0.48}\text{O}_3]$ ME composites ($x = 0.25, 0.5$ and 0.75)

Table 1: Structural properties of Co-ferrite (x) $[\text{Co}_{0.8}\text{Mn}_{0.2}\text{Fe}_2\text{O}_4]$ and (1-x) $[\text{PbZr}_{0.52}\text{Ti}_{0.48}\text{O}_3]$ ME composites ($x = 0.25, 0.5$ and 0.75)

Composition (x)	Lattice parameter (Å)			
	Ferrite 'a'	Ferroelectric		
		'a'	'c'	c/a
x = 0.25	8.4089	4.0677	4.13	1.02
x = 0.50	8.3923	4.0677	4.13	1.02
x = 0.75	8.3923	4.0677	4.12	1.01

3.2 Magnetic properties

The magnetic hysteresis plots for $x = 0.25, 0.5$ and 0.75 compositions of the composites at room temperature are shown in Fig. 2. All the samples exhibited $B-H$ hysteresis loop, typical of magnetic behaviour, and this indicates that the presence of an ordered magnetic structure existing in the mixed spinel-perovskite system. The values of saturation magnetization (M_s) residual magnetization (M_r), coercivity (H_c) and magnetic moment (μB) of the composites are given in Table 2. It is observed that the $M_s, \mu B$ as well as the H_c values increases with increase in ferrite content. This is because the magnetization in the composites is mostly contributed by ferrite phase while ferroelectric phase acts as a nonmagnetic component [14]. It is observed that the saturation magnetization for the composites is less than that for ferrites. In composites, the ferroelectric phase in the presence of magnetic field acts as pores among the grain causing a reduction in saturation magnetization. Hence results in reduction of magnetic properties of composites [15, 16].

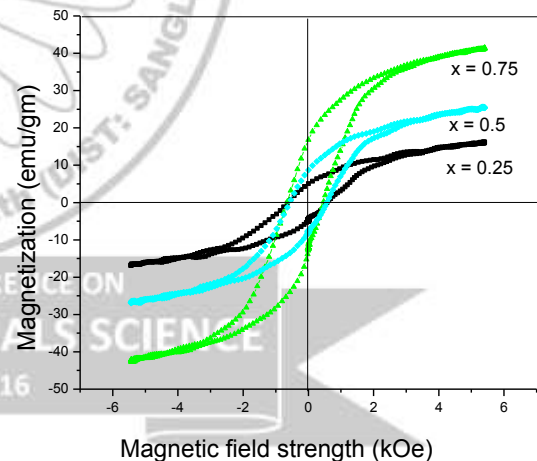


Figure 2: Magnetization curves of (x) $[\text{Co}_{0.8}\text{Mn}_{0.2}\text{Fe}_2\text{O}_4]$ and (1-x) $[\text{PbZr}_{0.52}\text{Ti}_{0.48}\text{O}_3]$ ME composites ($x = 0.25, 0.5$ and 0.75)

Table 2. Variation of magnetic properties of (x) $[\text{Co}_{0.8}\text{Mn}_{0.2}\text{Fe}_2\text{O}_4]$ and $(1-x)$ $[\text{PbZr}_{0.52}\text{Ti}_{0.48}\text{O}_3]$ ME composites(x= 0.25, 0.5, and 0.75).

Composition (x)	Remanence Mr (emu/gm)	Saturation magnetization Ms (emu/gm)	n_B (μ_B)	$(dE/dH)_H$ ($\mu\text{V}/\text{cmOe}$)
x = 0.25	5.90	16.20	0.6696	0.641
x = 0.50	9.89	25.59	1.0623	0.354
x = 0.75	13.31	41.42	1.7267	0.204

Conclusions

The present ME composites samples are prepared by standard ceramic method. The X-ray analysis reveals the formation of cubic spinel structure for the ferrite phase and tetragonal perovskite structure for the ferroelectric phase.. The saturation magnetization and magnetic moment are found to increase with increase in ferrite content. These ME composites, may be used as magnetic sensors for dc and ac magnetic field measurements, transducers and actuators.

References:

- G. Srinivasan, E. T. Rasmusen, Appl. Phys. A 78 (2004)721.
- Ce-Wen Nan, M. I. Bichurin, Shuxiang Dong, D. Viehland, G. Srinivasan J. Appl.Phys.103(2008) 031101.
- J. Ryu, S. Priya, K. Uchino, H.-E. Kim, J. Electroceram. 8 (2002) 107.
- J. Ryu, A.V. Carazo, K. Uchino, H.E. Kim, J. Electroceram. 7 (2001) 17.
- S.R. Kulkarni, C.M. Kanamadi, B.K. Chougule Mater. Res. Bull. 40 (2005) 2064.
- S.L. Kadam, C.M. Kanamadi, K.K. Patankar, B.K. Chougule, Mater. Lett.59 (2005) 215.
- J. Ryu, A. Vazquez Carazo, K. Uchino, H.-E.Kim, Jpn. J. Appl. Phys. 40 (2001) 4948.
- J. Zhai , N. Cai , Z. Shi, Y.Lin and C. W. Nan J. Phys. D:Appl. Phys. 37(2004)823.
- N. Ramamanohar Reddy, E. Rajagopal, K.V. Sivakumar, K.K. Patankar, V.R.K. Murthy, J. Electroceram. 11 (2003) 167.
- B.K. Bammannavar, L.R. Naik, B.K. Chougule, J. Appl. Phys. 104 (2008) 064123.
- S. V. Suryanarayana, Bull. Mater.Sci. 17(1994)1259.
- J.V. Boomgaard, R.A.J. Born, J. Mater. Sci. 13 (1978) 1538.
- S.L. Kadam, K.K. Patankar, V.L. Mathe, M.B. Kothale, R.B. Kale, B.K.Chougule, Mater. Chem. Phys.78 (2000) 178.
- Z. Yu, C. Ang, J. Mater. Sci.-Mater. Electron.13 (2002) 193.
- D.R. Patil, S.A. Lokare, S.S. Chougule, B.K. Chougule, Physica B 400 (2007) 77.
- A.C.F.M. Costa, E. Tortella, M.R. Morelli, R.H.G.A. Kiminami, J. Magn. Magn.

INTERNATIONAL CONFERENCE ON
ADVANCES IN MATERIALS SCIENCE
7-8 December 2016

Magnetodielectric properties of SBN–CMFO nanocomposites

S. R. Jigajeni^a, S. H. Kshirsagar^b

^aInstitute of Science, Nagpur., ^bN.B.Navale Shinagad college of engineering Solapur.

Email-sjjigajeni@gmail.com

Abstract

The paper reports synthesis of nanoparticles of $\text{Sr}_{0.5}\text{Ba}_{0.5}\text{Nb}_2\text{O}_6$ (SBN) and $\text{Co}_{1.2-x}\text{Mn}_x\text{Fe}_{1.8}\text{O}_4$ (CMFO) via ceramic and hydroxide co-precipitation routes, respectively. The nanopowders of SBN and CMFO0.3 (MSBN0.3) are compacted together to form the desired magnetodielectric (MD) composites. The paper reports synthesis, structural and MD studies on the MSBN composites. The results on the magnetocapacitance (MC) are observed interesting and could be correctly understood in terms of the stress induced variation in the dielectric constant. The MC is observed to remain fairly constant between 10 and 500 kHz and possess a useful magnitude of nearly 4 %.

Keywords: $(\text{SrBa})\text{Nb}_2\text{O}_6$, $(\text{CoMn})_{1.2}\text{Fe}_{1.8}\text{O}_4$ and Magnetocapacitance.

Introduction: The composites of ferroelectric and magnetostrictive compounds are known to exhibit a useful magnitude of magnetoelectric coupling (1, 2). These composites need the presence of ferroelectric/relaxor composition possessing a useful value of maximum polarization (P_{max}), remanent polarization (P_r) and piezoelectric coefficient (d), while the magnetostrictive phase is required to possess a large value of resistivity (ρ), magnetostriction (k) and low value of coercive field

H_c . As shall be seen in the next paragraph, the (SBN) and Mn-substituted cobalt ferrite form a correct choice for the formation of such compositions. This phenomenon was also attributed to the stress-induced change in polarization and therefore the dielectric constant. At present, the ME effect in such composites is better known but the magnetodielectric (MD) effect has rarely been investigated (3-5).

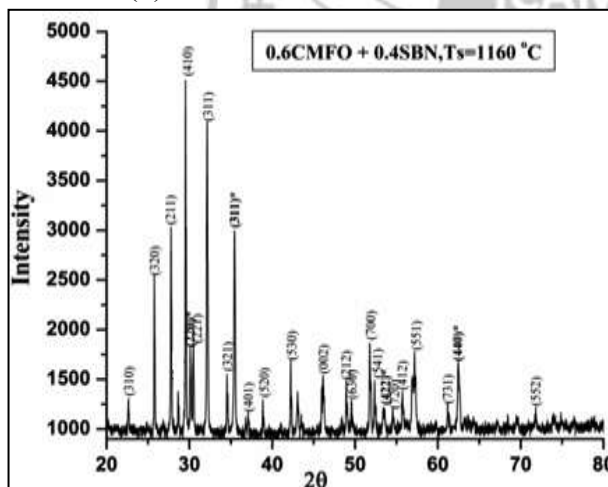


Fig. 1. XRD of y MSBN0.3 composite, $T_s=1160^\circ\text{C}$.

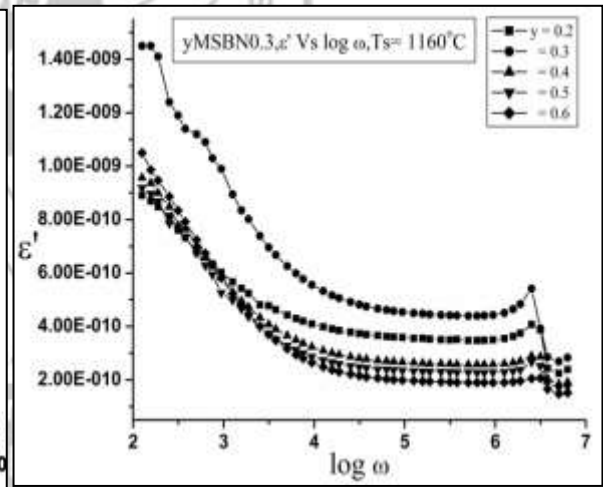


Fig. 2 : Variation of ϵ' vs $\log \omega$ for composites, $T_s=1160^\circ\text{C}$

Here, substitution of Mn at A or B site is observed to reduce the anisotropy energy and improve the magnetomechanical coupling of the CoFe_2O_4 . Therefore, considering virtues of Co and Mn ions in the ferrite system, CMFO has been selected as a piezomagnetic phase to form the MD composites (6,7) . As the physical properties of ferrites are dependent on the process of synthesis. For the present studies one ferrite compositions is selected, for $x = 0.3$ where k is comparatively low but q is high.

Further, the relaxors ferroelectrics are known to have very large electrostrictive response in addition to the piezoelectric coupling; however, most relaxors contain Pb and their lack of remanent polarization makes them unsuitable for piezoelectric applications. An exception is the $(\text{Sr}, \text{Ba}) \text{Nb}_2\text{O}_6$ family which can sustain remanent polarization after polling (8). Therefore, investigations on MD composites with $\text{Sr}_{0.5}\text{Ba}_{0.5}\text{Nb}_2\text{O}_6$ (SBN) as a piezoelectric phase are observed to be interesting.

Owing to the discussion above, the present paper reports synthesis and characterization of MD composites $y\text{MSBN} = y\text{CMFO} + (1-y)\text{SBN}$. The paper reports MD properties of the above system for CMFO possessing $x = 0.3$. The parent composition CMFO and SBN are initially studied to confirm the formation of the required SBN and CMFO phases and particle size in nanometer range. The paper reports investigations on crystal structure, dielectric and the magnetocapacitance (MC) defined through the relation $\text{MC} = ((\epsilon(H) - \epsilon(0)) / \epsilon(0)) * 100\%$. MC is determined with applied magnetic field H_{dc} . The dielectric properties are investigated as a function of temperature from 300 to 470 K and frequency (f) between 100 and 1 MHz, while MD properties are determined at room temperature as a function of f and H_{dc} up to 6 kOe.

Experimental:

Synthesis of CMFO and SBN: The hydroxide co-precipitation route has been adopted for the synthesis

of $\text{Co}_{1.2-x}\text{Mn}_x\text{Fe}_{1.8}\text{O}_4$ (CMFO). The $\text{Co}(\text{NO}_3)_2 \cdot 6\text{H}_2\text{O}$, $\text{Fe}(\text{NO}_3)_3 \cdot 9\text{H}_2\text{O}$ and MnCl_2 of AR grade are used as precursors for the hydroxide co-precipitation. The precipitates are thoroughly washed in distilled water keeping alkaline medium using NH_4OH (pH 9). The dried precipitates are calcined at 1,000 °C for 12 h, and final sintering is carried out at 1,200 °C for 24 h in two steps with intermediate grinding.

The SBN has been synthesized using standard ceramic route of synthesis because the precursors required for coprecipitation of niobium are not cost effective. High purity (99.9 %) BaCO_3 , SrCO_3 and Nb_2O_5 are used as precursors. Considering the earlier reports, pre-sintering and final sintering processes are carried out at 1,100°C for 24 h, and 1,250 °C for 12 h, respectively, to form the fine-grained SBN powder (8).

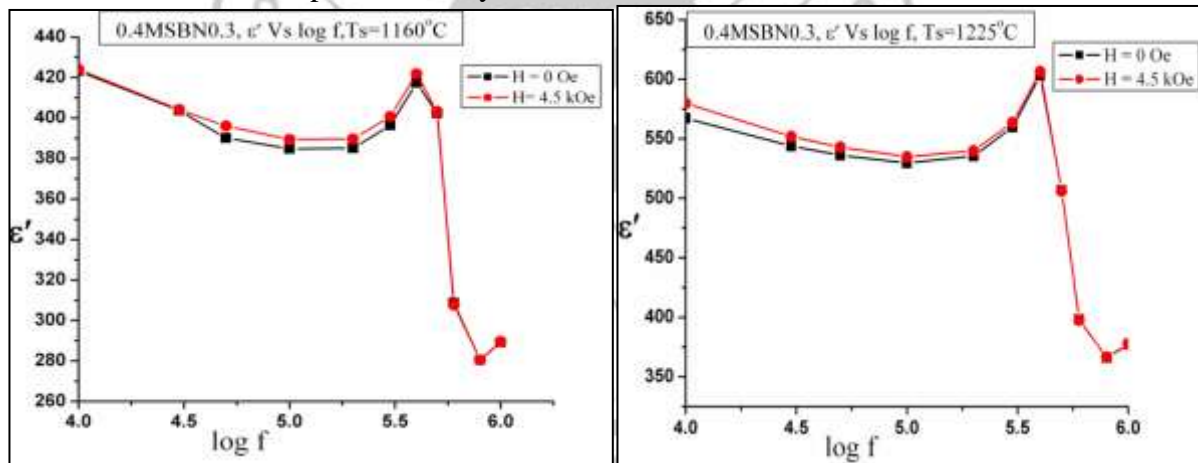


Fig. 3 and 4 : Variation of ϵ' with $\log f$ for 0.4MSBN0.3, at $T_s = 1160$ and 1225°C

	MC(1100°C) %		MC(1160°C) %		MC(1225°C) %	
	Parallel		Parallel		Parallel	
y	10 kHz	500 kHz	10 kHz	500 kHz	10 kHz	500 kHz
0.3	0.35	0.18	0.86	0.4	0.16	0
0.4	0.55	0.5	1.2	0.2	0.9	0.08
0.5	0.4	0.04	0.6	0.2	0.93	0.51

Table-1 Magnetocapacitance (MC) for $y\text{MSBN}0.3$

Formation of composites: The resulting powders of CMFO and SBN are ground thoroughly to form uniform and submicron level particle size. The powders of CMFO and SBN thus formed are used to

form the required MD composites using the following formula,

$$y(\text{CMFO}0:3) + (1-y) (\text{SBN}) = y(\text{MSBN}0:3)$$

where 0.3 represents the contents of Mn in CMFO and $y = 0.3, 0.4$ and 0.5 . Considering the earlier

reports, the composites are formed as pellet shaped samples of 1 cm diameter and three separate batches of the composites are formed with sintering temperature T_s equal to 1,100, 1,160 and 1,225 °C for y MSBN0.3 (9,10).

Results and discussion: The individual powders of the ferrite and the ferroelectric materials are investigated for structural studies for confirmation of the formation of the desired phase and the estimation of the particle size. The reflections are in confirmation with the JCPD data on cobalt ferrite possessing cubic spinel crystal structure. The XRD spectra of SBN powder which shows the reflections corresponding to TTB crystal structure and the spectra is in confirmation with the earlier reports. (9).

Figure 1 shows the XRD spectra of composites for 0.4MSBN sintered at 1,100 °C. The peaks corresponding to SBN and CMFO are separately identified in the XRD spectra of composites. The XRD spectra for remaining composites with y between 0.3 and 0.5 and for the sintering temperatures 1,100, 1,160 and 1,225 °C are similar to the XRD spectra as shown in figure 1.

Figure 2 shows variation of ϵ' at 1 kHz as a function of T for the MSBN0.3 series. It could be seen that the ϵ' versus T behavior shows a DPT at 103 °C. This DPT corresponds to the signature of DPT of SBN at $T_c = 103$ °C (8). Another interesting observation of ϵ' versus T behavior is that the ϵ' increases with T in paraelectric region above DPT.

The increase in the ϵ' is faster for increasing y . This feature is known to occur because of interfacial polarization occurring at boundaries between the SBN and CMFO phases due to difference in the resistivity (9). Interfacial polarization is known to be prominent at higher frequencies and increases as T increases. The present observation suggests that the increase in ϵ' in the paraelectric region appear to be due the presence of interfacial polarization.

Interesting observations are on the variations of dielectric constant (ϵ') as a function of applied field, i.e., the MD behaviour. Figure 3 and 4 show the variation of ϵ' as a function of applied frequency (f) and applied magnetic field (H_{dc}) for y MSBN0.3. The variation of ϵ' for other composition and sintering temperature T_s are similar in nature as shown in Fig. Further, Table 2 shows variation of MC as a function of y , T_s and for frequencies 10 and 500 kHz, respectively for y MSBN0.3. As discussed earlier, the MC occurs due to variation of dielectric constant because of the applied stress occurring due to the piezomagnetic effect in the ferrite phase (3). Further, the MC should be proportional to $\lambda \times k_m \times (d\epsilon/ds)$, where λ is magnetostrictive coefficient, k_m the magnetomechanical coupling coefficient, $d\epsilon/ds$ the rate of change of dielectric constant as a function of applied stress. For λ being positive, the stress would increase with increase in H_{dc} , while for λ negative stress would decrease with increase in H_{dc} and, therefore, ϵ' increases with H_{dc} .

Conclusions:

The observations on MC are promising and the results could be understood in terms of Landau thermodynamic theory. The MC has been observed to remain fairly constant for MSBN0.3 over a wide range of frequencies between 10 and 500 kHz. Also, the magnitude of MC is sufficiently large for 0.4MSBN0.3. The present observation suggests that further studies on MD composites are required to evolve compositions possessing useful value of MD properties.

Acknowledgement:

Author would like to express the gratitude towards the late prof. P.B.Joshi for being a moral suportor and guiding us to pursue the research carrier.

References:

1. Dong XW, Wu YJ, Wan JG, Wei T, et.al.(2008) ,J Phys D Appl Phys 41:035003. doi:10.1088/0022-3727/41/3/035003.
2. Gang Xu, Weng Wenjian, Yao Jianxi, Piyi Du, Han Gaorong (2003) ,Microelectron Eng 66:568–573.
3. Gridnev SA, Kalgin AV, Chernykh VA (2009), Integr Ferroelectr 109:70–75.
4. Caltun O, Chiriac C, Lupu N, Dumitru I, Rao BP (2007), J Optoelectron Adv Mater 9:1158.
5. Catalan G (2006) Magnetodielectric effect without multiferroic coupling. Appl Phys Lett 88:102902.
6. Bhamé SD, Joy PA (2006),J Appl Phys 99: 073901.
7. Bhamé SD, Joy PA (2007) , J Appl Phys 40:3263.
8. Kulkarni AR, Patro PK, Harendranath CS (2006) In: Proceedings of NSAE 2006, 55–64.
9. S.R. Jigajenia, A.N. Taraleb, D.J. Salunkheb, P.B. Joshib,n, S.B. Kulkarnic, Ceramics International 39 (2013) 2331–2341.
10. S.M. Salunkhe, S.R. Jigajeni, A.N. Tarale, M.M. Sutar & P.B. Joshi, Journal of Elec Materials, DOI 10.1007/s11664-013-2529-8.

Preparation and characterisation of lead iodide nanoparticles

K K Patil*

Department of chemistry, Rajaram College, Vidyanagar ,Kolhapur
kranti301@gmail.com

Abstract:

Lead iodide is a precursor material for fabrication of solar cell and hence its preparation in proper form is very important. In our research work we synthesized lead iodide by precipitation method. It is confirmed by XRD and characterised by optical properties

Key words: lead iodide, solar cell, precipitation method

1. Introduction:

Lead iodide has interesting photochemical, photoelectrochemical, and electrical properties^[1-9]. It has wide applications as photovoltaic material in direct positive image recording system to cathode material in ambient temperature solid state batteries. PbI₂ is also used as a high-energy photon detector for gamma-rays and X-rays, due to its wide band gap which ensures low noise operation.^[10-12]

Lead iodide is wide band gap material (2.32 & 2.55 eV at 4K) having high chemical stability with structural transition up to its melting point T_m(410°C) without degradation in laboratory. In the present paper, we report the preparation of PbI₂ nanocrystals by precipitation method and confirmed the prepared material by XRD and observed its optical properties.

Experimental: For the synthesis of PbI₂ nanoparticles, we have used analytical grade chemicals and doubly distilled water. The solution of lead acetate and potassium iodide is prepared. The stoichiometric quantity of potassium iodide solution is added to Lead acetate solution with constant stirring. Clear yellow solution was obtained, which ultimately converts in precipitate of lead iodide. The solution is filtered to obtain the lead iodide powder which is annealed at 200°C for one hour.

Characterisation: To perform the structural analysis of the synthesized nanostructure of PbI₂, we have recorded the powder X-ray diffraction pattern using D/MAX Ultima III XRD spectrometer (Rigaku, Japan) with Cu(K α) line of 1.5410 Å. The UV-visible spectroscopic measurement was done at room temperature in ethanol on Elico SL 159 UV-visible spectrophotometer. Using the recorded data

various optical parameters were calculated. Photoluminescence Spectra were recorded for the prepared nanostructured lead iodide sample at room temperature. The spectral band width was chosen 0.5 nm for emission monochromator.

Result and discussion

1. Structural analysis: The recorded powder X ray diffraction pattern of the synthesized lead iodide crystals is as shown in fig.1 It indicates the synthesized lead iodide is highly crystalline in nature and with hexagonal phase is in agreement with reported value JCPDS-07-0235.

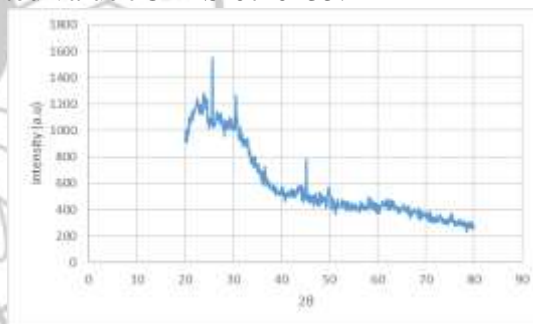


Fig.1

2. Optical studies: The UV-visible absorption spectrum was recorded for the prepared sample. The optical band gap (E_g) was calculated from absorption data. The absorption coefficient (α) with wavelength was evaluated by equation

$$\alpha = \frac{\text{Absorbance}}{\text{Path length}(l) \times \text{concentration}(c)}$$

The calculated absorption coefficient Vs wavelength plot is as shown in fig.2 and the optical band gap is found to be 3.5 eV from fig.3.

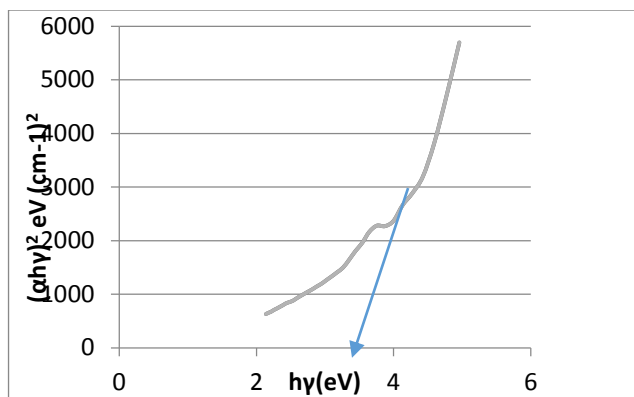


Fig.2

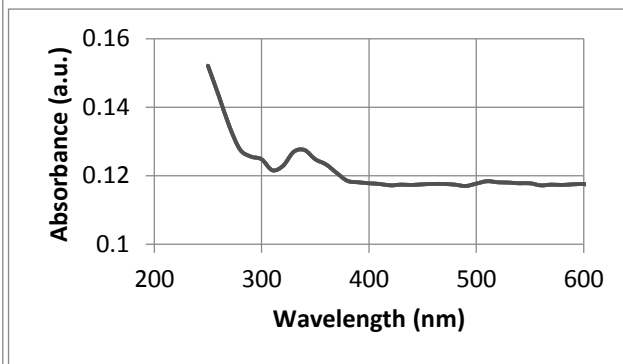


Fig.3

3. Photoluminescence study:

The recorded PL emission spectrum for the given sample is as shown in fig 3. To record the emission spectra the excitation wavelength was taken as 250 nm. The PL spectra shows a prominent peak at 400 nm.

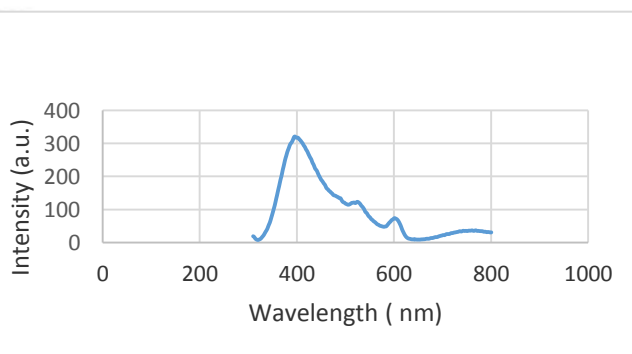


Fig.4

Conclusion:

Highly crystalline lead iodide nanocrystals can be prepared by this precipitation method. The band gap was calculated from UV-Visible data and it is 3.5 eV which is slightly greater than the reported value.

References:

1. J F Verwey, *J. Phys.Chem.Solids* 31 (1970) 163
2. J.Malinowski, *Phot.Sci.Eng.* 15 (1971) 175
3. L. and Ghita and M. Constantinescu, *Rev.Roun.Phys.* 16 (1971) 57
4. J.Schoonman, *Solid State Commun.* 13 (1973) 673
5. Hagiharo, K.Iwamoto, K.Fukumoto and N.Ayai, *J Phys(Paris)* 41(1980)C6-297
6. A.E.Dugan and H.K.Henisch, *J.Phys.Chem.Solids* 28 (1967) 1885
7. A.E.Dugan and H.K.Henisch, *Phys.Rev.* 171 (1968) 1047
8. S.Baidyaroy, W.R.Bottoms and P.Mork, *J. Phys.Chem.Solids* 33 (1972) 357
9. A.P.Lingras and G.Simkovich, *J. Phys.Chem.Solids* 39 (1978) 122
10. Patnaik (2002): *Handbook of Inorganic Chemicals*. McGraw-Hill. ISBN 978-0070494398
11. [Shah et al. 1996.](#)
12. L. Fornaro, E. Saucedo, L. Mussio, L. Yerman, X. Ma, A. Burger (2001): *Lead iodide film deposition and characterization* Proc. 11th Int. Workshop on Room Temperature Semiconductor X- and Gamma-Ray Detectors and Associated Electronics; in Nuclear Instruments and Methods in Physics Research Section A: Accelerators, Spectrometers, Detectors and Associated Equipment, volume 458, issues 1–2, pages 406–412. doi10.1016/S0168-9002(00)00933-5

Solvothermal synthesis of hierarchical ZnO microsphere and its application in dye-sensitized solar cells

Yogesh Waghadkar^{a, b}, Govind Umarji^a, Sunit Rane^a, Ratna Chauhan^a and Suresh Gosavi^{c*}

^aCentre for Materials for Electronics Technology, Off Pashan Road, Pune-411008, India.

^bDepartment of Technology, Savitribai Phule Pune University, (Formerly University of Pune) m Pune-411007, India.

^cCentre for Advanced Studies in Material Science and Solid State Physics, Department of Physics, Savitribai Phule Pune University, (Formerly University of Pune) Pune-411007, India

- Author to whom correspondence should be address Email: swg@physics.unipune.ac.in

Abstract

Hierarchically structured ZnO microspheres have been synthesized solvothermally at 180°C for 48 h by using ethylene glycol as a solvent, zinc acetate as precursor and ascorbic acid as structure directing agent. The XRD and FESEM reveal the formation of wurtzite hexagonal crystalline nature and porous microsphere like morphology. The synthesized ZnO microsphere (Z-2) have been used as photoanode in dye sensitized solar cell (DSSCs) which shows enhanced light harvesting properties than the commercial ZnO (Z-1) due to more specific surface area available for dye loading. ZnO microsphere (Z-2) shows current density and cell efficiency of 7.38 mA/cm² and 2.85 %, respectively.

Keywords: ZnO, Solvothermal, Microsphere, DSSCs

Introduction

Dye-sensitized solar cells (DSSCs) are the one of the potential alternative for future green energy demand due to their simplistic, low-cost, and environment-friendly fabrication procedure as compared to p-n junction photovoltaic cell [1, 2]. Several metal oxides such as TiO₂, ZnO, WO₃, Fe₂O₃, SnO₂, Nb₂O₅, and Ta₂O₅ [3] are used as photoanode materials in DSSCs. ZnO is considered as one of the most promising alternative of TiO₂ to overcome this challenge in DSSC technology. ZnO has various excellent properties to be a photoanode in DSSCs as: (i) ZnO energy band structure and physical properties are similar to those of TiO₂, (ii) it has much higher electron mobility (~115-155 cm² V⁻¹ s⁻¹) than TiO₂ (~10⁻⁵ cm² V⁻¹ s⁻¹), which favors the faster electron transportation with less recombination [4] and (iii) tailor made synthesis process for effortless alteration in shape, size and morphology of ZnO.

In this study we synthesized the ZnO microsphere through solvothermal route and characterize it by Uv-Vis, XRD and FESEM. We used ZnO

microsphere as photoanode in dye sensitized Solar cell (DSSC) and evaluated its performance.

Experimental

Synthesis of Zinc Oxide Material

In ZnO synthesis process, equimolar ratio of Zinc acetate (0.1M) and ascorbic acid (0.1M) was added to 100 ml ethylene glycol. The admixture was transferred in Teflon lined stainless steel autoclave and kept in oven at 180°C for 48hr. The resultant product was washed, dried and annealed at 400°C for 1h.

Result and Discussion

Powder XRD Analysis and UV-Vis Spectroscopy:

The XRD pattern of the synthesized ZnO microsphere shows wurtzite hexagonal crystalline nature, which were matched with JCPDS file no. 80-0074 (Figure 1). The UV-Vis spectroscopy of the ZnO microsphere shows the absorption peak at 361 nm with corresponding band gap of 3.43eV. The ZnO microsphere shows blue shift. (Figure 2)

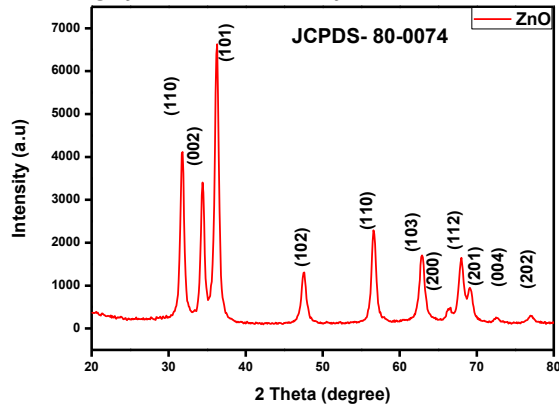


Figure 1: XRD of ZnO

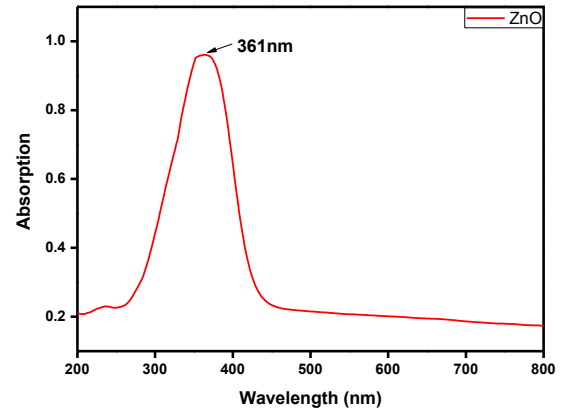


Figure 2: UV-Visible Spectroscopy

Field emission scanning electron microscopy (FESEM):

The FESEM image shows the highly porous microspheres like morphology for solvothermally synthesized ZnO. (Figure 3)

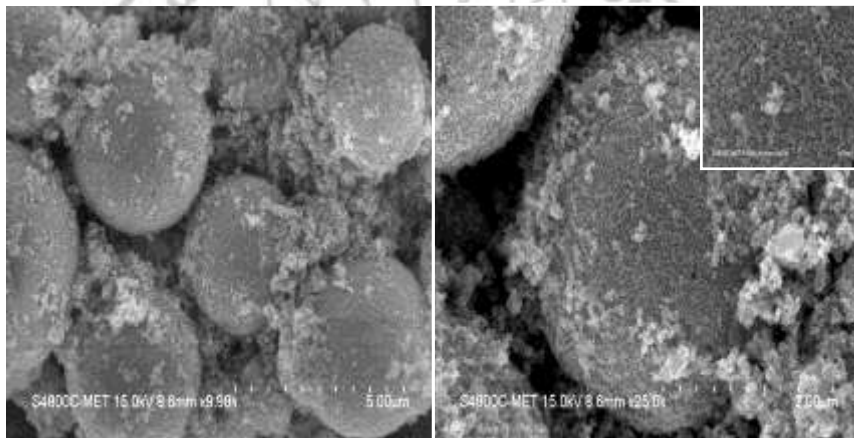


Figure 3: FESEM images of ZnO microsphere (Z-

Current –Potential Curve and Incident photon to current conversion efficiency:

The DSSC with porous ZnO microsphere (Z-2) shows excellent performance, with a short-circuit current density (J_{sc}) of 7.38 mA/cm², an open-circuit voltage (V_{oc}) of -0.638 V, a fill factor (FF) of 0.61 and a following power conversion efficiency (η) of 2.85 % (Figure 4). The efficiency of the cell fabricated with Z-2 is 4 fold greater than the commercial ZnO (Z-1) (Table 1). The photocurrent action spectra (Figure 5) display the wavelength distribution of the incident monochromatic photon-to-current conversion efficiency (IPCE). The maximum of IPCE in the visible region is located at 530-535 nm. This is approximately consistent with

the expected maximum based on the absorption spectrum for the N719 dye (with local maxima at 390 and 535 nm).

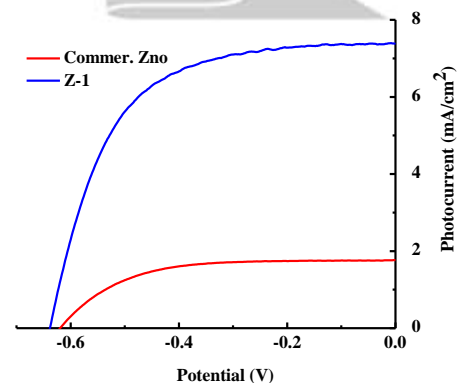


Figure 4: Current-Potential curve

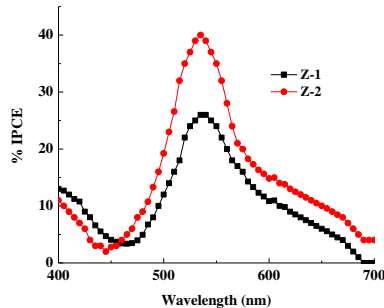


Figure 5: IPCE spectra

Table 1: Photovoltaic Parameters

	J_{sc} (mAcm ⁻²)	V_{oc} (V)	FF	η (%)	IPCE (%)
Z-1	1.76	-0.620	0.61	0.66	26
Z-2	7.38	-0.638	0.61	2.85	40

Conclusion

ZnO microspheres synthesized successfully at 180 °C for 48 h by solvothermal route and employed as photoanode in DSSCs with enhanced light harvesting properties than the commercial ZnO. ZnO microsphere shows maximum current density and cell efficiency of 7.38 mA/cm² and 2.85%, respectively. This enhancement in photovoltaic parameters can be attributed to highly ordered and porous nature of microspheres which provide more specific surface area for dye loading, retardation of recombination and better charge transport.

Acknowledgment: The authors RC and YW are grateful to Department of Science and Technology, New Delhi, Project No. (IFA12-CH-34) for the financial support.

References:

- O'Regan B, Gratzel M (1991) A low-cost, high-efficiency solar cell based on dye-sensitized colloidal TiO₂ films. *Nature* 353:737-740
- Zhang Q, Cao G (2011) Nanostructured photoelectrodes for dye-sensitized solar cells. *Nano Today* 6:91-109
- Hagfeldt A, Grätzel M (1995) Light-Induced Redox Reactions in Nanocrystalline Systems. *J Chem Rev* 95:49-68
- Chauhan R, Shinde M, Kumar A, Gosavi S, Amalnerkar DP (2016) Hierarchical zinc oxide pomegranate and hollow sphere structures as efficient photoanodes for dye-sensitized solar cells. *Microporous and Mesoporous Materials* 226:201-208

INTERNATIONAL CONFERENCE ON
ADVANCES IN MATERIALS SCIENCE
 7 – 8 December 2016

Structural and Magnetic Properties of $\text{Fe}_{0.5}\text{Mn}_{0.5}\text{Fe}_2\text{O}_4$ Ferrite Nanoparticles

Jyoti Dhumal¹, E. K. Kore¹, S. S. Bandgar¹, J. A. Ukirade² and G. S. Shahane^{1*}

¹Department of Electronics, DBF Dayanand College of Arts and Science, Solapur, MS, India

²PVPIT College, Budhgaon, Sangli, MS, India *Email: shahanegs@yahoo.com

Abstract

Nanocrystalline $\text{Fe}_{0.5}\text{Mn}_{0.5}\text{Fe}_2\text{O}_4$ particles of controlled size were synthesized by a facile chemical co-precipitation method. X-ray diffraction data confirms the synthesis of single phase of $\text{Fe}_{0.5}\text{Mn}_{0.5}\text{Fe}_2\text{O}_4$ ferrite nanoparticles of spinel structure with lattice parameter $a = 8.4421\text{\AA}$. The average crystallite size is 10nm. The SEM observation gives the morphology of the particles. The composition of the material obtained from EDS analysis is in good agreement with the initial composition. The formation of spinel ferrite is also supported by Fourier transform infrared spectroscopy (FT-IR). The magnetization measurements show superparamagnetic nature of the sample with zero remanence and coercivity. The saturation magnetization is 43emu/g. The synthesized particles are found suitable for ferrofluid application.

Keywords: XRD, EDS, nanoparticles, superparamagnetism

1. Introduction

In recent years, various technological applications are based on nano- ferrite materials due to unique magnetic and electrical properties. The ferrite nanoparticles in nanosized form are useful for a variety of applications such as biomedical applications, magnetic storage, ferrofluids etc. Among these particles, Fe-Mn ferrite nanoparticles have been widely studied because of their large number of applications, such as magnetic resonance imaging for clinical diagnosis, magnetic drug targeting, hyperthermia anti-cancer strategy and enzyme immobilization [1-4]. It is known that the physical properties of the ferrites are very sensitive to the method of synthesis and the type of substitution. The selection of an appropriate process is, therefore, the key to obtain good quality ferrites. There are various ways to prepare ferrite nanoparticles, such as arc discharge, mechanical grinding, laser ablation, micro emulsions, chemical co-precipitation, sol-gel, sonochemical reaction, high temperature decomposition of organic precursors etc. [5-9]. Among these methods chemical co-precipitation method has the advantage of better control on particle size and size distribution [10]. This paper presents structural and magnetic properties of $\text{Fe}_{0.5}\text{Mn}_{0.5}\text{Fe}_2\text{O}_4$ ferrite nanoparticles synthesized by chemical co-precipitation method.

2. Experimental Details

Fe-Mn ferrite nanoparticles were prepared by a facile chemical co-precipitation method. For synthesis, equimolar solutions of AR grade MnCl_2 , FeCl_2 and FeCl_3 were mixed in their stoichiometric ratio and homogenized at room temperature. The pH of the solution was adjusted by adding 1M

NaOH solution. Citric acid was used as a capping agent. The mixture was then heated at 80°C for about one hour. The particles were washed several times with de-ionized water to remove unwanted residual of salts and then dried at 35°C .

The X-ray diffraction patterns of the samples were recorded on Rigaku make powder X-ray diffractometer (Model- XRG 2KW) in the 2θ range from 20° to 80° at 40 kV, 30 mA using $\text{CuK}\alpha$ radiation ($\lambda=1.54059\text{ \AA}$). The surface morphology and compositional analysis of the films was recorded on SEM (JEOL JSM 6360) scanning electron microscope operating at 20 kV. FTIR transmission spectrum was recorded on Perkin Elmer Spectrum 65 Spectrometer from 4000 to 400 cm^{-1} . The magnetization measurements were carried out by vibrating sample magnetometer VSM Lake Shore Model 7307.

3. Results and Discussion

The XRD pattern of the as-synthesized sample is shown in Fig.1. The diffraction pattern provides a clear evidence for the formation of ferrite phase. The 'd' values and intensities of observed diffraction peaks match with the single crystalline spinel form of the Fe-Mn ferrites. The absence of any additional lines, in any of the XRD patterns, confirms the purity of the Fe-Mn ferrite phase in the sample. X-ray diffraction pattern shows broad peaks indicating ultrafine nature and small crystallite size of the sample. The lattice parameter was calculated and found to be 8.4421\AA . The crystallite size was then determined by the Scherrer relation:

$$D = 0.89\lambda/\beta \cos\theta$$

where, D is the crystallite size, λ is wavelength of X-ray, β is full width at half maximum (FWHM)

measured in radians and θ is the Bragg angle. Crystallite size is found to be of the order of 10nm.

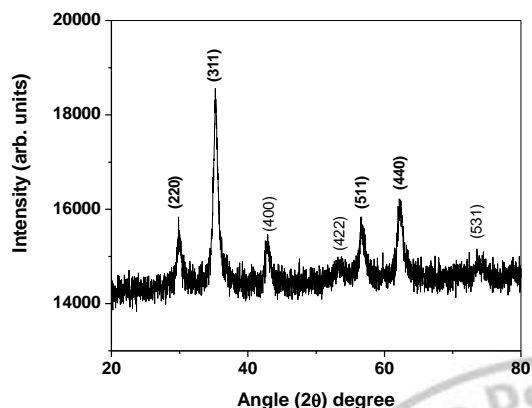


Fig.1 XRD pattern of $\text{Fe}_{0.5}\text{Mn}_{0.5}\text{Fe}_2\text{O}_4$ nanoparticles.

Compositional analysis of the sample was done by energy dispersive X-ray spectroscopy technique. The EDX technique supplies the effective atomic concentration of different constituents on top surface layers of the solid investigated. The energy dispersive X-ray spectra of $\text{Fe}_{0.5}\text{Mn}_{0.5}\text{Fe}_2\text{O}_4$ nanoparticles (Fig. 2) show the peaks of Mn, Fe and O peak. The composition of the material obtained from EDS analysis is in good agreement with the initial composition.

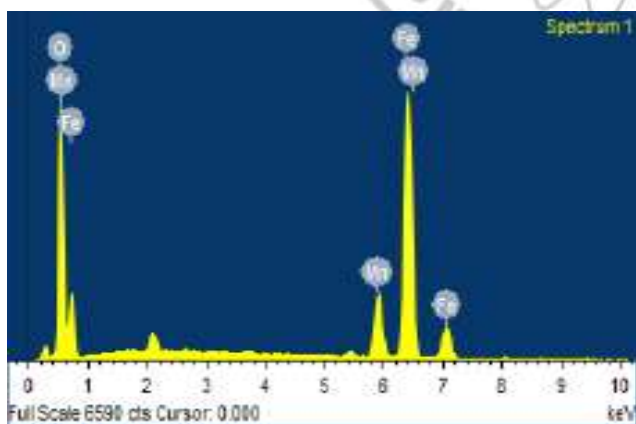


Fig. 2 EDX spectrum of $\text{Fe}_{0.5}\text{Mn}_{0.5}\text{Fe}_2\text{O}_4$ nanoparticles.

The surface morphology of the samples was studied with scanning electron microscope. The SEM images of $\text{Fe}_{0.5}\text{Mn}_{0.5}\text{Fe}_2\text{O}_4$ nanoparticles with different magnification are shown in Fig.

3. It is seen that sample consists of nanoparticles agglomerated together to form large grains.

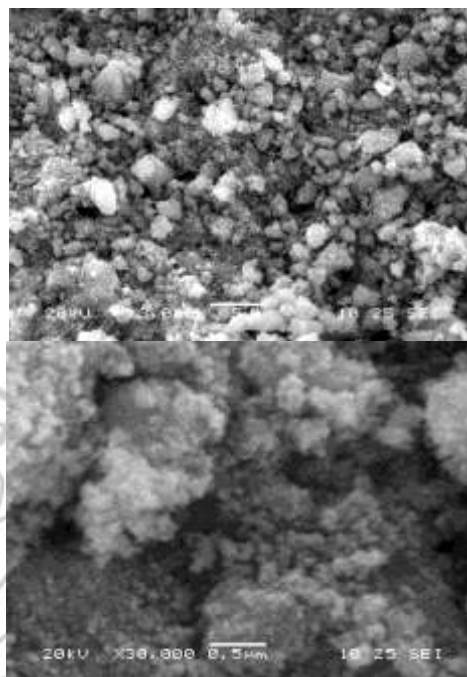


Fig.3 SEM images of $\text{Fe}_{0.5}\text{Mn}_{0.5}\text{Fe}_2\text{O}_4$ nanoparticles with different magnification.

Formation of the spinel ferrite was further supported by FTIR analysis. Fig.4 shows the FTIR spectrum of $\text{Fe}_{0.5}\text{Mn}_{0.5}\text{Fe}_2\text{O}_4$ ferrite nanoparticles recorded at room temperature. The spectra show two main absorption bands below 1000 cm^{-1} which is a common feature of ferrites. The characteristic peaks at around 572 cm^{-1} which corresponds to intrinsic stretching vibrations of the metal oxygen at the octahedral sites coordinated metal ions in the spinel structure, confirming that the prepared samples are spinel in structure. Peaks at around 1122 cm^{-1} can be attributed to the vibrations of $-\text{CH}$. Peaks at 1384 cm^{-1} is assigned to the vibrations of $\text{C}=\text{C}$ in citric acid. The strong peaks at around 1631 cm^{-1} and 3423 cm^{-1} can be assigned to stretching vibrations of $-\text{CH}_2$ and $-\text{CH}_3$ respectively. A broad band absorption peak appeared at 3412 cm^{-1} and a high frequency absorption peak was detected at 1631 cm^{-1} , confirming the presence of O-H groups in the sample [11,12].

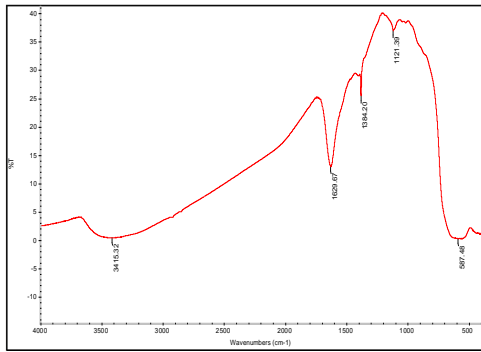


Fig. 4 FTIR spectrum of Fe_{0.5}Mn_{0.5}Fe₂O₄ sample.

Magnetic measurement was carried out at room temperature using vibrating sample magnetometer and Fig. 5 displays the magnetization curve for this sample. The magnetization curve demonstrates a typical superparamagnetic behavior of the as-synthesized sample. It is seen that saturation magnetism is 43emu/g and is small as compared to the bulk value. The smaller value of saturation magnetization is due to lattice defects, weaker magnetic superexchange interactions between A-

sites and B-sites, and existence of a magnetically inert layer at the surface of the nanoparticles [13,14].

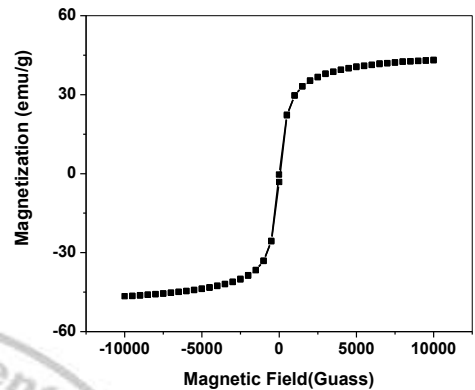


Fig.5. Magnetization curve of Fe_{0.5}Mn_{0.5}Fe₂O₄ nanoparticles.

3. Conclusion

A chemical co-precipitation method is used to synthesize size-controlled synthesis of Fe-Mn ferrite nanoparticles. The method is relatively simple, low cost and their particle size can be easily controlled. The X-ray diffraction pattern confirms the synthesis of single crystalline phase of Fe_{0.5}Mn_{0.5}Fe₂O₄ nanoparticles with lattice parameter 8.4421Å. The magnetic measurements show superparamagnetic nature of the sample. The saturation magnetization is 43emu/g. The superparamagnetic nature with high saturation magnetization makes these nanoparticles suitable for the synthesis of ferrofluid.

Acknowledgement

The author (GSS) is thankful to the Science and Engineering Research Board, Government of India, New Delhi, for the financial assistance under the Project Grant SB/S2/CMP-06/2013.

References

- W. Brullot, N. K. Reddy, J. Wouters, V. K. Valev, B. Goderis, J. Vermant and T. Verbiest, *J. Magn. Magn. Mater.*, **324** (2012) 1919.
- J. P. Dery, E. F. Borra, A. M. Ritcey, *Chemistry of Materials*, **20** (2008) 6420.
- C. L. Sansom, P. Jones, R. A. Dorey, C. Beck, A. Stanhope-Bosumpim and J. Peterson, *J. Magn. Magn. Mater.*, **335** (2013) 159.
- R. Patel, K. Parekh, R. V. Upadhyay and R. V. Mehta, *Ind. J. Engin. & Mater. Sci.*, **11** (2004) 301.
- L. M. Yu, S. X. Cao, Y. S. Liu, J. J. Wang, J. C. Zang, *J. Magn. Magn. Mater.*, **301** (2006) 100.
- J. Giri, T. Sriharsha, S. Asthana, T. K. G. Rao, A. K. Nigam and D. Bahadur, *J. Magn. Magn. Mater.*, **293** (2005) 55.
- A. Rana, O. P. Thakur and Vinod Kumar, *Mater. Lett.*, **65** (2011) 3191.
- K. V. P. M. Shafi, A. Gedanken, R. Prozorov, and J. Balogh, *Chem. Mater.*, **10** (1998) 3445.
- D. J. Fatemi, V. G. Harris, V. M. Browning, and J. P. Kirkland, *J. Appl. Phys.*, **83** (1998) 6867.
- G. S. Shahane, Ashok Kumar, M. Arora, R. P. Pant and K. Lal, *J. Magn. Magn. Mater.*, **322** (2010) 1015.
- S. Wu, A. Sun, F. Zhai, J. Wang, W. Xu, Q. Zhang, A. A. Volinsky, *Materials Letters*, **65** (2011) 1882.
- J. Sun, S. Zhou, P. Hou, Y. Yang, J. Weng, X. Li, M. Li, *J. Biom. Mater. Res. Part A* DOI 10.1002/jbm.a (2006) 333.
- K. H. Wu, T. H. Ting, G.P. Wang, C. C. Yang and B.R. Mc Garvey, *Mater. Res. Bull.* **40** (2005) 2080.
- B. P. Rao, A. Maheshkumar, K. H. Rao, Y. L. N. Murthy and O. F. Caltun, *J. Optoelectr. Adv. Mater.* **8** (2006) 1703.

Structural Study of Cobalt Sulphide Thin Films Synthesized By Successive Ionic Layer Adsorption Reaction Method

Bhadrashetti T.S., Sueba B.A.S., Sayyad R.A., M. S. Kavale ^{a*},

^{a*}Department of Physics, Sangameshwar College, Solapur 413003, M.S., India.

E-mail: mahendrakavale@gmail.com

Abstract

The Successive ionic layer adsorption and reaction (SILAR) method was used to prepare the cobalt sulphide thin films. The prepared greenish coloured samples were characterized by XRD technique for structural study of prepared copper hydroxide thin films. XRD reveals the hexagonal crystal structure of cobalt sulphide thin films. The crystallite size calculated was 18.42 nm.

Keywords: Successive ionic layer adsorption and reaction, cobalt sulphide, X-ray diffraction.

1. Introduction

Cobalt Sulphide is the chemical compound with a formula Co_xS_y . Cobalt sulphide species include minerals with the formula CoS_2 and Co_3O_4 and also the synthetic mineral Co_9S_8 . The sulphides of cobalt are black, semiconducting and insoluble in water. They react with strong acids to release hydrogen sulphide gas [1]. They are weak reducing agents and can be oxidized to cobalt sulphate. Cobalt sulphides precipitate when aqueous solutions of cobalt (II) ions are treated with hydrogen sulphide. This reaction is useful in the purification of cobalt from its ores as well as in qualitative inorganic analysis. In combination with molybdenum, the sulphides of cobalt are used as catalysts for the industrial process called hydrodesulphurization, which is implemented on a large scale in refineries [2-4].

There are numbers of physical and chemical techniques are used for the deposition of the thin films of the semiconducting material. The choice of technique depends on the material to be deposited, nature of substrate, required film thickness of thin film, application were the film used etc. The techniques used for the deposition of a semiconducting material are classified as physical and chemical techniques [5]. Chemical techniques are relatively economical and easier as compared physical methods. The SILAR method is used to create thin films from a variety of different substrates and to produce different coatings for applications i.e. in solar panels and semiconductors. The SILAR method is chemical bath solution method that is an extension of the similar chemical bath thin film production method [6]. The SILAR method uses the transfer of ions that provides better coverage of chemicals over the film and can result

in a finer grain structure than other deposition methods. The ease of application allows the thickness of thin films created using the SILAR method to be controlled more easily than in other applications.

2. Experimental

The glass substrate was used for the deposition of cobalt sulphide. The glass substrate were kept in glass container containing 500 ml distilled water and chromic powder. The glass substrate was boiled for 1-2 hours till the solution became half. The boiled substrate was washed using double distilled water and finally washed with acetone and then dried. 0.2 M 20ml solution of cobalt sulphate ($CoSO_4$) was taken in 1 beaker. Second beaker taken with 0.2M ammonia and in third beaker the doubled distilled water is taken. For first cycle the glass substrate was dipped in first beaker for 1Min then it was dipped in second beaker for 30 sec then it was dipped in third beaker for 15sec. The same procedure was repeated for 75 cycles to deposit greenish cobalt sulphide on glass substrate.

Weight of the deposited copper hydroxide on SS-substrate per unit area (mg/cm^2) was measured by digital weight balance which is about $\sim 0.1 mg/cm^2$. The internal structure of the copper hydroxide thin films were studied by using X-ray diffraction patterns carried out by X-ray diffractometer (XRD) (Rigaku D/max 2550Vb+18 kw with $CuK\alpha$ $\lambda=1.54056\text{\AA}$) in the range of diffraction angle 2θ from $20^\circ-80^\circ$.

3. Results and discussion

3.1 Structural characterization

Fig.1 shows the XRD patterns of cobalt sulphide thin film. It is observed that deposited cobalt sulphide sample was crystalline in nature. The peak

orientation along (100) indicates the formation of Co_3S_4 . The observed 'd' values well matches with standard 'd' values taken from JCPDS data card no.47-1738. The peak orientation along (010) indicates the formation of Co_4S_3 . The observed 'd' values well matches with standard 'd' values taken from JCPDS data card no.19-0364. We have confirmed the orthorhombic crystal structure phase. The XRD pattern confirms the formation of crystalline cobalt sulphide.

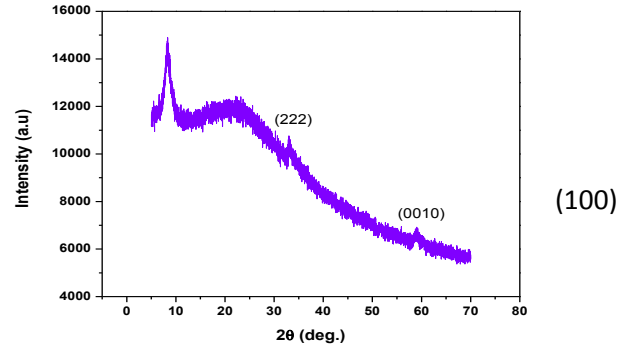


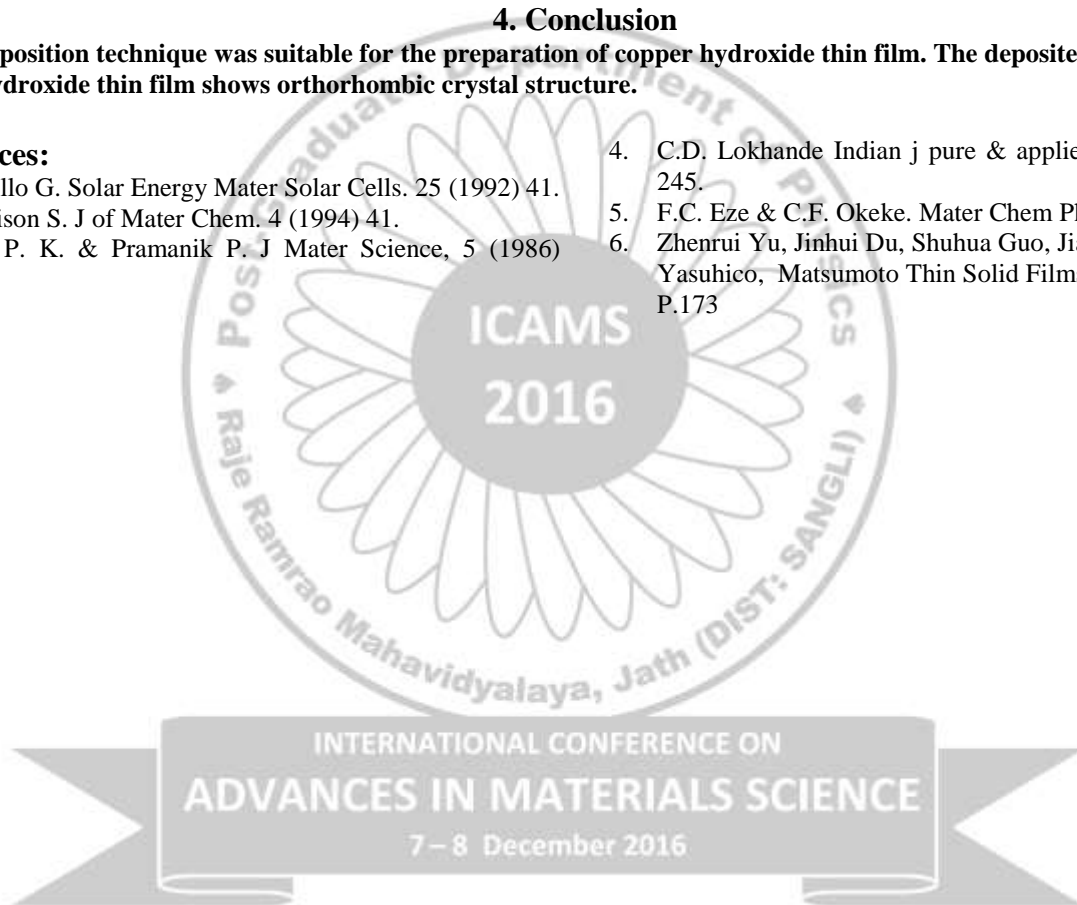
Fig. 1 XRD pattern of cobalt sulphide

4. Conclusion

Electrodeposition technique was suitable for the preparation of copper hydroxide thin film. The deposited brown coloured copper hydroxide thin film shows orthorhombic crystal structure.

References:

1. Gordillo G. Solar Energy Mater Solar Cells. 25 (1992) 41.
2. Dennison S. J of Mater Chem. 4 (1994) 41.
3. Basu P. K. & Pramanik P. J Mater Science, 5 (1986) 1216.
4. C.D. Lokhande Indian j pure & applied phys. 30 (1992) 245.
5. F.C. Eze & C.F. Okeke. Mater Chem Phys. 47 (1997) 31.
6. Zhenrui Yu, Jinhui Du, Shuhua Guo, Jiayon Zhang, Yasuhico, Matsumoto Thin Solid Films vol.415 (2002). P.173



Structural Study of Copper Hydroxide Thin Films By Electrodeposition

Mhamane D.R., Pise G.D., Shendage P.S., T.S. Ghadge, S.S. Karande ^{a*}

^{a*}Department of Physics, Sangameshwar College, Solapur 413003, M.S., India.

Abstract

Electrodeposition method was used to prepare Copper hydroxide thin films by using 0.1 M aqueous Copper sulphate solution. The preparation of Copper hydroxide thin films was carried out at 1.8 V deposition potential for 30 min. deposition time. The prepared brown coloured samples were characterized by XRD technique for structural study of prepared Copper hydroxide thin films. XRD reveals the orthorhombic crystal structure of Copper hydroxide thin films.

Keywords: Electrodeposition, copper hydroxide, copper sulphate, X-ray diffraction.

*Address to whom all correspondence can be addressed.

E-mail: karande1972@gmail.com

1. Introduction

Hydroxides and oxides of cobalt constitute an important class of materials characterized by good electrochemical, catalytic and optical properties. It is known [1] that cobalt hydroxide mainly exists in two polymorphic modifications, designated as α - and β -Co(OH)₂. Both forms have a hexagonal layered structure. α -Co(OH)₂ is isostructural with hydrotalcite-like compounds while β -Co(OH)₂ is brucite-like and consists of hydroxy groups with Co (II) ions occupying octahedral sites. The α -modification has hydroxy group deficiency and consists of positively charged layers with intercalated anions (e. g. NO₃⁻, Cl⁻, CO₃²⁻, etc.) and water molecules in the interlayer space to maintain charge neutrality [2]. The α -hydroxides have a larger interlayer spacing (>7.0 Å, depending on the intercalated anions) when compared to the β -form (4.6 Å) [3 - 11].

Copper hydroxide is the hydroxide of the metal copper with the chemical formula of Cu(OH)₂. Copper hydroxide is also known as cupric hydroxide. It contains copper in its +2 oxidation state. Copper hydroxide is apple blue, gelatinous solid. Copper hydroxide acts as a weak base in aqueous solution. Copper hydroxide is readily made by electrolysis of water.

There are numbers of physical and chemical techniques are used for the deposition of the thin films of the semiconducting material. The choice of technique depends on the material to be deposited, nature of substrate, required film thickness of thin film, application were the film used etc. The techniques used for the deposition of a semiconducting material are classified as physical and chemical techniques. Chemical techniques are

relatively economical and easier as compared physical methods.

Electrodeposition is process of depositing metal atoms on a substrate by passing direct current through solution containing the metal ions to be deposited. Electrodeposition is also known as electrochemical deposition or electrocrystallization. Electroplating is often called as electrodeposition. It is one of the most useful techniques for preparing thin films on the surface of substrate. The electrodeposition is the simplest chemical method for deposition. The electrolytic solution contains positively charged and negatively charged ions. Under the applied external electric field, the cations migrate to the cathode where they are discharged and deposited. The overall process is known as electrolysis.

2. Experimental

The stainless steel substrate (1.1 cm²) was used for the deposition of copper hydroxide thin films. The stainless steel was first polished with zero grade polish paper, cleaned with distilled water for 10-20 min. The deposition was done by using two electrode systems in which stainless steel substrate acts as a cathode where copper hydroxide was deposited while stainless steel acts as a counter electrode at anode. 0.1 M copper sulphate dissolved in distilled water was used as electrolyte. The quantity of 10 ml was used for deposition. The deposition was carried at 1.8 V deposition potential for 30 min. deposition time. The brown coloured copper hydroxide was deposited on stainless steel substrate.

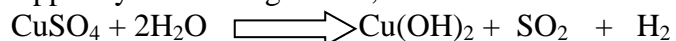
Weight of the deposited copper hydroxide on SS-substrate per unit area (mg/cm²) was measured by digital weight balance which is about ~ 0.1 mg/cm². The internal structure of the copper hydroxide thin films were studied by using X-ray

diffraction patterns carried out by X-ray diffractometer (XRD) (Rigaku D/max 2550Vb+18 kw with $\text{CuK}\alpha$ $\lambda=1.54056\text{\AA}$) in the range of diffraction angle 2θ from 20° – 80° .

3. Results and discussion

3.1 Film Formation mechanism

The possible reactions at cathode to form copper hydroxide is given as,



3.2 Structural characterization

Fig.1 shows the XRD patterns of copper hydroxide thin film. It is observed that deposited copper hydroxide sample was polycrystalline in nature. The peak orientation along (121) indicates the formation of orthorhombic copper hydroxide. The observed 'd' values well matches with standard 'd' values compared with JCPDS data card no.42-0746. The peak orientation along (111), (200) and (220) indicates the formation of pure copper having cubic crystal structure. The observed 'd' values well

matches with standard 'd' values taken from JCPDS data card no.85-1326. The XRD pattern confirms the formation of crystalline copper hydroxide.

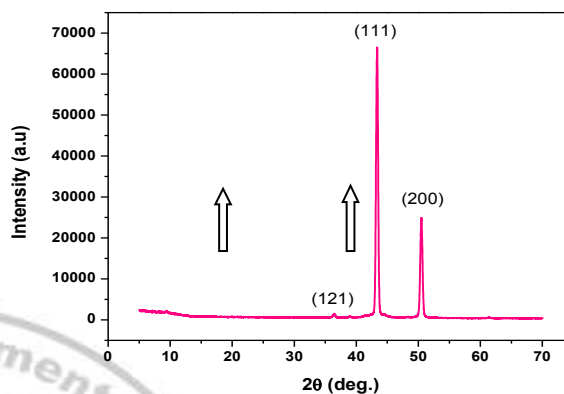


Fig. 1 XRD spectra of copper hydroxide

4. Conclusion

Electrodeposition technique was suitable for the preparation of copper hydroxide thin film. The deposited brown colored copper hydroxide thin film shows orthorhombic crystal structure.

References:

1. Oliva, P., Leonardi, J., Laurent, J. F., Delmas, C., Braconnier, J. J., Figlarz, M., Fievet, F., de Guibert, A. Review of the Structure and the Electrochemistry of Nickel Hydroxides and Oxy-hydroxides Journal of Power Sources 8 1982: pp. 229 – 255.
2. Lieth, R. M. A. (ed.) Preparation and Crystal Growth of Materials with Layered Structures. Kluwer Academic Publisher, Dordrecht, 1997.
3. Rajamathi, M., Kamath, P. V., Seshadri, R. Chemical Synthesis of α -cobalt Hydroxide Materials Research Bulletin 35 2000: pp. 271 – 287.
4. Dixit, M., Subbanna, G. N., Kamath, P. V. Homogeneous Precipitation from Solution by Urea Hydrolysis: a Novel Chemical Route to the α -hydroxides of Nickel and Cobalt Journal of Materials Chemistry 6 1996: pp. 1429 – 1432.
5. Zhu, Y., Li, H., Koltypin, Y., Gedanken, A. Preparation of Nanosized Cobalt Hydroxides and Oxyhydroxide Assisted by Sonication Journal of Materials Chemistry 12 2002: pp. 729 – 733.
6. Kurmoo, M. Hard Magnets Based on Layered Cobalt Hydroxide: The Importance of Dipolar Interaction for Long- Range Magnetic Ordering Chemistry of Materials (11)1999: pp. 3370 – 3378.
7. Yarger, M. S., Steinmiller, E. M. P., Choi, K.-S. Electrochemical Synthesis of Cobalt Hydroxide Films with Tunable Interlayer Spacings Chemical Communications(2) 2007: pp. 159 – 161.
8. Jayashree, R. S., Kamath, P. V. Electrochemical Synthesis of α -cobalt Hydroxide Journal of Materials Chemistry (9)1999: pp. 961 – 963.

Studies on $0.25(\text{Ba}_{0.7}\text{Sr}_{0.3}\text{TiO}_3) + 0.75(\text{BaLa}_2\text{Ti}_3\text{O}_{10})$ Polycrystalline Ceramic

V.C.Malvade¹, P.B. Abhange¹, A.A.Pawar², S.S.Patil², K.V.Rao³ and S.R. Kokare^{1,*}

¹Department of Physics, Raje Ramrao Mahavidyalaya, Jath, Dist: Sangli (M.S.) India.

²Department of Chemistry, PDVP College, Tasgaon, Dist: Sangli (M.S.) India.

³Jawaharlal Nehru Technology University, Hyderabad, India.

Abstract:

The Barium Strontium Titanate is one of the most widely used electronic ceramic materials having perovskite type structure. It has applications in barrier layer capacitor, oxygen gas sensor etc. The $0.25(\text{Ba}_{0.7}\text{Sr}_{0.3}\text{TiO}_3) + 0.75(\text{BaLa}_2\text{Ti}_3\text{O}_{10})$ powders were prepared through hydroxide co-precipitation method which is easy and low cost. The structure of the prepared samples was characterized by XRD and SEM. The dielectric constant measurement suggests that the dielectric constant is not significantly dependent on temperature variation. The frequency dependence of transition temperature is indicative that the synthesized material is of displacer type.

Introduction:

Barium Strontium Titanate (BaSrTiO_3) is one of the most widely used electronic ceramic materials which have a perovskite type structure. Its typical application is used as a grain boundary barrier layer capacitor. It is also used in oxygen gas sensor, epitaxial growth substrate for high temperature conductor thin films as well as catalytic material. Lithium doped SrTiO_3 not only is used as a substrate for thin film deposition of high T_c superconductors but also has a fundamental interest since stoichiometric SrTiO_3 is highly insulating but a slightly reduced composition shows superconductivity.

Experimental:

The $0.25(\text{Ba}_{0.7}\text{Sr}_{0.3}\text{TiO}_3) + 0.75(\text{BaLa}_2\text{Ti}_3\text{O}_{10})$ powders were prepared through hydroxide co-precipitation method. The starting raw materials were $(\text{BaNO}_3)_2$, $[\text{C}_6\text{H}_9\text{LaO}_6 \cdot \text{H}_2\text{O}]$, $[\text{K}_2\text{-TiO}(\text{C}_2\text{O}_4)_2 \cdot 2\text{H}_2\text{O}]$ and KOH in the form of powders (>99.9% pure.). The powders were weighed in stoichiometric proportions and dissolved in distilled water separately by constant stirring. These separate solutions were then mixed to form the precipitate at room temperature. The total amount of solution was adjusted to 1000 ml. by adding distilled water and heated up to 100°C for 1 hour by adding liquid ammonia as cleaning agent. After heating, the precipitate was allowed to settle down and the clean water was poured outside. The amount of solution was again adjusted to 1000 ml by adding distilled water and liquid ammonia and heated up to 100°C for 1 hour by constant stirring. This procedure of cleaning the solution was done three to four times and finally the precipitate was filtered using 0.4 no.

filter paper in Buckner funnel. The filtered material was kept under Infra-Red (IR) lamp for drying. Finally, the dried material was ground for 2 hours in agate mortar by adding acetone.

The ground powders were calcined at 1050°C for 5 hours. The calcined powders were again ground using acetone for 1 hour and pressed to form the pellets by applying pressure of about 500 MPa. Polyvinyl acetate (PVA) was used as an organic binder for pellet preparation. The prepared pellets were finally sintered in alumina crucible at 1150°C for 7 hours. After sintering the samples were annealed at the rate of $2^\circ\text{C}/\text{min}$ up to 400°C and then brought to room temperature by natural rate of cooling.

Result and discussion:

A) XRD: Figure 1 illustrates the X-ray diffraction pattern of sintered sample. From the XRD pattern it is observed that no additional peaks are observed. The crystal structure and lattice parameters are in good agreement with the reported data (1).

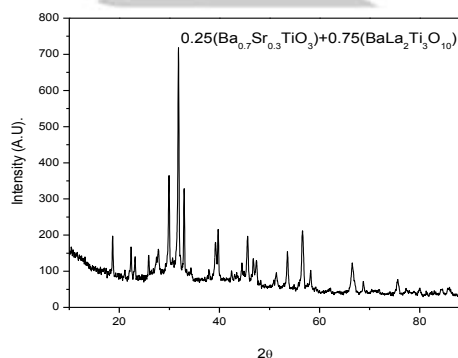


Fig. 1 XRD pattern of $0.25(\text{Ba}_{0.7}\text{Sr}_{0.3}\text{TiO}_3) + 0.75(\text{BaLa}_2\text{Ti}_3\text{O}_{10})$

B) SEM: Using scanning electron microscopy the surface morphology of the materials synthesized has studied, which confirms that the material formed

is sufficiently dense. Figure 2 shows the microstructure of synthesized samples. The SEM photograph gives the grain size of material is about one micrometer and which is far less than the earlier reported (2).

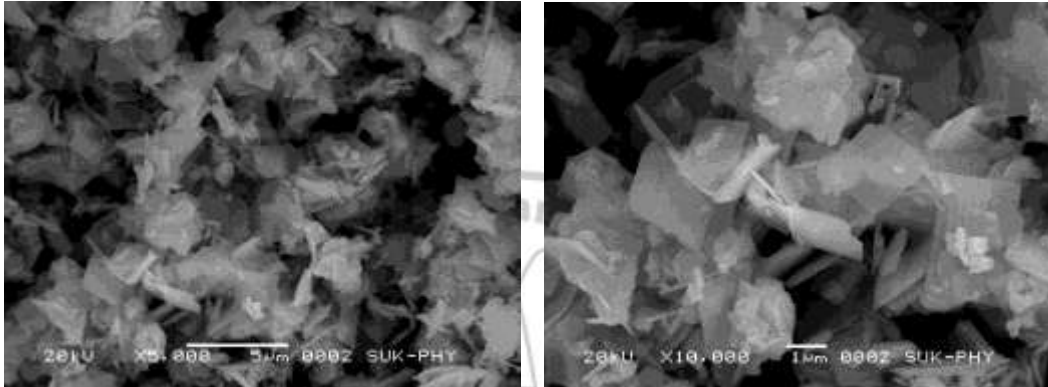


Fig. 2

SEM

photographs of $0.25(\text{Ba}_{0.7}\text{Sr}_{0.3}\text{TiO}_3) + 0.75(\text{BaLa}_2\text{Ti}_3\text{O}_{10})$

C) Dielectric constant: Figure 3 shows variation of dielectric constant with temperature for different frequencies. As, the Curie temperature is below room temperature (1) it gives decreasing trend of dielectric constant. It was found that the dielectric constant of the samples did not significantly depend on the temperature variation (3). However beyond the temperature range of 300 K the dielectric constant observed to slightly increases. Such types of materials are useful in microwave devices which has sufficient dielectric constant at very low loss.

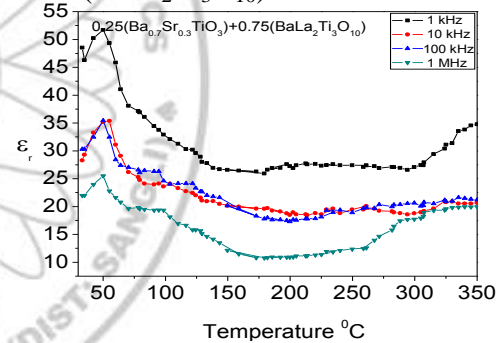


Fig. 3 Variation of Dielectric Constant with temperature for $0.25(\text{Ba}_{0.7}\text{Sr}_{0.3}\text{TiO}_3) + 0.75(\text{BaLa}_2\text{Ti}_3\text{O}_{10})$

Conclusion:

The synthesis method helps to improve the quality of material and brings down the particle size in the range of 1 micrometer. The temperature dependence of dielectric constant remains in the range below 100. The frequency dependence of transition temperature is indicative that the synthesized material is of displacer type.

References:

- 1) S.K. Singh, V.R.K. Murthy, "Crystal structure, Raman spectroscopy and microwave dielectric properties of layered-perovskite $\text{BaA}_2\text{Ti}_3\text{O}_{10}$ (A = La, Nd and Sm) compounds", *Mater. Chem. Phys.*, **160** (2015) 187–193.
- 2) R. Ratheesh, H. Sreemoolanadhan, M.T. Sebastian, P. Mohanan, "Preparation, characterization and dielectric properties of ceramics in the $\text{BaO-Nd}_2\text{O}_3\text{-TiO}_2$ system", *Ferroelectrics*, **211** (1998) 1–8.
- 3) C.H. Lu, Y.H. Haung, "Densification and dielectric properties of barium neodymium titanium oxide ceramics", *Mater. Sci. Eng. B*, **98** (2003) 33–37.

Studies on structural and optical properties of Zn doped CeO₂ nanoparticles

Bhagyashri Bhangare¹, Suresh Gosavi^{1*}

¹ Centre for Advanced Studies in Material Science and Solid State Physics,
Department of Physics, Savitribai Phule Pune University, (Formerly University of Pune)
Ganeshkhind, Pune - 411007, INDIA, Email: swg@physics.unipune.ac.in

Abstract

In the present work, nanocrystalline Zn doped CeO₂ nanoparticles have been synthesized by using chemical co-precipitation method. X ray diffraction (XRD), UV-visible spectroscopy and Transmission Electron Microscopy (TEM) were employed to carry out structural and elemental analysis of synthesized nanoparticles. The CeO₂ nanoparticles were further annealed at 200⁰C, 300⁰C and 400⁰C. The strain developed in the nanocrystallites, during annealing process was studied by using Williamson-Hall (W-H) method from XRD data. The decreasing trend in the strain as a function of increasing temperature was observed. The present material can laid down the valuable interest in the field of sensors and catalysis.

1. Introduction

Among the rare earth compounds, cerium oxide (ceria) is one of the important functional materials with high mechanical strength, thermal stability, excellent optical properties, appreciable oxygen ion conductivity and oxygen storage capacity. The use of CeO₂ nanoparticles in various research fields includes electronic ceramic, gas sensor, catalysis and fuel cells, spintronics and magneto-optoelectronic devices. The ceria doped with various metal oxides like tin oxide (SnO₂), zinc oxide (ZnO) and Iron Oxide (Fe₂O₃) shows most prominent use for CO, methanol, ethanol and acetone sensor application [1]. Ce-Zn oxide binary system has attracted interest in UV attenuators and as an up-converting phosphor host materials [2]. It is found that Zn²⁺ can be impregnated into the lattice of CeO₂ and may weaken the stability of Ce-Zn-O bonds leading to increase in O-vacancies [3]. Metal-doped Ce oxides find applications as clean catalysts in the oxidation of automotive exhaust, anticorrosion materials and gas sensors. The aim of the present work is to study the structural and optical properties of CeO₂ nanoparticles by simple and coast effective route.

2. Experimental

CeO₂ nanoparticles were prepared by using chemical co-precipitation method [2]. Cerium nitrate (0.5 M) is dissolved in 50 ml of ethanol solvent, and the contents are heated to 50 °C under stirring. After 30 min of stirring, 5 ml of ammonia solution is added into the reaction mixture slowly. The solution was turned to light brown colour. The reaction was maintained at 50⁰C for 5 h. The resultant solution was appeared to pale yellow in colour. After

completing the reaction, the precipitates were collected and washed with distilled water and ethanol three times. After washing, precipitate was dried under IR lamp for 5h. The obtained powder was used for further application. The obtained powder sample was annealed at different temperatures (200,300,400⁰C) and used for the further characterization.

Systematic studies on structural changes occurred during annealing process is being carried out using X-ray Diffractometer (Bruker D8-Advanced, Cu_{kα}=1.54Å). The band gap of the synthesized nanocomposites is estimated using UV-Visible spectroscopy (JASCO V-670 spectrophotometer). Surface morphology of the nanoparticles was observed by using Scanning Electron Microscopy (JEOL JSM -6360A analytical Scanning Electron Microscope) and Transmission electron microscopy (Technai G² 20- TWIN (SEI-Netherlands).

3. Results and Discussion

The X-ray diffraction patterns of CeO₂ nanoparticles annealed at different temperatures are given in figure 1a. It shows most preferred diffraction peaks correspond to (111), (200), (220), (311), (400) and (331) belongs to cubic crystal structure with fcc lattice (cubic fluorite structure). The obtained XRD results are well agreement with JCPDS# 81-0792. The crystallite size was calculated by using Debye Scherer formula, which is found to about ~10 nm for synthesized samples. In order to study the strain developed in lattice due to annealing process, the obtained XRD data was analyzed by using Williamson-Hall (W-H) plot [4, 5]. The W-H plots for CeO₂ nanoparticles along with annealed

samples at 200⁰C, 300⁰C and 400⁰C are given in figure 1c respectively. From the plots it is observed that, the strain developed in the lattice is decreases as annealing temperature increases. In further studies we have kept 400⁰C annealing temperature constant, wherein minimum strain in the lattices for CeO₂ nanoparticles is observed. The XRD patterns of Zn

doped CeO₂ nanoparticles are given in figure 1b. It is also observed from the W-H plot (figure 1d) analysis that, the doping of Zn in the CeO₂ increases the strain in the lattice which is found to be decreased after annealing. The crystallite size calculated from W-H plot is well matches with the size calculated from Debye Scherer formula.

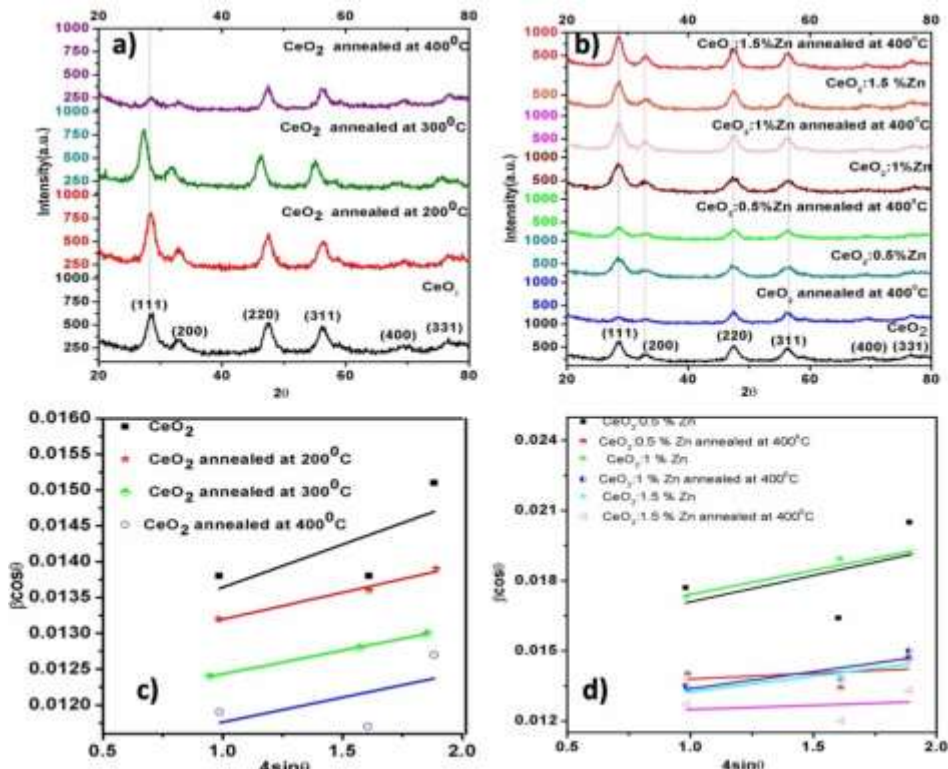


Figure 1. a) XRD patterns of CeO₂ nanoparticles annealed at different temperatures, b) XRD patterns of Zn doped CeO₂ nanoparticles without annealing and annealed at 400⁰C, c) W-H plot for CeO₂ nanoparticles annealed at different temperatures, d) W-H plot for CeO₂ nanoparticles doped with 0.5% and 1% Zn, annealed at 400⁰C temperature.

The UV absorption spectra of Zn doped CeO₂ nanoparticles is given in figure 2. After doping of Zn, it shows the red shift in the UV-Visible absorption spectra; also the same behaviour was observed for annealed samples. Doping of Zn into CeO₂ altered the shape and position of the UV-Visible absorption edge.

The morphology of the CeO₂: 1.5%Zn was studied by using the Transmission Electron Microscopy (TEM) and the corresponding

micrographs are given in figure 3a-e. The size of the nanoparticles is observed to be in the range of 5-10 nm which is also in agreement with the XRD analysis. The nanoparticles are agglomerated and all are in spherical shape. The SAED pattern of the nanoparticles shows ring structure which indicates the polycrystalline nanoparticles. The intense diffraction rings are labelled as (111), (200), (220), (311), (400) and (331) hkl planes.

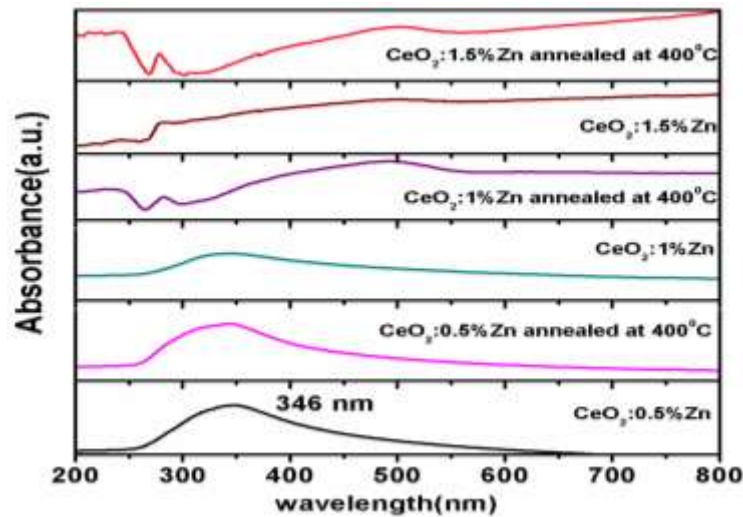


Figure 2. UV-Visible spectra of 0.5% and 1% Zn doped CeO₂ nanoparticles

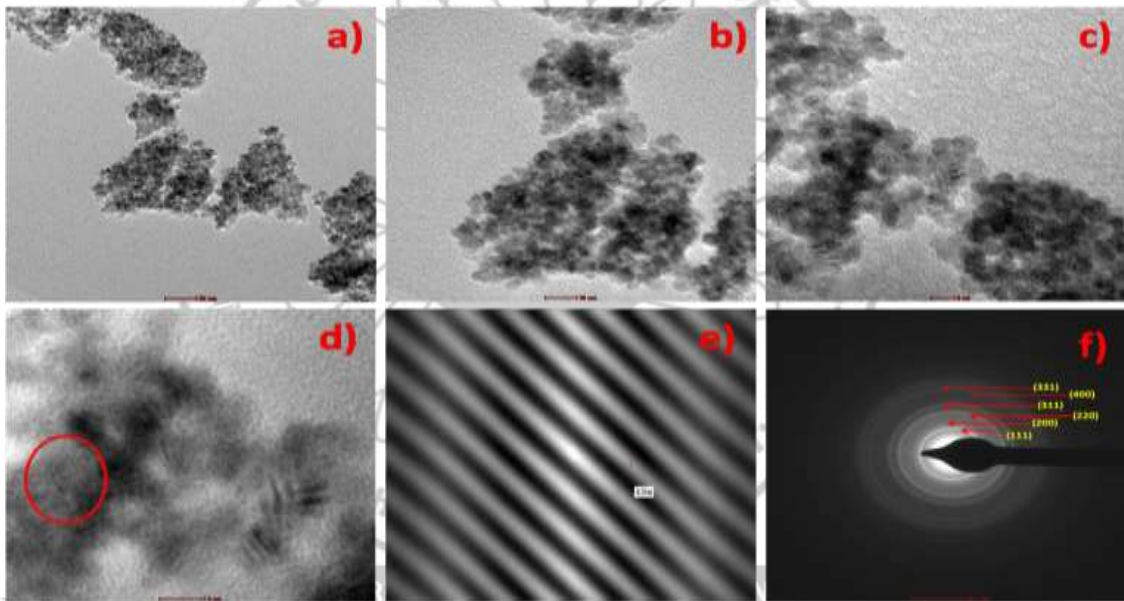


Figure 3. TEM micrographs for CeO₂:1.5%Zn nanoparticles (figure a-c), High resolution TEM showing fringes pattern (figure d, e) and SAED pattern (figure f).

7 – 4. Decer Conclusion

In the present work, the attempt was made to synthesize CeO₂ nanoparticles by using simple chemical co-precipitation. The effect of annealing and Zn doping on the structural and optical properties were studied by using XRD, UV-Visible spectroscopy and TEM. The XRD analysis shows increase in crystallite size of CeO₂ nanoparticles due to annealing. It is also observed from the W-H plot that, the strain developed in the lattice is found to decrease after annealing. The UV-Visible absorption analysis shows change in band gap and red shift as annealing temperature increases from 200 to 400°C. The red shift is also observed in the UV absorption spectra of Zn doped CeO₂ nanoparticles. The present work occupies a valuable interest in studying the elemental compositions and chemical status of Zn, Ce and O in the composites as these aspects are the valuable key parameters in the field of gas sensors, catalysis and heterostructure composite materials.

5. Acknowledgement

One of the authors BB, is grateful for financial support from BARC-SPPU (DAE, GOI-E-177) for providing financial support.

References

- [1]. Jiangyang Liu et al, ACS Applied Materials and Interfaces, 8, 6669–6677 (2016).
- [2]. B. Renganathan et al, Current Applied Physics, 14, 467–471(2014).
- [3]. Hongjing Wu, Liuding Wang, Yiming Wang, Shaoli Guo, Applied Surface Science 258 ,10047–10052(2012).
- [4]. V.D. Mote, Y Purushotham and B.N. Dole, Journal of Theoretical and Applied Physics, vol.5, 2251 (2012).
- [5]. M. Kahouli , A. Barhoumi , A. Bouzid , A. Al-Hajry , S. Guermazi, Superlattices and Microstructures ,vol.85 ,7 (2015).

Synthesis and characterization of Polypyrrole thin film for supercapacitor application

P. M. Kharade^a, S.G. Chavan^a, S.S. Mane^a, S.D. Chavan^b, J.V.Thombare^c, T.R. Mane^d,
S. B .Kulkarni^e, D. J. Salunkhe^{a*}

^a Nano- Composite Research Laboratory, K.B.P. Mahavidyalaya, Pandharpur, 413304.

^b Dayanand College of Arts and Science, Solapur.

^c Department of Physics, Vidnyan Mahavidyalaya Sangola, 413307.

^d Department of Physics, Sangola College Sangola, 413307.

^e Physics Department, The Institute of Science, Mumbai, 400032, India

*Corresponding Author: salunkhedj@rediffmail.com (D.J.Salunkhe)

Abstract:

The paper reports the electrodeposition of polypyrrole (PPy) thin film by galvanostatic mode of deposition on stainless steel substrate. The structural study of polypyrrole film is characterized by X-ray diffraction (XRD). The surface morphological study is carried out with Scanning Electron Microscope (SEM) techniques. The testing of polypyrrole film electrode as a supercapacitor is made with the help of cyclic voltammetry (CV), galvanostatic charge-discharge measurement study. The value of specific capacitance was found to be 361 F.g⁻¹ in 0.5 M Na₂SO₄ aqueous solution at scan rate 5 mV.s⁻¹. However, the value of Specific energy and Specific power of polypyrrole thin film electrode is observed to be 360.60 Wh.kg⁻¹ and 12.32 kW.kg⁻¹.

Keywords: Electrodeposition, Polypyrrole, Supercapacitor, Cyclic voltammetry, Galvanostatic charge-discharge study.

1. Introduction:

Nowadays supercapacitors have attracted much attention due to high energy density than conventional capacitors and higher power density than those of rechargeable batteries [1]. It can be used in variety of applications such as hybrid electric vehicles, memory back-up power sources and light weight electronic devices etc [1-2]. Supercapacitor can be classified into two types based on the charge storage mechanisms namely, Electrochemical double layer capacitor (EDLCs) and Pseudocapacitor (PCs). In EDLCs charge is stored in the non faradic process whereas in pseudocapacitor charge is stored faradaically [3-4]. The electrode materials used in pseudocapacitor are conducting polymer and metal oxide.

Conducting polymers used in supercapacitors are polypyrrole, polyaniline, polythiophene etc. Among these conducting polymers, polypyrrole is one the best conducting polymers thanks to environmental stability, availability of monomer, low cost, toxicity, high porosity, high voltage window, high conductivity in doped states and easy synthesis [5-7]. The electrochemical property of polypyrrole thin film electrode depends on the electrodes preparation methods and also the surface morphology [8] of the electrodes. Shinde et al [9] prepared chemical synthesis of polypyrrole thin film for supercapacitor application. They reported maximum specific capacitance of 329 F.g⁻¹ at scan rate of 5 mV.s⁻¹. So far, many research groups have

essentially focused on modification of polypyrrole based materials, such as preparative parameters including current density, concentration of pyrrole monomer, temperature, p^H value, etc. But there is much less attention has been given for improving specific capacitance of electrode by structuring the polypyrrole film electrode with large porosity.

Here we report an enhanced performance of polypyrrole thin film prepared by electrodeposition method, which shows a high specific capacitance, high coulombic efficiency, high specific energy and power density.

2. Experimental details:

2.1. Synthesis of polypyrrole thin film:

For synthesis of polypyrrole thin film we use an aqueous 0.1 M pyrrole was mixed with aqueous 0.1 M H₂SO₄ and PPy thin films were deposited on stainless steel (SS) substrates via galvanostatic electrodeposition method at constant current density of 5mA.cm⁻² for 10 minutes. Prior to deposition the SS substrates were pre treated with dilute HCl and rinsed thoroughly with distilled water and acetone. The films grown exhibit black colour indicating formation of PPy.

2.2. Characterization techniques:

The deposited film were characterized by X-ray diffraction (XRD) for crystallographic study using Bruker axis D8 Advance Model with copper radiation (K α of $\lambda = 1.54 \text{ \AA}$) in the 2 θ range from 20° to 80°. The surface morphology was studied using scanning electron microscopy (SEM), JEOL

JSM 6390. The cyclic voltammetry, galvanostatic charging-discharging studies were carried out using electrochemical workstation (CHI 660A). An electrochemical cell was constituted using three electrode systems, polypyrrole electrode film as a working electrode, graphite as a counter electrode and SCE as a reference electrode. The 0.5 M Na₂SO₄ was used as an electrolyte for electrochemical supercapacitor cell (ES).

3. RESULTS & DISCUSSIONS:

3.1. Structural and Surface Morphological studies:

Fig. 1(a) show the XRD patterns of polypyrrole thin film deposited on SS substrates. The spectrum of polypyrrole thin film doesn't show any characteristic broad peak. The peaks marks SS in the XRD spectrum is due to stainless steel substrate only. The XRD pattern confirms that the *amorphous* nature of the electrochemically deposited polypyrrole thin film. Similar types of results are reported for polypyrrole thin film deposited by electrochemical deposition [10]. It is well identified that the amorphous nature of material is feasible for supercapacitors application.

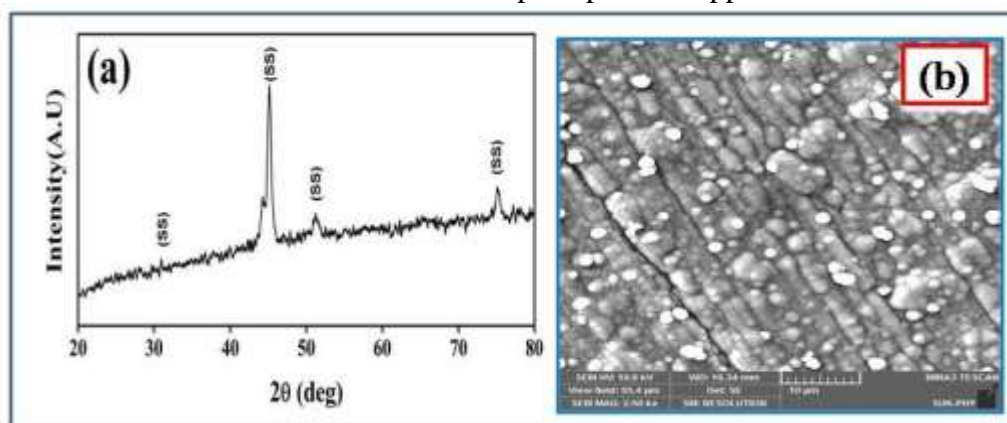


Figure 1:(a) X-ray diffraction; (b) SEM image of polypyrrole thin film.

The surface morphology of polypyrrole film was characterized by SEM instrument and the obtained picture is presented in Fig. 1(b). The SEM image of polypyrrole thin film shows granular (cauliflower) like morphology and they form interconnected network to create an extremely electrically conductive channel inside the thin film electrode which is reasonable for supercapacitor application. The polypyrrole film shows a typically observed homogeneous granular texture on the stainless steel substrate with a film thickness of 2-3 μm. Such morphology is favourable for supercapacitor application which provide higher surface area and fast transportation of ions from electrode to electrolyte.

3.2. Supercapacitive studies:

3.2.1 Cyclic Voltammetric (CV) study:

Specific capacity associated with electrode was carried with the help of cyclic voltammetry

(CV) measurement. Fig. 2(A) shows CV curves of polypyrrole electrode in 0.5 M Na₂SO₄ electrolyte solution in the potential range of -1.0 V to -1.0 V. The scan rate was varied such as 5, 50 and 100 mV.s⁻¹. From Fig. 2(A), it was observed that as scan rate increase current under increases and potential of the curve shift more towards positive and negative directions is indication of the capacitive behaviour of the prepared PPy electrodes. The value of specific capacitance (C_s) was obtained by using the following relation,

$$C_s = C/W \text{ ----- (a)}$$

Where, C is the capacitance in Farad, W is the weight of the active materials.

The polypyrrole electrode shows maximum specific capacitance of 361 F.g⁻¹ at scan rate of 5 mV.s⁻¹. The values of specific capacitance are decreases with increase in scan rate due to uncomfortable redox transitions of inner active sites.

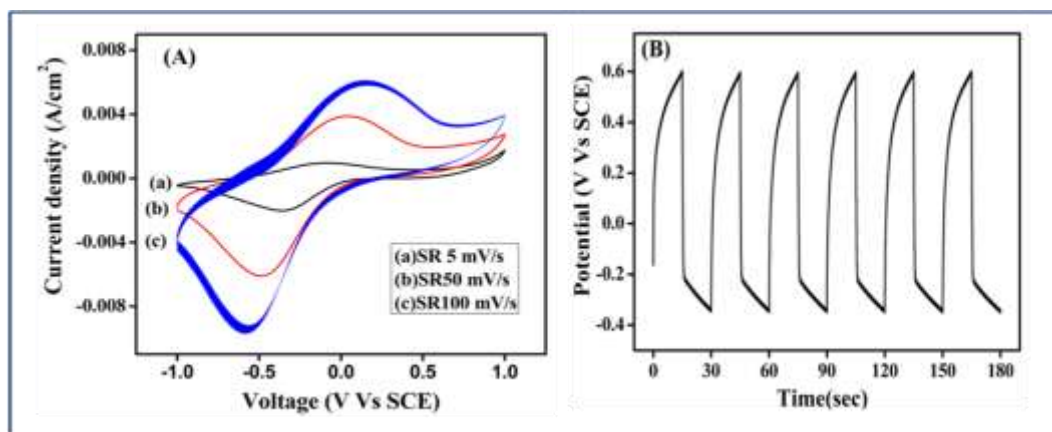


Figure 2:(A) Cyclic voltammetry; (B) Galvanostatic charging-discharging of polypyrrole thin film.

3.2.2. Galvanostatic charge-discharge study:

Fig. 2 (B) shows galvanostatic charging-discharging curves polypyrrole thin film electrode in 0.5 M Na₂SO₄ electrolyte at 5 mA.cm⁻² in order to understand the behaviour of polypyrrole electrode for supercapacitor applications. From the figure 2 (B), it was seen that, curve is not ideal straight line which suggests the process is to be a faradic reaction one. The value of coulombic

efficiency, specific power and specific energy is calculated using the following formulae [11].

It was observed that the polypyrrole electrode had a good electrochemical reversibility with a large specific capacitance (327 F.g⁻¹). The obtained value of specific capacitance from charge-discharge and CV technique are nearly similar.

4. Conclusions:

In summary, we have deposited polypyrrole thin films by galvanostatic electrodeposition method. Galvanostatic mode of electrodeposition is one of the best methods to deposit the uniform and thickness controlled film. The polypyrrole film electrode shows the amorphous and cauliflower like structures, which are feasible for supercapacitor applications. The CV curve concludes that the pseudocapacitive behaviour depending on the micro structural arrangement of the polymeric chain. The polypyrrole thin film shows good value of coulombic efficiency such as 94.54%. Therefore the prepared electrode is superior candidate for supercapacitor application.

Acknowledgment:

One of the authors PMK is grateful to Principal (Dr.) J. G. Jadhav, K. B. P. Mahavidyalaya, Pandharpur for providing laboratory facility and giving inspiration during research work.

References:

1. C. Yang, P. Liu, Y. Zhao. *Electrochim. Acta.* 55 (2010) 6857–6864.
2. [A.K Shukla, S. Sampath, K. Vijayamohan. *Curr. Sci.* 79 (2000) 1656-1661.
3. B.E Conway, *Electrochemical Supercapacitors: Scientific Fundamentals and Technological Applications*, Kluwer-Plenum, New York 1999.
4. D.P Dubal, S.V Patil, W.B Kim, C.D Lokhande, *Mater. Lett.* 65(2011) 2628–2631.
5. M. Kalaji, P. J. Murphy and G. O. Williams, *Synth. Met.*, 102 (1999) 1360-1361.
6. K.R. Prasad, K. Koga, N.Miura, *Chem. Mater.* 16(2004) 1845-1947.
7. L. Fan, J. Maier, *Electrochem. Commun.* 8(2006) 937-940.
8. J.V. Thombare, M.C. Rath, S.H. Han, V.J. Fulari, *Materials Physics and Mechanics.* 16 (2013) 118-125.
9. S. S. Shinde, G. S. Gund, V. S. Kumbhar, B. H. Patil, C. D. Lokhande, *European Polymer Journal*, <http://dx.doi.org/10.1016/j.eurpolymj.2013.07.032>.
10. D.P. Dubal, S.V. Patil, W.B. Kim, C.D. Lokhande, *Materials Letters.* 65(2011) 2628–2631.
11. P.M. Kharade, S.G. Chavan, D.J. Salunkhe, P.B. Joshi, S.M. Mane, S.B. Kulkarni, *Materials Research Bulletin.* 52(2014) 37-41.

Synthesis and Characterisation of ZnO Nanorods

Kardele Sandeep Ambadas and Dhoble Vaishali Shankar

Department of Physics, Dattajirao Kadam Arts, Science and Commerce College, Ichalkaranji

Abstract

The intension of this reserch is the construction of a novel photo-electrochemical cell based on the separation of charge production and charge transporatation. The electron flow through the semiconductor has been identified to be a hopping mechanism which exhibits slow non-exponential current and charge recombination thus limiting efficient charge transfer. ZnO is an important semiconductor material and has been investigated widely for its Catalytic electrical optical and photochemical properties for blue/ultraviolet (UV) Optoelectronic device and piezoelectric devices. This material posses the unique properties such as wide direct band gap (3.4 eV) and large exciton binding energy (60 meV) at room temperature. leading to a wide variety of potential appliat ZnO thin films in different forms have been prepared by various methods. Including anodic alumina template vapor-liquied-solid mechanism. metal-organic vapor phae epitaxial growth and common thermal evaporation method, However, all the above methods always require quite extreme conditions and expensive equipments (BI) the soft chemical processes provides low cost and well controlled method to develop small grain size materials. Many soft solutaion prossesses have been employed to favricate ZnO materials in nanoform includes thermal decomposition reaction in solvent and spray pyrolysis. Layer by layer (LbL) method has proved to be a simple but versatile technique for the construction of self-assembled fims with controlled thickness and comosition ions in catalyst, gas sensors, piezoelectric devices, and solar cells.

In case of CBD solution chemistry is chosen in such way that spontaneous reaction from liquied phase is possible. The formation of solid phase from a solution involves two steps as the nucleation and particle growth. The size of por\article of solid phase is independent upon the relative rats at which these two competing process take place. For any precipitate there is some minimum number of ions or move cute required to produce a stable phase in contact with solution called nucleus. The formation of nucleation is necessary for precipitate formation. The concept of numcleation in a solution is that the clusters of mollecules formed under goes rapid decomposition and particle combine to grow up to certain thickness of the film. Depending on deposition of condition such as bath temperature, stirring rate, PH solution concentration etc. properties and morphologies of deposit ar altered. The film growth can take place by ion-by-ion condensation of material or by adsorption of colloidal particles from the solution on substrate.

1. Introduction

Chemical Properties

ZnO occurs as white powder commonly known as zinc white or as themineral zincite. The mineral usually contains a certain amount of mangamese and other elements and is of yellow to red colour. Crystalline zinc oxide is thermo- chromic, changing from white to yellow when heated and in air reverting to white on cooling This is caused by a very small loss of oxygen at high temperatures to form the non- stoichiometric $Zn_{1-x}O$, where at $800^{\circ}C$, $x = 0.00007$.

Zine ozide is an amphotieric oxide It is nearly insoluble inwater and alcohol but in soluble in (degraded by) most acids such as hydrochloric acid $ZnO + 2HCl \rightarrow ZnCl_2 + H_2O$ (1)

bases also degrade the solid to give soluble zincates $ZnO + 2NaOH + H_2O \rightarrow Na_2(Zn(OH)_4)$ (2)

ZnO reacts slowly with fatty acids in oils to produce the corresponding carboxylates such as oleate or stearate. ZnO forms cement-like products when mixed with a strong aqueous solution of zinc chloride and these are best described as zinc hydroxy chlorides. This cement was used in dentistry.

ZnO also forms cement-like priducts when reacted with phosphoric acid, and this forms the basis of zinc phosphate cements used in dentistry . A major component of zinc phosphate cement produced by this reaction is hopeite, $Zn_3(PO_4)_2O$.

$ZnO + C \rightarrow Zn + CO$ (3)

Zinc oxide reacts violently with aluminum and magnesium powders, With chlorinated rebber and linseed oil on heating causing fire and explosion hazard.

When ointments containing ZnO and water are melted and exposed to ultraviolet light hydrogen perxide is produced.

Crystal Structures

Zinc oxide crystallizes in three forms; hexagonal wurtzite, cuic zinblende, and the rarely observed cubic rock salt. The wartzute structure is most stabel and thus most common at ambient conditions, The zinblende form can be stabilized by growing ZnO on substrates with cubic lattice structure. In both cases. the zinc and oxide are tetrahedral. The rock salt NaCl-yupe structure is only observed at relatively high pressures ---10GPa.

The hexagonal and zincblende ZnO lattices have no inversion symmetry (reflection of a crystal relatively any given point does not transform it into itself). This and other lattice symmetry properties result in piezoelectricity of the hexagonal and zinc blend ZnO and in pyro-electricity of hexagonal ZnO. The hexagonal structure has a point group $6mm$ (Hermann-Mauguin notation) or $C6v$ (Schoenflies notation) and the space group is $P63mc$ or $C6v$. The lattice constants are $a = 3.25 \text{ \AA}$ and $c = 5$

A ; their ratio $c/a = 1.60$ is close to the ideal value for hexagonal cell $c/a = 1.633$ as in most II-VI materials. The bonding in ZnO is largely ionic, which explains its strong piezoelectricity. Due to this ionicity, zinc and oxygen planes bear electric charge (positive and negative, respectively). Therefore, to maintain electrical neutrality those planes reconstruct at atomic level in most relative materials, but not in ZnO - its surfaces are atomically flat, stable and exhibit no reconstruction. This anomaly of ZnO is not fully explained yet.

2.3 : Electronic Properties

ZnO has a relatively large direct band gap of -3.3 eV room temperature therefore, pure ZnO is colorless and transparent. Advantages associated with a large band gap include higher breakdown voltages, ability to sustain large electric fields lower electronic noise, and high temperature and high-power operation. The band gap of ZnO can further be tuned from 3.4 eV by its alloying with magnesium oxide or cadmium oxide. Most ZnO has n -type character, even in the absence of intentional doping. Native defects such as oxygen vacancies or zinc interstitials are often assumed to be the origin of this, but the subject remains, controversial. An alternative explanation has been proposed, based on theoretical calculations, that unintentional substitutional hydrogen impurities are responsible. Controllable n -type doping is easily achieved by substituting Zn with group-III elements Al, Ga, In, or by substituting oxygen with group-VII elements chlorine or iodine, Reliable p -type doping of ZnO remains difficult.

This problem originates from low solubility of p -type dopants and their compensation by abundant n -type impurities, and it is pertinent not

only to ZnO, but also to similar compounds GaN and ZnSe. Measurement of p -type in "intrinsically" type material is also not easy because inhomogeneity results in spurious signals. Current absence of p -type ZnO does limit its electronic and optoelectronic applications which usually require junctions of n -type and p -type material. Known p -type dopants include group -I elements Li, Na, K; group-V elements N, P and As; as well as copper and silver, However, many of these form deep acceptors and do not produce significant p -type conduction at room temperature, Electron mobility of ZnO strongly varies with temperature and has maximum of $\sim 2000 \text{ cm}^2/(\text{V}\cdot\text{s})$ at 80 K . [21] Data on hole mobility are scarce with values in the range $5\text{-}30 \text{ cm}^2/(\text{V}\cdot\text{s})$

Experimental Details

In the formation of ZnO films using CBD most of researchers have used different Zinc ions containing precursor solutions complexes either ammonium hydroxide or sodium hydroxide solution. In our work preparation of ZnO thin film by CBD method was based on the heating of alkaline bath of zinc bath containing the substrate immersed in it. The source of zinc used was 0.1 M zinc nitrate ($\text{Zn}(\text{NO}_3)_2$) and occurs which get dissolved after further addition of aqueous ammonia. The well cleaned glass micro-slides substrates immersed and the bath was heated when the bath attained temperature of 343 K the precipitation started in the bath during the precipitation heterogeneous reaction on the substrate was resulting into the deposition of ZnO.

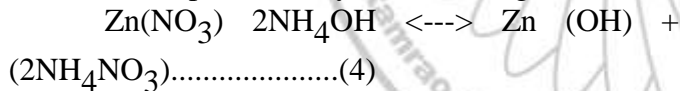
The temperature needed to obtain thin film deposition was at least 333 K . The deposition condition i.e. pH, the temperature and concentration of the bath have been varied to achieve deposition of the good quality, adherent thin films. The thickness of the film was controlled by dipping the substrate into the solution for specific length of time. The growth rate was also depends on the temperature of the bath and stirring condition for higher temperature the growth rate was found as high but for the same temperature the deposition without stirring was used to yield lesser growth rate than with stirring. In case of glass substrate only a very thin white layer of powdery coating was obtained. The pH of the bath was found

to play major role in this deposition irrespective of the concentration of bath . We take solution Zn (NO₃)₂ of .01M add the ammonia sloution in it drop wise, First white precipitate found, further adding of more ammonia until the solution become completely transparent with the help of magnitic stirrer, After completion of this process the glass substrate was depped in solution maintained at 343K for hour.

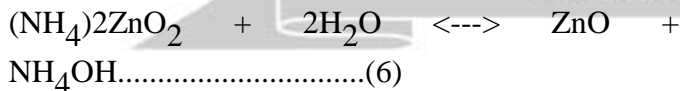
: DEPOSITION MECHANISM

Depending on different preparative conditions, different depostion mechanisam have been proposed in the literature, The chemical bath depostion is based on the formation of solid phase from a solution, which involves two steps as nucleation and particle growth, In the nyclearion, the clusters of molecules formed undergo rapid decomposition and particles combine to grow up to a certain thickness of the film by heterogeneous reactions at the substrate surface, For deposition of ZnO film Zn (NO₃)₂ was used as source of zinc. When ammonia was added to it, white prcipitate of Zn (OH)₂ occurred which got dissolved by addition more ammonia.

This can be represented by the following reactions.



when this solution is heated ZnO film forms on the substrate byte following reaction



: OPTICAL STUDY

In order to study the optical properties of the ZnO thin films deposited by DBD technique. The optical absorption spectra shown fig.

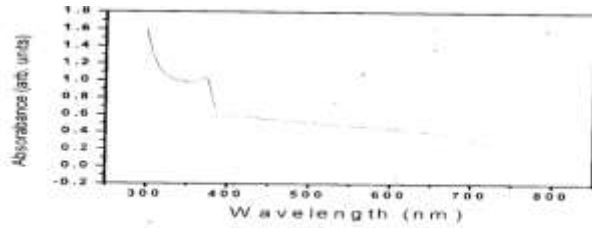


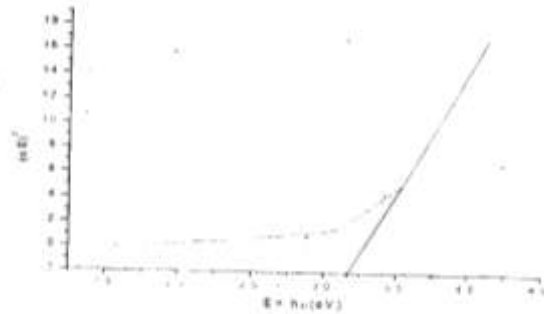
Fig. 1 UV spectra of the ZnO thin film.

By using fig. we can determine the energy band gap of ZnO by using the relation.

Thus the ZnO use like semiconducting material. ZnO is a wide band gap semiconductor that displays liminescent properties in the near ultr violet and the

Visible region. The emission properties of ZnO nenoparticle in the visible region widely depend on their systematic method as they are attributed to surface defect.

Measurement



Estimation of band-gap energy.

The variation of absorbance (au) with wavelength (alfa) for samples is shown in big. The spectra revealed that ZnO have low absorbance in the visible region. However absobandce decreased as the molar concentration of zinc nitrate solution was decreased, which ws consequence of increase in the porosity. Further, the absoption edge was seen to be shifted towards lower wavelength region (blue shift). This shift can be attributed to the decrease in size with molar concentration, The band gap was estimated using the relationship between the absorption coefficient, and the photon enegy. Hv for drect allowed transition, given by equation described in shows the plot of (ahv)² verses (hv) for different molar concentrations of sprayed solution, It is seen from the figure that the band gap is 3.20 eV for sample containing

The dense nano grains; while the porous nanobeads exhibited the band gap of 3.30 eV.

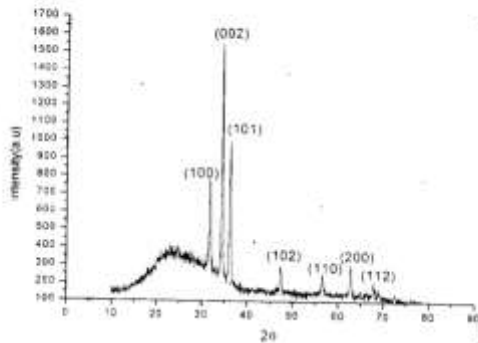


Fig (c) Shows the XRD patterns of samples respectively. The 'd' values of the ZnO obtained at all concentrations are in good agreement with those reported in the ($a^{1/4} 3.2499\text{\AA}$ and $c^{1/4} 5.2065\text{\AA}$) possessing hexagonal wurtzite structure, It is seen from the figure that the films exhibit a strong orientation along c-axis, i.e. along (0 0 2) plane . The intensity of (0 0 2) plane was decreased as the concentration of the solution was decreased, In all cases, the peak intensity of (0 0 2) is relatively high. Confirming its crystalline growth. Generally, (1 0 1) plane is a thermodynamically stable phase however in this case crystalline nanobead architecture may be the reason for preferential orientation along (0 0 2) plane. The (0 0 2) peak was used for grain Size calculation after scanning short-range XRD and measuring the half- width central maxima.

Morphological study

The morphologies of the deposited materials were examined using scanning electron microscopy (SEM).fig. 2(a). 2(b), & 2(c), shows different surface morphology of ZnO thin film. The overall surface structure shows flower like shape without any pore. The morphology of the ZnO film grown on the glass substate was non uniform, powdery, and adherent, In which the precipitated cluster are poorly absorbed on surface of the substrate.

The following fig. shows the photograpoh of Scanning Electron Microscope (SEM)

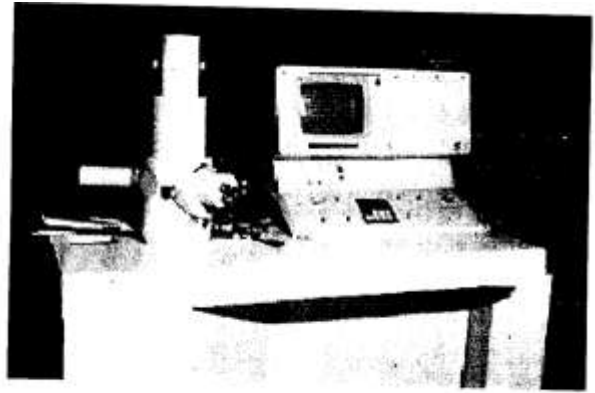


Fig. 5 Scanning Electron Microscope (SEM) (JEOL –JSM 5800)



Fig. 6 SEM image of ZnO thin film



Fig. 7 SEM image of ZnO thin film

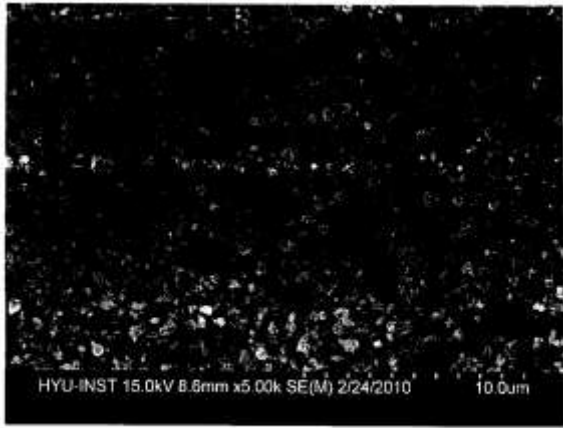


Fig. 8 SEM image of ZnO thin film.

We can also determined resistance as, $R_{air} = \frac{V_{in}}{-V_{air}} \times \text{resistance}$

$$V_{air}$$

Thus activation energy is. $a = \text{slope} \times \text{boltzman constant } eV$

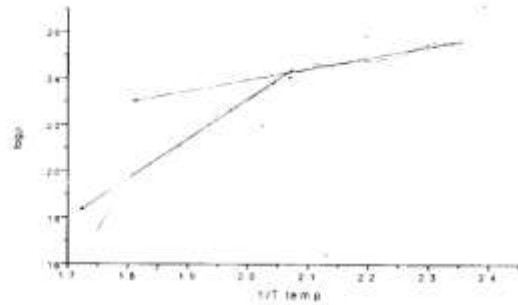


Fig. 9 graph for measuring activation energy.

Thus activation energy measured as 0.73 eV

Activation Energy

The energy that an atomic system must acquire before a chemical process (such as emission or reaction) can occur. The activation energy of materials can determined as follwong manner

$$p = Rt \dots \dots \dots (8)$$

Where,

- p is charge density
- T is thickness of film
- p also defined as

$$p = \frac{RI}{A}$$

Conclusions

The chemical bath deposition technique has been successfully used to prepare the ZnO thin fulm onto glass substrate. The structural. Opotical and morphological studies were carried out. The crystallite size and gap were found near about 3.20 eV. Band gap decreases with increase in crystallite size. The temperatre was found to influence of the crystallite growth of the ZnO at temperature above 50°C it has good crystallion result.

References

- [1]Liang Wang, et.al. Jacs Communication, (2010)10.1021
- [2]Yoshiteru Mizukoshi, et.al. J. Physics Chem, (2000) 10.1021
- [3]N.R. Jana et. al. Langmuir. 16 (2000) 2457.
- [4]K. Mallick at.al. Mater. Chem. Phys. 97 (2006) 283.
- [5]M.N. Nadagouda et.al. RSC Adv. 2 (2012) 7540
- [6]N. Cheval at.al. Nanoscale Res. Lett. 7 (2012) 182.
- [7]N.R. Jana et.al. J. Phys. Chem. B. 103 (1999) 115–121.

INTERNATIONAL CONFERENCE ON
ADVANCES IN MATERIALS SCIENCE



INTERNATIONAL CONFERENCE ON
ADVANCES IN MATERIALS SCIENCE

7 – 8 December 2016